Influence of secondary electron spectra on the enhanced effectiveness of ion beams

Einfluss von Sekundärelektronenspektren auf die erhöhte Wirksamkeit von Ionenstrahlen
Zur Erlangung des Grades eines Doktors der Naturwissenschaften (Dr. rer. nat.)
genehmigte Dissertation von Tabea Pfuhl aus Dieburg
Tag der Einreichung: 11.05.2021, Tag der Prüfung: 28.06.2021

1. Gutachten: PD Dr. Michael Scholz
2. Gutachten: Prof. Dr. Barbara Drossel
Darmstadt – D 17

TECHNISCHE UNIVERSITÄT DARMSTADT

GSI

Physics Department
GSI Biophysics

Influence of secondary electron spectra on the enhanced effectiveness of ion beams
Einfluss von Sekundärelektronenspektren auf die erhöhte Wirksamkeit von Ionenstrahlen

Doctoral thesis by Tabea Pfuhl

1. Review: PD Dr. Michael Scholz
2. Review: Prof. Dr. Barbara Drossel

Date of submission: 11.05.2021
Date of thesis defense: 28.06.2021

Darmstadt – D 17

Bitte zitieren Sie dieses Dokument als:
URN: urn:nbn:de:tuda-tuprints-191574
URL: http://tuprints.ulb.tu-darmstadt.de/19157

Dieses Dokument wird bereitgestellt von tuprints,
E-Publishing-Service der TU Darmstadt
http://tuprints.ulb.tu-darmstadt.de
tuprints@ulb.tu-darmstadt.de

Erklärungen laut §9 der Promotionsordnung

Hiermit versichere ich, dass ich die vorliegende Dissertation selbstständig angefertigt und keine anderen als die angegebenen Quellen und Hilfsmittel verwendet habe. Alle wörtlichen und paraphrasierten Zitate wurden angemessen kenntlich gemacht. Die Arbeit hat bisher noch nicht zu Prüfungszwecken gedient.

Darmstadt, 11.05.2021

T. Pfuhl

Abstract

A detailed understanding of physical and biological effects resulting from radiation exposure is crucial in the field of radiation research. Besides the hazardous character of radiation in the context of radiation protection and space research, radiation is applied beneficially in cancer radiotherapy. The radiation effect depends on several factors such as dose, energy and type of radiation. Therefore, radiobiological models are essential to predict the corresponding biological effects. Such models are crucial for instance in particle therapy for the optimization of radiation treatment plans or in space research for risk assessment for astronauts. The local effect model (LEM) is a widely applied model for the prediction of cellular radiation effects and enables the prediction of the increased relative biological effectiveness (RBE) of ion radiation in comparison to photon radiation. Over the years, the LEM was validated for several ion species and biological endpoints such as the prediction of cell survival in-vitro and in-vivo, the induction of secondary cancers, dose rate or cell cycle effects. In this work, a systematic validation was performed for the current version of the model, LEM IV, by comparing its RBE predictions for cell survival to 610 measurements of a comprehensive database. The analysis enabled a quantification of the systematic underestimation of RBE at larger ion energies, which was observed in previous model validations with single measurement datasets. Additionally, the LEM was further validated by predicting cell survival after mixed irradiations with ions and photons and comparing the results to measurement data.

In order to analyze the origin of the observed model deviations in the critical high-energy regime, a more profound understanding of deoxyribonucleic acid (DNA) lesion induction and interaction is necessary. In the LEM, the effect calculation after radiation exposure is based on the spatial distribution of double-strand-breaks (DSBs) in the DNA. For the determination of the DSB distribution in an ion track, the number of DSBs induced per dose unit is adopted from photon measurements. In this context the dose refers to energy depositions in nanometer-sized volumes. Thereby, the simplifying assumption is made that photon and ion radiation induce the same number of DSBs per dose unit. The DSBs are, however, predominantly induced by secondary electrons, which are ejected by the primary radiation species. Furthermore, it is well known that low-energetic electrons are more effective in DSB induction in comparison to high-energetic ones due to high ionization densities at electron track ends. Since the secondary energy spectra are substantially different for ions and photons, also different numbers of DSBs per dose unit are expected. In this work, this difference was quantified determining the mean DSB induction effectiveness of different radiation species based on their secondary electron spectra. To assess the mean effectiveness of a secondary electron spectrum, a quantification of the DSB induction effectiveness of single electrons is crucial. Therefore, the probability for DSB induction was derived from the mean free path between two ionizations along an electron track assuming that at least two ionizations are necessary within a defined threshold distance in order to induce a DSB. The DSB induction model was successfully applied to determine the effectiveness of different ion species but also for several photon radiation qualities. Furthermore, these findings were incorporated in the LEM, leading to a new model version LEM V. The more precise description of the DSB induction in dependence of the primary radiation species led to more accurate RBE predictions for cell survival after ion irradiation. Especially the observed underestimation of RBE for higher energetic ions for LEM IV was improved, leading to more precise effect predictions not only for radiotherapy applications but also for radiation risk assessment in space research.

Zusammenfassung

Ein detailliertes Verständnis der physikalischen und biologischen Effekte nach Strahlenexposition ist von entscheidender Bedeutung in der Strahlenforschung. Neben dem schädlichen Charakter von Strahlung im Rahmen des Strahlenschutzes und der Weltraumforschung wird Strahlung in der Krebstherapie vorteilhaft eingesetzt. Der biologische Effekt von Strahlung hängt von verschiedenen Faktoren wie Dosis, Energie und Art der Strahlung ab, weshalb radiobiologische Modelle wichtig sind, um die entsprechende biologische Wirkung vorherzusagen. Solche Modelle werden beispielsweise in der Partikeltherapie zur Optimierung von Strahlenbehandlungsplänen oder in der Weltraumforschung zur Risikobewertung für Astronauten eingesetzt. Das Lokale Effekt Modell (LEM) ist hierbei ein vielfältig verwendetes Modell zur Vorhersage von zellulären Strahlungseffekten und ermöglicht die Vorhersage der erhöhten Relativen Biologischen Wirksamkeit (RBW) von Ionenstrahlung im Vergleich zu Photonenstrahlung. Im Laufe der Jahre wurde das LEM für verschiedene Ionenspezies und biologische Endpunkte validiert, wie zum Beispiel für die Vorhersage des Zellüberlebens in-vitro und in-vivo, die Induktion von Sekundärkrebs sowie Dosisraten- oder Zellzykluseffekte. In dieser Arbeit wurde die aktuelle Version des Modells, LEM IV, systematisch validiert, indem RBW-Vorhersagen für Zellüberleben mit 610 Messdatensätzen aus einer umfassenden Datenbank verglichen wurden. Diese Analyse ermöglichte eine Quantifizierung der systematischen Unterschätzung der RBW bei größeren Ionenenergien, die schon bei früheren Modellvalidierungen mit einzelnen Datensätzen beobachtet wurde. Zudem wurde das LEM weiterführend validiert, indem das Zellüberleben nach gleichzeitiger Bestrahlung mit Ionen und Photonen vorhergesagt und die Ergebnisse mit entsprechenden Messdaten verglichen wurden.

Um den Ursprung der beobachteten Modellabweichungen im kritischen Hochenergiebereich zu analysieren, ist ein tieferes Verständnis der Induktion und Interaktion von DNA-Schäden erforderlich. Im LEM basiert die Effektberechnung nach Bestrahlung auf der räumlichen Verteilung von Doppelstrangbrüchen (DSBs) in der DNA. Zur Bestimmung der DSB-Verteilung in einer Ionenspur wird die Anzahl der pro Dosiseinheit induzierten DSB aus Messungen mit Photonen übernommen, wobei sich die Dosis in diesem Zusammenhang auf Energiedepositionen in nanometergroßen Volumina bezieht. Dabei wird die vereinfachende Annahme getroffen, dass Photonen- und Ionenstrahlung die gleiche Anzahl an DSBs pro Dosiseinheit induzieren. Die DSB werden jedoch überwiegend durch Sekundärelektronen erzeugt, die von den Primärstrahlungsspezies freigesetzt werden. Darüber hinaus ist bekannt, dass niederenergetische Elektronen aufgrund der hohen Ionisationsdichten an den Enden von Elektronenspuren im Vergleich zu hochenergetischen Elektronen wirksamer sind. Da sich die Sekundärelektronenspektren für Ionen und Photonen wesentlich unterscheiden, wird entsprechend auch eine unterschiedliche Anzahl an DSB pro Dosiseinheit erwartet. In dieser Arbeit wurde dieser Unterschied quantifiziert, um die mittlere DSB-Ausbeute verschiedener Strahlungsspezies basierend auf ihren Sekundärelektronenspektren zu bestimmen. Um die mittlere Ausbeute eines solchen Spektrums beurteilen zu können, ist eine Bewertung der DSB-Ausbeute einzelner Elektronen von entscheidender Bedeutung. Dazu wurde die Wahrscheinlichkeit für eine DSB-Induktion aus der mittleren freien Weglänge zwischen zwei Ionisationen entlang einer Elektronenspur abgeleitet, wobei angenommen wurde, dass mindestens zwei Ionisationen innerhalb eines definierten Schwellenabstands erforderlich sind, um einen DSB zu induzieren. Dieses DSB-Induktionsmodell wurde anschließend erfolgreich angewendet, um die Wirksamkeit verschiedener Ionenspezies und Photonenstrahlungsarten zu bestimmen. Darüber hinaus

wurde das Modell in das LEM integriert, was zu einer neuen Modellversion LEM V führte. Die detailliertere Beschreibung der DSB-Induktion in Abhängigkeit von der primären Strahlungsspezies resultierte in einer genaueren RBW-Vorhersage für Zellüberleben nach Ionenbestrahlung. Insbesondere die zuvor beobachtete Unterschätzung der RBW für höherenergetische Ionen im LEM IV wurde verbessert, was zu präziseren Effektvorhersagen nicht nur für Strahlentherapieanwendungen, sondern auch für die Bewertung des Strahlenrisikos in der Weltraumforschung, führte.

Table of Contents

1. Introduction

Natural background radiation is always present due to decays of heavy, naturally occurring radionuclides as well as through cosmic radiation [1]. Cosmic radiation is mostly deflected by the earth's magnetic field but with regard to manned travel to Mars it comprises a major unsolved challenge due to its hazardous effects on the human body [2, 3]. Besides these undesirable effects, radiation can also be applied beneficially for clinical purposes as for instance during X-ray or computer tomography (CT) scans. Furthermore, it is used in cancer therapy where radiation is applied locally to the body to inactivate malign cells. According to the World Health Organization (WHO), cancer is the second leading cause of death with nearly 10 million deaths in 2020 [4, 5]. The three main treatment options are surgery, chemotherapy and radiation therapy, where the latter is of major concern in this work. Conventionally, patients are irradiated with photons in radiotherapy treatments. However, already in 1946 Wilson recognized the therapeutic advantages of ions for radiotherapy [6]. One of those advantages is the inverse depth dose profile, leading to small doses in the entrance channel of the ion beam and a large dose concentration towards the end of the ions' range, forming the so-called Bragg peak [7]. Therefore, the maximum dose can be delivered in a deep-seated tumor whereas healthy tissue proximal and distal to the tumor is protected. A further advantage of the application of ions in radiotherapy is their increased relative biological effectiveness (RBE) in comparison to photon radiation [8]. In the 1990s a carbon ion pilot project started at GSI Helmholtzzentrum für Schwerionenforschung GmbH (GSI) where cancer patients were treated with carbon ion radiation [9]. In this context the local effect model (LEM) was developed in order to predict the RBE of carbon ions in dependence of their kinetic energy. Nowadays, the model is applied clinically in several ion therapy facilities [9, 10, 11, 12]. Apart from the LEM, other biophysical RBE models are available. For instance the Katz model developed in 1967 [13, 14] predicts the biological effect based on the amorphous track structure of ions, which was later adopted in the LEM. Japanese clinics apply the so-called microdosimetric-kinetic model (MKM) that calculates radiation effects from microdosimetric quantities [15, 16, 17, 18].

Over the years, the LEM was constantly optimized leading to the current version LEM IV. The model was validated for various radiobiological endpoints as for instance the prediction of in-vitro experimental data over a large range of different ion species from protons to oxygen ions [11, 19, 20, 21]. Next to in-vitro data, the model was found to accurately represent experimental in-vivo RBE data. This was shown by comparing model predictions to experimental data on the dose tolerance of the rat spinal cord [22, 23, 24]. Additionally, several radiobiological aspects as the induction of secondary cancers, dose rate or cell cycle effects as well as rejoining kinetics are found to be accurately reproduced by the LEM IV [12, 25, 26, 27]. This large variety of validation cases demonstrated strengths and weaknesses of the LEM IV for RBE prediction and already revealed a systematic underestimation of RBE in the high energy regime for carbon ions [12, 23]. In order to quantify these model deviations, the first aim of this work is a systematic and quantitative validation of the LEM IV by comparing its RBE predictions to a large dataset of 610 cell survival measurements collected in the Particle Irradiation Data Ensemble (PIDE) database [28, 29]. The data includes experiments with various ion species ranging from protons to iron ions as well as several cell types of varying radiosensitivity.

The second aim of this work is the analysis of the origin of the observed deviations in the RBE predictions of the LEM IV, especially in the critical high energy regime. Therefore, a more profound understanding of the induction of cellular lesions and their relevance for biological effects is essential. The biological damage to the cell, which determines its fate after radiation exposure is determined by the spatial distribution of double-strand-breaks (DSBs) within the deoxyribonucleic acid (DNA) [30, 31, 32]. Thereby, the relevance of the spatial clustering of DNA lesions on the nanometer and micrometer scale are well reported with regard to the radiation effect [33]. These two spatial scales are included in the LEM as follows:

- **Micrometer scale:** Several DSBs within DNA subvolumes of approximately half a micrometer are classified as complex DNA damages [12]. This idea was further conceptually validated in this work by applying the LEM IV to simulate the effect after mixed irradiations with ions and photons. Thereby, the radiation mixing process was performed by superposition of the DSB patterns of the single radiation species and by simulating their interaction on the micrometer scale [34].
- **Nanometer scale:** Damage interactions on the nanometer scale are considered in the calculation of the DSB distribution in an ion track. To calculate the probability for the production of a DSB, the number of DSBs induced per dose unit is taken from corresponding measurements with photons. Thus, it is assumed that photons and ions induce the same number of DSBs per dose unit. However, measurement and simulation studies show that the number of DSBs induced per dose unit is unique for every radiation quality [35, 36]. Therefore, it shall be tested in this work if this simplified assumption is the origin of the RBE deviations observed in the LEM IV for high energetic ions.

Consequently, the third aim of this work is a quantification of the differences between radiation species with regard to their effectiveness for DSB induction. DSBs are mainly induced by secondary electrons liberated by the primary radiation species [37]. Several previous works showed the dependence of the DSB induction effectiveness of electrons on their kinetic energy. Low-energetic electrons of approximately 100-1000 eV are reported to be 2-4 times more effective in comparison to higher-energetic electrons of a few MeV [38, 39, 40]. Therefore, a model is derived in this work for the description of the electron RBE for DSB induction as a function of their energy. With the combined knowledge about secondary electron spectra for different primary radiation species in connection with the DSB induction effectiveness of single electrons, the mean DSB yield can be assessed as a spectral weight for any desired primary radiation species.

The final aim of this work was to include this more detailed description of lesion interaction on the nanometer scale in the LEM and with that to enable more precise model predictions. The new model version LEM V, thus, includes a more profound calculation of the DSB distribution within an ion track based on the underlying secondary electron spectra. Up to model version LEM IV, the DSB distribution in an ion track was calculated directly from the local dose distribution in the ion track. In this new approach, the mean RBE for DSB induction of the liberated secondary electrons was additionally included in the calculation.

This thesis is structured as follows: After the presentation of the physical and biological background in Chapter 2, the methods applied in this work are described in Chapter 3. The results are split into three chapters. Chapter 4 includes the systematic validation of the LEM IV, chapter 5 the derivation and first application of the DSB induction model and Chapter 6 covers its implementation in the LEM framework. These chapters are connected to a direct discussion and short conclusion of the presented results. Finally, a complete conclusion is drawn together with an outlook for future works in Chapter 7.

2. Physical and biological background

Natural background radiation is present at all times in form of electromagnetic and particle radiation. Its major source are α-particles produced in decays of heavy, naturally occurring radionuclides such as radium [1]. Additionally, natural background radiation includes cosmic radiation, which is, however, mostly deflected by the earth's magnetic field. Nevertheless, in the planning of manned travel to Mars it comprises a major unsolved challenge due to its hazardous effects on the human body [2, 3]. Cosmic radiation includes protons from solar particle events as well as light ions and high energy and charge (HZE) particles from galactic cosmic radiation. Next to natural background radiation, humans are regularly exposed to artificial radiation for instance during the performance of an X-ray or CT scan. Next to diagnostic purposes, radiation is used in cancer therapy where it is applied locally to the body to inactivate malign cells.

Energy deposition by radiation in matter leads to excitations and ionizations of atoms. Ionization events occur if the radiation quality possesses sufficient energy to eject at least one orbital electron when interacting with an atom. The physical background of the interaction of ionizing radiation with matter is introduced in detail in Sec. 2.1. The frequency of such ionization processes and their local distribution are of highest relevance in radiobiological research. They can lead to DNA damages of different degrees of complexity that determine the fate of a cell. The corresponding biological aspects are described in Sec. 2.2.

2.1. Interaction of ionizing radiation with matter

To quantify the amount of energy absorbed in a certain mass, the property of absorbed dose D is commonly used. The absorbed dose is defined by the International Commission on Radiation Units and Measurements (ICRU) as the mean deposited energy dE per mass element dm [41]:

$$D = \frac{dE}{dm}\,. \tag{2.1}$$

The dose is given in units of Gray [Gy], where 1 Gy $=$ 1 J/kg. In the following sections, electromagnetic and particle radiation are introduced. Their interaction mechanisms with matter are explained in detail as these determine the amount and type of damage produced in a biological target determining its fate.

2.1.1. Electromagnetic radiation

Electromagnetic radiation covers a wide spectrum of energies. Lower-energetic electromagnetic radiation such as radio waves, microwaves, infrared radiation or visible light are non-ionizing. However, according to the common radiobiological knowledge, ionizations are the origin of DNA damage. As the damage to the DNA and its consequences are investigated in this work, the aforementioned types of lower-energetic

electromagnetic radiation are not further discussed here. Higher-energetic electromagnetic radiation as X-rays or γ-rays carry enough energy to ionize atoms. They interact with matter according to three different processes, two of which lie in the energy range relevant in radiobiology research and clinical applications:

A) **Photoelectric process:** Figure 2.1 A shows the concept of the photoelectric process, in which an electron of an inner atomic shell is liberated by an incident photon. In this process, which is dominant at photon energies below ≈30 keV, the photon loses all its energy [42]. Part of the photon energy is used to overcome the binding energy of the electron and the remaining energy is transferred to the liberated electron as kinetic energy. If the liberated "secondary" electron obtains enough kinetic energy to ionize more atoms, it is called a δ-electron. The vacancy in the atom's shell is filled by an electron of the outer shells or by a free electron from outside the atom. Due to the electron's change in energy levels, the difference in energy is emitted in form of a photon. As the atom's energy levels are discrete these photons carry defined energies known as characteristic X-rays.

B) **Compton effect:** The Compton effect, which is depicted in Fig. 2.1 B dominates in an energy range of ≈30 keV-30 MeV in water/soft tissue [42]. The incoming photon interacts with a loosely-bound electron of the outer shells of an atom of the absorbing material. Consequently, a part of the photon energy is transferred to the electron as kinetic energy. The photon is deflected and its reduced energy is reflected in a decreased wave length.

C) **Pair production:** In the pair production process the energy of a photon is converted into an electron and a positron of 511 keV each. This process is not depicted in Fig. 2.1 as it occurs at photon energies that exceed energies relevant in this work.

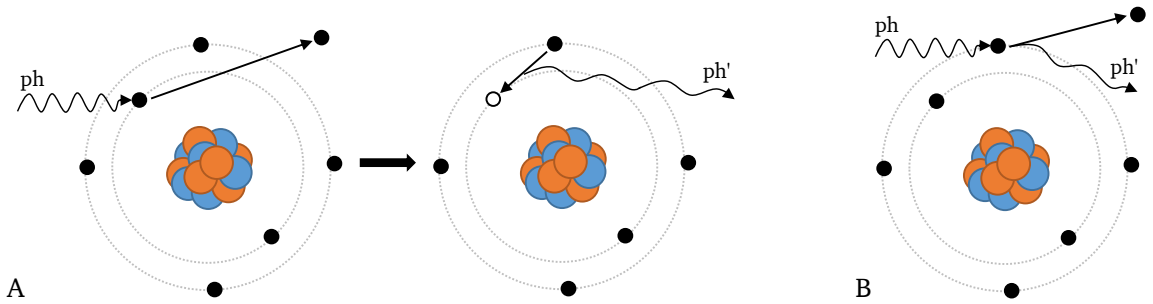

Fig. 2.1.: Schematic representation of two electromagnetic interaction processes, which are relevant in this work. The photoelectric process (A) is dominant at lower photon energies, whereas the Compton effect (B) occurs more often at higher photon energies.

In radiobiological experiments, cell or tissue probes are in most cases not irradiated by monoenergetic photons but rather by a photon spectrum with a broad energy range. Commonly used are X-ray spectra produced by an X-ray tube. In an X-ray tube, electrons are accelerated by a high voltage towards an anode of a specific material (typically wolfram). When the electrons interact with the atoms of the anode, both, Bremsstrahlung and characteristic X-rays are produced. Bremsstrahlung is the result of the deflection of an electron in the atomic nucleus' Coulomb field. If an accelerated electron liberates a target electron from an inner shell of the target atoms, the vacancy is filled by an electron of an outer shell, leading to the emission of a photon of a defined energy, the material-specific characteristic X-rays. The full X-ray spectrum follows the shape of a triangle, meaning that low-energetic photons dominate the spectrum. As low-energetic photons have a short range in matter and lead to additional dose within the first millimeters to centimeters in the target medium, they are filtered out for clinical purposes, leading to the typical shape of an X-ray

spectrum. In Fig. 2.2 A an X-ray spectrum is shown for a wolfram anode with voltage $U = 250$ kV and 7 mm beryllium, 1 mm aluminum and 1 mm copper as filter material. The acceleration voltage of the X-ray tube determines the maximum energy of produced photons. The mean photon energy is positioned at approximately half of the maximum photon energy.

If biological tissue or cells are irradiated with photons, the photons themselves only play a minor role in the DNA damage process. The secondary electrons, however, which are liberated by the primary photons dominate with regard to the induction of ionizations leading to DNA strand breaks. The secondary electron energy spectrum resulting from an irradiation with such an X-ray spectrum is depicted in Fig. 2.2 B. The characteristic "box shape" of the spectrum is visible, meaning that all electron energies occur in a similar amount.

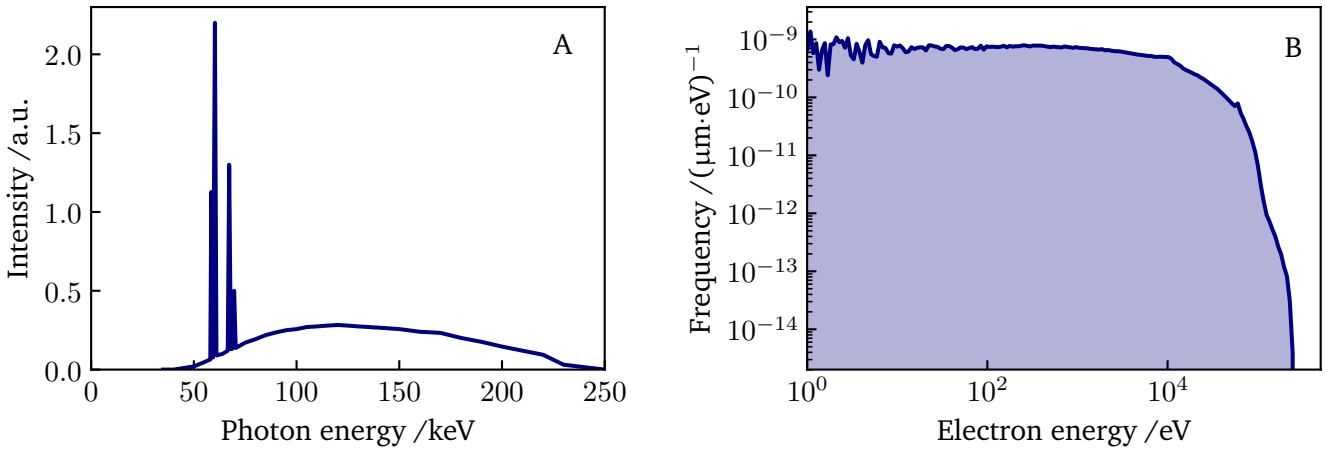

Fig. 2.2.: A: X-ray energy spectrum produced by an X-ray tube at a voltage of 250 kV. B: Secondary electron energy spectrum (only first generation) produced by X-rays as shown in (A) impinging on a water target. The electron energy spectrum is simulated with the Monte Carlo (MC) Code Geant4-DNA. The length scale in the y-label of panel B refers to the path traveled by the incident photons in water.

The energy loss of photons traversing matter can be described by the absorption law, where the intensity I decreases exponentially with the traversed material thickness d [42]:

$$I(d) = I_0 \cdot e^{-\mu d}, \tag{2.2}$$

with the initial radiation intensity I_0 at the entrance of the absorption material. The extend to which the radiation flux is reduced while it passes a certain material depends on the material-specific attenuation coefficient μ.

As described above the primary photon radiation liberates electrons while it loses its energy traversing material. These secondary electrons carry their transferred kinetic energy further into the material. Thus, they influence the shape of the depth-dose-profile and form the so called "dose build-up effect". The peak of the dose profile is reached as soon as the highest-energetic electrons stop, which were liberated directly at the entry position of the photons into the target. Consequently, the depth at which the electron spectrum reaches an equilibrium state increases with increasing incident photon energy. However, the spatial extension of the build-up region is small in relation to typical tumor positions even for high-energetic photons. The photon depth-dose-profile is depicted in Fig. 2.3.

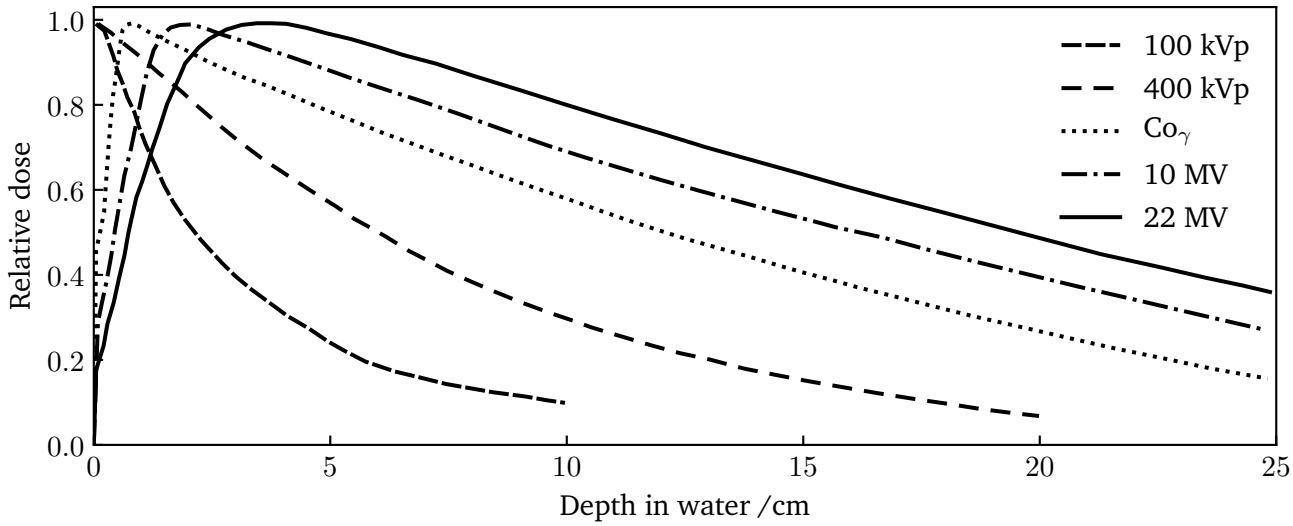

Fig. 2.3.: Depth-dose-profile for several photon radiation qualities. Modified from [43].

2.1.2. Ion radiation

Similar to electromagnetic radiation, charged particles interact with the atoms of the traversed target material. The following section focuses on ion radiation, whereas specific details of the interaction of electron radiation with matter are discussed in Sec. 2.1.3. The three predominant types of ion interactions relevant in ion beam therapy are schematically illustrated in Fig. 2.4 [44]. They are described in the following section in detail.

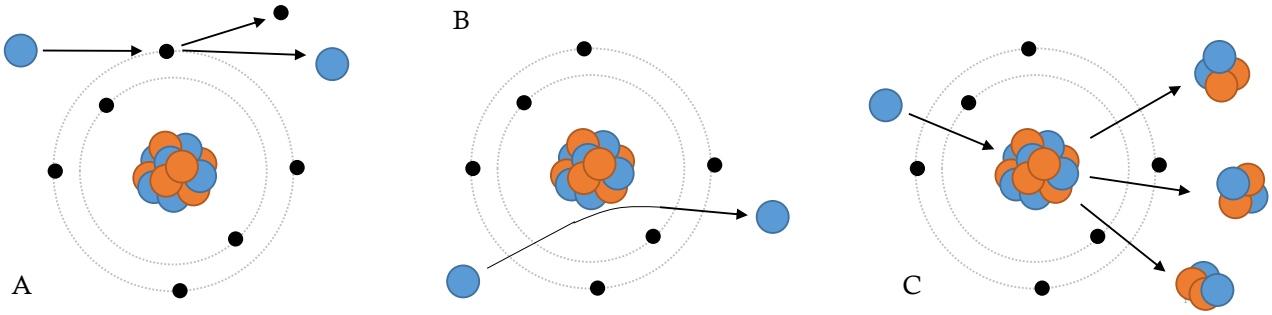

Fig. 2.4.: Schematic representation of the main interaction processes of an ion with the target atoms and nuclei. The processes are shown exemplary for a proton colliding with a carbon atom. A: Inelastic Coulomb interaction with an atomic electron, B: Elastic Coulomb interaction with a target nucleus, C: Inelastic nuclear interaction.

A) **Coulomb interactions with atomic electrons:** The ions' energy loss is dominated by inelastic Coulomb interactions of the primary particle with the atomic target electrons (ionizations and excitations). The ionization process is schematically illustrated in Fig. 2.4 A. After the collision, the ion continues on its path due to its by far larger mass compared to the electron mass ($m_\mathrm{p} \approx 1832 \times m_\mathrm{e}$). In contrast to that, the liberated electrons can be released in any direction. Several different projectile-electron interaction processes influence the electron energy spectrum. If the impact parameter is

significantly larger than the atomic radius, the particle can be deflected elastically by the Coulomb field of the whole atomic shell [42]. If the incident particle excites or ionizes the atom in a "soft collision" it loses a few eV and changes its direction. The liberated electrons carry small energies. Soft collisions are responsible for ≈50% of the energy loss of charged particles [42]. If the impact parameter of the collision is in the range of the atomic radius, also interactions with electrons of inner atomic shells become possible. In such "hard collisions", the ion's energy loss is larger compared to soft collisions. Hard collisions are also described as binary encounter collisions [45] as they can be understood as a simple two-body collision. The liberated high-energetic electrons are called δ-electrons. They continue to travel further into the medium losing their energy mainly by soft collisions.

B) **Coulomb interactions with the atomic nucleus:** Fig. 2.4 B shows a schematic representation of an elastic Coulomb interaction of the ion with the atomic nucleus. If an ion passes a nucleus within a small distance, the projectile is deflected due to repulsive Coulomb forces. As a result of the similar masses of the two positively charged interaction bodies the ion's deflection angle is typically small. This process contributes to the lateral broadening of an ion beam while it traverses material.

C) **Nuclear reactions:** The third process is a nuclear interaction, as illustrated in Fig. 2.4 C. Inelastic nuclear interactions are rare in comparison to the two other interaction processes described above. During such an interaction the projectile transmits a part of its kinetic energy to the atomic target nucleus initiating the ejection of target fragments. These nuclear fragments usually carry low kinetic energies and relatively high atomic numbers. Therefore, even though the number of fragments is small in a radiation field, they can become relevant concerning dosimetric aspects. At ion energies applicable for radiobiology research protons only induce target fragmentation whereas heavier ions can also undergo projectile fragmentation leading to a dose tail behind the dose maximum [46].

Similar to photons, ions themselves only contribute little to DNA damage. The majority of DNA strand breaks are initiated by secondary electrons, which are ejected due to ionizations of the target by the projectile ions. Secondary electrons carry their energy further into the target before they deposit it in the medium. Consequently, also for ion radiation an electron build-up effect is present in the depth-dose-profile. The minimum kinetic energy for an electron to cause further ionizations is ≈12 eV, corresponding to the smallest electron binding energy of liquid water. The mean energy dissipated per ionization event is defined by the W-value and is ≈34 eV in dry air [42]. The electrons liberated by inelastic Coulomb interactions of incident ions with target electrons show an electron spectrum that follows an $1/E^2$ dependence on electron energy. Exemplary electron energy spectra are shown in Fig. 2.5 for protons of energies between 1 and 1000 MeV. At ≈540 eV a peak is visible due to Auger processes [47]. The prerequisite for the production of an Auger electron is a vacancy of an electron of an inner atomic shell. If the vacancy is filled by another electron, which stems from the atom's outer shells, the released energy can be transferred to a further atomic electron resulting in its liberation [42]. The Auger peak energy (≈540 eV) is in the range of the electron binding energy of atomic oxygen in the 1s orbital. The liberated secondary electrons cause further ionizations when traversing material. Thus, electrons of later generations are produced that are, however, not included in the spectra shown in Fig. 2.5.

Due to the interaction processes described above, the ions lose their energy in the target material until they stop. The particles' energy loss per path length dE/dx is called stopping power and is divided into two contributing parts: collision stopping power S_{col} and radiative stopping power S_{rad} [42, 44]:

$$S_{\mathrm{tot}} = \left(\frac{dE}{dx}\right)_{\mathrm{tot}} = S_{\mathrm{col}} + S_{\mathrm{rad}}\,. \tag{2.3}$$

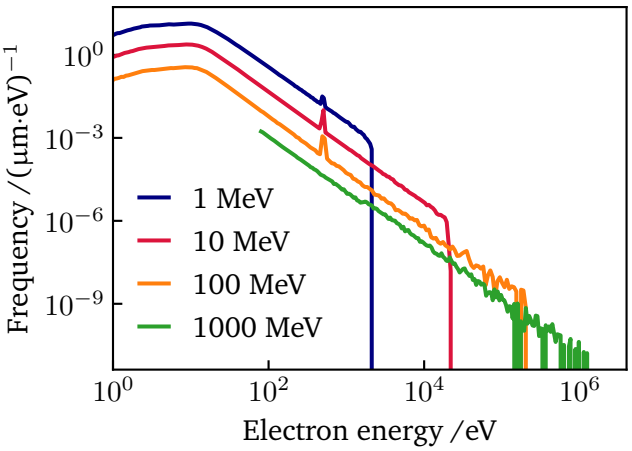

Fig. 2.5.: Secondary electron energy spectra produced by monoenergetic protons impinging on a water target. The spectra are calculated with the MC code Geant4-DNA. For protons with energies >100 MeV Geant4-DNA models are not available. Thus, classical Geant4 models are used that limit the electron production to electron energies >78 eV. The length unit in the y-label refers to the path traveled by the incident proton.

As the radiative stopping power only plays a minor role for ion radiation at radiobiological energies, the corresponding function is not stated explicitly but can be found in the literature [42]. Heavy charged particles transfer their energy to a medium mainly through Coulomb interactions of the charged particles with orbital electrons of the absorber atoms. Inelastic Coulomb interactions between heavy charged particles and nuclei of absorber atoms are negligible and thus ignored [43]. The collision stopping power can be approximated by the "Bethe-Bloch" formula as:

$$S_{\mathrm{col}} = \left(\frac{dE}{dx}\right)_{\mathrm{col}} = C_0 \frac{Z}{A}\frac{z^2}{\beta^2} \cdot R_{\mathrm{col}}(\beta)\,, \tag{2.4}$$

with

$$C_0 = \rho 4\pi N_{\mathrm{A}} \left(\frac{e^2}{4\pi\ \epsilon_0}\right)^2 \frac{1}{m_{\mathrm{e}}c^2} = \rho 4\pi N_{\mathrm{A}} r_{\mathrm{e}}^2 m_{\mathrm{e}} c^2\,, \tag{2.5}$$

and ρ as the density of the absorber, N_{A} as the Avogadro number and r_{e} as the classical electron radius. Z and A denote the atomic number and mass of the target material, z the projectile's charge and β its relative velocity [42]. The dimensionless residual function $R_{\mathrm{col}}(\beta)$ includes special model corrections. For instance, a shell correction is relevant at low energies if the particle's velocity is close to the velocity of atomic electrons. Equation (2.4) clarifies the dependence of the stopping power on specific particle properties: The energy loss is proportional to the inverse square of the particle's velocity and proportional to the square of the ion's charge. Furthermore, the stopping power depends on the physical characteristics of the target material, which is included by the term (Z/A). Low-energetic ions can capture electrons from the target material with a certain probability, decreasing the effective charge of the projectile. To account for this effect the empirical Barkas formula can be applied to replace the charge z in Eq. (2.4) with the effective charge z_{eff} [41]:

$$z_{\mathrm{eff}} = z\left[1 - e^{-125\beta z^{-\frac{2}{3}}}\right]. \tag{2.6}$$

The range R of a charged particle can be calculated as the integral of the reciprocal stopping power over the

projectile's energy E:

$$R(E_0) = \int_0^{E_0} \left(-\frac{dE}{dx}\right)^{-1} dE\,. \tag{2.7}$$

The stopping power is shown in Fig. 2.6 in dependence on ion energy in the therapeutic energy range. In general, it is visible that the stopping power of an ion increases with decreasing energy. For heavier ions, a further decrease in stopping power is observed at very small energies.

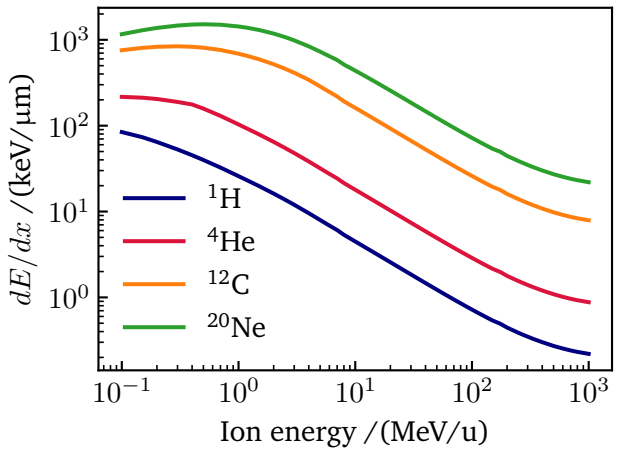

Fig. 2.6.: Energy loss of various projectile ions in water as a function of the ion energy, which are applied in this work.

In physics, the term stopping power is commonly used to describe the energy loss of a particle. In radiobiology, however, the term linear energy transfer (LET) is frequently applied in this context. Whereas the stopping power can be understood as the effect of an absorber material on the particle beam, the LET is defined as the energy transfer of the ion to the surrounding medium per path length. It is a measure of the degree of ionization in the traversed medium. The LET is typically given in keV/µm and is identical to the electronic stopping power of the ion.

The curve describing the energy loss of a particle as a function of depth is the so-called "Bragg curve". While the particle traverses medium, its energy loss increases until it reaches a maximum, the "Bragg peak". After the energy loss peak, the curve drops to zero. The characteristic shape of a Bragg curve is shown in Fig. 2.7 for protons and carbon ions of different energies with the applied dose calculated based on the linear energy transfer LET of the considered particle, the particle fluence F and the mass density ρ of the target material [41]:

$$D = \frac{LET \cdot F}{\rho}\,. \tag{2.8}$$

The characteristic shape of the ions' energy loss with depth is one of the main advantages of using ions in cancer therapy in comparison to conventional irradiation with photons. While photons show their maximum dose already after a few millimeters to centimeters under the skin, for ions the position of the Bragg peak can be chosen in a way that the maximum dose is applied even to deep seated tumors. By varying the ion energy, the position of the Bragg peak in depth can be varied, which allows a very selective irradiation of the tumor volume. By superposition of several Bragg curves of ions with different energies, spatially extended tumors can be treated.

Fig. 2.7.: Depth-dose-profile for photons (18 MV), protons (135 MeV) and carbon ions (254 and 300 MeV/u). Modified from [48].

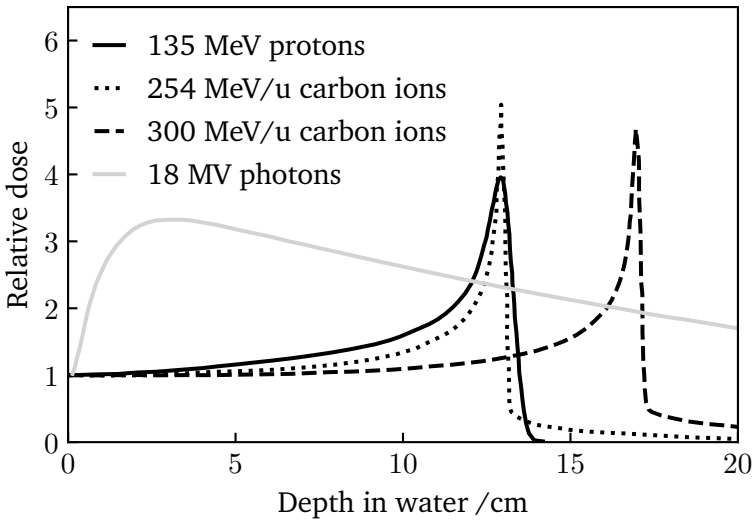

2.1.3. Electron radiation

For photon and ion radiation, electrons dominate in the induction of biological damage in the radiation field as they are created as secondary particles. However, electrons do not only occur as secondary particles in radiation therapy but can also directly be used as projectiles for clinical purposes. Like ions, electrons interact with matter by inelastic Coulomb interactions with the target atoms' electrons leading to excitations and ionizations of the target atoms (see Fig. 2.4 A). Furthermore, electrons interact by elastic Coulomb interactions with target electrons or nuclei (see Fig. 2.4 B). In contrast to ions, electrons do not interact with the atomic nucleus by strong interactions if the impact parameter of the collision is in the range of the radius of the atomic nucleus. Electrons only interact with the nucleus via Coulomb forces, remain free particles and are thus not absorbed by the nucleus [42]. For the calculation of the stopping power of electrons, the radiative stopping power needs to be included in contrast to ion radiation [42]. Electrons cause further ionizations when traversing the target until they stop. Similar to photon and ion radiation, electrons as primary particles show an electron build-up effect with depth in the target, which is caused by electrons of later generations. The full depth-dose-profile resulting from the characteristic slowing down of electrons in matter is depicted in Fig. 2.8 and resembles a similar course as for photons.

Fig. 2.8.: Depth-dose-profiles for electron radiation of different energies. Modified from [43].

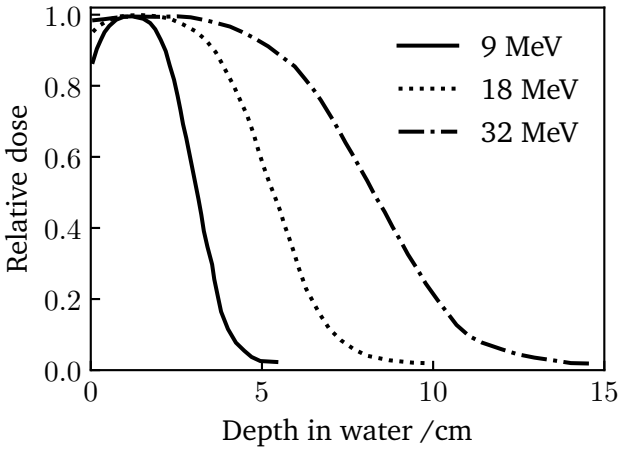

Low-energetic electrons as they are produced by e.g. by ultrasoft X-rays (0.1-5 keV) as secondary particles are highly effective in the induction of biological damage. Similar as for ions, the electrons' LET increases while they slow down and passes a maximum at an electron energy of ≈100-200 eV [47]. This leads to a local accumulation of energy depositions on the nanometer scale just before the electrons stop. As the DNA has a diameter of ≈2 nm, the so-called electron "track ends" are highly effective in DNA damaging by inducing strand breaks through clustered ionizations. Therefore, the physical characteristics of low-energetic electrons are of great interest in the radiobiological research community and also highly relevant in this work. The ionization pattern of a 1 keV electron is depicted in Fig. 2.9. The initial electron starts at position (0,0); each ionization is marked as a dot. Two more δ-electrons are created in hard collisions and their paths are indicated in orange and red. For all three electrons, an increased ionization density is observed towards the end of their range. The biological effectiveness of different particle species concerning cell inactivation or DSB induction is further described in Sec. 2.2.5 with regard to the particles' kinetic energy.

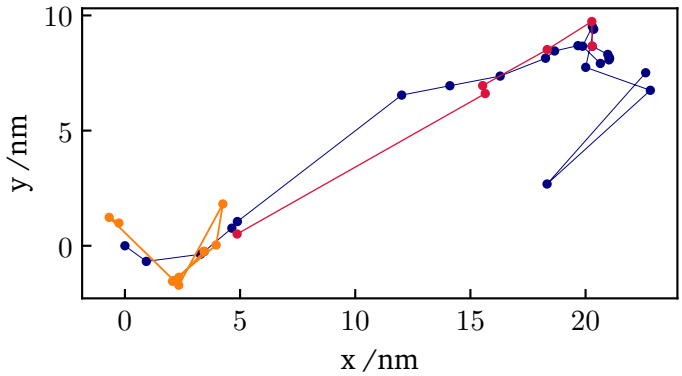

Fig. 2.9.: 2D-Ionization pattern of a 1 keV electron in water simulated with Geant4-DNA. The electron is initialized at coordinates (0,0) (blue). Along its track two δ-electrons are liberated (red, orange). Each ionization is depicted as a dot.

2.1.4. Track structure

As mentioned above, the degree of biological damage is determined by the microscopic energy deposition pattern of the considered radiation species. Thus, the knowledge about the so-called track structure is essential to assess the biological effect after irradiation with different radiation species. The track structure can be described as the pattern of discrete physical interactions with defined spatial positions. Such track structures can be obtained in two ways: First, they can be calculated by Monte Carlo (MC) radiation transport codes and, second, track structures can be approximated by an amorphous track structure model, which describes an average energy deposition as a function of the radial distance r to the ion track center. The energy depositions follow a r^{-2} dependence meaning that the majority of energy is deposited close to the ion track center. For many radiobiological applications the consideration of an amorphous track structure is sufficient to describe the local dose distribution induced by radiation. All radiation species including ions, electrons and photons form a track structure when traversing matter. The term "track structure" and "(radial) dose profile" are commonly used to describe the local energy deposition pattern of ions, which is in line with the usage of those terms in this work.

Various detailed MC radiation transport codes exist and enable the simulation of discrete energy depositions leading to a track structure (Geant4-DNA [47, 49, 50, 51], TRAX [52, 53, 54], PARTRAC [55], etc.). The functionality of such codes is described in detail in Sec. 3.4. The main limitation of the application of radiation transport codes for the calculation of track structures is the large uncertainty for low-energy cross sections of physical interaction processes due to lack of measurement data. Additionally, several MC codes introduce a low-energy cut-off below which particles are not tracked any further and their remaining

kinetic energy is deposited locally. This cut-off is introduced as for many simulation applications with larger structural scales, as e.g. for the simulation of macroscopic dose, the spatial resolution of very low-energetic particles is negligible. However, this affects only low energetic particles and MC codes are able to well reproduce the experimentally observed r^{-2} dependence of the local dose as a function of radial distance r to the ion track center. Figure 2.10 shows the 3D track structure for a proton and a carbon ion with an energy of 1 MeV/u in water. Each dot represents an energy deposition along the ion's track, including ionizations and excitations. The amount of energy deposited is indicated with the color bar in units of eV. For both ions it can be seen that the ion continues on its path without major change of direction while it liberates electrons of different energies. High-energetic δ-electrons exit the track center and induce further ionizations in a cylinder around the track axis. The higher LET of the carbon ion in comparison to protons at the same kinetic energy is expressed by the larger density of the energy deposition pattern. As a result carbon ions exhibit an increased RBE compared to protons at the same kinetic energy in MeV/u. Both ion tracks were simulated with Geant4-DNA.

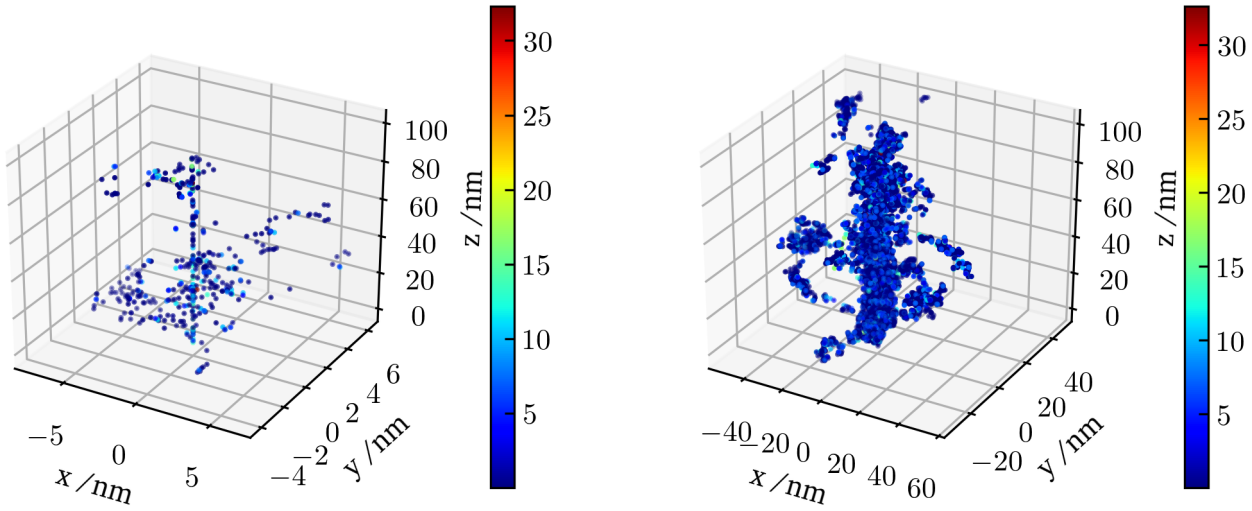

Fig. 2.10.: Track structure of a 1 MeV proton (left) and a 1 MeV/u carbon ion (right). Local energy depositions are shown as dots, the amount of energy deposited in each event is indicated by color in units of eV. The track structures are calculated by the MC code Geant4-DNA, which is introduced in Sec. 3.4. Note the different length scales on the x- and y-axes.

The detailed simulation of all particle interactions and energy depositions by MC simulations requires large amounts of computation time, especially for heavy high-LET particles. Therefore, the concept of amorphous track structure can be applied to describe the radiation track structure: The energy depositions of all particles are approximated by a radial dose profile. The amorphous track structure is described by the local dose $D(r)$, which mainly shows a r^{-2} dependence with r as the distance to the ion track center [56]. Several models exist for the description of the amorphous track structure based on the Coulomb interactions of ions. The most prominent models are briefly described in the following and a comparison of all presented approaches is shown in Fig. 2.11 [57].

Katz model: The approach derived by Butts and Katz in 1967 is based on several simplifying assumptions [13]: First, all electrons are assumed to be ejected perpendicular to the ion's path; and second, their range in water R is described by an empirical formula $R = kE_\mathrm{e}$ with the electron's energy E_e and the constant k.

The radial dose distribution $D(r)$ is consequently described by:

$$D(r) = \begin{cases} \dfrac{C z_{\text{eff}}^2}{2\pi\beta^2 r}\left(\dfrac{1}{r} - \dfrac{1}{r_{\text{p}}}\right) & \text{for } r < r_{\text{p}}\,, \\ 0 & \text{for } r \geq r_{\text{p}}\,, \end{cases} \tag{2.9}$$

with $C = 4\pi e^4 m_{\text{e}}^{-1} c^{-2}$, the effective ions charge z_{eff} as defined in Eq. (2.6) and β as the velocity of the ion relative to the speed of light c. The parameter $r_{\text{p}} = kE_{\max}$ describes the maximum radius reached by electrons, which carry a maximum kinetic energy $E_{\max}$. As a consequence of its definition, the dose is undefined at the ion track center ($r = 0$).

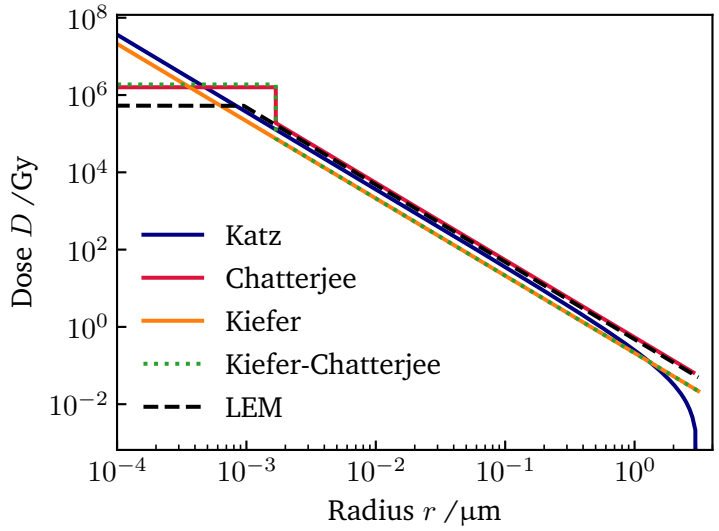

Fig. 2.11.: Radial dose profile calculated according to several amorphous track structure models for 10 MeV/u ^{12}C ions. The track structure of the LEM refers to model version IV.

Kiefer model: The Kiefer model considers a more detailed description of the underlying physical interactions [56]. Collision dynamics are included to describe the dependence of the electrons' deflection angle on the energy of an electron. Thus, electrons are not assumed to be all ejected perpendicular to the ion track but with an energy dependent angle leading to an ellipsoid shape describing the maximum range of electrons (see Sec. 3.3 for more details on the Kiefer model). However, in accordance to the Katz model, secondary electrons are assumed to travel on straight lines. Furthermore, the electron range is described by an empirically found formula $R \propto E_{\text{e}}^{1.7}$, and the maximum penumbra radius can be derived based on the Kiefer formalism as Eq. (3.14). Finally, the dose profile is calculated by Eq. (2.10); its derivation can be found in [56]:

$$D(r) = \begin{cases} 1.25 \cdot 10^{-4} \dfrac{z_{\text{eff}}^2}{\beta^2} \dfrac{1}{r^2} & \text{for } r < r_{\text{p}}\,, \\ 0 & \text{for } r \geq r_{\text{p}}\,. \end{cases} \tag{2.10}$$

The model well reproduces the r^{-2} dependence of dose as a function of the radial distance r to the ion track center. However, similar to the Katz model, the dose is not defined in the track center at $r = 0$.

Chatterjee model: The amorphous track structure model derived by Chatterjee and Schäfer [58] in 1976 distinguishes between the track's core and its penumbra. In the core, a constant dose is assumed up to the core radius r_{c}, which depends on the energy of the primary particle as $r_{\mathrm{c}} = 11.6\ \mathrm{nm}\ \cdot \beta$. The penumbra region is defined between the core radius r_{c} and the penumbra radius r_{p}, whose value is determined experimentally.

$$D(r) = \begin{cases} \dfrac{1 + 2\pi K}{2\pi r_{\mathrm{c}}^2} \cdot LET & \text{for } r < r_{\mathrm{c}}\,, \\ \dfrac{2K}{r^2} \cdot LET & \text{for } r_{\mathrm{c}} \leq r < r_{\mathrm{p}}\,, \\ 0 & \text{for } r \geq r_{\mathrm{p}}\,, \end{cases} \tag{2.11}$$

with $K = \left[4\pi \cdot \ln(\sqrt{e} \cdot \frac{r_{\mathrm{p}}}{r_{\mathrm{c}}})\right]^{-1}$. The model considers a semi-empirical equipartition: Approximately half of the energy stored in the core of the track is dispensed for ionization events and the other half of the energy deposited in the penumbra is dispensed for excitation.

Kiefer-Chatterjee model: The Kiefer-Chatterjee model combines features of both aforementioned models with the value of K made variable to partition between core and penumbra region. Kiefer's approach is applied to describe the dose in the penumbra region whereas Chatterjee's model is used in the track core. The Kiefer-Chatterjee model is applied in the RBE-predictive microdosimetric-kinetic model (MKM) to describe the amorphous track structure for several ion species [59]. More details on the formalism of the MKM can be found in Sec. 2.3.3. The dose profile according to the Kiefer-Chatterjee concept is calculated as:

$$D(r) = \begin{cases} \dfrac{1}{\pi r_{\mathrm{c}}^2} \left(\dfrac{LET}{\rho} - 2\pi K_{\mathrm{p}} \ln\left[\dfrac{r_{\mathrm{p}}}{r_{\mathrm{c}}}\right] \right) & \text{for } r < r_{\mathrm{c}}\,, \\ 1.25 \cdot 10^{-4} \dfrac{z_{\mathrm{eff}}^2}{\beta^2} \dfrac{1}{r^2} \equiv K_{\mathrm{p}} \dfrac{1}{r^2} & \text{for } r_{\mathrm{c}} \leq r < r_{\mathrm{p}}\,, \\ 0 & \text{for } r \geq r_{\mathrm{p}}\,. \end{cases} \tag{2.12}$$

Local effect model: The amorphous track structure model used in the local effect model (LEM) also differentiates between a track core and penumbra region [60]. The radius of the inner core is calculated as $r_{\mathrm{min}} = v_{\mathrm{i}}/c \cdot r_{\mathrm{c}}$ where v_{i} is the velocity of the ion, c the speed of light and the constant r_{c}. The outer radius of the ion track corresponds to the maximum lateral range of liberated electrons and is calculated by $r_{\mathrm{max}} = \gamma E^{\delta}$. The parameter r_{max} is given in µm, the ion's energy E in MeV/u, $\gamma = 0.062$ and $\delta = 1.7$ as derived in the Kiefer model [56]. The radial dose profile is proportional to the LET and anti-proportional to the square of the radial distance. It is consequently calculated as:

$$D(r) = \begin{cases} \dfrac{\lambda \cdot LET}{r_{\mathrm{min}}^2} & \text{for } r < r_{\mathrm{min}}\,, \\ \dfrac{\lambda \cdot LET}{r^2} & \text{for } r_{\mathrm{min}} \leq r < r_{\mathrm{p}}\,, \\ 0 & \text{for } r \geq r_{\mathrm{p}}\,, \end{cases} \tag{2.13}$$

where λ denotes a normalization constant to ensure that the LET is reproduced by the radial integral of the track for a medium with density ρ:

$$\lambda = \frac{1}{\pi\rho\left[1 + 2\ln\left(\frac{r_\mathrm{p}}{r_\mathrm{min}}\right)\right]}\,. \tag{2.14}$$

The dose profiles calculated according to all presented models follow a similar shape, as visible in Fig. 2.11. They all describe the decrease of dose with distance to the ion track center with an r^{-2} dependence. Furthermore, the dose is assumed to be proportional to the LET in all described models. The Katz model and the Kiefer model do not consider a separate track core as the other three models, leading to the fact that for them the dose is not defined at the track center itself ($r = 0$). The calculation of the penumbra radius varies slightly among the different models but is always calculated as a function of the ions' kinetic energy. As a result, low-LET particles such as high-energetic protons exhibit a large track radius but a low dose in the track center. In contrast to that, high-LET particles, such as low-energetic carbon ions, show narrow tracks with large local doses in the track center. The dependence of the radial dose profile on ion species and energy is visualized in Fig. 2.12 exemplary for the amorphous track structure model applied in the LEM.

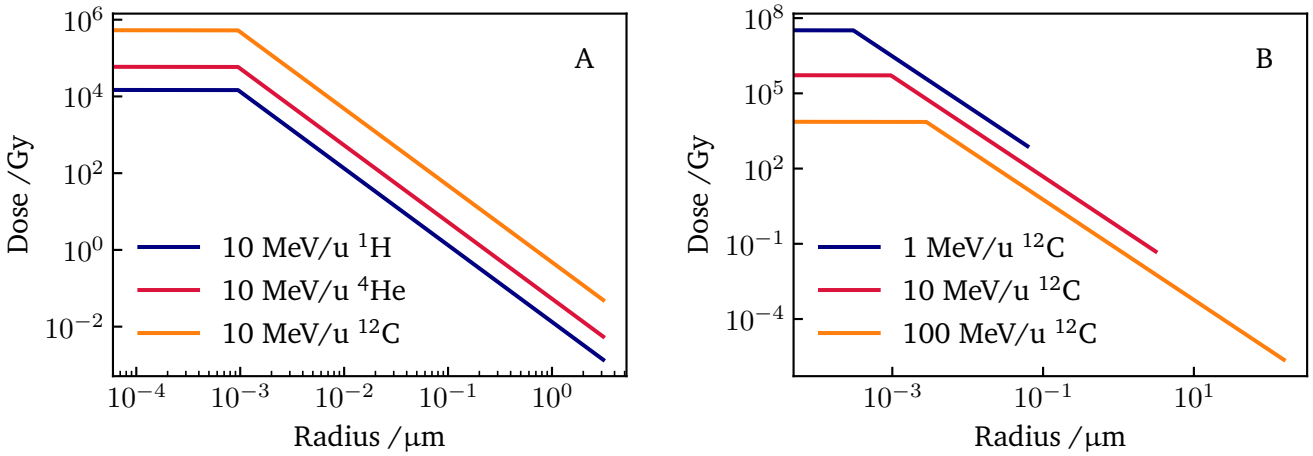

Fig. 2.12.: Amorphous track structure for different ion species (A) and energies (B) as applied in the LEM. Outside the flat inner core of the track structure the dose profile follows a r^{-2} dependency. All dose profiles are plotted up to their maximum radius.

2.2. Biological radiation effects

Radiation damage occurs via a chain of multiple processes stretched over many spatial and temporal orders of magnitude [1]. The physical interactions described in the previous sections take place in a time span in the order of 10^{-15} seconds. Together with chemical interactions that take place in the order of 10^{-6} seconds, they can lead to the breakage of a molecular bond. The period between such a breakage and the expression of a biological effect can, however, be hours or days for cellular damage. In the case of cancer, it can take several years until a macroscopically visible cancer has developed. If the damage was induced in a germ cell leading to a hereditary mutation, it may only be expressed after generations.

The origin of radiobiological effects are damages at the DNA, initiated by ionizations. These DNA damages might occur e.g. in form of single-strand-breaks (SSBs) or DSBs, which are described in the following section together with the concept of direct and indirect action of radiation. At the end of the chapter, the concept of RBE is introduced, which can be used to quantify the effectiveness of different radiation species concerning cell killing or other radiobiological endpoints.

2.2.1. DNA damages

The deoxyribonucleic acid (DNA) is a large molecule with a double-helical structure, which contains the genetic information. It is stored in the cell nucleus in eucaryotic cells and as the genetic code is necessary for cellular replication, it is considered as the critical target during radiation exposure. The DNA is folded and packed in a complex structure forming chromosomes, as depicted in Fig. 2.13. In its unfolded form, the DNA consists of two helically twisted strands. The backbone of each strand is built of alternating sugar and phosphate groups. Each sugar molecule is connected to a base, which forms the bridge to the second DNA strand by hydrogen bonds. The order of bases, which are connected to the backbone, stores the genetic information.

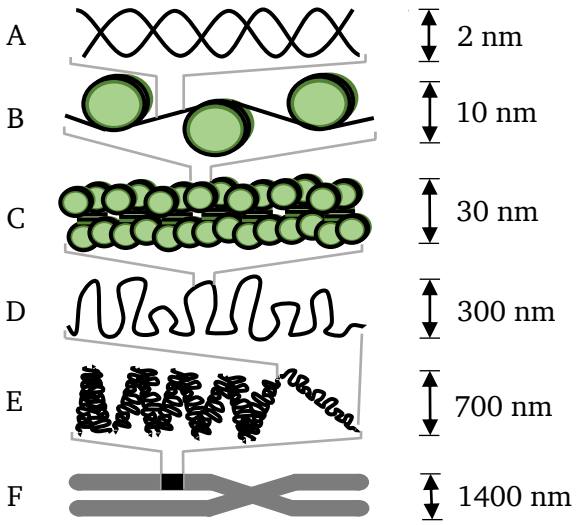

Fig. 2.13.: Schematic representation of the structure of a chromosome with several stages of DNA packaging and folding. A: Unfolded DNA double-helix, B: "Beads on a string" - DNA is wound around histones, C: Nucleosomes packed to form 30 nm fiber, D: Chromatin loops, E: Condensed part of chromosome, F: Entire metaphase chromosome. Modified from [1, 42].

Radiation can induce several types of DNA damage such as base damages, SSBs or DSBs. Therefore, the cell has several repair mechanisms whose activation depends on the type of damage and current cell cycle phase. DNA damages are of high interest in radiobiology as misrepair can lead to a loss or change of the sequence of bases. Such mutations can lead to the modification of cellular functions, cell death, etc. Base

damages and SSBs are relatively simple to repair as the opposite strand can be used as a template. DSBs, or even their local accumulation, form more complex damages as they result in the cleavage of chromatin into two or more pieces. The most important DNA damage types are shown schematically in Fig. 2.14.

There are several biophysical models grouping DNA damages according to their complexity and corresponding lethality for cells. In the LEM two forms of DNA damages are considered: isolated double-strand-breaks (iDSBs) consist of a single DSB within a chromatin loop. If there are two or more DSBs within such a DNA loop, the damage is counted as a complex double-strand-break (cDSB) [12]. Nikjoo et al. classify DNA breaks by complexity, leading to a detailed model with additional damage types called e.g. DSB+ or DSB++ pointing to additional SSBs within a few base pairs to the original DSB [30]. Recent scientific findings confirm that clustering of DNA damage on both the nanometer and micrometer scale leads to enhanced cell inactivation compared to more homogeneous lesion distributions. Consequently, both coexisting processes need to be included in the determination of the resulting damage on a cellular level [33].

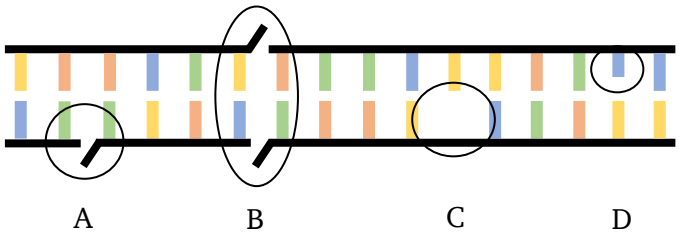

Fig. 2.14.: DNA damage types induced by ionizing radiation. The DNA is displayed simplified in a 2D structure. A: SSB, B: DSB, C: base loss, D: base modification.

2.2.2. Direct and indirect action of radiation

The damage to the DNA in form of strand breaks can be induced either by direct or indirect action of radiation. If the ionization takes place directly at an atom of the DNA molecule, it is called a direct effect. Next to direct ionizations, the radiation can alternatively interact indirectly with e.g. a water molecule and produce a hydroxyl radical OH· via the production of the ion radical H_2O^+. The hydroxyl radical then diffuses with a lifetime of about 10^{-9} seconds through the cell. It is assumed that free radicals produced in a cylinder with diameter two times the radius of the DNA helix can affect the DNA [1].

While for photons approximately two-thirds of the DNA damage is induced indirectly, the direct action is dominant for high-LET radiation. The degree of occurrence of indirect effects may be modified by free radical scavengers.

2.2.3. Cell survival curves

For the description of the cells' sensitivity to radiation, the measurement of cell survival curves is the gold standard nowadays. Cell survival curves themselves describe the relationship between the radiation dose and the proportion of cells surviving the irradiation. In this context, "survival" is understood as the retainment of reproductive integrity; meaning the ability of cultured cells to proliferate indefinitely to produce a large clone or colony. Therefore, the term "clonogenic survival" is usually used for measurements of in-vitro cell survival curves. Two exemplary cell survival curves are depicted in Fig. 2.15 for X-rays and ^{12}C ions.

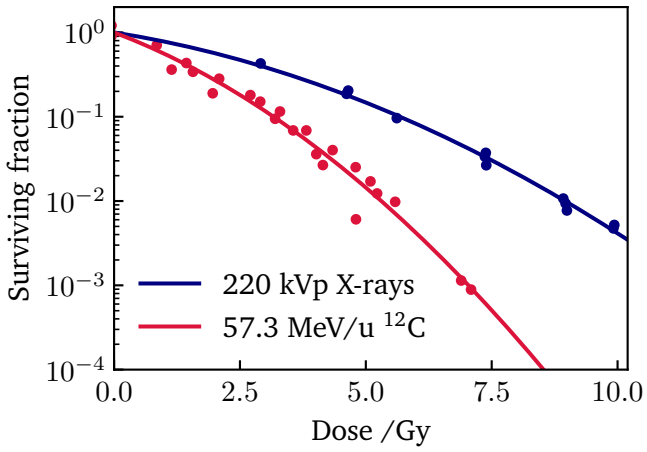

Fig. 2.15.: Survival curves for T1 cell irradiation with 220 kVp X-rays and 57.3 MeV/u ^{12}C ions. Data taken from [61].

2.2.4. Linear-quadratic model for cell survival

The linear-quadratic (LQ) model is the most widely used model to describe and fit the shape of cell survival curves in the field of radiobiology [62]. It assumes that there are two components to cell killing initiated by radiation. The first component is proportional to the irradiation dose and the second one to its square. In the model cell survival S is expressed as a function of dose D as [1]:

$$S(D) = e^{-\alpha D - \beta D^2}\,, \tag{2.15}$$

with the constants α and β as the so-called LQ parameters that are cell line specific. The argument of the exponential function $(\alpha D + \beta D^2)$ can be understood as the mean number of lethal events. Correspondingly, cell survival S is equated as the probability for exactly no lethal event according to Poisson statistics.

Survival curves are usually plotted on a semi-logarithmic scale with the dose D given on a linear-scaled horizontal axis and survival on a log-scaled vertical axis. Consequently, the survival curve appears as a linear ($\beta = 0$), quadratic ($\alpha = 0$) or linear-quadratic curve, as reflected in the name of the LQ model. In Fig. 2.16 two exemplary survival curves are shown for sparsely and densely ionizing radiation species as X-rays and high-LET ions, respectively. For the sparsely ionizing radiation example, the contribution of the linear and quadratic component to the full survival curve is indicated. The contribution to cell death of the linear and quadratic dose component are equal when $D = \alpha/\beta$.

The introduction of a component, which is proportional to the square of the irradiated dose, points to the concept of dual radiation action [63]. This means that two independent damages need to occur and combine for the occurrence of a lethal event. Based on this understanding, the α term represents lethal damage caused by a single incident particle ("single hit") and the β term reflects sublethal damage ("multiple hit"), i.e. cell death resulting from the damage interaction of different radiation tracks [62].

2.2.5. Relative biological effectiveness (RBE)

As described above, the biological radiation effect depends on the track structure of the considered radiation species. Thus, a type of densely ionizing radiation may result in a larger cellular effect compared to a loosely ionizing radiation species at the same delivered dose. In order to quantify the effectiveness of different radiation qualities, the relative biological effectiveness (RBE) is introduced, which is defined as the ratio

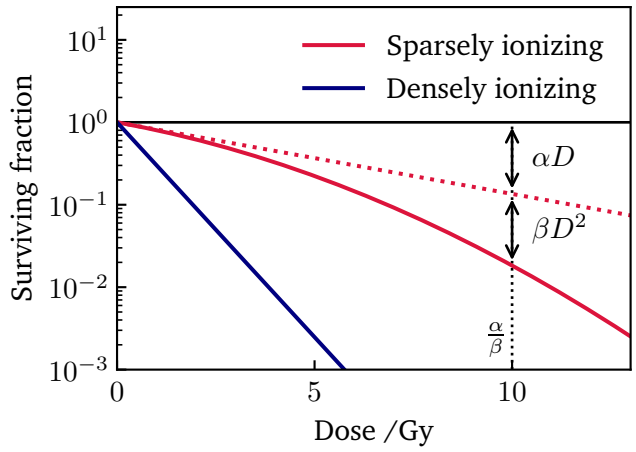

Fig. 2.16.: Exemplary cell survival curves for sparsely and densely ionizing radiation species described by the LQ model. The dose at which the linear and quadratic component contribute to the same degree to cell death is shown as a vertical black dotted line. Inspired by [1].

of two radiation doses leading to the same effect for a certain endpoint such as cell inactivation. X-rays or γ-rays are typically used as a reference radiation. The RBE describes the relative effectiveness of any radiation quality in comparison to photon radiation:

$$RBE = \left.\frac{D_{\mathrm{ref}}}{D_{\mathrm{i}}}\right|_{\mathrm{Isoeff}} . \tag{2.16}$$

As the RBE is dose dependent, it is typically given together with the considered survival level as an index. For instance, the RBE_1 refers to the biological effectiveness at 1% cell survival level. Additionally, the RBE in the zero dose limit $D \to 0$ is called RBE_α. The concept of RBE is visualized in Fig. 2.17. In the example, the RBE is calculated for a specific type of ion radiation compared to a reference radiation at a survival level of 1%.

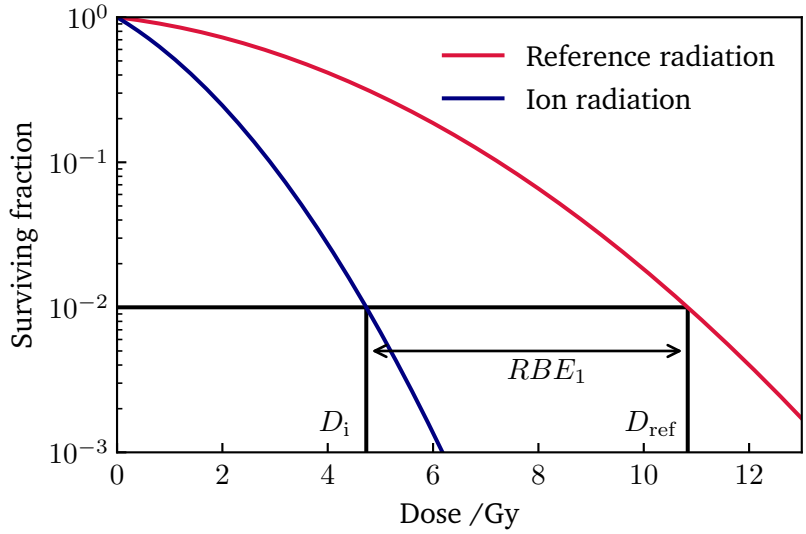

Fig. 2.17.: Concept of RBE calculation for a specific ion species. In this example a survival level of 1% is chosen as the evaluated effect level.

RBE is a complex quantity depending on many physical and biological aspects such as radiation species (ion species, energy, LET), dose, effect level, cell line, cell cycle state, oxygenation, etc. The dependency on LET is shown in Fig. 2.18 for several ion species and effect levels. The underlying measured cell survival data is taken from [64] and fitted by a suitable smooth function reflecting the course of the data points. The RBE

generally increases with LET, reaching a maximum at ≈200 keV/µm before it drops again at even larger LETs. The existence of the RBE maximum is due to a saturation effect at a certain LET value. At this point, additional damages do not lead to an additional effect and, therefore, the radiation becomes less effective per unit dose. As the RBE is defined as the effectiveness in comparison to a reference radiation, the RBE decreases again with increasing LET beyond the RBE maximum. This region of the RBE-LET curve is called "overkill region". The existence of the RBE maximum can be explained on three spatial scales:

- **Nanometer scale:** At the LET corresponding to the RBE maximum, the average distance between ionizations is in the range of the size of a DNA double-helix (2 nm). If the LET increases further, more ionizations are induced per track. Thus, more ionizations are present than necessary for the breakage of the DNA, which is why the radiation is less effective per unit dose. Note that in this approach, no distinction between ion species is made, which determines the detailed distributions of ionizations in the ion track.
- **Micrometer scale:** DNA damages are typically classified as simple and complex damages. If the density of damages is large enough, all damages transform to complex damages. As a result, the induction of further damages does not lead to a more complex damage pattern.
- **Macroscopic scale:** At high LET values, the corresponding ion energies are low, resulting in narrow ion tracks smaller than the extension of a cell/nucleus. As a result, an ion only hits a single cell while traversing the medium with more energy deposited in a nucleus than it would be necessary for cell inactivation. Several cells of the biological probe remain without any hit. In comparison to that, photon reference radiation is loosely ionizing, leading to a random pattern of energy depositions among all cells. Consequently, the ratio of photon and ion doses needed to reach the same effect decreases.

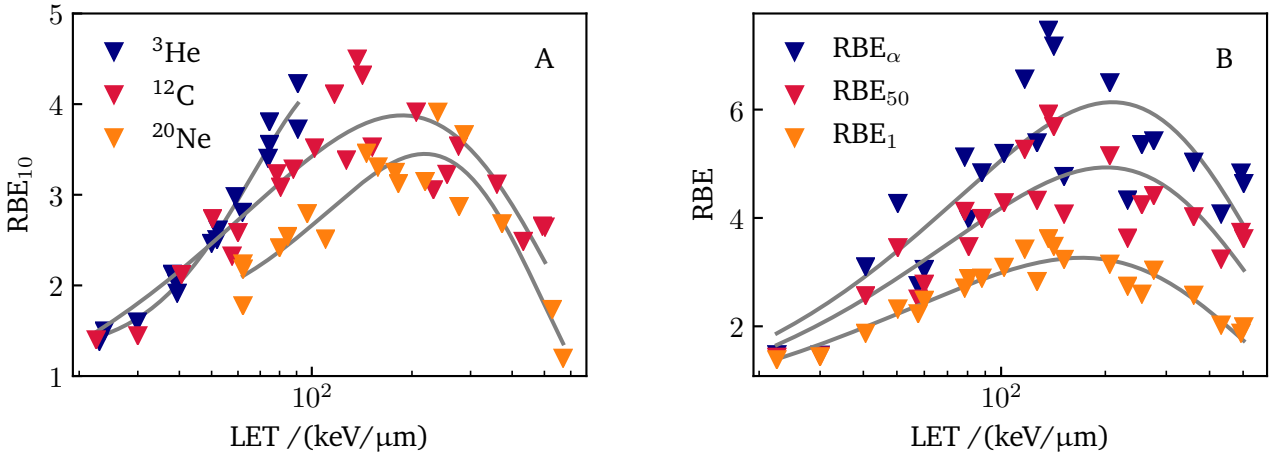

Fig. 2.18.: A: RBE dependence on LET for ^{3}He, ^{12}C and ^{20}Ne ions at 10% cell survival level. B: The RBE-LET dependence on survival level is shown exemplary for ^{12}C ions. Data for V79 cells from [64].

RBE for DSB induction of electrons: In the preceding paragraph, the general concept of RBE was introduced. This was done for the biological effectiveness of ion radiation in comparison to photon radiation with the endpoint of cell survival. The concept of RBE can, however, also be applied for any other radiation species and radiobiological endpoint, such as DSB induction.

In this work, the biological effectiveness of electrons is of great relevance. This is due to the fact that primary radiation species as ions or photons (and also primary electrons) liberate secondary electrons along their path through matter. Thereby, the shape of the secondary electron energy spectra depends on the type and energy of the primary radiation quality. Secondary electrons are responsible for the majority of biological damage, e.g. in form of DSBs in the DNA. The effectiveness of an electron for DSB induction can be quantified by their RBE as a function of electron energy. With the knowledge of the shape of the secondary electron spectra for different primary radiation species together with the RBE of electrons, the mean effectiveness of any primary radiation can be described. The RBE of electrons for DSB induction is shown in Fig. 2.19 for measurement and simulation data present in the literature. For the ion RBE with the endpoint of cell survival, typically X-rays or Co_γ radiation are used as a reference. For the determination of the RBE for electrons with the endpoint of DSB induction, however, several other reference radiation species are applied in experiments. The two most prominent reference radiation species are Co_γ and high-energetic electrons (10^5-10^6 eV). As a result, in Fig. 2.19 RBE data obtained with several reference radiation species is shown, which needs to be taken into account for further data analysis or application. The data illustrates that the RBE for electrons with the endpoint of DSB induction exhibits a maximum at a few hundred eV and tends towards unity for larger doses. The exact energy at which the RBE is equal to unity depends on the choice of reference radiation.

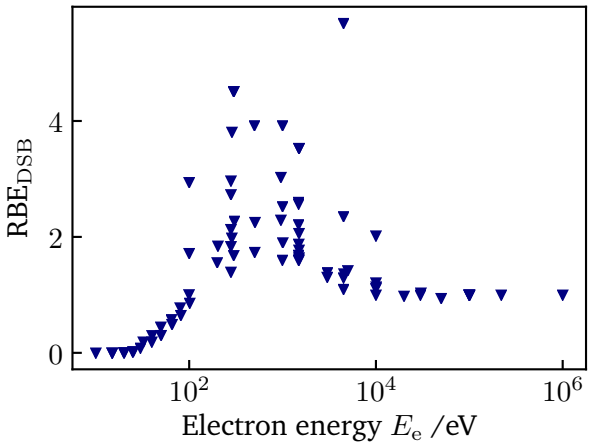

Fig. 2.19.: RBE for DSB induction for electrons over electron energy. The values are collected from published measurement and simulation data as summarized in Tab. A.5.

2.3. Radiobiological effect models

Since the performance of first radiotherapy treatments over a century ago, mathematical modeling has played a vital role in radiobiology research [62]. Radiobiological models enable the understanding of underlying physical, chemical and biological processes leading to biological effects. In the following chapter, three RBE-predictive models are described: The Katz model, the local effect model (LEM) and the microdosimetric-kinetic model (MKM). The latter two are currently used in clinical application in the context of tumor treatment planning. As this work is based on predictions with the LEM, it is described in more detail than the other two models. Finally, two biophysical survival models are introduced that can be applied to predict cell survival after irradiation with mixed radiation fields.

2.3.1. Katz model

The Katz model was introduced in 1967 and can be applied to predict cell survival after ion irradiation [13, 14]. It uses a form of amorphous track structure model to describe the radial dose profile around the ion track as introduced in Sec. 2.1.4. In order to describe the transition from a shouldered to a purely linear survival curve for high-LET radiation, two "modes" are introduced: The γ-kill and ion-kill mode. The γ-kill mode is expressed by the multi-target single-hit (MTSH) model:

$$S_\gamma(D_\gamma) = 1 - \left(1 - e^{-\frac{D_\gamma}{D_0}}\right)^m . \tag{2.17}$$

The model makes the assumption that the cell nucleus is divided into sub-volumes; D_0 describes the dose at which there is on average one hit per sub-volume and the number of such volumes is included in the formalism through the fit parameter m. The ion-kill component is calculated according to the single-target single-hit (STST) model as:

$$S_\mathrm{i}(D_\mathrm{i}) = e^{-\sigma F} , \tag{2.18}$$

where σ indicates the inactivation cross section and F the particle fluence. The total irradiation dose is thus split between the two modes $D = D_\gamma + D_\mathrm{i}$ and the final cell survival is calculated as:

$$S(D) = S_\gamma(D_\gamma) \cdot S_\mathrm{i}(D_\mathrm{i}) . \tag{2.19}$$

Next to the number of sub-volumes m, the values for σ and D_0 are obtained by fitting the model to photon and ion cell survival data.

2.3.2. Local effect model (LEM)

The local effect model (LEM) was initially developed for a pilot project carried out at GSI Helmholtzzentrum für Schwerionenforschung GmbH (GSI) in Darmstadt, Germany, from 1997 to 2008 where 440 patients with head and neck tumors were treated with carbon ions [9, 10, 60, 65]. The development of the LEM was necessary as carbon ions inhibit an increased RBE compared to photons or protons and varies strongly with penetration depth. Thus, the RBE needs to be considered in treatment planning to reach optimal results.

The initial version of the LEM (LEM I) is still used clinically in several ion beam therapy centers. Over the years, the LEM was constantly validated and revised resulting in model versions II-IV. Table 2.1 provides an overview of the different versions' main pillars. The LEM IV has proven to be a successful RBE model, which allows predictions for various radiobiological endpoints such as the prediction of in-vitro experimental data for several ion species ranging from protons to oxygen ions [11, 19, 20, 21]. Furthermore, the model was found to accurately represent RBE measurements for in-vivo experiments. This was demonstrated by comparing model predictions to measurement data on the dose tolerance of the rat spinal cord [22, 23, 24]. Additionally, several radiobiological aspects as the induction of secondary cancers, dose rate or cell cycle effects as well as rejoining kinetics could be accurately reproduced by the LEM IV [12, 25, 26, 27].

Tab. 2.1.: Overview of existing LEM versions, the year of publication, version-specific features and corresponding references.

Version	Year	Features	References
LEM I	1997	The basic idea of the LEM is that same local doses lead to the same biological effects - independent of the radiation quality that is responsible for the energy deposition. The local dose distribution is calculated according to an amorphous track structure model.	[10]
LEM II	2007	The enhanced effectiveness of ions due to clustering of SSBs in close proximity leading to additional DSBs is introduced (η-factor). Also, radical diffusion, which modifies the dose profile is considered by folding the physical dose distribution with a 2D-Gaussian profile.	[60]
LEM III	2008	The dependence of the extension of the inner core of the radial dose profile on the energy of the ions is included in the model.	[65]
LEM IV	2010	An intermediate step is introduced assuming that similar DSB patterns lead to the same effects. Thus, the complexity of the DSB pattern induced by ions is compared to a photon irradiation case leading to the same damage complexity. The new model enables the prediction of the RBE for all clinically relevant ion species. Earlier model versions were developed with the focus set on carbon ions.	[11, 12]

As indicated by the model's name, the main pillar of the LEM is the assumption that same local doses lead to same local effects. Thus, it is assumed that local effects are independent from the original type of radiation responsible for the energy deposition. In the LEM IV, an additional step was introduced including the spatial clustering of DNA damages in the effect calculation.

In the LEM IV, the microscopic, local dose distribution of an ion is calculated based on the ion's amorphous track structure (see Sec. 2.1.4). Based on the microscopic dose distribution, the spatial distribution of DSBs within the cell nucleus is calculated by random sampling. Next, the complexity of the resulting DSB pattern is calculated and compared to DSB patterns produced by the photon reference radiation. As a result, a photon dose can be determined, which leads to the same DSB pattern complexity as in the ion case. By finally normalizing the result to the amount of affected DSB domains in the reference radiation case, cell survival after ion irradiation can be calculated. The full calculation procedure of LEM IV is described below in detail.

Amorphous track structure: First, the amorphous track structure of the considered ion is calculated according to the formalism provided in Sec. 2.1.4. Track segment conditions are assumed, which means that the ion's energy loss during its traversal of the cell nucleus is neglected. The track structure follows a

r^{-2} dependence with r as the distance to the ion track center and is calculated according to Eq. (2.13). The primary track structure is then convolved with a 2D Gaussian distribution in order to mimic the dose smear-out by diffusion of highly reactive radicals into the surrounding medium. The local dose $D(r)$ is shown in Fig. 2.20 for a 10 MeV/u carbon ion before and after the consideration of radical diffusion.

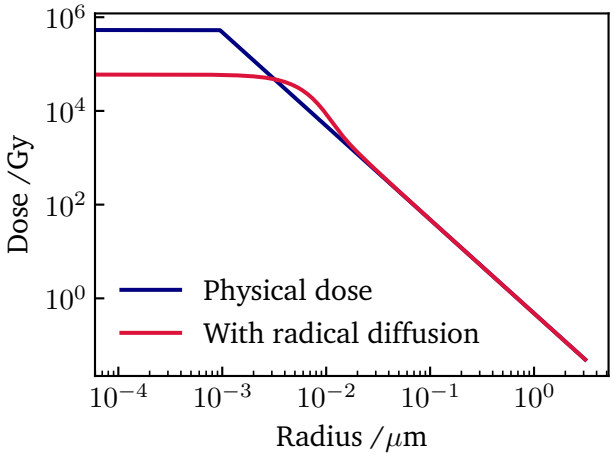

Fig. 2.20.: Amorphous track structure of a 10 MeV/u carbon ion calculated by Eq. (2.13). The consideration of radical diffusion broadens the local dose distribution at radii r<50 nm.

DSB distribution: In accordance with multiple other radiobiological models, the cell nucleus is considered as the radiation sensitive target. The complexity of radiation damage to the DNA in the cell nucleus is believed to determine the fate of a cell. The DSB distribution in the cell nucleus is calculated by simulating DSBs in the ion track. In the LEM, the cell nucleus is typically simulated as a cylinder, whereas a volume of $V_{\mathrm{nuc}} = 500\ \mu\mathrm{m}^3$ is chosen in this work. The probability of producing a DSB is determined directly from the local dose distribution and the knowledge that photons produce approximately 30 DSB in a cell nucleus per Gy [12]. At very large local doses (>100 Gy), additional DSBs need to be included due to the combination of independent SSBs (created by separate electron tracks). This is included by the DSB enhancement factor η [66] that is described in detail at the end of this section. A schematic representation of a DSB distribution along an ion track is shown in Fig. 2.21.

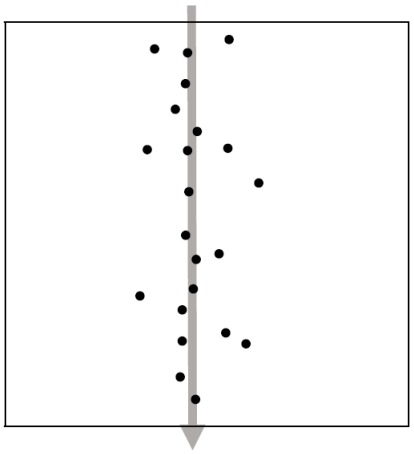

Fig. 2.21.: Schematic representation of a DSB distribution along an ion track in a cell nucleus. The ion's direction of flight is indicated by a gray arrow. Each DSB is represented by a black dot and the cell nucleus is illustrated as a square outlined in black. Mind that in the LEM, the cell nucleus is modeled as a 3D cylinder.

Cluster index: The cell nucleus is divided into sub-compartments representing single chromatin loops. Such a DNA domain contains approximately two mega base pairs (Mbp) [67, 68, 69, 70] and is represented

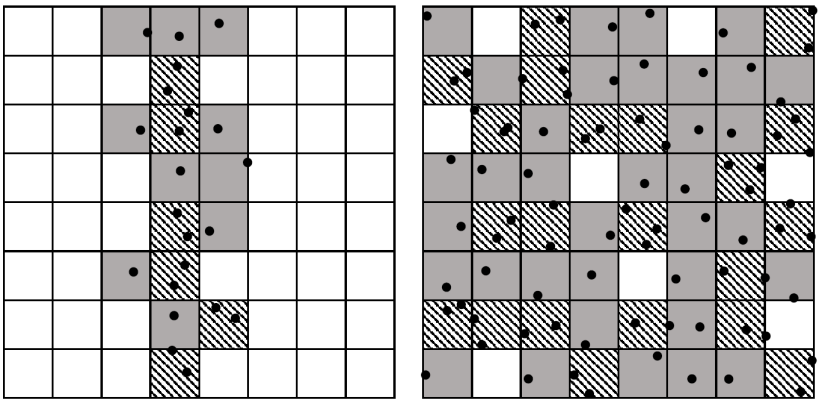

Fig. 2.22.: Left: The amount of clustered and isolated DSBs is determined according to the amount of DSBs within each chromatin loop. Isolated DSBs are shown with a gray background, clustered DSBs with a striped pattern and chromatin loops without any DSBs are illustrated in white. Right: Photons deposit their energy more equally leading to a random DSB pattern. According to the cluster index calculated for the ion, an equivalent photon case with the same cluster index is found.

by a cube of 540 nm side length [12] as schematically illustrated in Fig. 2.22. Next, it is checked for each domain whether it contains zero, one or more than one DSB. This enables a classification of chromatin loop damages into two categories: iDSBs with a single DSB within a loop and cDSBs with multiple DSBs. Chromatin loops with two or more DSBs are hypothesized to be far more lethal than chromatin loops with only a single DSB due to the reduced repair probability for clustered lesions [12]. Finally, the classification of DNA damages into iDSB and cDSB enables the determination of a cluster index C_i, which represents a measure for the complexity of the damage pattern:

$$C_\mathrm{i} = \frac{n_\mathrm{cDSB,i}}{n_\mathrm{iDSB,i} + n_\mathrm{cDSB,i}}\,, \tag{2.20}$$

with $n_\mathrm{iDSB,i}$ and $n_\mathrm{cDSB,i}$ as the number of isolated and clustered DSBs induced by the ion, respectively.

Equivalent photon case: In contrast to ions, photons deposit their energy more homogeneously in the medium leading to a random DSB distribution in the cell nucleus after photon irradiation. Thus, a specific applied photon dose is connected to a fixed amount of DSBs within the nucleus. As the distribution of DSBs is random in a first approximation, each photon dose leads to a specific cluster index C_γ according to the LEM concept. By finding the photon dose, which leads to the same cluster index as it was determined for the ion in the previous step, an equivalent photon case is found:

$$C_\gamma(D_\mathrm{eq}) = \frac{n_\mathrm{cDSB,\gamma}}{n_\mathrm{iDSB,\gamma} + n_\mathrm{cDSB,\gamma}} \stackrel{!}{=} C_\mathrm{i}\,, \tag{2.21}$$

with $n_\mathrm{iDSB,\gamma}$ and $n_\mathrm{cDSB,\gamma}$ as the number of isolated and clustered DSBs produced at a certain photon dose D_eq, respectively. Figure 2.22 shows schematic representations of DSB distributions for ions and photons with the same cluster index C.

Effect calculation: Finally, the effect $E_{\gamma,eq}$ at equivalent photon dose D_{eq} is calculated according to a modified version of the LQ model, which is introduced in Sec. 2.2.4 and applied in all existing LEM versions. A characteristic of the LQ model is the monotonic decrease of survival with increasing dose. At larger doses, which lie above the usually applied doses per fraction in radiotherapy, experiments indicate a re-transition to a linear behavior of cell survival with dose [71, 72, 73]. Therefore, the linear-quadratic-linear (LQL) model is introduced that considers a purely linear shape of survival curves at doses above a threshold dose D_{t} to better fit experimental findings. The purely linear shape at large doses is defined by the final slope of a cell survival curve $s_{\max} = \alpha_\gamma + 2\beta_\gamma D_{\mathrm{t}}$. Finally, the effect $E_{\gamma,eq}$ at equivalent photon dose D_{eq} is calculated as:

$$E_{\gamma,\mathrm{eq}}(D) = \begin{cases} (\alpha_\gamma D + \beta_\gamma D^2) & \text{for } D < D_{\mathrm{t}}\,, \\ s_{\max} \cdot (\eta(D) D - D_{\mathrm{t}}) + (\alpha_\gamma D_{\mathrm{t}} + \beta_\gamma D_{\mathrm{t}}^2) & \text{for } D \geq D_{\mathrm{t}}\,. \end{cases} \tag{2.22}$$

The value of D_{t} is difficult to determine experimentally as it often lies in the range of relatively high irradiation doses where the cell survival is close to zero. Thus, D_{t} is a critical parameter, which often needs to be determined empirically. In this work, the threshold dose D_{t} is calculated according to an empirically found formula with α_γ and β_γ as the LQ parameters of the photon cell survival curve [28]:

$$D_{\mathrm{t}} = 4 + 1.1 \cdot \frac{\alpha_\gamma}{\beta_\gamma}\,. \tag{2.23}$$

Rescaling: As the total amount of chromatin loops containing DSBs is potentially different for the ion and the dose-equivalent photon case, the effect $E_{\gamma,\mathrm{eq}}$ needs to be rescaled. Graphically represented, the DSB distribution of the ion can be understood as a cutout of the equivalent photon case. The effect after ion irradiation E_{i} is finally obtained by:

$$E_{\mathrm{i}}(D) = E_{\gamma,\mathrm{eq}}(D) \cdot \frac{n_{\mathrm{iDSB,i}} + n_{\mathrm{cDSB,i}}}{n_{\mathrm{iDSB},\gamma} + n_{\mathrm{cDSB},\gamma}}\,. \tag{2.24}$$

At last, cell survival S_{i} after ion irradiation is calculated as:

$$S_{\mathrm{i}}(D) = e^{-E_{\mathrm{i}}(D)}\,. \tag{2.25}$$

The amount and distribution of DSBs depend on the respective position of the ion traversal in the cell nucleus. As in cell irradiation experiments several cells are irradiated with a random pattern of ion traversals, this needs to be taken into account in the simulations. Thus, in the so-called "full simulation" the position of each ion hit in relation to the cell nucleus is determined by random sampling. From a single ion hit up to a combination of multiple ion hits, all relevant scenarios (hit classes) are calculated with randomly chosen hit positions. Finally, the overall cell survival is obtained by weighting the hit classes' results (S_{i}) according to the requested irradiation dose level.

DSB enhancement factor η: In the LEM, the amount of produced DSBs within the cell nucleus is calculated based on the local dose. Therefore, the experimentally found relation $\alpha_{\mathrm{DSB}} = 30$ DSB/Gy/nucleus is used [12]. The linear character of the DSB yield is, however, only valid for doses below ≈100 Gy. In this dose range, each DSB is produced by "intra-track" effects meaning that the SSBs leading to the DSB are initiated by the same electron. At very large local doses >100 Gy, the contribution of "inter-track" effects is no longer

negligible. Due to large doses, electron tracks overlap and SSBs induced by different electrons can combine to form a DSB. In order to account for these effects in the LEM, the "Eta-factor" η was developed [66, 12, 60, 57]. It describes the increase of the number of DSBs induced per dose unit due to inter-track effects ($N_{\mathrm{DSB,inter}}$), which occur in addition to intra-track effects ($N_{\mathrm{DSB,intra}}$) at large doses:

$$\eta(D) = \frac{N_{\mathrm{DSB,intra}}(D) + N_{\mathrm{DSB,inter}}(D)}{\mathrm{N}_{\mathrm{DSB,intra}}(D)} \,. \tag{2.26}$$

Based on experimentally found values for the SSB ($\alpha_{\mathrm{SSB}} = 1250$ DSB/Gy/nucleus) and DSB ($\alpha_{\mathrm{DSB}} = 30$ DSB/Gy/nucleus) yields, the densities ρ_{SSB} and ρ_{DSB} of the two types of DNA strand breaks are defined by Eq. (2.27) and Eq. (2.28), respectively. Here, L_{Gen} denotes the length of the DNA in base pairs:

$$\rho_{\mathrm{SSB}} = \alpha_{\mathrm{SSB}} D / L_{\mathrm{Gen}} \,, \tag{2.27}$$

$$\rho_{\mathrm{DSB}} = \alpha_{\mathrm{DSB}} D / L_{\mathrm{Gen}} \,. \tag{2.28}$$

The threshold distance SSB_{t} defines the maximum distance in base pairs, which is allowed between two SSBs such that they can combine and form an additional DSB. A value of $SSB_{\mathrm{t}} = 25$ bp was found by comparing LEM predictions to measurement data. The η-factor is given as:

$$\eta(D) = 1 + \frac{1 - e^{-\rho_{\mathrm{SSB}}(D) SSB_{\mathrm{t}}}}{3 - e^{-\rho_{\mathrm{SSB}}(D) SSB_{\mathrm{t}}}} e^{-\rho_{\mathrm{DSB}}(D) SSB_{\mathrm{t}}} \cdot \frac{\alpha_{\mathrm{SSB}}}{\alpha_{\mathrm{DSB}}} \,. \tag{2.29}$$

The detailed derivation of Eq. (2.29) can be found in the original publication on the η-factor development [66]. This factor is derived assuming that the contribution of SSBs per electron per unit dose is independent of the electron spectrum. Furthermore, the assumption is made that the SSBs are randomly distributed in the cell nucleus. Thus, the factor is valid in a first approximation for highly energetic electrons, as they dominate in the radiation field of γ-rays. The quantity $\eta(D)$ is plotted for $SSB_{\mathrm{t}} = 25$ bp in Fig. 2.23. In the literature, values for SSB_{t} are found to range from below 10 bp up to 60 bp [60]. In biophysical models/simulations, a threshold of $SSB_{\mathrm{t}} = 10$ bp is often used. Thus, η is shown additionally in Fig. 2.23 for this DNA strand break threshold.

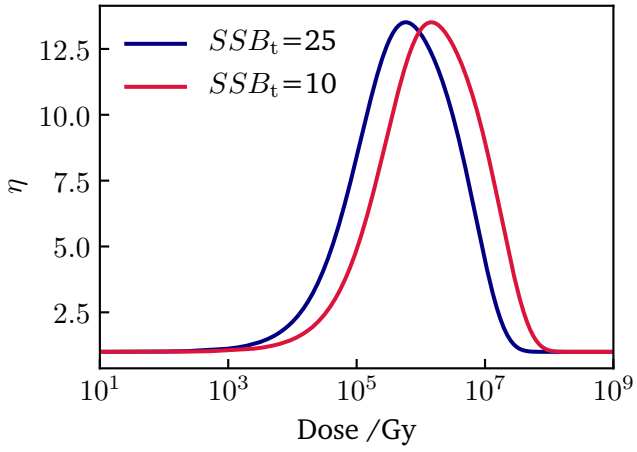

Fig. 2.23.: Local DSB enhancement η due to inter-track effects of overlapping electron tracks at large local doses.

Single particle approximation: Due to the CPU-time consuming character of the full LEM simulation, an approximation was developed, which made the LEM accessible for ion treatment planning where computation time is limited [10, 74]. In the approximation, the passage of exactly one ion through the nuclear volume along the axis of the cylindrical nucleus is calculated for the determination of the biological effect. The difference of both methods in the predicted values α_{i}, β_{i} and RBE has shown to be small and the final result can be reasonably approximated by the simulation of a single ion hit [10]. The approximation is used in all LEM calculations in this work if not stated otherwise. As only a single ion hit is considered in the approximation, the specific energy d_1 can be directly calculated from Eq. (2.30). The prefactor of 0.16 accounts for the unit conversion to Gy if the LET is given in keV/µm^3 and the area of the cell nucleus A_{nuc} in µm^2:

$$d_1 = 0.16 \frac{LET}{A_{\mathrm{nuc}}} \,. \tag{2.30}$$

The calculation procedure is then followed for the full simulation as described above. Thus, the mean biological effect E_{i} after the central ion hit is calculated according to Eq. (2.24). The mean efficiency of a single ion hit is then given by the "intrinsic parameter" α_{z}:

$$\alpha_{\mathrm{z}} = \frac{E_{\mathrm{i}}}{d_1} \,. \tag{2.31}$$

In order to calculate the LQ parameter α_{i}, its definition according to the LQ model is used: The parameter α describes the gradient of the survival curve in the limit of $D \to 0$, which leads to [10]:

$$\alpha_{\mathrm{i}} = \frac{1 - \exp(-E_{\mathrm{i}})}{d_1} \,. \tag{2.32}$$

For the determination of β_{z}, a relation can be derived based on the LQL model as given in Eq. (2.22). Due to the inhomogeneous dose distribution within an ion track, a central ion hit must always be more effective compared to an equivalent photon dose with a homogeneous distribution. Thus, the maximum slope of the ion survival curve must always be greater or equal to the maximum slope of the photon curve [10]. At large doses, the mean effect enhancement $\overline{\eta}$ is not negligible and needs to be taken into account:

$$\overline{\eta} \cdot s_{\mathrm{max},\gamma} = s_{\mathrm{max,i}} \,. \tag{2.33}$$

Furthermore, the assumption is made that the threshold dose D_{t} is equal for both the ion and photon radiation quality. Inserting the maximum slope of the cell survival curve according to the LQL model leads to:

$$\overline{\eta} \cdot (\alpha_\gamma + 2\beta_\gamma D_{\mathrm{t}}) = \alpha_z + 2\beta_{\mathrm{z}} D_{\mathrm{t}} \,. \tag{2.34}$$

Through rearrangement of Eq. (2.34), the value of the second intrinsic parameter β_{z} is extracted. Finally, the LQ parameter β_{i} is obtained through a scaling relation between the intrinsic parameters α_{z} and β_{z} with the parameters α_{i} and β_{i} [74]:

$$\frac{\beta_{\mathrm{i}}}{\beta_{\mathrm{z}}} \approx \left(\frac{\alpha_{\mathrm{i}}}{\alpha_{\mathrm{z}}} \right)^2 \,. \tag{2.35}$$

Values for α_z can be pre-calculated for different energies and LETs values for several ion species, which enables an accelerated simulation with the approximation approach compared to the full simulation. The import of pre-calculated model predictions into a treatment planning system enables an efficient evaluation of the expected effect at any position within a complex irradiation field.

2.3.3. Microdosimetric-kinetic model

The MKM is an RBE-predictive model that is based on the concept of energy depositions in micrometer sized volumes. The model was originally developed by Hawkins in 1996 [15, 16] and later adapted for clinical use in heavy ion therapy centers in Japan [17, 18]. The energy depositions in target domains of micrometer's size is quantified by the microdosimetric quantity y, the so called "lineal energy", that is calculated as:

$$y = \frac{\epsilon}{l}\,, \tag{2.36}$$

with ϵ as the amount of energy deposited within a critical target of mean chord length l. As in radiation experiments typically a mixture of radiation species is present rather than a single one, the average lineal energy is used for RBE assessment. Thus, the dose-weighted mean value $\overline{y}$ is calculated from the microdosimetric spectrum of y, which is measurable. Furthermore, similar to the concept of the LEM, the MKM uses the LQ parameters α_γ and β_γ of the photon survival curve as input parameters. As a result, the effect after ion irradiation E_i is obtained by:

$$E_\mathrm{i}(D) = \alpha_\mathrm{i} D + \beta_\gamma D^2 = (\alpha_0 + z_\mathrm{1D})\, D + \beta_\gamma D^2\,. \tag{2.37}$$

Here, α_0 represents the initial slope of the survival curve in the limit of LET = 0 and can be approximated by $\alpha_0 = \alpha_\gamma$. The parameter z_1D denotes the dose-averaged specific energy absorbed in a domain in a single event. As Eq. (2.37) shows a continuous increase of α_i with increasing z_1D, the formula does not reproduce the characteristic drop in RBE for large LET values. To account for this effect, a correction was introduced [17], which enables a realistic reflection of the dependence of RBE on LET in the overkill region. Note that in the MKM approach the β-parameter is the same for ion as well as for photon radiation. Finally, cell survival S_i after ion irradiation is calculated as:

$$S_\mathrm{i}(D) = e^{-E_\mathrm{i}(D)}\,. \tag{2.38}$$

2.3.4. Cell survival models for mixed radiation fields

The above introduced models can in principle also be used to simulate cell survival after mixed radiation fields as they naturally exist in most irradiation scenarios. Due to time limitations e.g. in cancer radiation treatment planning, the RBE models are only used to predict cell survival for each present radiation species. The process of calculating the mixed radiation effect is then performed by a simplified and fast model. For instance, the Zaider-Rossi model (ZRM) is used in combination with the LEM within the treatment planning systems TRiP and Syngo [74]. In the following, the ZRM and an alternative model - the lesion additivity model (LAM) - are briefly described.

Zaider-Rossi model: The Zaider-Rossi model (ZRM) [75] is based on the microdosimetric approach theory of dual radiation action (TDRA) assuming that sublesions interact in pairs to form lesions [63]. The cell survival after mixed irradiation S_{mix} can be calculated according to the LQ formalism (see Sec. 2.2.4) as:

$$S_{\mathrm{mix}}(D) = e^{-\alpha_{\mathrm{mix}} D - \beta_{\mathrm{mix}} D^2}\,, \tag{2.39}$$

with the total dose D and α_{mix} and β_{mix} as the LQ parameters of the mixed radiation field. The LQ parameters, which describe the mixed beam, are calculated as weighted averages of the plain LQ parameters of the constituents of the mixed field:

$$\alpha_{\mathrm{mix}} = \sum\nolimits_j f_j \alpha_j\,, \tag{2.40}$$

$$\sqrt{\beta_{\mathrm{mix}}} = \sum\nolimits_j f_j \sqrt{\beta_j}\,, \tag{2.41}$$

with the partial doses

$$f_j = \frac{D_j}{D}\,. \tag{2.42}$$

The parameter D_j denotes the dose delivered by radiation quality j. For two types of radiation A and B, cell survival after mixed beam irradiation can be calculated by inserting Eq. (2.40) to (2.42) in Eq. (2.39):

$$S_{\mathrm{mix}}(D) = \exp\left[-(\alpha_{\mathrm{A}} D_{\mathrm{A}} + \beta_{\mathrm{A}} D_{\mathrm{A}}^2) - (\alpha_{\mathrm{B}} D_{\mathrm{B}} + \beta_{\mathrm{B}} D_{\mathrm{B}}^2) - 2 D_{\mathrm{A}} D_{\mathrm{B}} \sqrt{\beta_{\mathrm{A}} \beta_{\mathrm{B}}}\right]\,. \tag{2.43}$$

The last term in the exponent of Eq. (2.43) is the so-called interference term [75]. The term is equal to zero if at least one of the radiation species A or B shows a purely linear survival curve, meaning that the β component is equal to zero. In such a case, the interaction of the different radiation species is handled as a simple additivity of the effects of both radiation components. The diminishing of the interference term for purely linear survival curves can be interpreted as the lack of sublethal lesions. If no sublethal lesions exist, they cannot interact with each other, prohibiting the production of additional lesions and an increased effect.

Lesion additivity model: The lesion additivity model (LAM) [76] is based on the concept of additive radiation action or Loewe additivity. Each component of the mixed radiation beam is assumed to produce a common form of intermediate lesions. These lesions are not distinguishable any further at some point along the radiation inactivation chain and therefore become additive. The isobologram method is commonly used for assessment of drug dose interaction and can also be applied for radiation dose interaction [77]. The concept is clarified in Fig. 2.24.

According to the isobologram method, one obtains for two radiation components A and B with D_{A} and D_{B} as the doses, which would be needed if the full effect was obtained by a single radiation quality:

$$\frac{1}{D} = \frac{f_{\mathrm{A}}}{D_{\mathrm{A}}} + \frac{f_{\mathrm{B}}}{D_{\mathrm{B}}}\,, \tag{2.44}$$

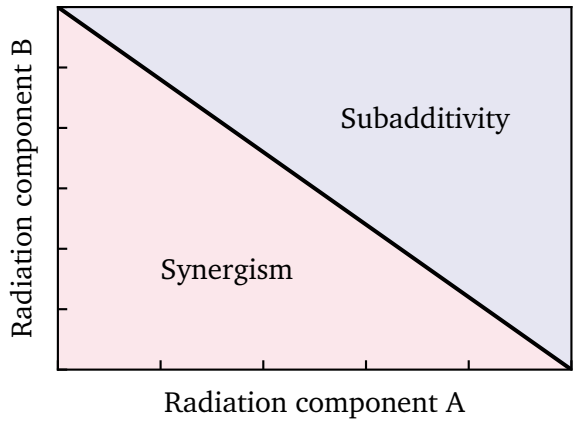

Fig. 2.24.: Schematic representation of the isobologram method: Dose contributions of the two radiation components A and B are shown on the axes. The isobole (solid line) represents combination doses that all lead to the same effect due to interaction in an additive manner. In the area below the isobole (red area), the interaction is synergistic and above the isobole (blue area), the radiation components are subadditive. Inspired by [77].

with

$$f_{\mathrm{A}} = \frac{D_{\mathrm{a}}}{D}, f_{\mathrm{B}} = \frac{D_{\mathrm{b}}}{D}\,, \tag{2.45}$$

and $D = D_{\mathrm{a}} + D_{\mathrm{b}}$ as the partial doses of the two radiation species. In order to calculate cell survival curves with a mixed radiation compositions, the LQ model (Eq. (2.15)) is transformed for the dose D as shown in Eq. (2.46). The mixed radiation dose can be calculated inversely for any requested cell survival level S_{mix}:

$$D_{\mathrm{i}} = -\frac{\alpha_{\mathrm{i}}}{2\beta_{\mathrm{i}}} + \sqrt{(\frac{\alpha_{\mathrm{i}}}{2\beta_{\mathrm{i}}}^2) + \frac{-\ln(S_{\mathrm{mix}})}{2\beta_{\mathrm{i}}}}\,. \tag{2.46}$$

By solving Eq. (2.46) for two radiation qualities A and B and inserting the results in Eq. (2.44), S_{mix} can be calculated numerically.

3. Material and methods

In this chapter, applied mathematical methods, model adjustments and reference databases are described. First, in Sect. 3.1 the PIDE database is introduced, which is used throughout this work to calculate RBE reference data for model validation. Furthermore, applied error estimation and averaging procedures in the context of PIDE data are described in detail. In Sect. 3.2, the concept of synergism and additivity is mentioned with regard to mixed radiation fields. Additionally, the necessary LEM adjustments for its application to mixed radiation fields are introduced together with a dataset of cell survival after mixed field irradiation that was collected and used for further model validation purposes. Next, the Kiefer model for the calculation of secondary electron spectra is given in Sect. 3.3, followed by the description of the corresponding extension to radial electron spectra. Finally, in Sect. 3.4 the MC code Geant4-DNA is described. The radiation transport code was used in this work to validate model predictions as well as to calculate model inputs.

3.1. The PIDE database

The Particle Irradiation Data Ensemble (PIDE) database contains more than 1100 experiments on in-vitro clonogenic cell survival after irradiation with photons and ions compiled from 115 publications [28, 29]. Each experiment (=database entry) consists of two separate cell irradiation experiments performed with an ion species and a photon reference radiation under the same conditions. The database contains information on the experimental conditions such as the applied cell line, cell cycle stage, photon reference radiation source, particle species and particle energy. Furthermore, the dose response concerning cell survival is given in form of LQ parameters for both the photon and ion irradiation. The database is freely available to the research community and can be accessed via the GSI biophysics web page (`https://www.gsi.de/bio-pide`).

As mentioned above, the dose response of each experiment is parameterized by the LQ model (see Sec. 2.2.4). Consequently, the α and β parameters are given in the database for each measured photon and ion survival curve. There are two sets of LQ parameters given in the data collection:

- The first set consists of the LQ parameters directly provided by the authors of each experiment in the original publications.
- If the raw data of the measured survival curves (dose-survival pairs) are given in the publication (e.g. within survival plots), this data was extracted by the authors of the database and used to generate uniform LQ fits. These LQ parameters comprise the second set of parameters, which is chosen in this work to perform model validations as the parameters were determined directly from the raw data and fitted according to the same concept for each survival curve.

Since PIDE version 3.1, the raw data of the measured cell survival curves is provided by the authors of the PIDE together with the main database [29]. This gives the user even more flexibility with regard to analyzing impacts of different experimental settings on the endpoint cell survival. Besides, the PIDE is

a unique tool to investigate RBE characteristics as for each experiment data on photon as well as on ion irradiation are provided. Therefore, the RBE of each experiment can be calculated and used e.g. for the validation of any RBE model. The newest version of the database is the PIDE 3.2, which is used throughout this work to validate RBE predictions obtained with the LEM.

3.1.1. Validation process of the LEM with the PIDE database

The workflow for the determination of the accuracy of LEM predictions with the PIDE database is shown schematically in Fig. 3.1. For each experiment listed in the PIDE, the RBE was calculated directly from the LQ parameters tabled in the database as well as predicted by the LEM. For the direct calculation, Eq. (2.15) is solved for the dose D; the LQ parameters for both the ion and photon irradiation are taken from the database and inserted in the equation. The obtained doses D_i and D_γ can then be inserted into Eq. (2.16) to calculate the RBE at a specific cell survival level. For the RBE prediction by the LEM, the information of the considered ion species in form of its energy and LET is inserted into the model together with the photon LQ parameters α_γ and β_γ. Finally, the RBE values predicted by the LEM can be compared to the measured RBEs. For the LEM calculations, the following default parameters are applied: A nuclear radius of 5 µm, a nuclear volume of 500 µm^3 and a chromatin loop size of 540 nm.

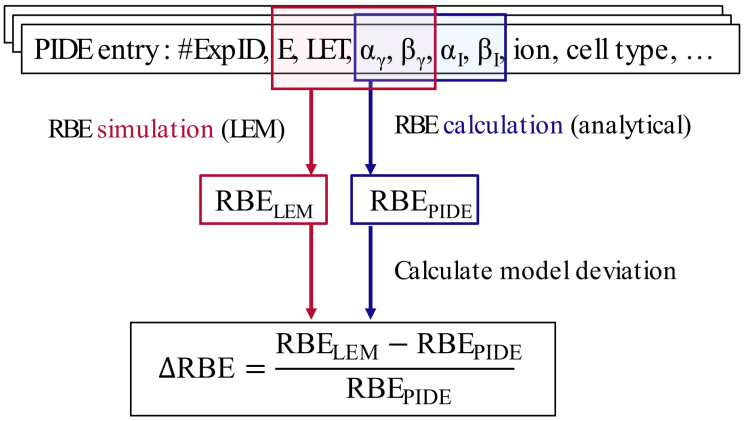

Fig. 3.1.: Schematic workflow of the LEM validation with the PIDE database. For a selected set of PIDE entries, the RBE is simulated with the LEM based on the photon LQ parameters α_γ and β_γ, the LET and energy of the considered ion. Additionally, the RBE is calculated analytically using the photon LQ parameters α_γ and β_γ as well as the ion LQ parameters α_i and β_i as input. Finally, by comparing the two RBE values, the deviation of the LEM prediction compared to experimental data is obtained for each PIDE entry.

Each experiment has a maximum dose and minimum survival level down to which the measurements were originally performed. To avoid extrapolations into dose regions not covered by experiments, the RBE calculations were restricted in a way that the RBE at a certain survival level was only calculated/predicted if the underlying survival curves were measured down to the considered survival level. For instance, the RBE_1 was only calculated if both the survival curve for the ion as well as for the photon radiation was measured down to a survival level of 1%. In order to use the PIDE data for model validation, further filter criteria are defined and listed in the following:

- As the LEM is a model, which predicts the biological effect of monoenergetic ions, only such experiments were considered. As a consequence, cell survival experiments performed within the spread-out Bragg

peak (SOBP) were neglected.

- As mentioned above, extrapolations into dose regions not covered by measurement data were avoided. Thus, the availability of raw data for each experiment is requested to determine the largest applied dose and lowest measured cell survival level.
- To be compatible with the LEM concept and in order to ensure biological interpretations, the database was filtered for experiments with $\alpha_\gamma > 0$, $\beta_\gamma > 0$ and $\alpha_i > 0$. Experiments with $\beta_i < 0$ were allowed, even if no negative beta values will be predicted with the LEM concept. Negative values for beta occur if subpopulations of cells with varying radiation sensitivities exist within one sample. The LEM simulations are limited to a single cell population with a unique radiosensitivity.
- The experiment with ID 1040 [78] was excluded as inconsistencies with the original publication were found in the raw data.

Due to the filter criteria defined above, 610 PIDE entries remain for model validations. The number of experiments and filter criteria are summarized in Tab. 3.1. The resulting number of experiments for each ion species is given in Tab. 3.2.

Tab. 3.1.: Overview of the filter criteria of the PIDE for validation purposes of the LEM and corresponding number of experiments.

Filter criteria	**Number of experiments**
Amount of experiments in the PIDE	1118
Subset of monoenergetic ions	925
Subset with raw data available for photons	891
Subset with raw data available for ions	784
Subset of experiments with $\alpha_\gamma > 0$	717
Subset of experiments with $\beta_\gamma > 0$	630
Subset of experiments with $\alpha_i > 0$	611
Subset with exclusion of ambivalent experiments	610

Tab. 3.2.: Number of PIDE experiment pairs considered for each ion species after data filtering according to the criteria given in Tab. 3.1. A minimum of 20 PIDE entries are required for an ion to be included in the validation process.

Ion	**^{1}H+^{2}H**	**^{3}He+^{4}He**	**^{12}C**	**^{20}Ne**	**^{40}Ar**	**^{56}Fe**	**Other**	**Sum**
Amount of experiment pairs	69 (55+14)	104 (39+65)	244	96	22	21	54	610

3.1.2. RBE calculation and error estimation

The precision of the LQ fits to the survival curves of the PIDE experiments directly influences the accuracy of the calculated RBE values. Thus, the uncertainty for each calculated RBE was obtained by accounting for the typically observed covariance of the LQ parameters. A standard Gaussian error propagation was not chosen as it is connected to several difficulties in the application for RBE error calculation. For example, the errors of the parameters used to calculate the RBE are often in the same range as the parameters themselves. Furthermore, the RBE uncertainty does not necessarily express the shape of a Gaussian normal distribution.

As a result, a MC sampling method is applied, which is described in detail in [79] and will be published soon.

The procedure of the MC method for RBE determination is summarized in Fig. 3.2. Based on the LQ fits (Fig. 3.2 A), potential pairs of LQ parameters, α and β, are determined by random sampling from a bivariate normal distribution, which is defined according to the covariance matrix of the fits (Fig. 3.2 B). This procedure is chosen as randomly fluctuating values are found around the best fit values whereas the shape of fluctuations in the α-β parameter space is given by the information in the covariance matrix. In this work, 10000 pairs of LQ parameters were sampled from the ellipsoid-shaped parameter distribution. The dose for each parameter pair, which is connected to the requested survival level was calculated by Eq. (2.15) (Fig. 3.2 C). This procedure was performed for the photon as well as the ion survival curve. Next, the obtained doses D_γ and D_i are matched randomly. For each pair, the RBE is then determined by Eq. (2.16) resulting in a distribution of 10000 RBE values (Fig. 3.2 D). The median of the obtained RBE distribution is taken as the final RBE value. At last, the RBE uncertainty ΔRBE_MC can be calculated based on the RBE distribution:

$$\Delta RBE_\mathrm{MC} = \frac{1}{2}(Q_{84} - Q_{16})\,, \tag{3.1}$$

with Q_{84} and Q_{16} as the quantiles for 84% and 16% of the RBE distribution, respectively. These specific quantiles ensure that the error represents an equivalent to the 1-σ range in a Gaussian distribution. The RBE uncertainties were calculated for the PIDE data according to the method described above. To determine the uncertainty of the LEM predictions, the uncertainties of the model input parameters need to be considered. However, due to practical reasons, the RBE uncertainties obtained for the PIDE data were also used to describe the accuracy of the corresponding LEM predictions.

3.1.3. Running averages

Running averages are a powerful tool to provide smooth curves through data points in case the fit function is unknown. They represent a weighted average of data points, which are included in a specific data window. In this work, the weighting was performed according to [79] and [28] with a Blackman window $w_\mathrm{BM}(x, x_\mathrm{i})$ and the inverse squares of the absolute errors Δy_i for each data point (x_i, y_i) in the considered window:

$$w(x, x_\mathrm{i}) = \frac{w_\mathrm{BM}(x, x_\mathrm{i})}{(\Delta y_\mathrm{i})^2}\,. \tag{3.2}$$

A Blackman window follows a similar shape as a Gaussian function in the interval between -1/2 and 1/2 and is set to zero outside this interval:

$$w_\mathrm{BM}(x, x_\mathrm{i}) = \begin{cases} \frac{1}{50}\left(21 + 25\cos(2\pi z) + 4\cos(4\pi z)\right) & \text{for } -\frac{1}{2} \leq z \leq \frac{1}{2}\,, \\ 0 & \text{else}\,, \end{cases} \tag{3.3}$$

with $z = (x_\mathrm{i} - x)/b$ where b denotes the full width of the Blackman window. The standard error of the average is calculated in order to provide an "error band" around the running average. In comparison to the standard deviation, it is proportional to $1/\sqrt{N_\mathrm{eff}}$ with $\sqrt{N_\mathrm{eff}}$ as the effective number of data points included

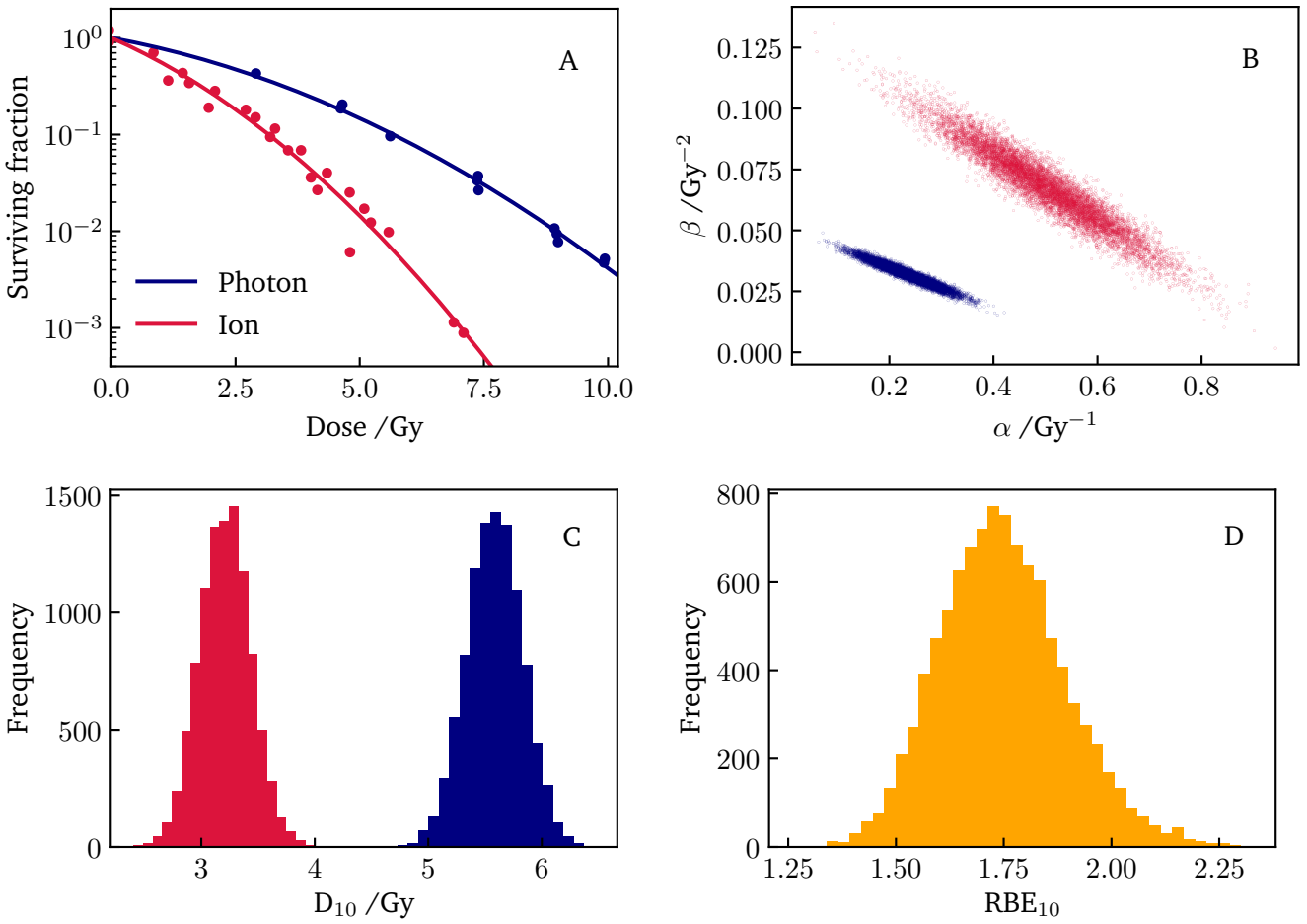

Fig. 3.2.: Schematic representation of the major steps in the MC method for RBE calculation for PIDE experiments. The method is demonstrated at the example of RBE_{10} for T1 cell irradiation with 220 kVp X-rays (blue) and 57.3 MeV/u ^{12}C ions (red) (PIDE experiment ID: 28, [61]). A: Dose-survival measurement data with LQ fit, B: Pairs of α and β sampled from a bivariate normal distribution of curves in A, C: D_{10} distribution for randomly sampled photon-ion pairs from B, D: RBE distribution for randomly matched D_{10} pairs.

in the averaging process. The standard error of the running average SEM is calculated analogous to the standard error of a mean by:

$$SEM = \frac{\sigma}{\sqrt{N_{\text{eff}}}}, \tag{3.4}$$

with the standard deviation σ:

$$\sigma^2 = \frac{\sum_i w(x, x_i)(y_i - \hat{y})^2}{\sum_i w(x, x_i)}, \tag{3.5}$$

the mean value $\hat{y}$ and

$$N_{\text{eff}} = \frac{(\sum_i w(x, x_{\text{i}}))^2}{\sum_i w(x, x_{\text{i}})^2} \,. \tag{3.6}$$

3.2. Application of the LEM for mixed field irradiation

The LEM in its basic implementation can be used to simulate cell survival after irradiation with a single monoenergetic ion species. In the next section, the application of the LEM concept is described with regard to the simulation of the biological effect after mixed irradiations with ions and X-rays. The mixing of the two radiation species is performed on the chromatin loop level meaning that the induction of DSBs is simulated separately for both radiation species before they can potentially interact as potentially lethal lesions and form additional lesions in form of cDSBs. This procedure enables the validation of the LEM concept of interacting DNA damages on the chromatin loop scale. Similar to the interaction of drugs in the human body, the interaction of two radiation doses can be described by the concepts of synergism and additivity as explained in the following section. Next, the necessary modifications in the existing LEM framework are presented and a database of cell survival measurements after mixed radiation fields is described, which was compiled to validate corresponding LEM predictions.

3.2.1. Concept of synergism and additivity for mixed radiation fields

The concept of synergism and additivity can be used in order to describe the degree of interaction of two radiation doses D_a and D_b. The mechanistic interaction of potentially lethal lesions in cells is still not completely understood with regard to relevant interaction scales. Both synergism and additivity were reported in cell survival experiments where low- and high-LET radiation were mixed [80, 81, 82, 75].

There are several concepts to define additivity [83, 84]. This work follows the concept of "Bliss independence" [85], which means the statistical independence of action of any two agents. Thus, the excess effect of radiation mixtures can be interpreted in terms of DNA lesion interaction. Then, additivity is given if the total radiation effect is equal to the sum of both single radiation effects:

$$E(D_\mathrm{a} + D_\mathrm{b}) = -\ln(S(D_\mathrm{a} + D_\mathrm{b})) = E(D_\mathrm{a}) + E(D_\mathrm{b}) \tag{3.7}$$

and concerning cell survival S:

$$S(D_\mathrm{a} + D_\mathrm{b}) = S(D_\mathrm{a}) \cdot S(D_\mathrm{b})\,. \tag{3.8}$$

In the case of synergism, the combined effect is greater than the sum of the partial effects:

$$E(D_\mathrm{a} + D_\mathrm{b}) > E(D_\mathrm{a}) + E(D_\mathrm{b})\,, \tag{3.9}$$

i.e. in terms of cell survival probabilities:

$$S(D_\mathrm{a} + D_\mathrm{b}) < S(D_\mathrm{a}) \cdot S(D_\mathrm{b})\,. \tag{3.10}$$

Note that the definitions for synergism do not only apply to the mixture of two different radiation species such as two ion species of different energy but also to two dose treatments of the same radiation species. This is due to the nonlinearity of dose response curves: As a consequence, the radiation effect after a dose D is larger than after two separate irradiations with dose $D/2$ if no interaction between the two separate dose

treatments is possible. Such a scenario is given if e.g. sufficient time is provided for DNA damage repair between the two irradiations.

3.2.2. Modification of the LEM code

In order to facilitate the prediction of cell survival after mixtures of an ion species with X-rays, the LEM code was adjusted. As the interaction of the two radiation species is simulated on the chromatin loop scale, a modification in the calculation of the microscopic DSB distribution is necessary. Next to the DSBs produced by the ion, the additional DSBs initiated by the photon radiation need to be determined and added. The number of additional DSBs induced by photons is determined according to a yield of 30 DSBs/Gy/nucleus [12]. Since photons deposit their energy homogeneously within the irradiated volume in a first approximation, the additional DSBs are randomly distributed in the cell nucleus by MC algorithms and coexist with the DSBs created by the ions.

Exemplary DSB distributions are schematically demonstrated in Fig. 3.3 for a pure ion irradiation, a pure photon irradiation and an irradiation with a mixture of ions and photons. The cell nucleus is illustrated as a large square consisting of chromatin loop subdomains (see Sec. 2.2.1 and 2.3.2). Each dot represents a DSB. The discrimination between iDSBs and cDSBs is made as chromatin loops with two or more DSBs are hypothesized to be far more lethal than if only a single DSB exists in a loop due to the reduced repair probability for clustered lesions. Fig. 3.3 demonstrates the mechanism of interaction of two radiation qualities. The formation of additional cDSBs (marked in orange) resulting from two interacting iDSBs is the origin of the synergistic effect of mixed radiation fields. In the depicted example, an additional cDSB was obtained by superimposing both fields. After the calculation of the combined DSB pattern for the mixed irradiation, the LEM calculation is continued as for a standard monoenergetic case as described in Sec. 2.3.2.

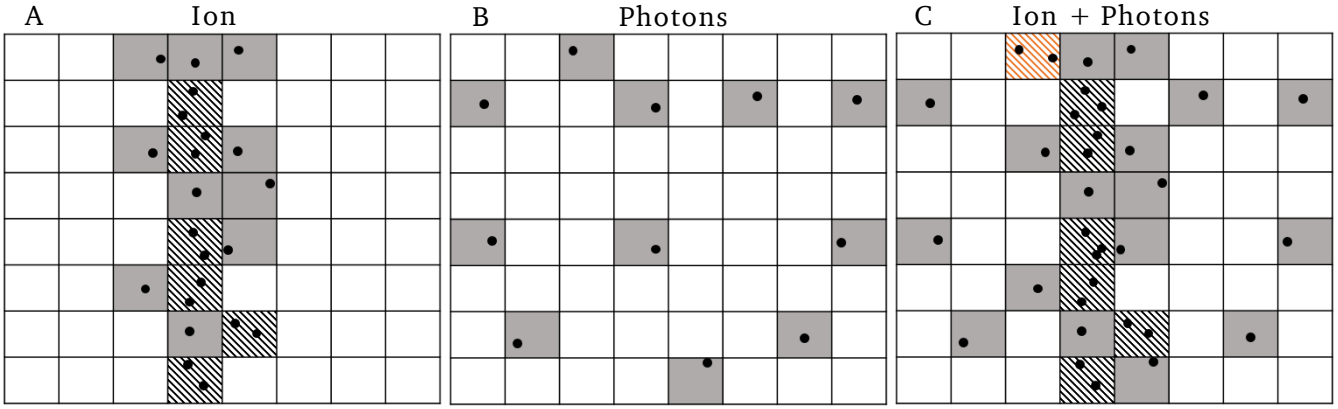

Fig. 3.3.: Exemplary DSB distribution in a schematic cross section of the cell nucleus after irradiation with ions only (A), photons only (B) and a mixture of ions and photons (C). The subvolumes represent chromatin loops. If they include iDSBs or cDSBs, they are marked with a gray filled and striped background, respectively. Additional cDSBs as a result of the interaction of photons and ions are shown in orange.

3.2.3. Database of cell survival after mixed photon and ion irradiation

The results of the LEM simulations of cell survival after exposure to mixed fields are compared to experimental data in order to evaluate the precision of the predictions. In total, 14 published cell survival experiments of

irradiations with mixtures of X-rays and ions were collected and summarized in Tab. 3.3. The choice of experiments is based on the following criteria:

- Measurement data of survival curves need to be available for both the photon and the ion radiation species.
- Track segment conditions are required, meaning that the ion's energy loss is approximately constant while the ion traverses a cell nucleus.
- The measurement dataset was limited to experiments with monoenergetic ions to keep the investigations clear and simple.
- The radiation qualities are either given simultaneously or sequentially with a minimum time interval between irradiations to avoid DNA repair between the two irradiations.

Conditions 2 and 3 are typically not fulfilled in experiments with e.g. α-particles, which are produced in radioactive decays, because of their short remaining range within the cells and due to their angular distribution and corresponding spread in energy and LET. To meet the criteria of track segment conditions, a minimum remaining particle range of 25 µm was required for the experiments to be included in the database. As a result, the experiments reported in [80, 86, 87, 88, 89] are not included in this study. One further experiment [90] is excluded, although it meets all the requirements listed above, because the measured mixed survival curves cross each other, pointing to some inconsistency that cannot be explained by any radiobiological concept.

The radiobiological experiments selected based on the requirements listed above are summarized in Tab. 3.3. They cover five different ion species ranging from ^{12}C to ^{56}Fe. The experiments were performed according to two different concepts:

- Either the ratio of the dose proportions of both radiation qualities remained constant for each data point. In these cases the radiation mixture is given in the table according to the format (ion dose : photon dose).
- Or a fixed dose of one radiation quality is given first, followed by a varying dose fraction of the second radiation quality.

All experiments were performed with Chinese hamster V79 cells, except for the experiment of Demizu et al. [81] in which human salivary gland (HSG) cells were used. In Demizu's experiment, not every data point was measured with exactly the same ratio of photon to ion dose but all dose ratios are close to 1:2.

As the LEM predictions are based on the knowledge of the cells' response to photon irradiation, the LQ parameters α and β for the pure X-ray survival curve are required for the LEM simulations. Therefore, the LQ parameters are obtained by fitting the corresponding X-ray survival data by the LQ model according to Eq. (2.15), leading to the fit parameters shown in Tab. A.1. Next to the photon fit parameters, which are needed as an input for LEM, the LQ parameters of the ion and mixed survival curves are listed.

Tab. 3.3.: Set of cell survival experiments with mixed radiation fields consisting of ions (I) and X-rays (X). The mixtures are given in ratios of (ion dose : photon dose). A number is assigned to each survival experiment for identification purposes (ID).

Publication	ID	Ion	E/ (MeV/u)	LET/ (keV/µm)	Mixture (I:X)	Cell type
Furusawa et al. [91]	1	^{40}Ar	550	86	1:1	V79
	2	^{40}Ar	550	86	1:4	V79
	3	^{56}Fe	115	442	1:1	V79
	4	^{56}Fe	115	442	1:4	V79
Tilly et al. [92]	5	^{14}N	37	78.4	1:1	V79
	6	^{14}N	14.9	164.5	1:1	V79
Demizu et al. [81]	7	^{12}C	48.1	46.6	≈1:2	HSG
Ngo et al. [93]	8	^{20}Ne	31	183	1:1	V79
	9	^{20}Ne	31	183	0.94 Gy X+I	V79
	10	^{20}Ne	31	183	2.36 Gy X+I	V79
	11	^{20}Ne	31	183	3.30 Gy X+I	V79
	12	^{20}Ne	31	183	4.13 Gy X+I	V79
	13	^{20}Ne	31	183	5 Gy I+X	V79
	14	^{20}Ne	31	183	8 Gy I+X	V79

3.3. Kiefer model for secondary electron spectra

An analytical model for track structure calculations was developed by Kiefer and Straaten in 1986 [56]. It enables the calculation of secondary electron spectra of first generation liberated by ion radiation based on classical collision dynamics. Kiefer's model is based on three assumptions:

1) Heavy ions liberate electrons according to classical collision dynamics. Classical is meant here in terms of neglect of quantum-mechanical effects.

2) The energy distribution of secondary electrons follows an T^{-2} dependence with T as the electron energy.

3) Only the production of secondary electrons is considered, meaning that cascades of electrons of later generations are neglected. The secondary electrons are assumed to travel on straight lines. Thus, changes in direction of flight due to physical interactions along the electron tracks are neglected. The electron range is calculated by a simple power function, which depends on the electron's kinetic energy.

A schematic representation of the track structure resulting from the assumptions described above is shown in Fig. 3.4. The ion liberates electrons along its track. The δ-electrons travel further away from the ion trajectory via an angle, which is defined by the electron's kinetic energy.

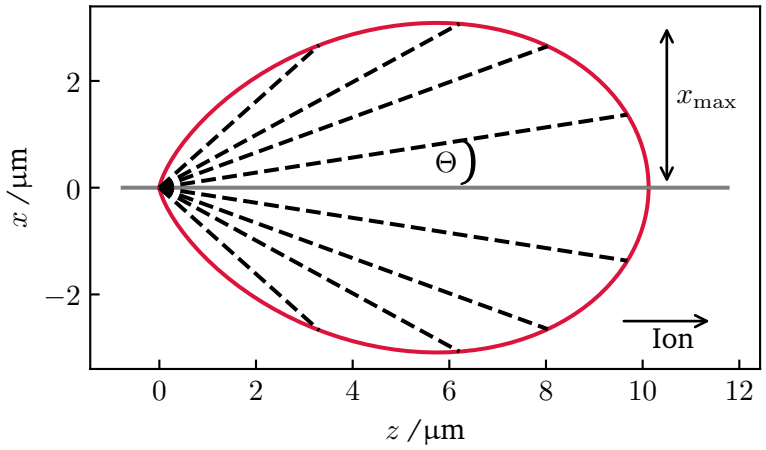

Fig. 3.4.: A 10 MeV/u ^{12}C ion traverses the medium on a straight line in z-direction. Electrons are emitted via angle Θ, which depends on their kinetic energy (black dashed lines); their maximum range is indicated in red.

Secondary electron spectra can be calculated as $d^2N/dT_0/dz$ with the number of liberated electrons dN per kinetic energy interval dT_0 per length segment dz:

$$\frac{d^2N}{dT_0\,dz} = C\frac{z_{\text{eff}}^2}{\beta^2}\frac{1}{dT_0^2}\,, \tag{3.11}$$

with z_{eff} as the effective charge calculated according to the Barkas formula as given in Eq. (2.6). The parameter β denotes the relativistic ion velocity and C denotes a prefactor, which is equal to 8.5 eV/µm in liquid water. The derivation of Eq. (3.11) is based on the same concept as the derivation of the Bethe-Bloch equation (see Eq. (2.4)). Its main pillars are the consideration of the electron number density in the target material and the momentum transfer to any electron at a certain impact parameter to the ion trajectory.

The emission angle Θ by which an electron is liberated into the medium depends on the electron's kinetic energy:

$$\sin^2\Theta = \frac{1 - \frac{T_0}{T_\mathrm{m}}}{1 + \frac{T_0}{2m_\mathrm{e}c^2}} \,. \tag{3.12}$$

The range R of an electron is given as a function of its kinetic energy T with the empirically found formula:

$$R(T) = KT^\alpha \,, \tag{3.13}$$

with the constants $K = 4.18 \cdot 10^{-11}$ cm eV$^{-\alpha}$ and $\alpha = 1.7$. Electrons at intermediate energies reach a maximum lateral (radial) range x_max (see Fig. 3.4) that can be approximated by:

$$x_\mathrm{max} = 0.062 \cdot E^{1.7} \,. \tag{3.14}$$

Here, the parameter x_max is given in µm, the ion's energy E in MeV/u, γ = 0.062 and δ = 1.7. Several properties such as the range R, emission angle Θ, radial range x and the electron number are calculated and plotted as a function of electron energy in Fig. 3.5 for a 10 MeV/u ^{12}C ion.

Kiefer-GSI extension for radial electron spectra: Based on the Kiefer approach presented above, an extension was developed by T. Friedrich, which will be called Kiefer-GSI model in the following [94]. The publication of the formalism is in preparation. The extension includes the employment of the full relativistic formalism of the relations derived by Kiefer. Furthermore, the Kiefer-GSI model enables the calculation of secondary electron spectra at any radial distance to the ion track center. These radial secondary electron spectra are applied in this work to describe the secondary electron composition in dependence on the radial distance in an ion track. This enables the assessment of the mean effectiveness of the electron mixture (e.g. for DSB induction) present at any distance to the ion track center.

In the first part of the GSI-Kiefer model, the function to describe secondary electron spectra at a radial distance $r = 0$ is extended to its relativistic description by including the momentum transfer in its relativistic form. Then, Eq. (3.11) transforms to:

$$\frac{d^2N}{dT_0\, dz} = C \frac{1 + \frac{T_0}{m_\mathrm{e}c^2}}{(1 + \frac{T_0}{2m_\mathrm{e}c^2})^2} \frac{z_\mathrm{eff}^2}{\beta^2} \frac{1}{dT_0^2} \,, \tag{3.15}$$

with m_e as the electron mass and c as the speed of light in vacuum. The maximum kinetic energy can be transferred in a binary encounter head-on collision (see Sec. 2.1.2). Thus, the maximum transferred energy T_m can be calculated, with the relativistic factor $\gamma = 1/\sqrt{1-\beta^2}$ and the rest mass of the ion M, via:

$$T_\mathrm{m} = \frac{2m_\mathrm{e}c^2\beta^2\gamma^2}{1 + \frac{2\gamma m_\mathrm{e}}{M} + (\frac{m_\mathrm{e}}{M})^2} \approx 2m_\mathrm{e}c^2\beta^2\gamma^2 \,. \tag{3.16}$$

The second part of the GSI-Kiefer model includes the derivation of the secondary electron spectra as a function of the radial distance to the ion track center. The formalism is presented in the following starting from relations arising from the original Kiefer model. Figure 3.6 depicts a schematic drawing of a liberated

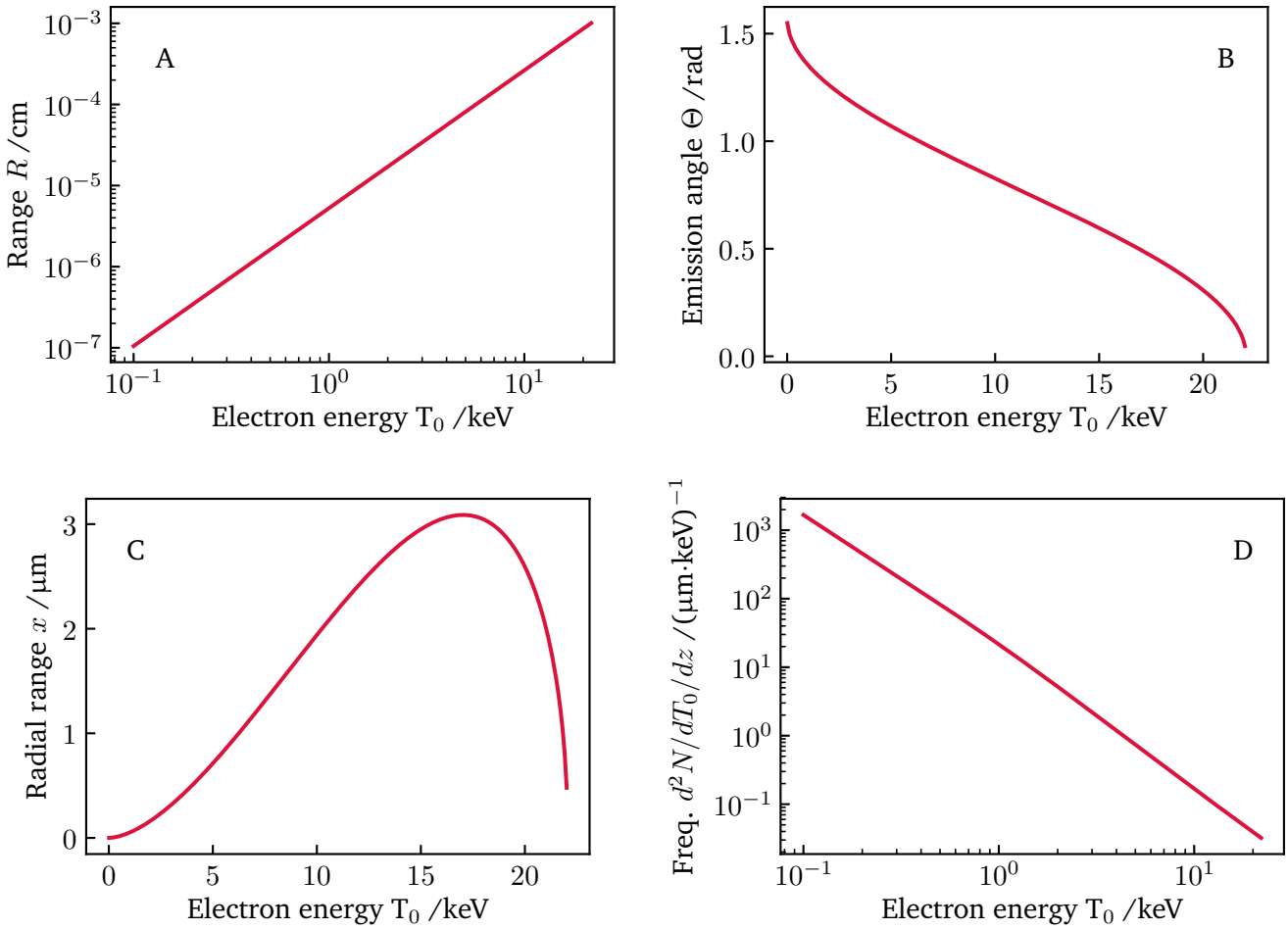

Fig. 3.5.: Physical properties of secondary electrons according to the Kiefer model for 10 MeV/u ^{12}C ions as a primary radiation species.

electron along its track in relation to the ion's direction of flight. The ion travels in the horizontal plane and liberates an electron with total range R, which is deflected via the angle Θ. At the radial distance x, the electron has traveled the total distance R_a.

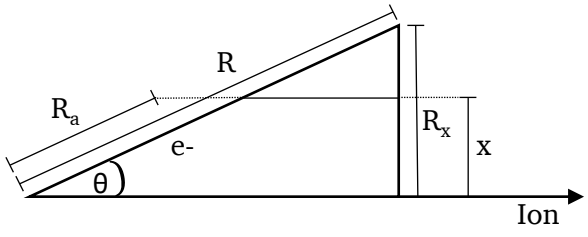

Fig. 3.6.: Schematic illustration of an electron's geometric position in relation to the ion's path.

There is a unique relation between electron energy and range. Thus, the remaining energy T of an electron at distance x to the ion track center with initial kinetic energy T_0 can be calculated by solving Eq. (3.13) for the energy T according to the Kiefer model:

$$T(x, T_0) = \left[\frac{R - R_\mathrm{a}}{K}\right]^{1/\alpha} . \tag{3.17}$$

Solving Eq. (3.13) for the constant K and inserting into Eq. (3.17) leads to a function for the remaining kinetic energy T dependent on the initial electron energy T_0, the range R and the already passed distance R_a:

$$T(x, T_0) = T_0 \left[1 - \frac{R_\mathrm{a}}{R}\right]^{1/\alpha} . \tag{3.18}$$

With the geometric relation

$$\frac{x}{R_\mathrm{a}} = \frac{R_\mathrm{x}}{R} , \tag{3.19}$$

the remaining energy T of an electron at distance x to the track center with initial energy T_0 can be formulated as:

$$T(x, T_0) = T_0 \left[1 - \frac{x}{R_\mathrm{x}(T_0)}\right]^{1/\alpha} . \tag{3.20}$$

Here, the radial range R_x can be calculated through the geometric relation (see Fig. 3.6):

$$R_\mathrm{x}(T_0) = R(T_0) \cdot \sin(\Theta) . \tag{3.21}$$

The remaining electron energy is calculated according to Eq. (3.20) for three radial ranges for a 10 MeV/u ^{12}C ion. The corresponding curves are shown in Fig. 3.7 A. In Fig. 3.7 B, the remaining range is enlarged for a radial distance of $x = 2$ µm. Additionally, the two initial electron energies $T_{0,1}$ and $T_{0,2}$ are indicated. Electrons with exactly these initial kinetic energies stop at the radial distance x. As a result, only electrons with initial energies $T_{0,1} < T_0 < T_{0,2}$ reach beyond the radial distance x and can contribute to the energy deposition outside x. The values of $T_{0,1}$ and $T_{0,2}$ can be equated by numerically calculating the roots of Eq. (3.20). Finally, based on the initial electron energy spectrum $d^2N/dz/dT$ and Eq. (3.20), the distribution of electron energies at radial distance x can be calculated. Therefore, the inverse of the derivative of Eq. (3.20) needs to be calculated and evaluated at the two minimum and maximum initial energies $T_0 = T_{0,1}$ and $T_0 = T_{0,2}$ needed to reach the radial distance x. The inverse of the derivative is used as it gives a measure for the probability fo find an electron in a specific small remaining energy interval. The indices in Eq. (3.22) refer to the energy point of evaluation:

$$\frac{d^2N}{dz\, dT}(T, x) = \frac{d^2N}{dz\, dT_0} \cdot \left|\frac{dT_0}{dT}\right|_{\mathrm{T_{0,1},x}} + \frac{d^2N}{dz\, dT_0} \cdot \left|\frac{dT_0}{dT}\right|_{\mathrm{T_{0,2},x}} . \tag{3.22}$$

Equation (3.22) is plotted in Fig. 3.8 for several radial distances x to the ion track center. The shape of the electron spectra changes while the radial distance increases: While for small radial distances low-energetic electrons dominate the spectrum, this behavior is inverted for larger radii. The GSI-Kiefer model shows a sharp increase of the electron frequency at the maximum kinetic energy for a specific radial distance. This peak is due to a singularity, which originates from the definition of the electron spectra in Eq. (3.22). As visible in Fig. 3.7, the remaining energy as a function of the initial energy shows a maximum. At this position, the slope of the curve is zero and the inverse of the derivative applied in Eq. (3.22) is not defined.

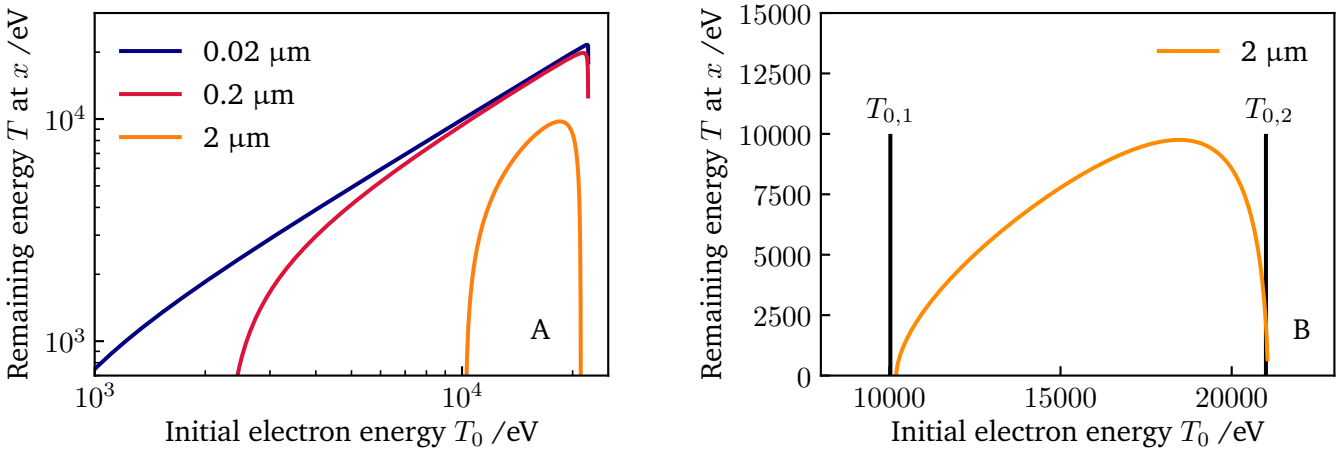

Fig. 3.7.: Remaining kinetic electron energy T as a function of the secondary electron's initial energy T_0 for three radial distances x to the track center for a 10 MeV/u ^{12}C ion (A). Initial electron energies between ($T_{0,1}$; $T_{0,2}$) correspond to electrons passing the distance x (B). Note that in (A) a log-log scale was chosen in contrast to the linear-linear scale in (B).

The presented GSI-Kiefer model includes an extension to radial electron energy spectra based on the original Kiefer model. The knowledge about the secondary electron spectra for different radiation species is essential in order to assess their effectiveness for DSB induction. Because photons liberate electrons in a random pattern, the secondary electron spectra induced by photons can be assumed to be constant in an irradiation field in a first approximation. For ions, however, the secondary electron spectra vary considerably with the radial distance to the track center. Therefore, a model for the description of the shape of secondary electron spectra in dependence on the radial distance to the ion track center is indispensable for the detailed description of the mean biological effectiveness in an ion track.

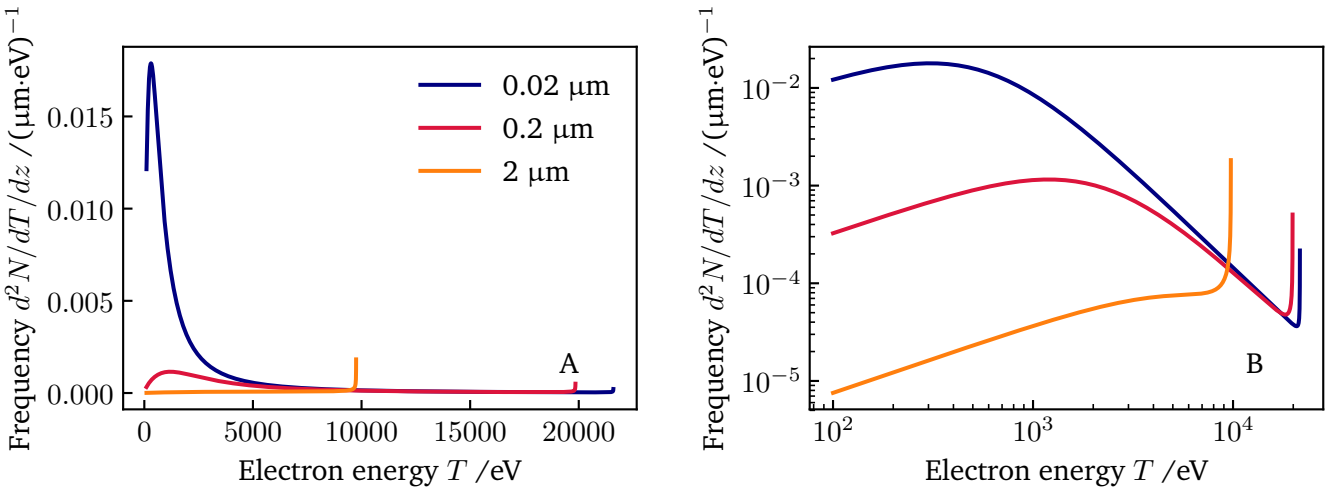

Fig. 3.8.: Radial electron energy spectra at three distances to the ion track center on a linear-linear (A) and a log-log (B) scale. These spectra correspond to secondary electrons liberated by a 10 MeV/u ^{12}C ion. The x-axes in this figure are equivalent to the y-axes in Fig. 3.7.

3.4. Geant4-DNA Monte Carlo simulations

Radiation transport codes enable the calculation of several physical properties of radiation based on cross sections of the underlying physical processes. Such codes play a vital role in radiotherapy research and application. For instance, for the dose calculation of cancer treatment plans, analytical pencil beam algorithms are applied. These require e.g. Bragg curves as basic input data, which are calculated in clinical practice with radiation transport codes such as the MC code FLUKA [95, 96]. Particle transport codes are powerful tools to access radiation track structures and associated physical quantities if the corresponding mathematical problems are either very time-consuming to solve or not analytically solvable at all. In this work, the MC code Geant4-DNA is used to simulate several physical quantities. Geant4-DNA is a low-energy extension to the open-access Geant4 general purpose MC toolkit developed by CERN [97, 98, 99]. The extension enables the simulation of ionizing radiation inducing early biological damage at the DNA scale [47, 49, 50, 51]. This is realized by simulating step-by-step physical interactions down to very low energies (≈10 eV) in liquid water or DNA constituents. As eucaryotic cells are composed by 80% of water, water is used in this work as a medium to simulate a cellular environment.

MC codes can be generally classified as condensed history or track structure codes. Condensed history codes such as FLUKA or standard Geant4 are on the one hand efficient in calculation time by grouping several physical interactions together. On the other hand, the maximum spatial resolution of physical interactions is reduced. The more time consuming track structure codes enable a high resolution of spatial scales relevant for DNA damage due to detailed simulation of step-by-step interactions of each physical event. Exemplary microscopic track structures simulated with the track structure code Geant4-DNA for a 10 keV and 1 keV electron are shown in Fig. 3.9 in form of local energy depositions. A corresponding figure for track structures of protons and carbon ions can be found in Sec. 2.1.4, Fig. 2.10.

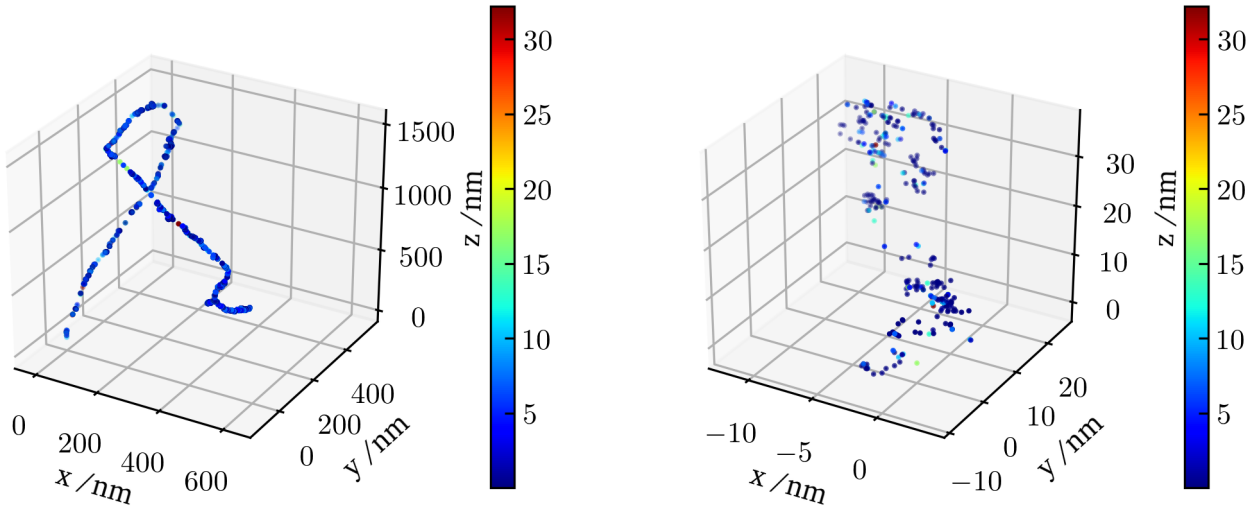

Fig. 3.9.: Track structure of a 10 keV electron (left) and a 1 keV electron (right) originating at position (0,0). Local energy depositions are shown as dots, the amount of energy deposited in each event is indicated by color in units of eV.

3.4.1. Interaction models

In this work, Geant4-DNA simulations are used for validation purposes as well as for the calculation of model inputs. For instance, secondary electron spectra are simulated in order to validate the analytical Kiefer model, which is applied in this work to calculate corresponding spectra. Another example is the mean free path of an electron that is used as a basis for the DSB induction model developed within the scope of this work. Thus, a wide range of ion and electron energies are of interest as well as a large set of different ion species and photons. As these requirements exceed the energy range of available Geant4-DNA cross sections, a combination of the DNA models with standard Geant4 models was used in the simulations. This combination of different physics lists (=compilations of cross section models and data) was introduced in [47] and is distributed as a simulation example with the standard Geant4 installation (dnaphysics example). In this simulation mode, Geant4-DNA models are used whenever corresponding cross section data are available; outside these ranges the standard electromagnetic models of classical Geant4 are applied. Currently, three recommended sets of Geant4-DNA cross section data/models exist for the simulation of discrete particle interactions in liquid water [47]. The default option is Geant4-DNA option 2, which is also used throughout this work. The interaction models for electrons and corresponding energy ranges of the combined cross sections are given in Tab. 3.4 [47].

Tab. 3.4.: Description of the models used in the automatic combination of Geant4-DNA option 2 and classical Geant4. Taken from [47].

Physical process	**Geant4-DNA electron model**	**Geant4 electron standard electromag. model**
Elastic	Partial wave (<1 MeV)	Urban (multiple scatt., >1 MeV) or Coulomb (single scatt., > 1 MeV)
Electronic excitation	Emfietzoglou-Kyriakou (<10 keV) and default (10 keV-1 MeV)	n/a
Ionization	Emfietzoglou-Kyriakou (<10 keV) and default (10 keV-1 MeV)	Moller-Bhabha (>1 MeV)
Vibrational excitation	Sanche (<100 eV)	n/a
Attachment	Melton (<13 eV)	n/a

3.4.2. Simulated physical properties

Several physical properties are simulated with Geant4-DNA in this work. In the following section, those properties are briefly described together with their corresponding simulation setup. If International Commission on Radiation Units and Measurements (ICRU) recommendations are available for certain quantities, the simulation outputs are compared to those.

Mean free path between ionizations for electrons: For the induction of a DSB by a single electron track at least two ionizations in close proximity are necessary. The mean distance between physical interaction processes can be described by the mean free path l. It is connected to the cross section through Eq. (3.23) with the material *molecule* density ρ and the interaction cross section σ:

$$l = \frac{1}{\rho \cdot \sigma} \,. \tag{3.23}$$

The mean free path l between two interactions along an electron track was simulated by applying the "mfp" example provided with the Geant4-DNA package [47]. In the example, a water sphere with a radius of 10 m is constructed in which each interaction of an electron is tracked. The mean free path was calculated for 109 log-spaced electron energies between 1 eV and 10^6 eV with 10^6 simulated primary particles per energy. The simulation results are depicted in Fig. 3.10 A, not only for the mean free path between ionizations, but also including other physical interactions. Furthermore, analytical data for the mean free path between ionizations provided by NIST is shown [100].

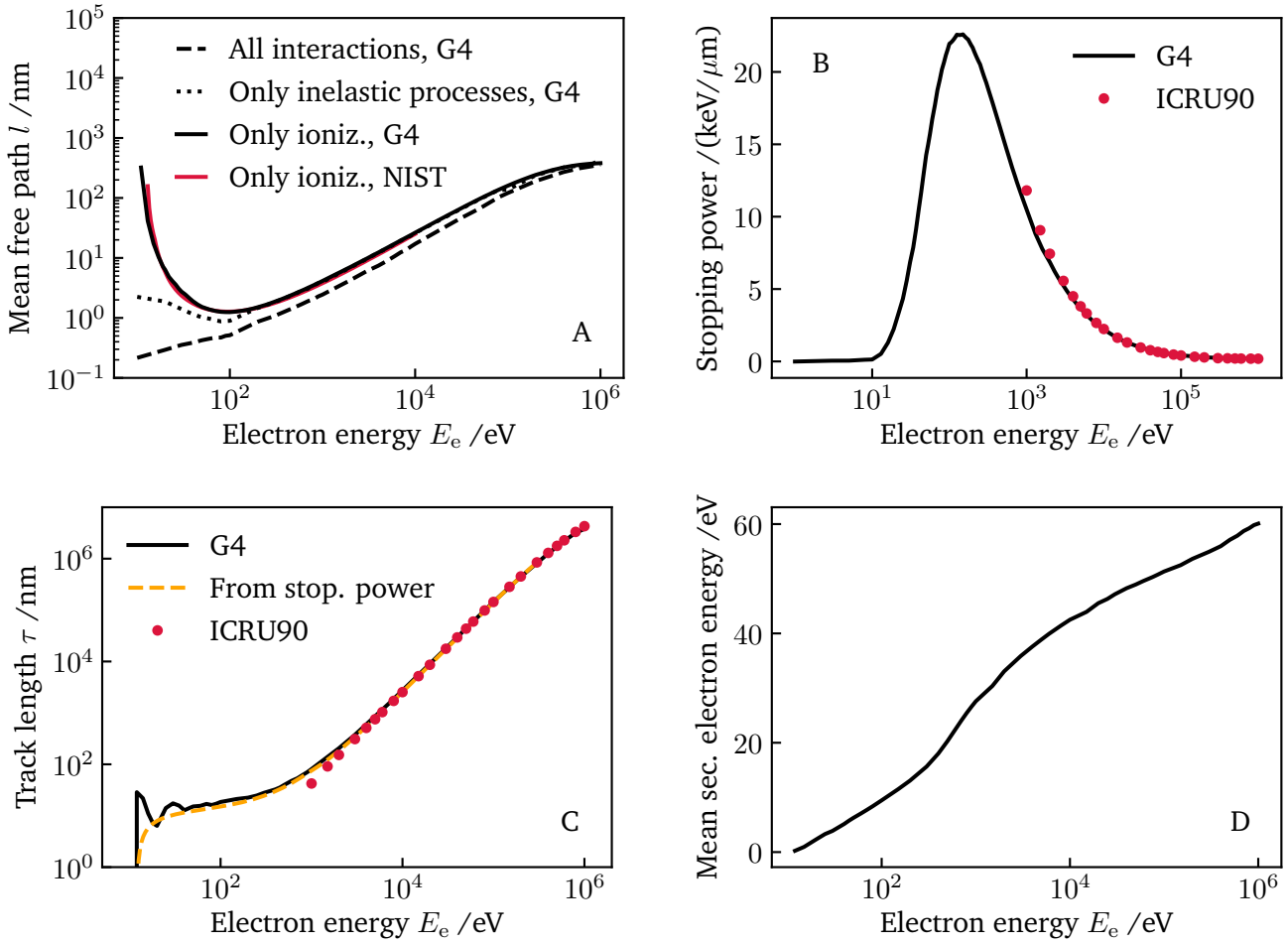

Fig. 3.10.: A: Mean free path of electrons calculated with Geant4-DNA for all interactions, inelastic interactions and ionizations only. B: Dependence of stopping power on electron energy. C: Range of electrons calculated by Geant4-DNA compared to recommendations by ICRU90 and the integral of the inverse of the stopping power over energy (see Eq. (2.7)). D: Mean energy of liberated secondary electrons dependent on the incident electron's energy.

Electron stopping power: The stopping power of electrons is used in this work to describe the amount of energy deposited on small spatial scales ("local"). For the corresponding simulation, the "spower" Geant4-DNA example was used with a water sphere with a radius of 1 m. For the simulation of the stopping power a stationary mode is activated, meaning that the kinetic energy of the primary particle is artificially set to its

starting energy at each simulation step. This ensures the correct simulation of the stopping power according to its definition [47]. Secondary particles are not transported. In total, the stopping power was calculated for 118 log-spaced electron energies between 1 eV and 10^6 eV. For electrons with energies below 10 keV 10^6 particles were simulated and for electrons with energies above or equal to 10 keV 10^5 particles were considered. The results are depicted in Fig. 3.10 B together with data recommended by ICRU [101].

Electron range: The electron range can be simulated with the Geant4-DNA "range" example, in which a water sphere of 1 m radius is applied as the target. The range refers here to the sum of all step lengths of an electron, which is in contrast to the "penetration range" referring to the distance from the starting point of the electron to its stopping point. The minimum energy down to which the electrons are tracked on their path is set to the allowed minimum, ensuring the consideration of the full track. In total, 53 log-spaced electron energies between 12 eV and 10^6 eV were simulated. For the lowest energies 10^7 particles were simulated to achieve sufficient statistical power. At the largest electron energies 100 particles were simulated for acceptable computation time. The range of electrons is shown in Fig. 3.10 C. The oscillations at very low energies are due to rapidly decreasing cross sections for inelastic interactions and are, thus, not due to statistical fluctuations [47]. In order to avoid these oscillations, the electron range was alternatively calculated by Eq. (2.7) as the integral of the inverse of the stopping power over energy. To ensure compatibility with Geant4-DNA output a lower integration limit of 12 eV was chosen (= minimum ionization energy). Additionally, values recommended by the ICRU for the range of electrons are plotted for comparison [101].

Secondary electron spectra: In this work, secondary electron spectra are of interest for several different radiation species, such as photons, ions or incident electrons. For the simulation of secondary electron spectra, the incident radiation species were tracked while traversing a large cubic water target. Along the passage of a 1 µm thick layer of water, each liberated electron of the first generation was scored and its energy tabulated. For primary electrons, a thinner layer thickness of 10 nm was applied due to the reduced range of electrons in the relevant energy range. By binning the obtained data, secondary electron spectra are calculated as shown in Fig. 3.11 for incident protons (A) and electrons (B). The secondary electron spectrum, which corresponds to 250 kVp X-ray photons is shown in Fig. 2.2 B. The spectra show the energy distribution of liberated secondary electrons per primary particle and per traveled primary path length. For ions, next to the Geant4-DNA simulations, calculations by the Kiefer model (see Sec. 3.3) are depicted. For electron energies greater than ≈20 eV the analytical model matches the simulations with great accuracy. However, the Auger peak at around 540 eV is not included in the analytical model. Whereas the simulations indicate a decrease of the number of electrons produced for electron energies smaller than ≈20 eV, the analytical model shows a further increase in that energy range. However, it should be noted that there are only few measurement data available in this low-energy energy regime. Thus, the exact physical behavior at such small kinetic energies is unknown, which needs to be considered when applying and analyzing simulation results.

Based on the secondary electron spectra, the mean energy of these electrons can be calculated as plotted for incident electrons in Fig. 3.10 D. For these simulations, 51 electron energies between 12 eV and 10^6 eV were simulated with logarithmic energy spacing. The lowest energy was set to 12 eV as this is the minimum ionization energy for water. Each simulation consists of $5{\cdot}10^6$ to $2.5{\cdot}10^9$ tracked primary particles, whose tracking was stopped as soon as they left the scoring layer of 10 nm. The figure shows that even high-energetic electrons liberate electrons of further generations with small kinetic energies. Thus, the ionization cascade of a secondary electron can be pictured by a branch of a tree with several short side shoots as shown schematically in Fig. 3.12 A. The same behavior is observed for incident ions.

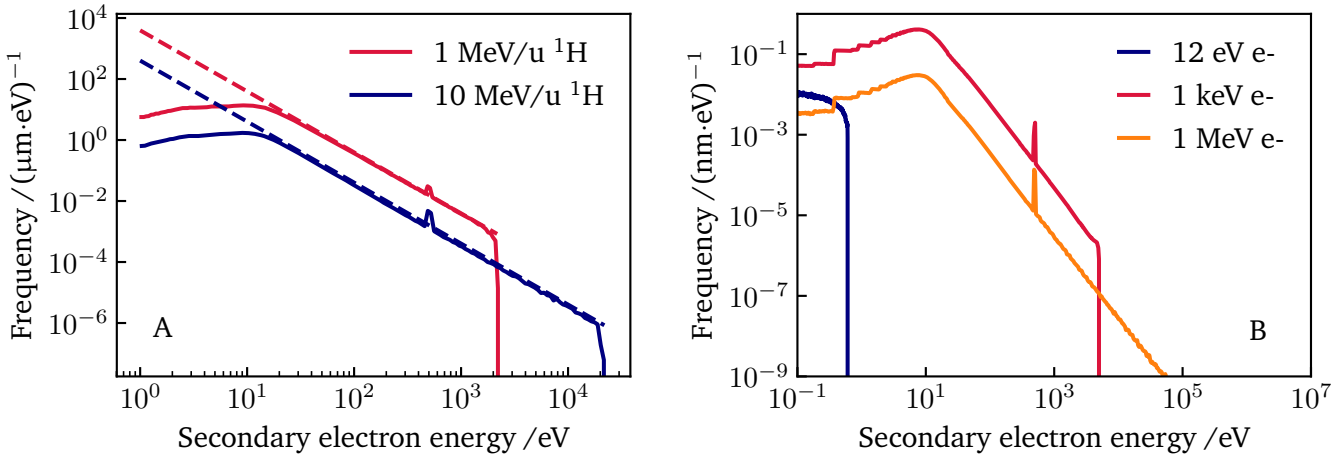

Fig. 3.11.: Secondary electron spectra induced by protons (A) and primary electrons (B) in water. Geant4-DNA simulations are shown as solid lines whereas the analytical Kiefer model is shown as dashed lines. The peaks at ≈540 eV are due to Auger processes.

Radial secondary electron energy spectra for ions: Ions liberate secondary electrons when traversing medium, which have an energy distribution as described above. These electrons travel further away from the ion's track center and slow down due to Coulomb interactions with the target material. Therefore, the secondary electron spectra for ions vary with the radial distance to the ion track center. The corresponding secondary electron spectra are scored in cylindrical shells around the primary particle's track according to the procedure shown schematically in Fig. 3.12 B. The ion's position and direction of flight are shown as a red point and a red arrow, respectively. The ion interacts with the target electrons and releases them into the surrounding medium. This is a simplified illustration of the physical processes as only the secondary electrons' tracks are shown, ignoring further generations of electrons. Furthermore, for simplification purposes the electrons are drawn to travel on straight lines, which does not reflect reality as the direction of flight changes due to interactions of the electrons with the target material. The blue lines indicate cylindrical shells in which the electron spectra are scored.

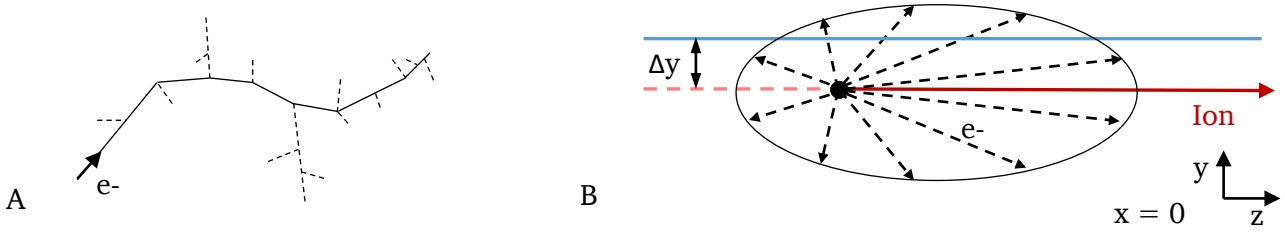

Fig. 3.12.: A: Schematic electron track (solid line) with low-energetic secondary electrons (dashed lines). B: Cross sectional plot of schematic MC scoring method for radial electron energy spectra for incident ions. The blue lines indicate cylindrical shells in which the electron spectra are scored.

The resulting electron energy spectra, which vary with the radial distance to the track center are displayed in Fig. 3.13. Mind that here only the first generation of liberated electrons is shown as these electrons considerably dominate the shape of the ion/dose track. The greater the radial distance, the lower the relative number of lower-energetic electrons. The MC spectra agree well with the electron energy spectra calculated by the Kiefer-GSI model. Only for low-energetic electrons <100 eV, where only few measurement data are

available, the models diverge. Furthermore, the GSI-Kiefer model shows defined peaks at the maximum secondary electron energies present for a specific radial distance. These peaks are of mathematical nature and explained in Sec. 3.3.

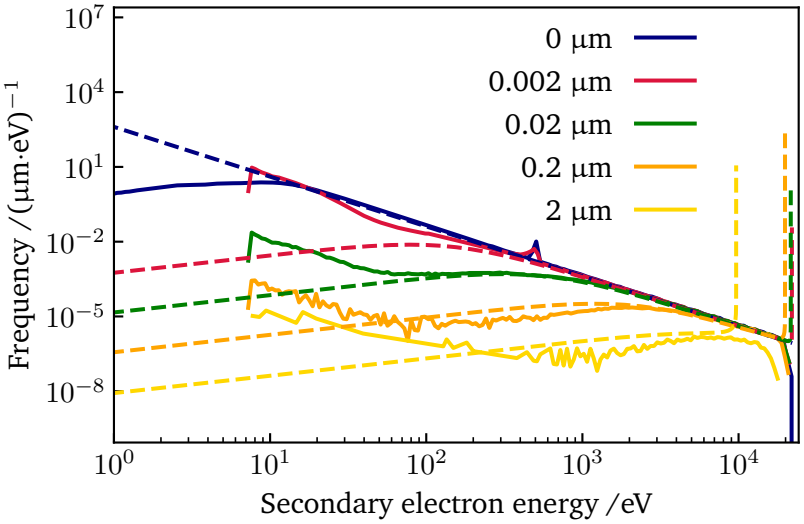

Fig. 3.13.: Radial electron energy spectra for secondary electrons generated by a 10 MeV proton traversing a 1 µm thick layer of water. Geant4-DNA simulations are shown as solid lines and the corresponding calculations with the Kiefer-GSI model as dashed lines. Electrons of later generations are not included.

Simulation of photon radiation: The paragraphs above are focused on the simulation of physical characteristics of ion and electron radiation. As in radiobiological experiments photons are typically used as a reference radiation species, their simulation is described separately. In this work, two photon radiation species are of interest because they are also commonly used in experiments: X-rays and Co_γ radiation. The physical characteristics of photons are described in Sec. 2.1.1. Figure 2.2 A shows a typical X-ray spectrum for a acceleration voltage of $U = 250$ kV. The spectrum consists of a broad energy distribution with a maximum frequency at approximately half of the maximum photon energy. This spectrum is used in this work as an input to Geant4 for the simulations of secondary electron spectra. The secondary electron spectrum for X-rays is shown in Fig. 2.2 B and resembles a "box shape". The procedure for the calculation of the energy spectra is described in an earlier paragraph above together with the analogous simulation procedure for other radiation species than photons. Next to the secondary electron spectra of X-rays, such spectra are of interest for the second relevant photon radiation species in radiobiology: Co_γ. The term "Co_γ" describes the photon radiation liberated in the β-decay of ^{60}Co. Next to two photons with 1.173 and 1.332 MeV, additionally an electron is liberated in the decay. The electrons are, however, typically filtered out in radio-therapeutic applications. Note that these electrons, which are produced directly in the decay of ^{60}Co are independent from the secondary electrons liberated by the photons created in the decay. Thus, in this work, Co_γ radiation is simulated as two photons of the above mentioned kinetic energies. The probability of their occurrence is assumed to be the same for both decay channels, which is an appropriate approximation. Therefore, Co_γ radiation consists of photons with two distinct relatively high energies ($\approx$1 MeV) whereas X-rays show a full photon energy spectrum in the low- to intermediate energy range (<250 keV). Similar as for X-rays the secondary electron spectrum induced by Co_γ radiation follows a box shape. Finally, it should be noted that for photons no specific Geant4-DNA models exists as for ions or electrons such that physical interaction processes for photons are processed by the standard Geant4 models.

3.5. Database for DSB yield and RBE for DSB induction of electrons

In the course of this work, a DSB induction model was developed to allow the evaluation of the relative effectiveness of electrons for DSB induction as a function of the electrons' energy. The reference data used to optimize free parameters of this DSB induction model was collected from published experimental data and simulations. The data cover experiments with primary electrons in a large energy range as well as with incident photons with kinetic energies <10 keV. Low energetic photons are allowed here as a primary radiation because they are assumed to solely interact via the photoelectric process. Thus, the full kinetic energy of the photon minus the binding energy is transferred to an ejected electron. Therefore, in this case the data can be handled as if electrons were directly applied as the primary radiation species. The optimization of the free fit parameters of the DSB induction model was performed on two sets of data: DSB yields per dose as a function of electron energy and the RBE for DSB induction as a function of electron energy. Note that both quantities are correlated and therefore the same data is used in a different form twice for model optimizations. The data, which were collected from 21 publications, are visualized in Fig. 3.14 and summarized in Tab. A.5 in the appendix.

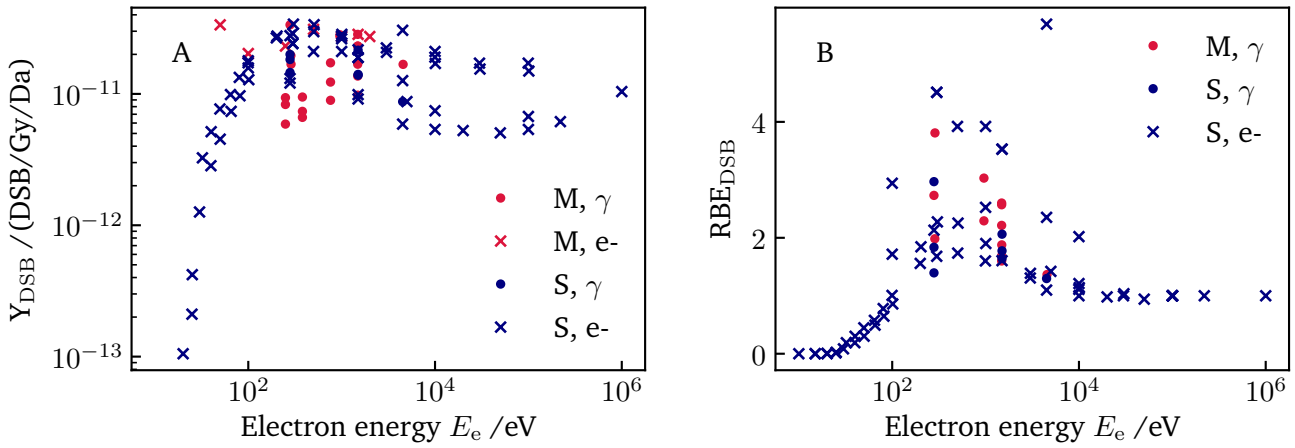

Fig. 3.14.: Experimental data collected from measurements and simulations published in the literature as summarized in Tab A.5. M: Measurement, S: Simulation, e-: Electron, γ: Photon, Da: Dalton, molecular mass unit.

As only few cross section data exist for low energetic electrons, data from simulation studies for electrons with kinetic energies $E_e \leq$100 eV are not included in the optimization process. As a result, 76 experiments with measurement/simulation data on the number of DSBs induced per electron are included in the fit procedure. For 58 of these experiments additionally the RBE (endpoint: DSB induction) was measured or calculated and could therefore be used in the optimization process, too.

4. Systematic validation of the Local Effect Model IV by in-vitro cell survival data

The local effect model (LEM) is a biophysical model, which enables the prediction radiation effects as a result of DNA damage for various ion species based on the cells' response to photon radiation. Its mechanistic concept and formalism are described in detail in Sec. 2.3.2. Over the years, the model was continuously optimized, leading to the current version LEM IV. Within the framework of this thesis, the model was further improved by including the specific effectiveness of secondary electrons concerning DSB induction, introducing LEM version V.

In the course of time, the concept of the LEM IV for RBE predictions has been validated for various radiobiological endpoints as e.g. for the prediction of in-vitro experimental data over a larger range of different ion species from protons to oxygen ions [11, 19, 20, 21]. Next to in-vitro data, the model was found to accurately represent experimental in-vivo RBE data. This was shown by comparing model predictions to experimental data on the dose tolerance of the rat spinal cord [22, 23, 24]. Additionally, several radiobiological aspects as the induction of secondary cancers, dose rate or cell cycle effects as well as rejoining kinetics are found to be accurately reproduced by the LEM IV [12, 25, 26, 27]. This large variety of validation cases demonstrated strengths and weaknesses of the LEM for RBE prediction and already revealed systematic dependencies such as a general underestimation of RBE in the low-LET regime for carbon ions [12, 23]. However, in order to quantify such model deviations a model comparison to a large dataset is essential. Therefore, in the following section the latest version of the model, LEM IV, is systematically validated by comparing its RBE predictions with the endpoint of cell survival to measurement data listed in the PIDE database. The data and plots presented in this chapter are based on a publication by Pfuhl et al., which is in preparation [102]. Additionally, to further confirm the concept of interacting DSBs within certain DNA chromatin compartments, the LEM IV is applied to simulate cell survival after combined irradiations with ions and X-rays. The results concerning the application of the LEM to mixed radiation fields are published in similar form in [34].

4.1. Results

In the following section, the results of the systematic validation of the LEM IV are presented. The section is split into two parts: First, the results of the comparison of model predictions to measurements listed in the PIDE database are described. Second, the outcomes of the application of the LEM concept for combined irradiations with ions and photons are demonstrated.

4.1.1. Validation of RBE predictions with the PIDE database

Large databases such as the PIDE (see Sec. 3.1) allow for a comprehensive model performance test. They enable the determination of model dependencies that potentially stay hidden by comparison of model predictions to single data sets. In order to validate the LEM, a set of PIDE experiments is selected according to certain filter criteria summarized in Sec. 3.1.1. Then, for each experiment the RBE is calculated at several cell survival levels based on the LQ parameters provided by the database. For each experiment, the RBE is also predicted by the LEM, which enables a direct assessment of the model precision for RBE prediction. The procedure for the quantification of model accuracy is shown schematically in Fig. 3.1. In the following section, most of the results are shown exemplary for ^{12}C ions as they comprise the most common particle species listed in the PIDE. A further argument for the choice of ^{12}C as an exemplary ion species is the fact that the LEM was initially developed to predict biological effects after irradiation with ^{12}C ions (LEM I). After a detailed analysis of the accuracy of RBE predictions, potential deviations in the prediction of LQ parameters are investigated.

Precision of RBE prediction: Figure 4.1 shows a scatter plot of measured ($\mathrm{RBE}_{\mathrm{PIDE}}$) and simulated ($\mathrm{RBE}_{\mathrm{LEM}}$) RBE values for the subset of 244 ^{12}C PIDE experiments performed with monoenergetic ions. The data points are split into two subgroups with LET values $\leq$150 keV/µm and >150 keV/µm. The results are shown for four cell survival levels: The RBE_{α} in the zero dose limit and the RBEs at 50, 10 and 1% cell survival. The values are subject to large fluctuations, which demonstrates the variability in experiment execution in different laboratories, between cell lines and other biological and physical experiment parameters. Furthermore, it can be seen that the maximum observed RBE strongly correlates with the considered cell survival level: Small doses and large cell survival levels show the largest scatter of data as well as the largest absolute RBE values. The LEM is able to reproduce the larger/smaller RBE values for larger/smaller cell survival levels, respectively. For all considered cell survival levels a clear correlation between measured and simulated data is visible. In order to quantify the model deviation the data points were fitted with a simple linear function $f(x) = mx$. The parameters obtained for the slope m as well as the corresponding standard errors are listed in Tab. 4.1. In general, it can be seen that the accuracy of the LEM predictions is higher for LET values >150 keV/µm. In that LET range, the LEM slightly overestimates the RBE ($0.96 \leq m \leq 0.92$). For smaller LET values, however, the LEM tends to underestimate the RBE ($1.19 \leq m \leq 1.12$) whereas it was found that the deviation increases with decreasing cell survival level. For larger LETs such a characteristic was not observed.

Tab. 4.1.: Slope with standard error for linear fits to data shown in the RBE- RBE scatter plot in Fig. 4.1.

	$\mathbf{RBE}_{\alpha}$	$\mathbf{RBE}_{50}$	$\mathbf{RBE}_{10}$	$\mathbf{RBE}_{1}$
LET $\leq$150 keV/µm	1.12 $\pm$ 0.03	1.16 $\pm$ 0.03	1.18 $\pm$ 0.02	1.19 $\pm$ 0.04
LET >150 keV/µm	0.93 $\pm$ 0.04	0.96 $\pm$ 0.03	0.92 $\pm$ 0.03	0.94 $\pm$ 0.03

To further analyze the accuracy of the model predictions the RBE is plotted as a function of LET in Fig. 4.2 for ^{12}C ions. The results are shown for the measured RBE values (blue) as well as for the predicted ones (red), each together with a running average to guide the eye. The general characteristics of an increasing RBE with LET can be clearly seen, as well as the drop in RBE for very high LETs due to the overkill effect. Furthermore, the experimentally-determined LET for which the RBE reaches a maximum is well reproduced by the model. The absolute values of the model predictions are in the range of the measured ones. In agreement with Fig. 4.1, the RBE_{α} values are subject to large scatter. For all considered cell survival levels,

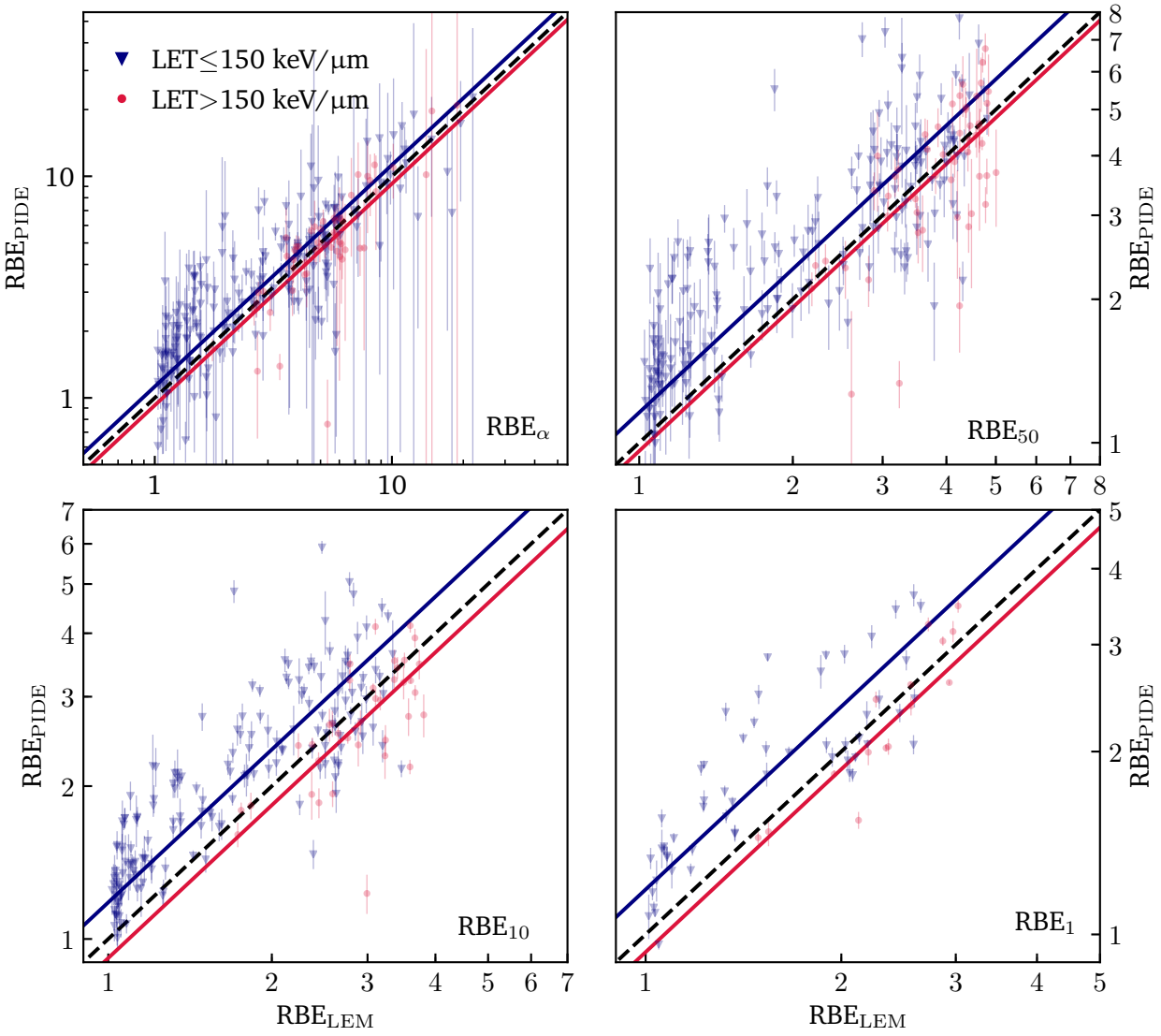

Fig. 4.1.: Scatter plot of measured (RBE_{PIDE}) and predicted (RBE_{LEM}) RBE values for ^{12}C ions at four different cell survival levels together with linear fits to the data. A 1:1 correspondence line is plotted to facilitate the optical assessment of the accuracy of the predictions. The error bars for the LEM predictions are not displayed to keep the figure clear. For the calculations of the linear fits (red and blue line) to the data the LEM uncertainties are assumed to be in the same order as the corresponding PIDE uncertainties and thus taken to be equal in a first approximation. Note the different maximum RBE values for different cell survival levels.

the predicted values lie on average below the measured RBE values for LETs < 150 keV/µm as visible from the running averages. For larger LETs, in the overkill region, the model tends to overestimate the RBE slightly. The absolute model deviation is in a similar range for all considered cell survival levels.

In accordance with the concept of Fig. 4.2 RBE predictions and measurements for RBE as a function of LET are displayed in Fig. 4.3 for several ion species at a cell survival level of 10%. The RBE predictions were investigated for lighter ions as well as heavier ions relevant in particle therapy or radiation protection. The

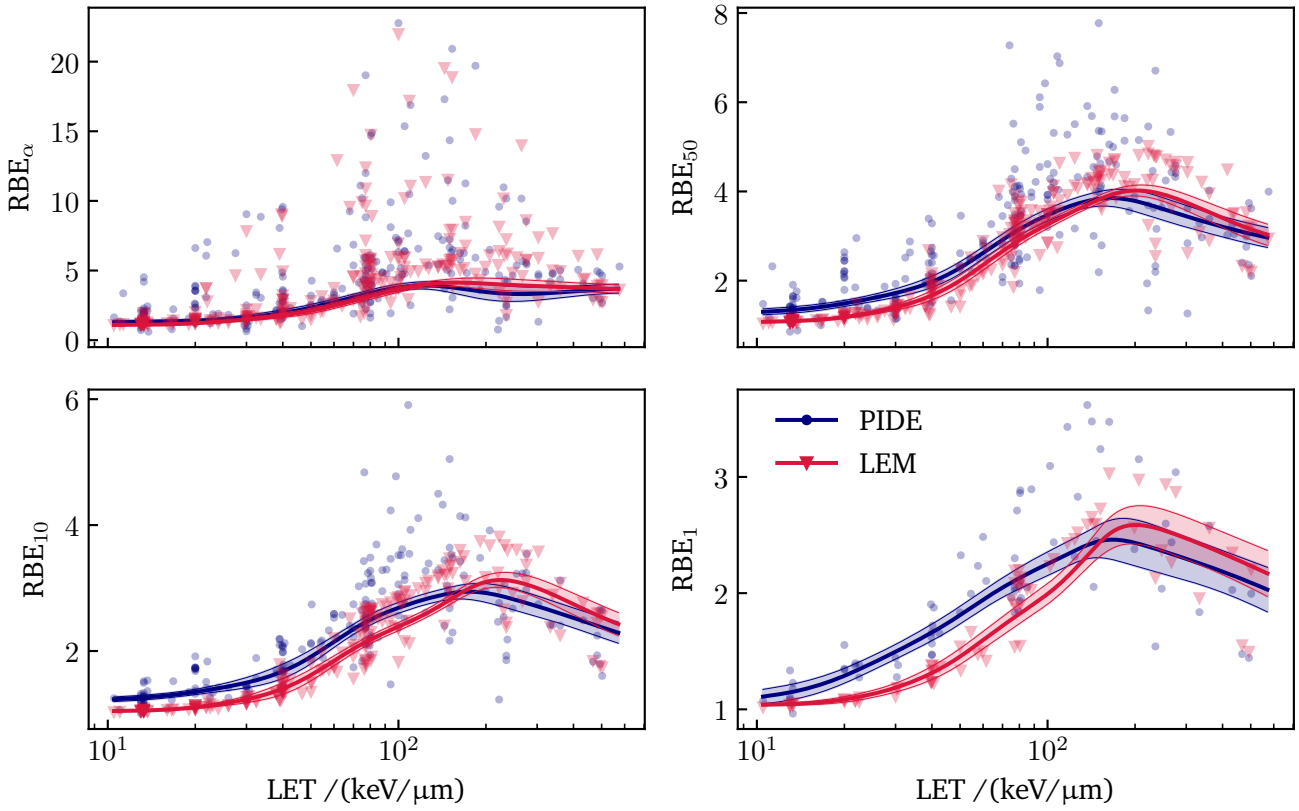

Fig. 4.2.: RBE as a function of LET for ^{12}C experiments listed in the PIDE (blue) as well as predicted by the LEM (red) at four different effect levels. Error bars for the specific data points are not displayed to keep the figures clear. However, they are included in the determination of the running averages to weight individual data points and to retrieve the uncertainty band, reflecting the standard error of the running average according to Eq. (3.4).

overall deviation in RBE is the smallest for ^{12}C ions for which the LEM was initially developed. At small LET values the model underestimates the RBE for all considered ion species with an increasing deviation with increasing atomic number. At larger LET values an overestimation of RBE is found for lighter ions (H and He ions) whereas model predictions match experimental data well for heavier ions. For ^{40}Ar and ^{56}Fe ions the limited amount of measurement data (22 and 21 data points, respectively) results in an imprecise course of the running averages. More measurement data are needed to precisely determine model deviations for heavy ions. However, the systematic model dependencies can be recognized.

To better compare the model deviations dependent on the considered cell survival level and ion species, the RBE deviation is investigated with regard to the ions' LET. Therefore, the relative RBE deviations of the model predictions are calculated point-wise according to:

$$\Delta RBE = \frac{RBE_{\mathrm{LEM}} - RBE_{\mathrm{PIDE}}}{RBE_{\mathrm{PIDE}}} \,. \tag{4.1}$$

The relative model deviations are shown as a function of LET for the RBE$_{10}$ in the top panel of Fig. 4.4 for ^{12}C ions. Each data point corresponds to one experiment of the PIDE database. Error bars and a running average to the data are shown to determine the average deviation. An underestimation of RBE is visible

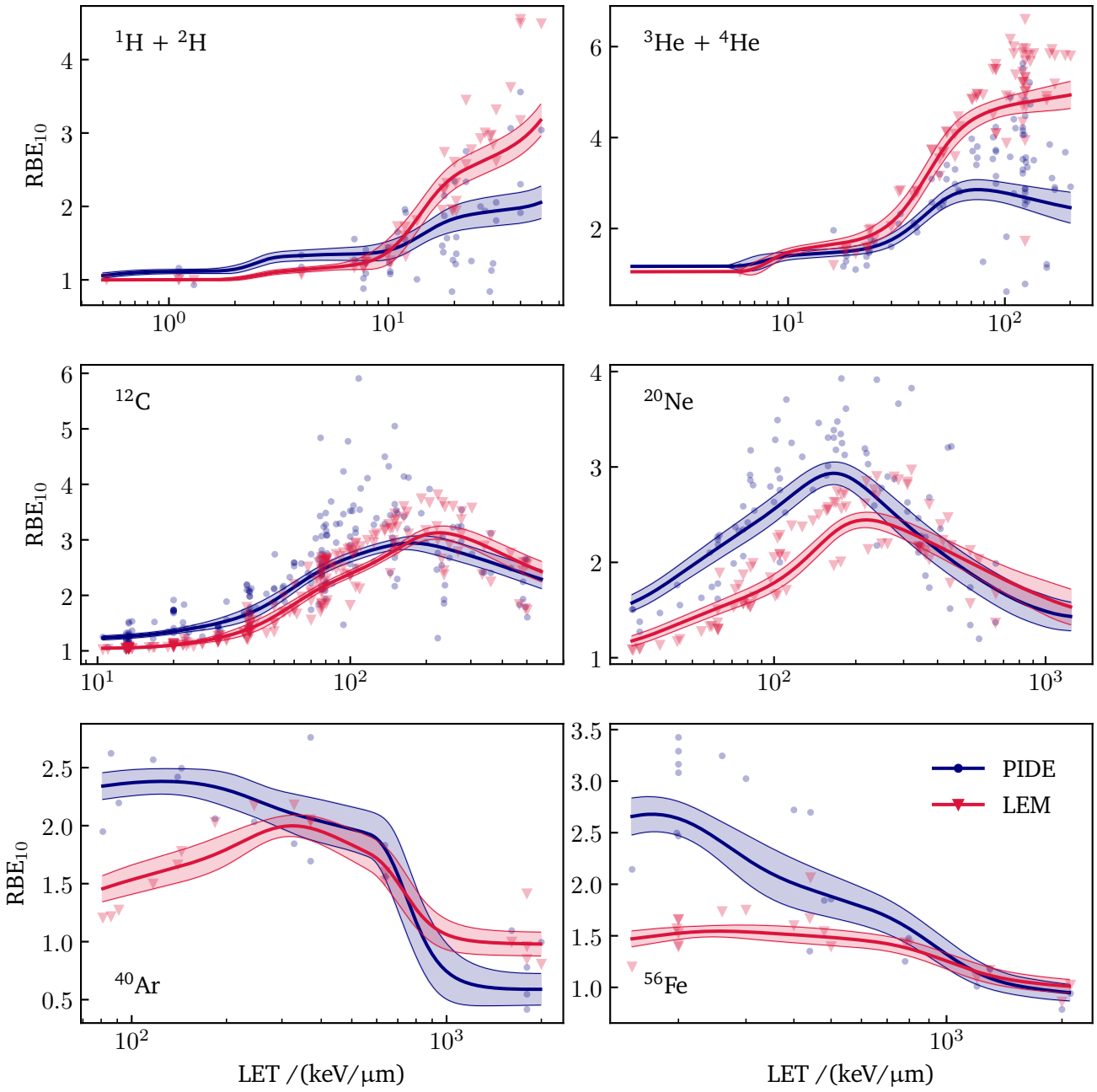

Fig. 4.3.: RBE as a function of LET for several ions listed in the PIDE (blue) as well as predicted by the LEM (red) at a cell survival level of 10%. Error bars for the specific data points are not displayed to keep the figures clear. However, they are included in the determination of the running averages.

in the low- to intermediate LET region, whereas for larger LETs the predictions match experimental data well. Deviations are in the range of the error bars for the measured RBE values. At small LET values (<30 keV/µm) deviations vary between -10% and -30% with the decreasing deviations for smaller cell survival levels. At intermediate LETs (30-150 keV/µm) RBE deviations are in the range of -20% and no clear dependence on cell survival level is visible. Finally, at large LET values (>150 keV/µm) model deviations

are in the order of a few percent with the largest deviations found for small cell survival levels.

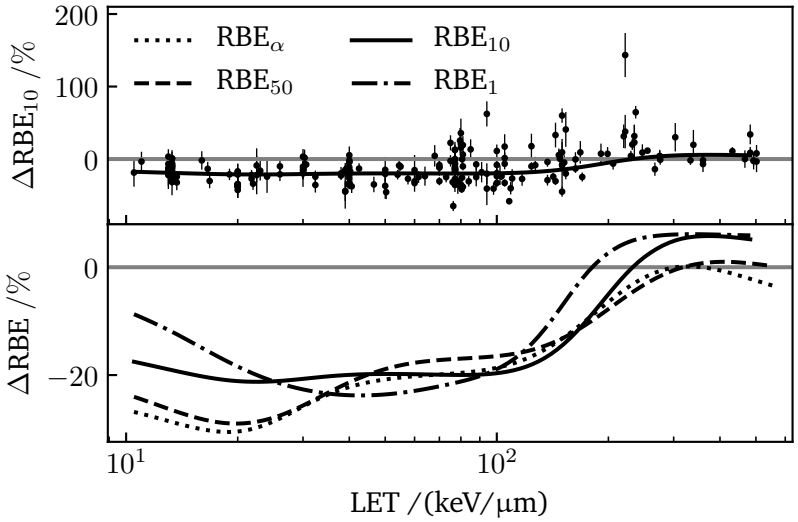

Fig. 4.4.: Relative deviations in RBE as a function of LET for ^{12}C as predicted by the LEM compared to measurements listed in the PIDE database for 10% cell survival (top) and several cell survival levels (bottom).

Figure 4.5 shows the relative model deviations for RBE_{10} for several ions ranging from ^{1}H to ^{56}Fe. This covers ion species relevant in the fields of particle therapy, radiation protection and space research. All ions follow a similar trend as ^{12}C ions of an underestimation of RBE at larger ion energies, i.e. smaller LET values. The observed deviation increases with the ions' atomic number. Furthermore, H and He ions show an overestimation of RBE at higher LETs up to ≈30% and ≈50% at maximum, respectively. However, it should be noted that in this LET range, light ions carry energies in the range of a few MeV/u. At these kinetic energies track segment conditions are not necessarily fulfilled, which the LEM uses as a basic assumption. Therefore, in that energy range, the LEM needs to be applied with caution. Also, the performance of corresponding experiments are challenging with regard to probe positioning etc. All ions heavier than He show a reasonably good fit at larger LET values in the overkill region.

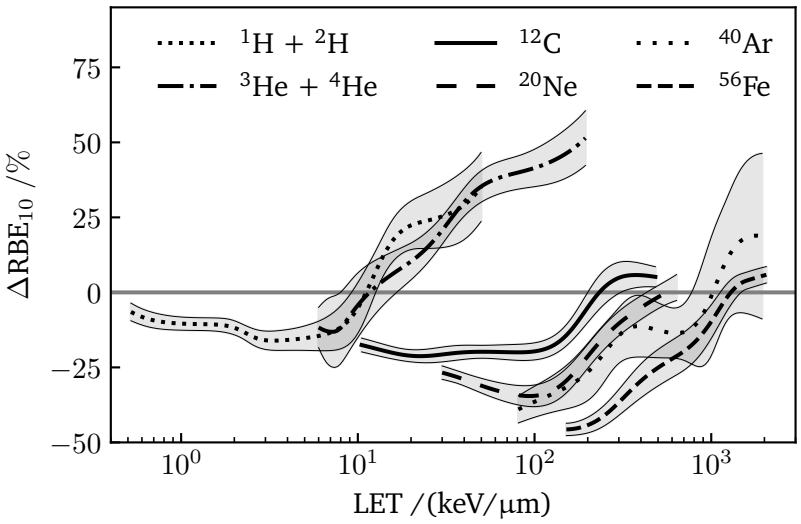

Fig. 4.5.: Relative deviations in model predictions for the RBE_{10} for several ions as a function of LET.

In Fig. 4.2 it is demonstrated that the LEM is capable of reproducing the characteristic shape of the RBE-LET curve. A further characteristic behavior of RBE is shown in Fig. 4.6. It shows the LEMs ability to reproduce the characteristic dependence of RBE on the $\beta_\gamma/\alpha_\gamma$ ratio of the photon survival curve. Whereas a linear increase of RBE with $\beta_\gamma/\alpha_\gamma$ is observed in measurements as well as in LEM simulations in the zero dose

limit (RBE_α), no clear dependence of RBE on $\beta_\gamma/\alpha_\gamma$ is found for lower cell survival levels. The RBE values are shown as blue and red data points for measurements and simulations, respectively. The data are selected from PIDE experiments for ^{12}C in the limited LET range of $70 \leq$ LET < 80 keV/µm as the RBE is an LET-dependent quantity. For both, the experiment and simulation data, a linear fit $f(x) = mx + b$ was calculated and plotted in the figure. The corresponding fit parameters are summarized in Tab. 4.2. For the RBE_{50} and RBE_1 the parameters of the fit to the predicted data lie within the error bars of the measured ones. For the RBE_α, however, the slope of the fit curve to the measured values is smaller compared to the predicted one, and vice-versa for the offset of the fit curves. This anti-correlation is due to the fact, that an increased slope can be partially compensated by a decreased offset. Consequently, the LEM predictions reflect the dependencies observed in experiments with good accuracy. This confirms the model's ability to correctly include the cells' radiosensitivity in the prediction of high-LET effects. The findings agree with previous investigations in which the same analysis was performed with a smaller subset of experimental data [28].

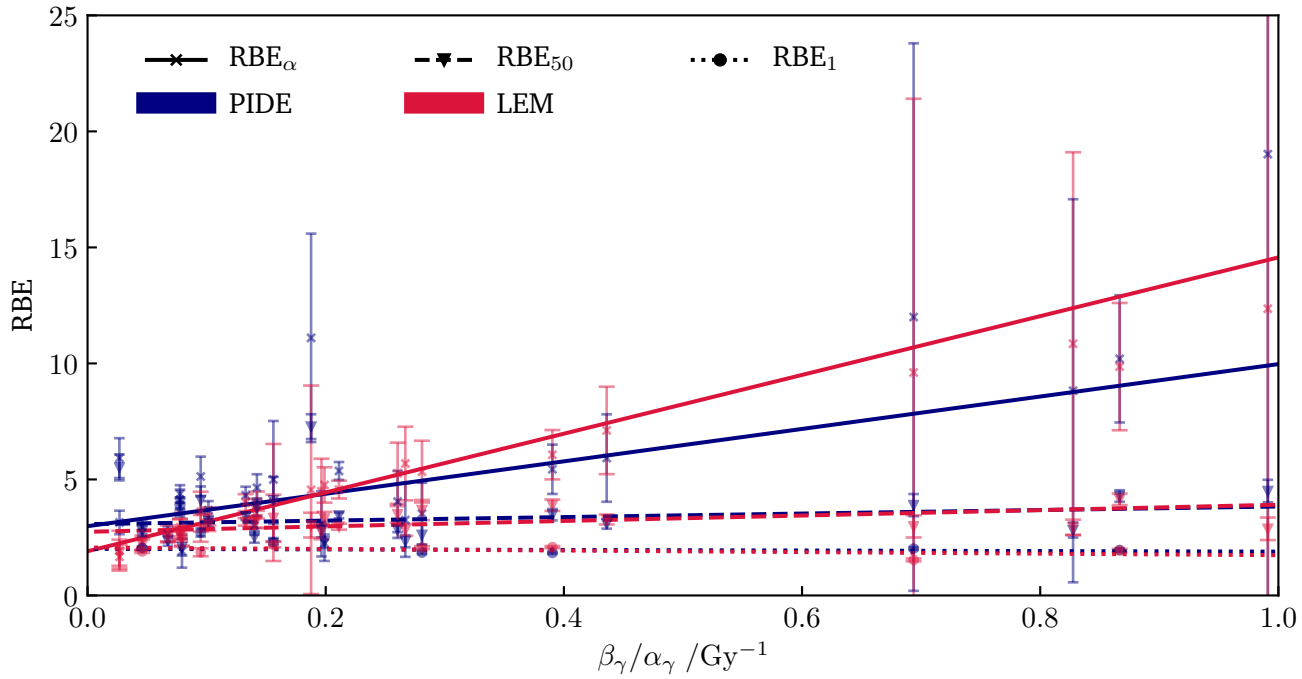

Fig. 4.6.: RBE as a function of $\beta_\gamma/\alpha_\gamma$ ratio for ^{12}C PIDE experiments with an LET ≥ 70 and < 80 keV/µm. The measured RBE_α, RBE_{50} and the RBE_{10} are shown in blue and the corresponding simulations in red. The linear fits to the data are presented as solid, dashed or dotted lines dependent on the considered survival level.

Tab. 4.2.: Fit values with standard deviations for the function $f(x) = mx + b$ shown in Fig. 4.6 for RBE as a function of $\beta_\gamma/\alpha_\gamma$ for several cell survival levels.

	PIDE			LEM		
	RBE_α	RBE_{50}	RBE_1	RBE_α	RBE_{50}	RBE_1
m	6.98±2.40	0.76±0.67	-0.12±0.27	12.66±0.78	1.17±0.35	-0.33±0.31
b	2.99±0.33	3.07±0.23	2.01±0.14	1.91±0.11	2.74±0.12	2.07±0.15

Precision of LQ-parameter prediction: The investigations above demonstrate that the LEM is generally capable of an RBE prediction for various experimental scenarios. However, when investigating RBE deviations as a function of LET certain systematics were observed. To further analyze the origin of these model deviations the predicted LQ parameters of the ion survival curves are compared to the corresponding parameters provided by the PIDE database. As the LQ parameters for the photon and ion cell survival curves are required for RBE calculations, the RBE deviations observed before are also expected to be reflected in the predicted parameters α_i and β_i. Scatter plots of the predicted and simulated parameters are given for H, ^{12}C and ^{56}Fe ion PIDE experiments in Fig. 4.7 for two subgroups of cells. The investigations are performed for experiments with an $\alpha_\gamma/\beta_\gamma$ ratio $\leq$4 Gy and an $\alpha_\gamma/\beta_\gamma$ ratio >4 Gy. A small $\alpha_\gamma/\beta_\gamma$ ratio indicates repair proficiency and, thus, potential radio resistance. This is typically expressed by a large shoulder in the cell survival curve (and vice versa). Between both subgroups of cells, no clear difference in model accuracy is observed. Thus, the precision of the LEM results appears to be independent of the radio-sensitivity of the considered cell types.

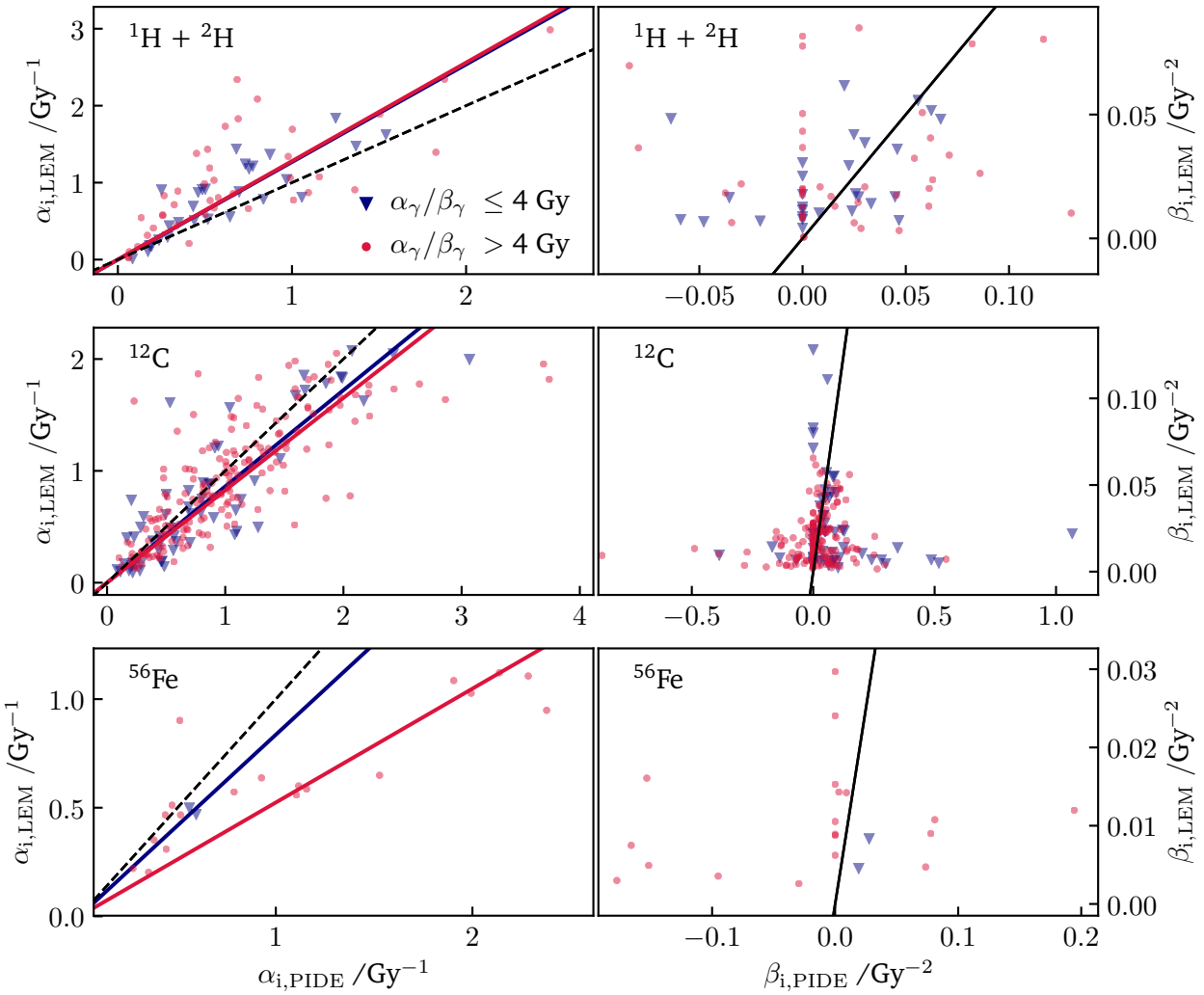

Fig. 4.7.: Predicted α_i and β_i parameters as a function of the corresponding measured values. The blue and red dots differentiate between radio-resistant ($\alpha_\gamma/\beta_\gamma$ ratio $\leq$4 Gy) and radio-sensitive ($\alpha_\gamma/\beta_\gamma$ ratio >4 Gy) cells, respectively.

Next to the data points, fits through the origin $f(x) = mx$ are provided for the LQ parameter α. The fits

elucidate that α_{i} is generally overestimated for light ions and underestimated for heavier ions. The LEM's over-/underestimation of α_{i} of the ion survival curve directly results in an over-/underestimation of RBE as previously observed. The parameter β_{i} is subject to large scatter and no clear tendency is found. Especially for ^{12}C ions an accumulation of data points at (0,0) was found, which is not visible in the figure due to the representation style of the data. Therefore, a linear fit through the data would give a biased impression, which is why it is not shown in the corresponding panels for β_{i}.

In Fig. 4.8 the ratios $\alpha_{\mathrm{i}}/\alpha_\gamma$ (=RBE$_\alpha$) and $\beta_{\mathrm{i}}/\beta_\gamma$ are plotted as a function of the experiments' LET to illustrate the LET dependence of the LQ parameters' deviations. A similar investigation was performed in an earlier study with a smaller subset of experimental data [28]. The data points as well as running averages are shown for ^{1}H, ^{2}H, ^{12}C and ^{56}Fe ions. As visible in the left panels of the figure, the running averages for $\alpha_{\mathrm{i}}/\alpha_\gamma$ lie above the expected average. This is due to the fact that for the calculation of the running averages no error bars were included. The corresponding values are subject to large fluctuation and statistical outliers with very large $\alpha_{\mathrm{i}}/\alpha_\gamma$ values typically have large error bars. The reason for the exclusion of error bars in the determination of the running averages is that for several PIDE experiments, a purely linear LQ fit was found to better represent experimental data. Therefore, in these cases no beta term exits and, therefore, is included with $\beta_{\mathrm{i}}/\beta_\gamma = 0$ in the figure. As a result, no error bars exist for these values and the running average cannot be calculated taking into account the uncertainty of each value for $\beta_{\mathrm{i}}/\beta_\gamma$. In order to apply the same calculation procedure for both LQ parameters, the error bars were assumed to be equal for all data points including $\alpha_{\mathrm{i}}/\alpha_\gamma$. Since general deviations between measurements and predictions are of interest, this procedure is reasonable. At the example of ^{12}C ions the previously observed deviations in RBE can be explained: In the LET region <150 keV/µm a small underestimation of α_{i} is observed. This corresponds to the LET range in which an underestimation of RBE was found (c.f. to Fig. 4.2 and 4.4). Similarly, the overestimation of α_{i} for H ions at LET values >10 keV/µm is directly transferred into an overestimation of RBE in that LET range. Correspondingly, for ^{56}Fe ions, an underestimation of α_{i} is observed with decreasing LET, which is translated into an underestimation of RBE as visible in Fig. 4.4. For ^{12}C and ^{56}Fe ions, a slight but artificial overestimation of β_{i} is observed at large LETs, which occurs due to the inclusion of the η-factor in the determination of β_{i} in the approximation method of the LEM (see Eq. (2.33)). To further analyze the origin of this deviation for heavier ions, a detailed study is necessary, which is beyond the scope of this work.

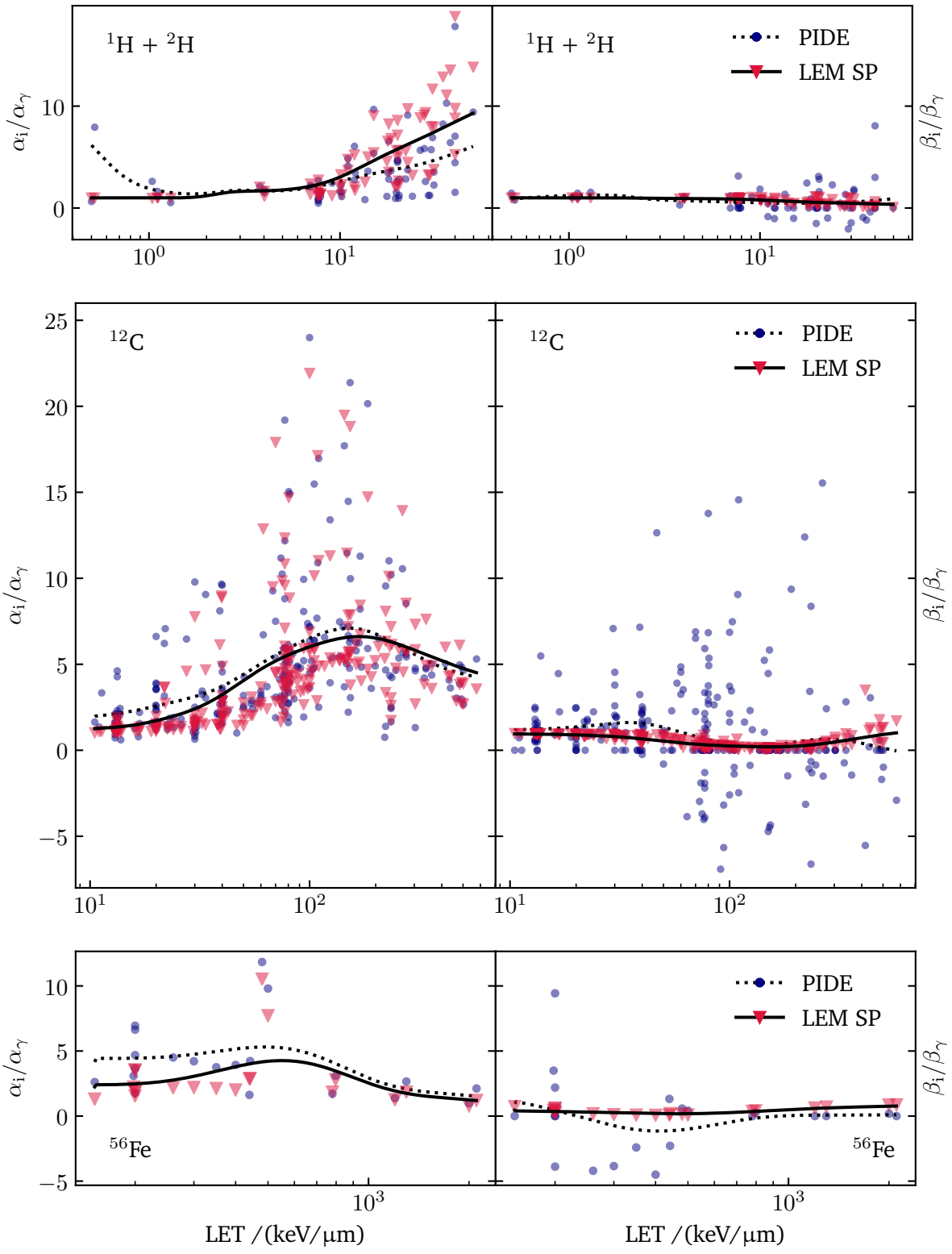

Fig. 4.8.: Data points and running averages for the ratios α_i/α_γ and β_i/β_γ as a function of LET for LEM predictions and measurements. The data is shown for ^{1}H, ^{2}H, ^{12}C and ^{56}Fe ion experiments listed in the PIDE database. Note that running averages are calculated without consideration of the data points' error bars.

4.1.2. Prediction of cell survival after irradiation with mixed radiation fields

In Sec. 2.3.2 the LEM formalism is described with regard to the interaction of DNA damages on the chromatin loop scale. This concept was tested before, e.g. concerning its application for pure photon irradiation, damage repair kinetics or dose rate effects [103, 25, 26]. In this work, the concept of interacting DSBs on the chromatin loop scale was further validated by applying the LEM to simulate cell survival after mixed radiation fields rather than after irradiation with a single ion species. The adjustments in the LEM code to enable simulation of cell survival after irradiation with mixed fields are described in Sec. 3.2.2.

To validate the LEM predictions, published experimental data were collected in which cell survival was measured after simultaneous irradiation with ions as well as X-rays. The corresponding experiment filter criteria and the resulting data collection are given in Sec. 3.2 and in Tab. 3.3, respectively. The LQ parameters for the measured survival curves are summarized in Tab. A.3. Each experiment was simulated with the LEM and the results were compared to the measurement data. In Fig. 4.9 cell survival curves are shown for the largest existing dataset of such mixed fields experiments. It was measured by Ngo et al. by sequential irradiation of V79 cells with ^{20}Ne ions and X-rays [93]. The figure shows the pure X-ray survival curve as well as several survival curves after irradiation with ^{20}Ne ions followed by irradiation with X-rays. The ^{20}Ne doses values range from 0.94 Gy up to 4.13 Gy leading to a decrease of cell survival at an X-ray dose of 0 Gy. Together with the LEM predictions, the predictions of two other alternative models are shown. The Zaider-Rossi model (ZRM) and the lesion additivity model (LAM) are described in detail in Sec. 2.3.4 and 2.3.4, respectively. The corresponding LQ parameters are listed in Tab. A.4 for the ZRM and LAM.The loss of the shoulder with increasing ion dose is clearly visible and can be reproduced reasonably well by the LEM and the LAM. The ZRM, however, overestimates the survival after irradiation with the mixed fields, which is due to the fact that the pure ion curve is purely linear (see Fig. 4.10 for the ion survival curve), which leads to $\beta_{\mathrm{i}} = 0$. Consequently, the interference term in Eq. (2.43) diminishes and the survival is calculated as if there was no interaction among the two radiation species.

In Fig. 4.10 measurement and simulation results are shown for a fixed photon dose followed by a variable dose of ion irradiation. The LEM and the LAM represent measurement data well for a fixed X-ray dose of 5 Gy. For a higher primary X-ray dose of 8 Gy both models show good agreement with measurement data up to a ^{20}Ne dose of 2 Gy. At larger dose values they tend to overestimate cell survival. However, it should to be noted that error bars for measurements at such low cell survival levels are large. For the predictions by the ZRM, similar characteristics as in Fig. 4.9 are observed. Due to the purely linear ion curve no synergistic effects due to the mixing of the radiation species are considered. Thus, pure additivity is assumed leading to the observed overestimation of cell survival after the mixed irradiation.

Figure 4.11 shows the results of eight experiments performed with a constant dose ratio for both radiation qualities. The ID numbers given in the bottom left corner of each subfigure identify the experiments. The measured X-ray and ion curves are shown in gray together with an LQ fit. For all experiments each measured survival point was simulated with all three models. Next, an LQ fit was performed according to Eq. (2.15) for each modeled survival curve and the resulting curve is shown in the figure. The LEM does not require the LQ parameters of the pure ion survival curve as an input but rather predicts the effect of the mixed radiation field based only on the LQ parameters of the photon survival curve. Therefore, the LEM was additionally applied to predict the survival curve of the pure ion irradiation. By comparing the measured ion survival curve to the predicted one, it can be differentiated if a model deviation stems from a deviating prediction of the shape of the pure ion survival curve or rather from the LEM concept of interacting isolated DSBs on the chromatin loop level.

In most cases the LEM is able to compete with the ZRM and the LAM, which is remarkable considering that the LEM does not need input information about the pure ion survival curve (α_{i} and β_{i}) as the other models.

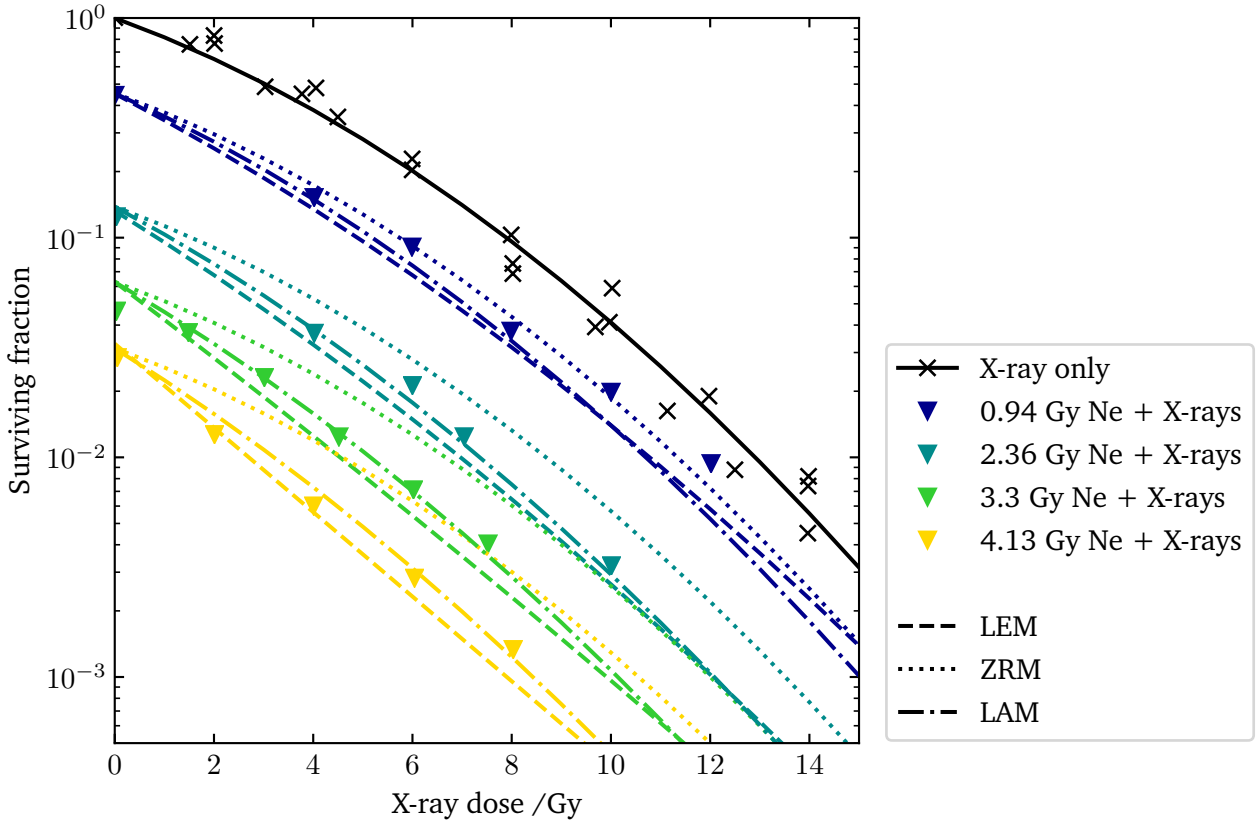

Fig. 4.9.: Experimental data by Ngo et al. for sequential irradiations with 183 keV/µm ^{20}Ne ions and X-rays (crosses and triangles). Additionally, the corresponding predictions of the LEM, LAM and ZRM are displayed. The depicted measurement data correspond to experiment ID numbers 9-12 in Tab. 3.3.

This clarifies the fundamental difference between the different model approaches. The LEM results are predictions per se, whereas the results obtained from ZRM and LAM can be understood as special methods for the determination of mean effects. Even if in most cases the LEM agrees well with the other models, certain deviations are observed for the LEM predictions. These are listed in the following:

- For several experiments (ID: 1, 2, 5, 6, 7) the LEM overestimates the cell survival after mixed irradiation. In these cases an overestimation of cell survival is already observed for the prediction of the pure ion survival curve. This deviation directly propagates into the prediction after mixed fields irradiation and is in agreement with the LEM validation results shown in Sec. 4.1.1.

- Experiment 1 and 2 were performed with the same irradiation conditions with the only difference that the dose ratio was changed from 1:1 to 1:4 (ion dose : photon dose). Whereas the mixed survival curve at a dose ratio of 1:4 is reproduced reasonably well the LEM deviation is more pronounced for a dose mixture of 1:1. This is connected to the issue described in the bullet point above: If the LEM prediction deviates for the pure ion survival curve deviations are also expected for the mixed irradiations. For the 1:4 dose mixture the relative proportion of ions to the total dose is smaller than in the 1:1 mixture. As a result, the impact of the ion survival curve on the mixed survival curve is reduced. Thus, the LEM prediction of the 1:4 mixture delivers more precise results compared to the 1:1 dose mixture.

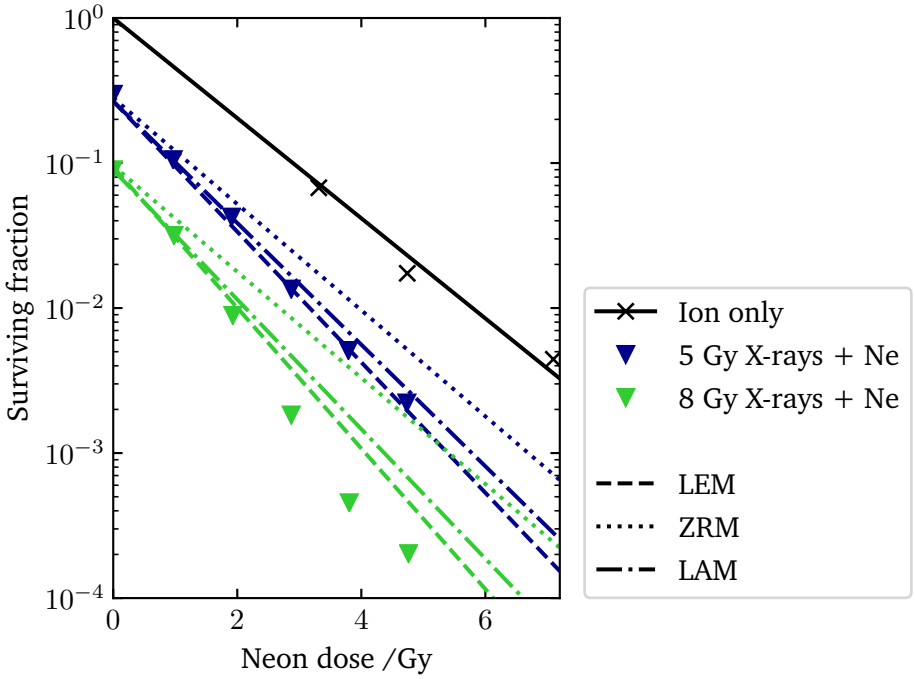

Fig. 4.10.: Experimental data by Ngo et al. for sequential irradiations with X-rays and 183 keV/µm ^{20}Ne ions. Additionally, the corresponding predictions of the LEM, LAM and ZRM are displayed. The depicted experimental data correspond to experiment ID numbers 13 and 14 in Tab. 3.3.

- The predictions of experiment 5 and 6 show a somewhat linear behavior with increasing dose for mixed fields. The measured survival curves, however, exhibit a quadratic component. This property strongly correlates with the choice of the threshold dose D_t determining the dose above which the photon survival curve is expected to be purely linear. With the empirical formula 2.23, which is applied consistently throughout this work for all LEM IV calculations, a D_t of approximately 8.3 Gy is obtained. Thus, the LEM predictions are based on an X-ray survival curve, which is expected to be purely linear starting at a dose of ≈8.3 Gy. However, in comparison to the experimentally determined survival curve, it is clear that D_t must be greater than 8.3 Gy.

Sensitivity analysis of the model: Since the LEM predictions are based on the LQ parameters of a photon cell survival curve, small variations in the fitting procedure of the photon curve affect the obtained LQ parameters and propagate directly into the LEM simulation results. To be able to assess the dependence of the LEM predictions on its input parameters a sensitivity analysis is performed for the mixed fields irradiations. Therefore, the LEM simulations shown in the previous section are repeated with two other sets of LQ parameters $\alpha_\gamma^{'}$ and $\beta_\gamma^{'}$ or $\alpha_\gamma^{''}$ and $\beta_\gamma^{''}$, which are defined as:

$$\alpha_\gamma^{'} = \alpha_\gamma + \Delta\alpha_\gamma \quad \text{and} \quad \beta_\gamma^{'} = \beta_\gamma - \Delta\beta_\gamma\,, \tag{4.2}$$

$$\alpha_\gamma^{''} = \alpha_\gamma - \Delta\alpha_\gamma \quad \text{and} \quad \beta_\gamma^{''} = \beta_\gamma + \Delta\beta_\gamma\,. \tag{4.3}$$

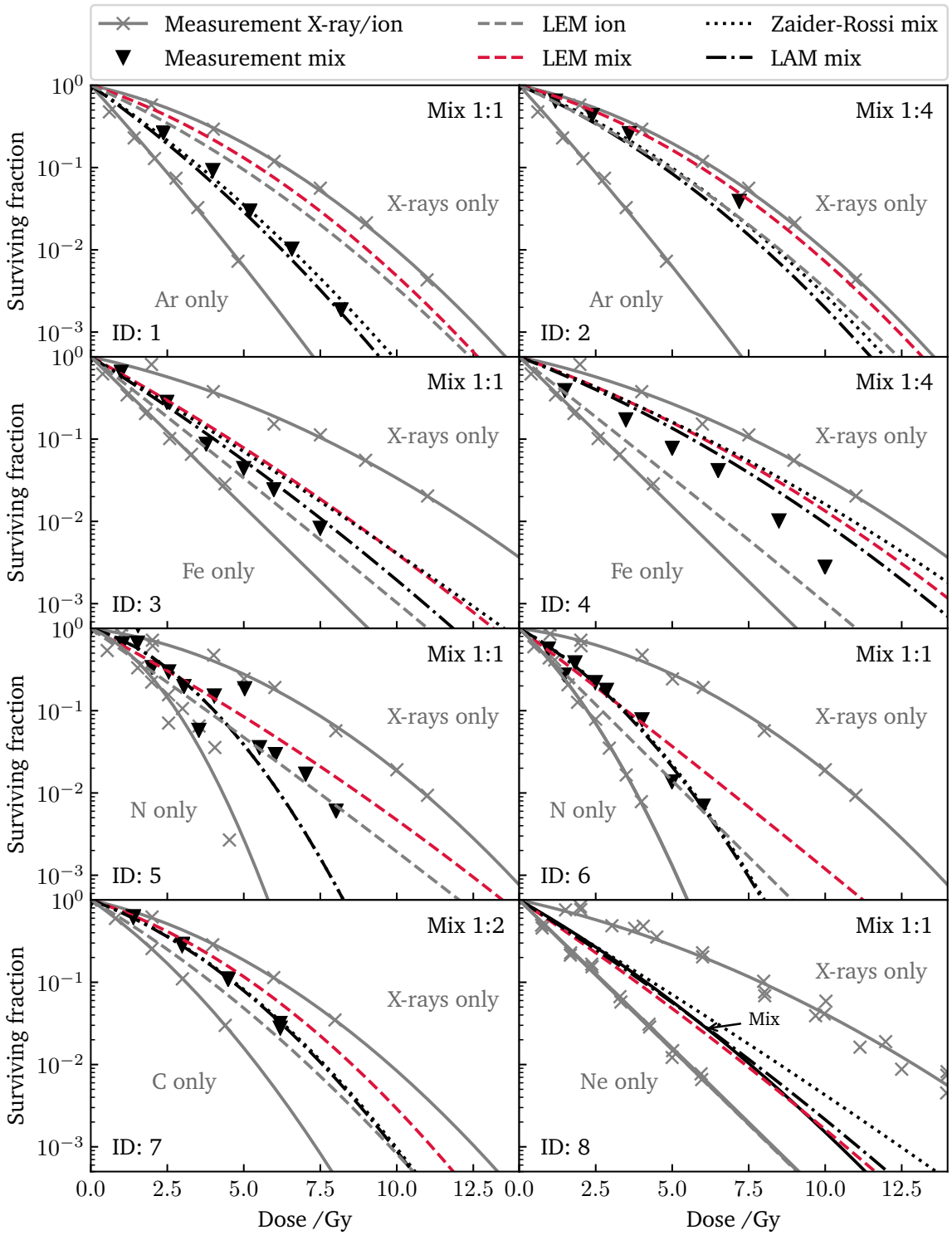

Fig. 4.11.: Cell survival data for experiments with a constant mixture ratio of ion and photon dose together with corresponding simulation results of the LEM, the ZRM and the LAM. The presented experimental data match the experiment ID numbers 1-8 in Tab. 3.3. The measurement points for the mixed irradiations are plotted as black triangles with the only exception of the experiment with ID number 8, where the measurement data was given as a line in the original publication instead of specific data points.

The standard deviations $\Delta\alpha_\gamma$ and $\Delta\beta_\gamma$ are obtained from the correlation matrix of the original LQ fits. As the LQ parameters are found to be anticorrelated, $\Delta\alpha_\gamma$ is added to α_γ if the standard deviation $\Delta\beta_\gamma$ is subtracted from β_γ (and the other way around). As a measure of change due to the parameter variation the RBE at initial dose RBE_α is considered. Fig. 4.12 A shows the measured and predicted RBE_α for all 14 mixed fields experiments. The error bars indicate the changes in RBE resulting from the adjustment of the LQ parameters of the ion survival curve as described above. Note that the shown RBE_α values refer to the ion survival curves and not to the mixed survival curves. The deviation is smaller in the simulations of the mixtures compared to the simulations of the pure ion curves. In Fig. 4.12 B the impact of the parameter variation is shown for the survival curves for the experiment by Tilly et al., with ^{14}N at 164.5 keV/µm [92]. This experiment is chosen for demonstration purposes as it shows the maximum observed RBE_α variation when varying α_γ and β_γ. The analysis demonstrates that the LEM predictions are quite robust for all simulations. Thus, the observed deviations in the predictions of the mixed fields experiments cannot be fully explained by the uncertainty of the input parameters. Furthermore, this investigation demonstrates how a possible deviation of the simulation of the pure ion survival curve propagates into the simulation of the mixed fields survival curve.

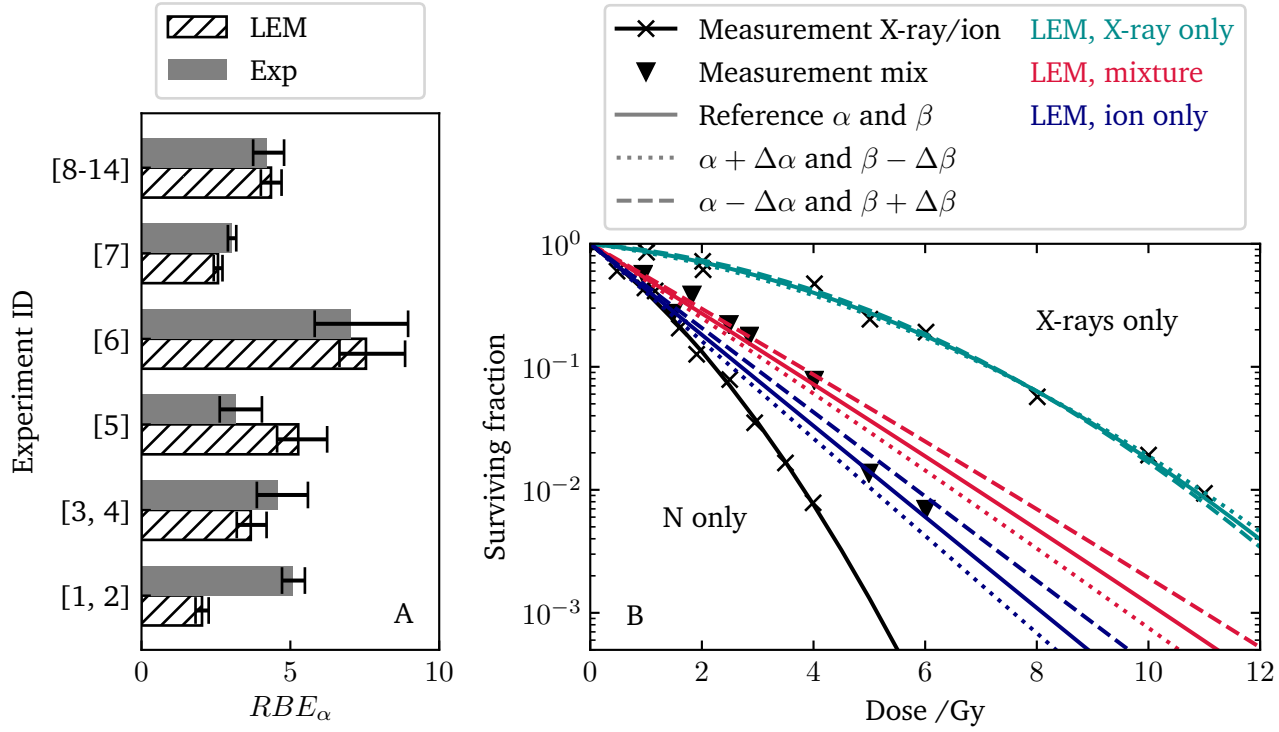

Fig. 4.12.: Sensitivity analysis of the LEM simulations on the LQ parameters, which are used as a LEM input. A: The variations in RBE_α for different input parameter sets are used as a measure for the robustness of the LEM calculations for each experiment. B: The changes in the form of the predicted survival curves when adjusting the LQ input parameters is shown for the experiment with the maximum variation in RBEα when changing the LQ parameters (Tilly et al. [92] with ^{14}N, 164.5 keV/µm, Experiment ID: 6).

4.2. Discussion

The systematic validation and quantification of the LEM with the PIDE database elucidated that at small LETs an underestimation of RBE is observed, which increases with the ion's atomic number. At larger LETs an overestimation of RBE is found for lighter ions as e.g. for H or He while the predicted RBE values for heavier ions match measurement data well. The tendency of an increasing underestimation of RBE with decreasing LET < 150 keV/µm for ^{12}C ions was observed earlier for V79 Chinese hamster cells in vitro [12] as well as for the tolerance of rat spinal cord in vivo [22] by comparison to single measurement data sets. Furthermore, the same trend was recently reported in an in vitro study with four different tumor cell lines [104]. A study for the biological effectiveness of ^{4}He radiation showed a small underestimation of RBE in the low-LET regime, which can, however, not be clearly confirmed to follow a general systematics due to lack of measurement data in this LET range for helium ions [105]. In general, the investigations confirm the broad applicability of the LEM IV for the prediction of cell survival and complements earlier validation approaches for several other radiobiological aspects as the induction of secondary cancers, dose rate or cell cycle effects, rejoining kinetics as well as gold nanoparticle (GNP) radiosensitization [12, 25, 26, 27, 106].

The results of the application of the LEM to simulate mixed ion and X-ray fields confirm the above described model systematics. In several cases an overestimation of cell survival after mixed irradiation was found by the LEM. However, in each case the cell survival of the pure ion survival curves was overestimated, too. Thus, it can be concluded that the deviation in the predictions of the mixed survival curves stems from an incorrect LEM prediction of the pure ion survival curve. This confirms the applicability of the LEM concept of interacting DSBs on the chromatin loop level of DNA and, thus, agrees with earlier validations of the concept for its application for pure photon irradiation, damage repair kinetics or dose rate effects [103, 25, 26]. The observed overestimations of cell survival directly translate into underestimations of RBE. This, is due to the fact that the RBE calculation is based on the photons' and ion's LQ parameters. Thereby, the RBE deviation seems to be dominated by the accuracy of the prediction of α_{i}. For light ions a general tendency to overestimate α_{i} was found, whereas for heavier ions including carbon an underestimation of α_{i} was reported. The prediction of β_{i} is, however, subject to large scatter including a large number of experiments with $\beta_{\mathrm{i}} = 0$. This is partly due to the fact that several experiments show cell survival curves with $\beta_{\mathrm{i}} < 0$, whereas LEM predictions are limited to $\beta_{\mathrm{i}} \geq 0$. Experimental values of $\beta_{\mathrm{i}} < 0$ point to the existence of at least two subpopulations of cells, which exhibit different radiosensitivities. The LEM, however, only considers a single population represented by adequate LQ parameters in each simulation [10].

The following discussion is split into tree parts. First, the impact of the PIDE database is discussed with regard to model validation purposes. Second, specific LEM parameters are reviewed concerning their role in RBE prediction. Finally, the LEM concept of simulating mixed fields is discussed and compared to other model approaches.

4.2.1. The PIDE database as a model validation tool

While certain systematics stay hidden when comparing model predictions to single experiments, they are clarified by model comparisons to a large data set [28]. As a consequence, the PIDE comprises a powerful tool for researchers in the field of radiobiology and is of great value with regard to the quantification of any RBE model. The demonstrated results comprise the first systematic validation of the LEM comparing RBE predictions of 610 cell survival experiments, covering several ion species from protons to iron ions as well as several cell types of varying radiosensitivity. The database can be applied in a similar way to validate also other RBE models besides the LEM, in order to enable an assessment of the accuracy of different competing

models. This is especially of interest in certain LET ranges where models diverge from each other. For the special case of protons, a separate database exists as assembled by [107] with a large overlap with the PIDE proton data. Its consideration might be useful for certain experimental settings with spatially extended cell survival measurements, as it contains more data on SOBP irradiations. The PIDE database proved to be a powerful tool concerning its application for a LEM validation. The database covers the typical experiment settings such as cell type, cell cycle stage, reference radiation species or conditions of the ion beam for each experiment. Thus, an individualized filtering of all experiments listed in the PIDE can be performed with regard to the specific requirements of any general cell survival model validation. If additional specific information is requested such as the oxygenation status of the cells in an experiment, the database can be easily extended.

4.2.2. Specific comments for LEM simulations

The accuracy of the LEM predictions is remarkable considering the small amount of input data needed to simulate the effect after ion irradiation: Next to the energy and LET of the simulated ion species, only the LQ parameters of the corresponding photon survival curve are needed. Several specific aspects of the model validation are discussed in the following paragraphs.

Single particle approximation and full simulation: As mentioned earlier, all LEM simulations in this work are preformed with the "single particle approximation" if not stated otherwise. The LEM can be also executed as a "full simulation" and both modeling concepts are introduced in Sec. 2.3.2. As the validation of the LEM was performed with the single particle approximation, the impact of the simulation technique is of interest in order to evaluate the results. Its relevance is demonstrated in Fig. 4.13 for the prediction of the LQ parameters for selected PIDE experiments with ^{12}C ions. Running averages for the ratios $\alpha_\mathrm{i}/\alpha_\gamma$ and $\beta_\mathrm{i}/\beta_\gamma$ are plotted over LET for the PIDE data as well as for the LEM predictions according to the two possible simulation techniques. By applying the full LEM simulation, the accuracy of the prediction of α_i is slightly larger in the low-LET region where its relative deviation from measurement data is the largest. Note that theoretically both simulation methods lead to the same alpha values [12]. However, the exact values depend on the applied method to perform the LQ fit, which leads to the observed slight difference between the two methods. For β_i a good agreement between both techniques is found for LET values $<$100 keV/µm. At larger LET values β_i increases artificially for the approximation, which is due to the fact that the mean η-factor of the ion track is included in the determination of β_i in the approximation method (see Eq. (2.34)). Corresponding solutions are planned to be implemented in a future model version. The data points used to calculate the shown running averages are plotted in Fig 4.8 for the LEM approximation and the PIDE data. As the application of the full LEM simulation only slightly improves the prediction of the ion LQ parameters for carbon ions, the same behavior is found concerning the accuracy of RBE prediction. Thus, the RBE deviations seem to be an inherent model property, which goes beyond the LEM simulation technique.

Choice of the threshold dose D_t: The threshold dose D_t describes the dose in a dose response curve at which the shape of the survival curve transits back to a purely linear behavior [71, 72, 73]. Since these threshold dose values often lie beyond practically measurable cell survival levels, an empirically found formula (Eq. (2.23)) is used in the LEM IV to calculate D_t. The formula for the threshold dose was optimized by fitting LEM predictions to a specified set of high-LET data and is used in the same form ever since for all experimental scenarios [28].

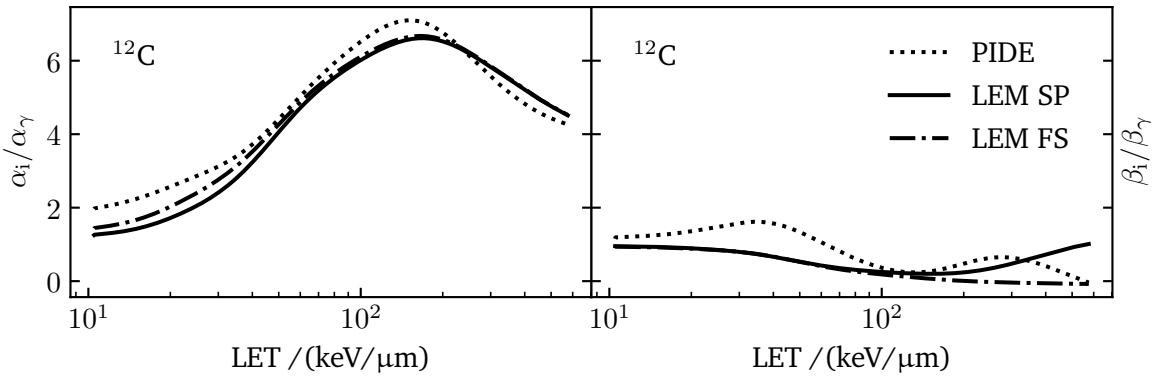

Fig. 4.13.: Running averages for the ratios α_i/α_γ and β_i/β_γ as a function of LET for the predicted and measured values of ^{12}C listed in the PIDE database. The LEM results are given in its two variants: As the single particle approximation (SP), consistent with all other results shown in this work, and as the full simulation (FS).

In Fig. 4.14 the potential impact of the choice of D_t on LEM predictions is shown for a mixed irradiation cell survival experiment where ^{14}N ions were mixed with X-rays [92]. In Fig. 4.14 A the parameter D_t was calculated according to Eq. (2.23) leading to a threshold dose of 8.3 Gy. The corresponding photon survival curve that the LEM receives as an input is depicted as a yellow dotted line. At doses D below 10 Gy, a small deviation of photon cell survival is observed compared to measured cell survival data. The predicted ion- and mixed fields survival curves overestimate cell survival in comparison to measurement data. Alternatively, in Fig. 4.14 B the threshold dose is manually set to a larger value of 12 Gy. This leads to a better agreement of the photon survival curve inserted into the LEM with the measured curve in the dose range in which survival data are available. As a result, a better agreement of the LEM predictions for ions as well as for mixed radiation fields with the experimental data was obtained. The presented example is the only one of all experiments assembled for validation of the simulation of mixed field irradiations, where D_t visually diverged from the value obtained with the standard Eq. (2.23). For all other experiments D_t is in the range of 11.5 to 20 Gy. Thus, the transition dose to the purely linear part of the survival curve exceeds the dose range in which measurement data are available. In order to keep the calculation procedure consistent for all compared experiments D_t was approximated by the empirically found Eq. (2.23) for each experimental scenario. The investigations demonstrate the sensitivity of LEM predictions on the choice of D_t. The parameter D_t is calculated as a function of the $\alpha_\gamma/\beta_\gamma$ ratio of the photon survival curve and is subject to large uncertainties due to its dependence on the quotient of α_γ and β_γ which are also afflicted with errors [28, 108].

4.2.3. Simulation of cell survival after mixed radiation fields

The investigation of biological effects after exposure to mixed radiation fields are in the focus of current research especially in the field of space radiation protection. Exposure to cosmic radiation is still one of the main show stoppers for manned travel to outer space [2, 3]. It consists of mixtures of ion species ranging from protons up to iron ions in a broad energy range. Typically experiments for radiation response are performed with a single radiation species as only few facilities are able to accelerate different ion species and to rapidly exchange between them. Recent updates at the Brookhaven NASA Space Radiation Laboratory (NSRL) now allow the performance of experiments with several one-ion beams in a fast sequence [109]. However, the realistic representation of space conditions in experiments is still challenging because typically

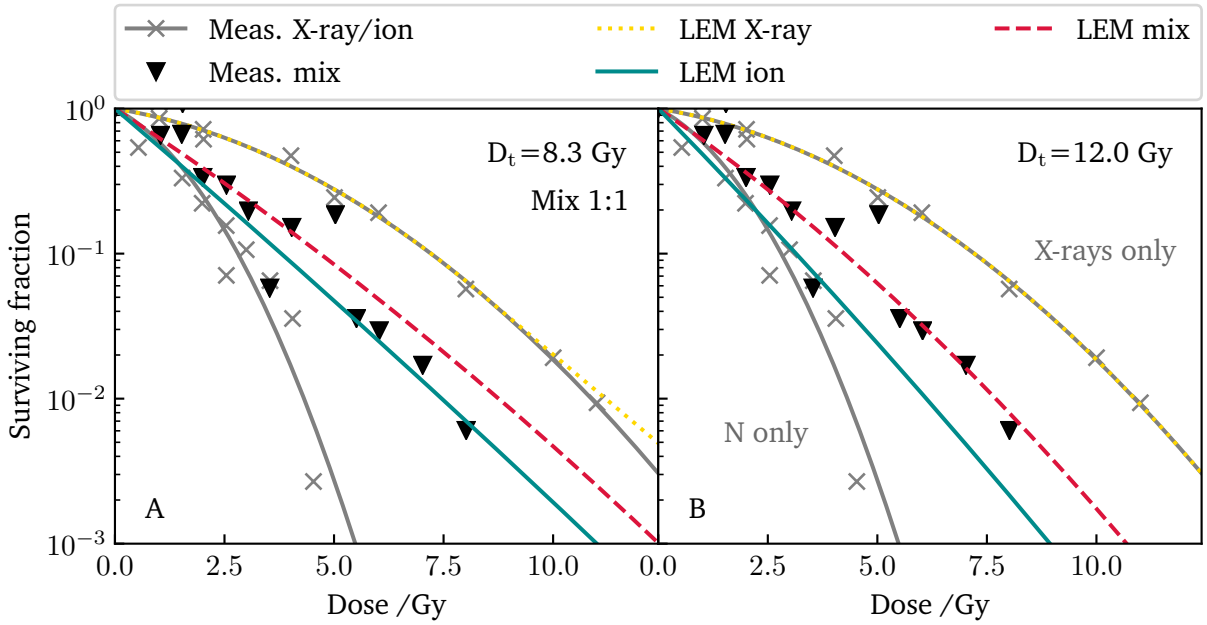

Fig. 4.14.: Impact of the threshold dose D_t on the LEM result for mixtures of ^{14}N ions with X-rays [92]. The predictions of the pure ion survival curve and the mixed survival curve are given for two scenarios: First, the threshold dose D_t is calculated according to Eq. (2.23) (A). Second, the threshold dose is set manually to 12 Gy (B).

the complex mixed fields occur at low dose rates and long exposure times. As a result, the simulation of radiation effects after exposure to mixed fields are still indispensable for risk assessment and also in order to develop counter measures for radiation exposure. Next to space research applications, mixed fields are relevant in nearly all scenarios of radiation exposure. For instance in tumor therapy a mixture of ions is present in the target due to the energy loss and nuclear fragmentation of projectiles.

Comparison to other mixed fields model approaches: Next to the LEM, other models exist for the simulation of radiation effects after exposure to mixed fields. One published approach was performed based on a modified version of the microdosimetric model MKM [110], which is introduced in Sec. 2.3.3. The effects after a mixture of low- and high-LET radiation were simulated on the level of "radiation events" in domains in the nucleus. The hypothesis was tested if the radiation mixture leads to an enhanced effect of individual actions as a result of the increase of radiation events in domains provided by the low-LET radiation [110]. In the study, synergistic effects between low- and high-LET radiation could be partly confirmed and the model approach showed to reproduce measurement data well. The validation data used to test the application of the MKM for mixed fields is a subset of the validation data used to test the LEM in this work [64, 93, 88]. In a further study, the effects after mixed fields irradiation were investigated by comparing measurement data on mixtures of ^{1}H, ^{28}Si and ^{56}Fe ions with simulations [109]. The simulation approach is based on the concept of incremental effect additivity (IEA), which is derived from the LAM theory used in this work [111, 112]. The endpoint of the study is the tumorigenesis of the murine harderian gland. Synergy was observed in one of three cases whereas in the other cases neither synergy nor antagonism was reported. Finally, a recent simulation approach should be mentioned, which includes several spatial scales [113]. Energy spectra of mixed irradiation scenarios were obtained from Geant4 simulations. These were inserted into the RITRACKS model (relativistic ion tracks), which is a track structure model used to simulate stochastic

energy distributions on the nanometer scale. By insertion of these profiles into the biological damage and repair model RITCARD (radiation-induced tracks, chromosome aberrations, repair and damage), the yield of chromosome aberrations could be predicted. Similar to the LEM, the presented model is a multi-scale model. The RITCARD model includes the simulation of chromosomes by random walk, the calculation of chromosome breaks induced by radiation tracks by pre-calculated differential voxel dose maps as well as the repair of DNA damages [113]. The presented results agree well with measurement data. In the LEM, the interaction of different radiation qualities was performed by simulating the interaction of DSBs on the chromatin loop level. Thus, two iDSBs created by independent irradiations are allowed to interact within a chromatin loop and to form an additional cDSB, which is more difficult to repair. This concept proved to describe the interaction of different radiation species reasonably well.

Application of the ZRM in treatment planning: In addition to the predictions with the LEM, the ZRM and the LAM were used to simulate the shape of the survival curves after mixed field irradiation. In most cases all model predictions showed similar accuracy. This gives further support for the application of the ZRM within a hybrid approach in treatment planning for ion beam therapy, where it was implemented for reasons of simplicity and computational speed [74, 114]. In the treatment planning system TRiP98, the LEM is only used to predict the dose response curves for all individual components of the radiation field, which is stored in an RBE table. The ZRM is then used to determine the combined effective LQ parameters for the mixed field in each voxel. This modular structure is feasible as the biological effects can be precalculated and used for the calculation of any irradiation scenario with different irradiation fields or doses. Next to the biological base data, the program requires input of physical base data.

Temporal effects due to DSB repair between irradiations: Temporal effects as DSB repair are not considered in the simulations in this work, since in the experiments either both radiation qualities were applied exactly at the same time [91] or the time between irradiations was kept to a minimum while keeping the cells on ice, thus minimizing repair within that short time interval. Therefore, in a first approximation for all cases both radiation qualities were assumed to be applied simultaneously.

Nature of interaction terms of the LEM, ZRM and LAM: The LEM only requires the LQ parameters of the photon survival curve as an input together with the energy and LET of the considered ion species to predict the effect after mixed irradiation. The two other empirical models ZRM and LAM, however, require the LQ parameters of both the photon and the ion survival curve as an input. The difference of these concepts is clarified in a certain experimental scenario: If two ions with identical cell survival curves but different ion energies are each mixed with X-rays, the ZRM and the LAM predict the same effect for both radiation mixtures. The result of the LEM predictions, however, depends on the spatial DSB distribution induced by the radiation species. X-rays are known to deposit their energy in a rather random pattern leading to a random DSB distribution in the first order. Ions, however, show a strongly localized dose and DSB distribution around the ion track center. Depending on the ion energy, the track structure width varies leading to a variation in the proportion of cDSBs to all DSBs. As a cDSB is defined as the combination of two or more DSBs within one chromatin loop, an additional DSB within that chromatin loop will have no additional effect on the final result. If a DSB is formed in the same chromatin loop with an already existing iDSB, they form a cDSB, which leads to an increased effect, i.e. decreased cell survival. This demonstrates that the LEM, in contrast to the ZRM and the LAM takes not simply the individual effects of the constituent radiation components into account to describe the combined action, but also the spatial combined DNAs lesion distribution, which actually causes the observed combined effect.

Proposal for a decisive experiment to test model concepts: As described in the preceding paragraph, the different model approaches of the LEM, ZRM and LAM will lead to diverging predictions for certain mixtures of ions and X-rays. An exemplary combination of two ions mixed with X-rays was investigated by the LEM. As the first radiation quality 31 MeV/u ^{20}Ne ions with an LET of 183 keV/µm were chosen. This radiation quality was selected as corresponding measurements already exist by Ngo et al. [93]. The second radiation quality was chosen by iteratively applying the LEM to find the energy of ^{12}C ions, which will lead to a very similar survival curve. Matching survival curves were found for 2.5 MeV/u ^{12}C ions with an LET of 437 keV/µm. The corresponding LQ parameters α and β, which describe the shape of the cell survival curves are given in Tab. 4.3. It should be noted that for carbon ions with 2.5 MeV/u track segment conditions might not be fulfilled, which are assumed in the LEM calculations. This is subject to further investigations and potential alternative suitable ion pairs should be determined for the proposed experiment.

Tab. 4.3.: Properties of two ion beams, which show almost identical cell survival curves according to the LEM. The ratio of cDSBs to the total number of DSBs is extracted from the LEM and refers to a single ion traversal of the nucleus.

Ion	E /(MeV/u)	LET /(keV/µm)	α_i /Gy^{-1}	β_i /Gy^{-2}	cDSBs/DSBs
^{20}Ne	31	183	0.822	0.001	0.19
^{12}C	2.5	437	0.800	0.001	0.80

In a hypothetical experiment the two ion species were mixed with X-rays. The resulting mixed radiation survival curves are shown in Fig. 4.15 for the LEM, LAM and ZRM. Whereas for the ^{20}Ne ions a significant synergistic effect is predicted by the LEM, for the ^{12}C ions almost no interaction between the high-LET and photon component is expected. In Fig. 4.15 this behavior is shown for two measurement scenarios mixing 5 or 8 Gy of X-rays with ^{20}Ne or ^{12}C ions. This radiation mixing concept is adapted from existing measurements by Ngo et al. [93]. The shape of the X-ray survival curves was also adapted from their measurements with V79 cells.

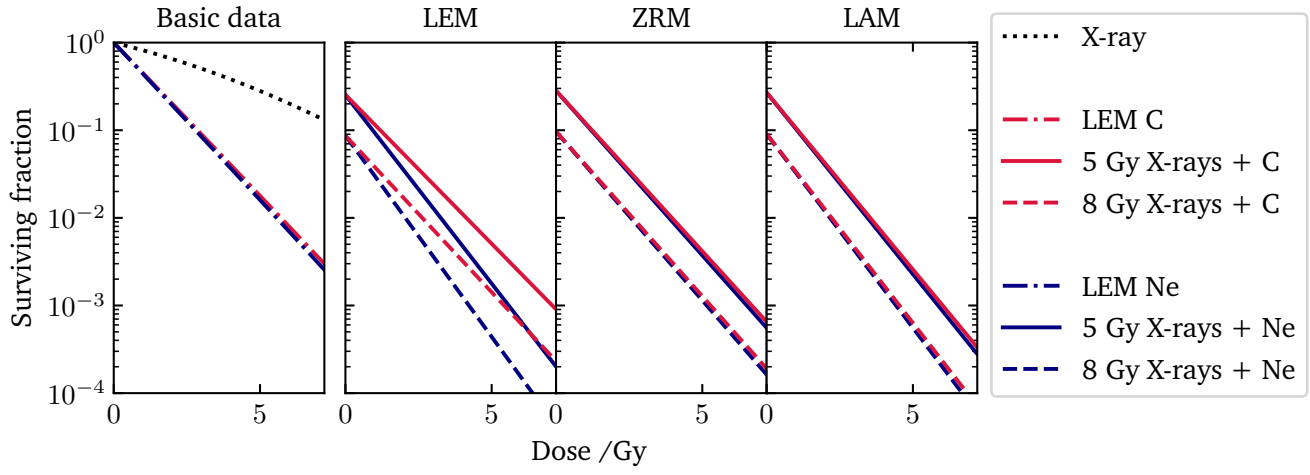

Fig. 4.15.: Hypothetical experiment of mixing X-rays with two ion species with nearly identical survival curves. In the left panel the pure survival curves of the two ions and the X-rays are displayed. In the right panels the predicted survival curves of the mixed radiation fields are depicted for the LEM, ZRM and LAM.

The increased synergistic effect predicted by the LEM for the ^{20}Ne ion in comparison to the ^{12}C ion can be

easily understood by visualization of the LEM concept of interacting DSBs. This is shown schematically in Fig. 4.16. As the higher-energetic ^{20}Ne ion primarily produces iDSBs, which can be understood as potentially lethal lesions, the iDSBs can interact to a large degree with the iDSBs produced by the X-rays. The ^{12}C ion, however, assembles mainly cDSBs preventing increased damage as only few additional cDSBs can be created by the interaction of both radiation species. As a result, one expects a steeper mixed survival curve for the mixture with the higher-energetic ^{20}Ne ion in comparison to the low-energetic ^{12}C ion where only a small portion of iDSBs is present. The ratios of cDSB/DSB for both ions are calculated with the LEM and are given in Tab. 4.3. They explain the predicted difference in interaction.

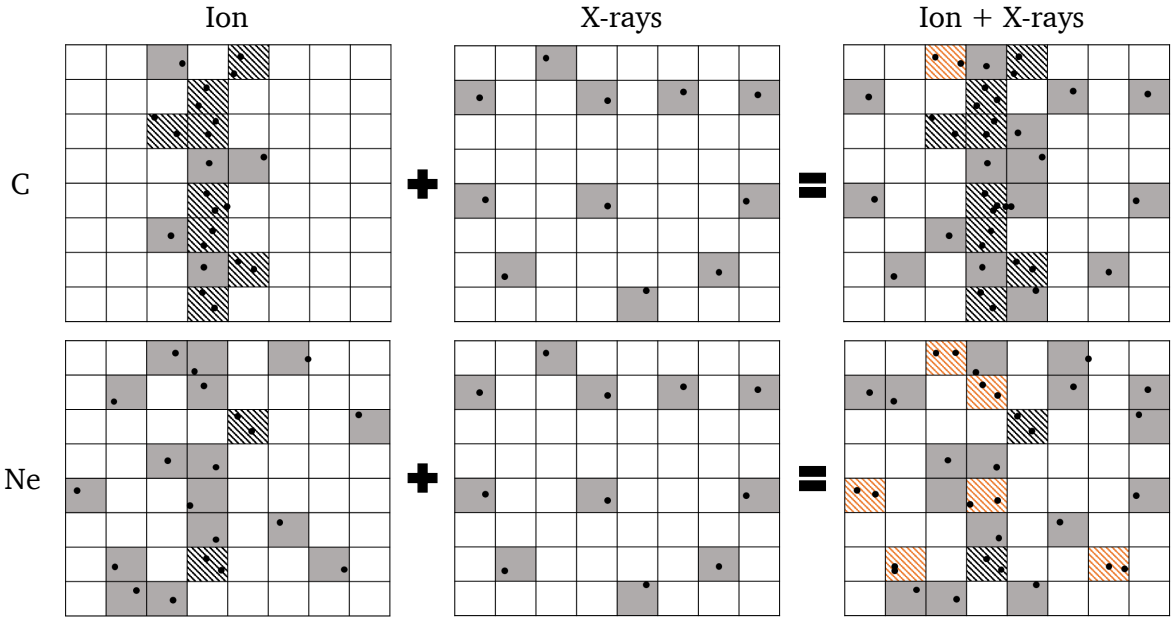

Fig. 4.16.: Schematic sketch according to the concept of Fig. 2.22. The figure clarifies the origin of the different degree of synergism for two ion species interacting with X-rays according to the LEM concept. The DSB distributions are fictitious and approximately match the ratio of cDSB/DSB of 0.2 and 0.8 for the ^{20}Ne and ^{12}C ion, respectively.

Performing the above proposed experiment would challenge the concept of considering the interaction of DNA damages on the chromatin loop scale for the prediction of cell survival after mixed radiation fields. According to the LEM, experiments with a mixed beam of 2.5 MeV/u ^{12}C ions and X-rays would complement the existing measurement data by Ngo et al. [93] with 31 MeV/u ^{20}Ne ions and X-rays. The experiment would facilitate further differentiation between the LEM, ZRM and LAM concerning their predictive power of cell survival effects after mixed irradiation. This investigation is of great value as in most cases of radiation exposure a mixture of radiation qualities is present. In clinical applications several different ion energies are present in the irradiated volume due to the employment of a SOBP. Furthermore nuclear fragmentation leads to an additional dose contribution by several ion species. Concerning radiation protection in space research, mixed fields play a role as cosmic radiation consists also of a large variety of ion species and energies. However, in space research typically low dose rates are observed, which enables repair between the damage induction of independent ions. Thus, a reduced interaction of damages by separate ions is expected in space research applications.

Synergism/Additivity for mixtures of α-particles with X-rays: As α-particles exhibit a low energy they can be expected to show a less pronounced synergistic effect than higher energetic beams at similar LET. By increasing the ion dose the probability of iDSBs production increases and with that also the probability of interaction with iDSBs produced by a second radiation species, as e.g. X-rays. This would explain why Barendsen et al. [86] observed additivity when mixing α-particles with X-rays but McNally et al. [115] repeating Barendsen's experiment with higher ion doses observed a synergistic behavior. Unfortunately, the LEM cannot be easily applied to simulate the experiments with α-particles as the experimental conditions do not fulfill track segment conditions, meaning that the change in LET could be neglected throughout the particle's traversal trough the cell nucleus. This is due to the typical low energy of the ions and their energy spread at the probe position during irradiation with α-particles. Thus, a direct quantitative comparison with the experimental data for α-particle irradiation is hardly feasible with the current implementation of the LEM. However, the qualitative explanation of the observed degree of synergism matches the observations in earlier measurements of mixing α-particles with X-rays. These examinations further support the mechanistic concept of the LEM.

DNA damages of different complexities: In the LEM only a single type of initial DSBs is considered. Furthermore, DSBs are assumed to interact on the micrometer scale to form complex damages (cDSBs). This is a rather simple approach considering the various possible types of DNAs damages ranging from a simple DSB over DSBs with an additional DNA damage in close proximity to the spatial clustering of several DSBs [31]. The complexity of DNA damages determines the repair pathway choice and defines the probability for the occurrence of repair errors [31]. However, the temporal and spatial information on how such lesions are processed and repaired is sparse [116]. Several theoretical and experimental concepts exist for the classification of DSBs according to their complexity [30, 31]. In experiments, DNA damages are typically visualized by fluorescent proteins leading to microscopically visible nuclear domains, so-called foci. Often the occurrence of a focus is assumed to be equal to the existence of a DSB, whereas they are only marks of chromatin modifications [117]. The complexity of DNA damages as well as temporal repair can be studied e.g. by live cell imaging by following the evolution of individual foci [32]. Due to the exceptional sensitivity of the γH2AX foci technology, DNA damages can be investigated on small spatial scales, allowing e.g. for the measurement of the r^{-2} dependence of local dose on the distance r to the ion track center [118]. In recent years, new molecular biology methods became available, which might facilitate the more precise evaluation of spatial and temporal effects for DNA damages of any complexity [119]. This is useful in the determination of the role of SSBs, DSBs or DSB clusters for the final radiation effect and can be realized by sequence specific genome editing with CRISPR/Cas9. The approach allows to investigate the induction and processing of various forms of DNA damages in selected locations in the DNA [119]. Such detailed experiments could be used to validate several existing model approaches that include the different degrees of complexity of DNA damages [30, 12, 120].

4.3. Conclusion

In the LEM, several interaction scales of radiation damages are considered. The probability of DSB induction is proportional to local energy depositions on a nanometer scale. Next, individual DSBs interact on the micrometer scale within structural chromatin loops. Finally, the complexity of the DSB pattern is evaluated within the cell nucleus with its DNA as the target for radiation on the $\approx$10 micrometer scale. Recent scientific findings confirm that clustering of DNA damage on both the nanometer and micrometer scale leads to enhanced cell inactivation compared to more homogeneous lesion distributions [33]. This supports the idea that both coexisting processes need to be included in the determination of the resulting damage on a

cellular level. As the LEM concept of interacting DSBs on the micrometer scale could be further confirmed in this work and the dimensions of nuclei are measurable, the deviations of the LEM predictions observed in the validation process of the preceding chapter must originate on the nanometer scale. Furthermore, a sensitivity analysis of several LEM parameters, including the size of the chromatin loops, confirmed that the systematic model deviations cannot be explained by a simple input parameter variation [108]. Additionally, the origin of the deviation by target fragmentation or by the LEM simulation method could be excluded. Thus, the question arises if the concept of the "photon equivalent effect" is correctly realized in the LEM.

This concept is applied in the LEM for the calculation of the DSB distribution in an ion track. It implies that a certain local dose always leads to the same local effect, independent from the radiation quality responsible for the radiation exposure. Thereby, "local" refers to small spatial scales in the nanometer range. In a microscopic picture, the dose distribution of photons can be assumed to be homogeneous is a first approximation. Ions, however, show a highly localized dose distribution within a single ion track. In the core of the ion track large local doses are present, which decrease with increasing radial distance to the ion track center. Therefore, the DSB density is largest in the track core. In LEM the concept of "photon equivalent effect" is used to determine the DSB distribution in an ion track. Therefore in small "local" subunits within the ion track the local dose is determined. The probability for DSB induction in that subvolume is then calculated from a relation of the number of DSBs induced per dose obtained from photon measurements. At this point the simplifying assumption is made that a local dose induced by ions has the same effect as if the same local dose was initiated by photons [10].

However, DSBs that occur as a result of photon or ion radiation exposure are mainly induced by their secondary electrons [121, 37]. The shape of the secondary electron spectra varies substantially with the primary radiation quality. For ions, low-energetic electrons dominate the spectrum whereas for photons a rather homogeneous electron spectrum is present. Furthermore, it is known that the effectiveness of electrons for DSB induction depends on their kinetic energy. As a result, for different secondary electron spectra, different effects are expected even if the local dose is the same. In order to assess the mean effectiveness of a secondary electron mixture a function for the DSB induction effectiveness of a single electron is necessary as a function of electron kinetic energy. Several experimental methods exist for the determination of DSB yields, which, however, are highly challenging and give partly inhomogeneous results [35, 36, 118]. Furthermore, several theoretical models exist for the determination of DSB yields [30, 12, 120]. However, they typically provide values in dependence of macroscopic dose, whereas here, the "local" dose is of interest. Therefore, in the remainder of the presented thesis, a biophysical model is developed that enables the assessment of the relative effectiveness of electrons concerning DSB induction with regard to their kinetic energy. Furthermore, the implementation of this model in the LEM formalism is described. Its inclusion enables a more precise prediction of the DSB distributions within an ion track and therefore also improved RBE predictions of the LEM.

5. Development of DSB induction model for electrons

In the previous chapter, the LEM IV was systematically validated and discussed. Systematic model deviations were found for high-energetic ions and the origin of these deviations was determined to be the neglect of secondary electron spectra in the calculation of the DSB distribution in an ion track. In LEM versions I-IV the probability for DSB induction is determined directly from the present local dose in the track independent of the underlying secondary electron spectra [122]. However, the secondary electron spectrum depends substantially on the radial distance to the ion track center and also differs from the ones initiated by other radiation qualities such as X-rays [123, 39]. Furthermore, the effectiveness of a single electron for DSB induction depends on its kinetic energy [38, 39, 40]. Thus, for different secondary electron spectra, different DSB yields are expected. Consequently, it is of interest to determine the variable effectiveness of different radiation species for DSB induction based on their secondary electron spectra. In order to describe the mean effectiveness of such a spectrum, a function for the electron RBE for DSB induction is essential, next to the knowledge about the shape of secondary electron spectra. Therefore, in this chapter a DSB induction model is derived that provides the RBE of electrons with the endpoint of DSB induction as a function of electron energy. In the model the effectiveness of an electron for DSB induction is determined directly from the mean free path between two ionizations along an electron track assuming that at least two ionizations are necessary in a spatial cluster for the formation of a DSB. This simple concept contrasts with other alternative DSB induction models, which include detailed simulations of energy depositions, radical formation as well as a high resolution of the spatial structure of the DNA [124, 125, 126]. At the end of this chapter the model is applied to calculate the mean RBE for DSB induction for several primary radiation species based on their liberated secondary electron spectra.

5.1. Results

In the following section, the derivation of the DSB induction model is presented. After the mathematical formulation of the DSB induction processes, the RBE of electrons with the endpoint of DSB production is described. At last, the derived model is applied to estimate the degree of DSB induction for several primary radiation species based on their secondary electron spectra.

5.1.1. DSB formation based on mean free path of electrons

The prerequisite for an electron to produce a DSB is the formation of an ionization cluster of at least two ionizations. This concept forms a bridge between physical interactions (ionizations) and biological effects (DSBs) [127]. Therefore, the electrons' effectiveness in DSB induction can be derived from the probability of an electron to induce two or more ionizations in close proximity. This probability is energy-dependent and can be determined from the electrons' mean free path $\bar{l}$ between two ionizations. The ionization density

ρ along an electron track is calculated from the electrons' mean free path $\bar{l}$ between two ionizations as a function of its kinetic energy E_e by:

$$\rho(E_\mathrm{e}) = \frac{1}{\bar{l}(E_\mathrm{e})} \,. \tag{5.1}$$

Consequently, the expected number of ionizations N_I per path length s of an electron equates to:

$$N_\mathrm{I}(E_\mathrm{e}, s) = \frac{s}{\bar{l}(E_\mathrm{e})} = s \cdot \rho(E_\mathrm{e}) \,. \tag{5.2}$$

In the following, the mathematical description of two physical processes is derived, which both lead to the induction of DSBs along an electron track. The biophysical mechanisms of both processes are depicted schematically in Fig. 5.1. The first process is called process A as it occurs at all electron energies relevant in radiobiology research. In contrast to that process B is mostly relevant at lower electron energies. However, as the mathematical description of process A requires the knowledge about process B, process B is described first.

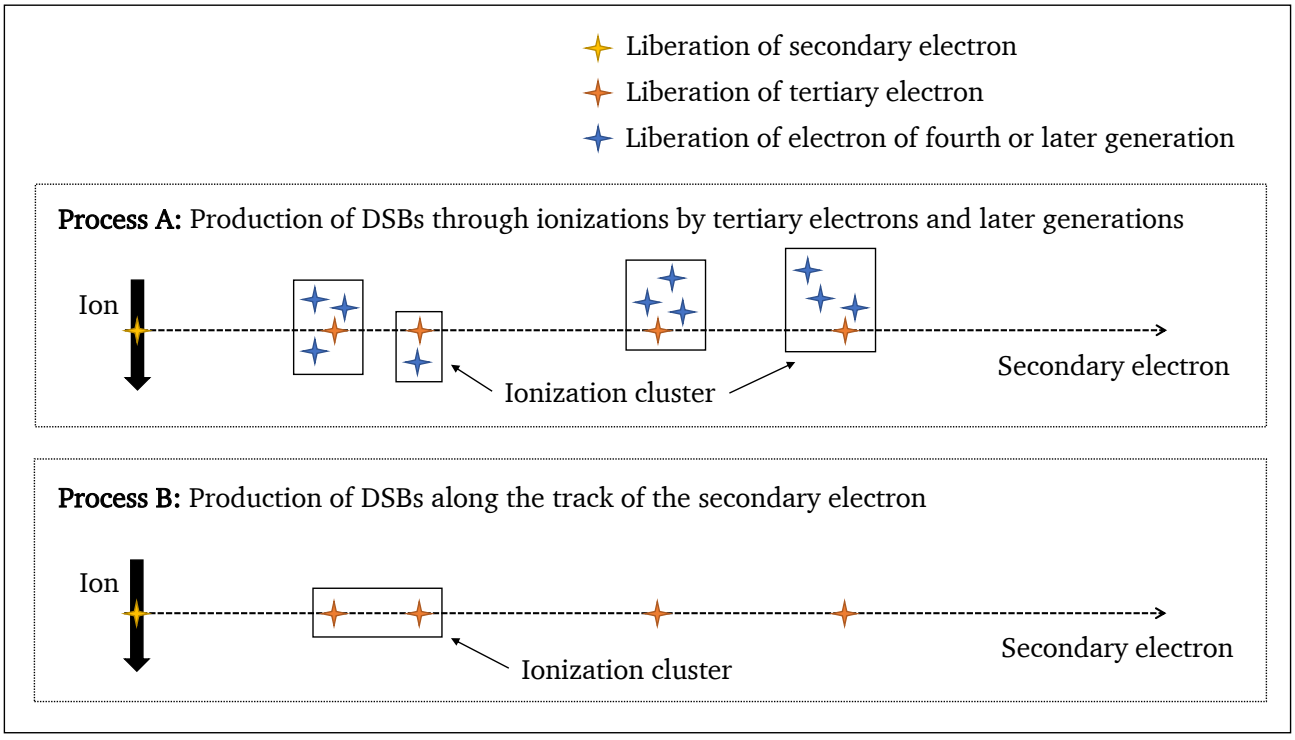

Fig. 5.1.: Schematic representation of two processes relevant for the production of ionization clusters along an electron track. The primary radiation quality is represented by an ion but could also be a photon or a primary electron. The ion liberates a secondary electron, which induces ionizations along its track. The path of the secondary electron is represented in a simplified manner by a straight line. Ionizations result in the ejection of tertiary electrons, which potentially lead to further ionizations. If ionization clusters are dense enough, they may lead to the formation of a DSB.

Process B: Process B is mainly relevant for lower energetic electrons (<10 keV). With decreasing electron energy the ionization density increases leading to an increased probability that two ionizations form a cluster directly along the track of the secondary electron (See bottom panel of Fig. 5.1). At higher electron energies the mean free path between ionizations is larger, which leads to only very few ionizations in close proximity. The probability for the formation of an ionization cluster of two or more ionizations within a threshold distance t is calculated based on the assumption that the probability for an ionization process follows a Poisson distribution:

$$P_{\mathrm{cluster}}(E_{\mathrm{e}}) = 1 - e^{-\rho(E_{\mathrm{e}})t}\,. \tag{5.3}$$

The quantity ρt describes the mean number of ionizations within the threshold distance t. The exponential function is thus the probability that for a given ionization there is no other ionization within a distance t downstream the electron track. The complementary probability is equal to the probability for at least one more ionization within that distance. If the distance between two ionizations is larger than t the damages are considered to be independent from each other and, thus, not able to form a cluster. Therefore, the number of ionization clusters along the electron's path by process B is obtained by multiplying the number of ionizations $N_{\mathrm{I}}(E_{\mathrm{e}}, s)$ for a specific path length s by the cluster probability:

$$N_{\mathrm{cluster}}(E_{\mathrm{e}}, s) = N_{\mathrm{I}}(E_{\mathrm{e}}, s) \cdot P_{\mathrm{cluster}}(E_{\mathrm{e}}) = N_{\mathrm{I}}(E_{\mathrm{e}}, s) \cdot \left[1 - e^{-\rho(E_{\mathrm{e}})t}\right]\,. \tag{5.4}$$

The number of DSBs per path length s is finally calculated multiplying N_{cluster} with κ, which weights the number of clusters by their probability to form a DSB. The parameter κ ensures the consideration of structural effects within the cell nucleus. Only a fraction of the nuclear volume is occupied by the DNA molecule with the rest mainly being filled by water and proteins. Furthermore, in many cases only a single ionization is located on the DNA. A second ionization might occur within the requested threshold distance but outside the DNA molecule and, as a result, a direct interaction of the two ionizations leading to a DSB is prohibited. Likewise, both ionizations could be placed on the same DNA strand and thus would also not result in a DSB. This approach neglects the indirect effect of radiation as introduced in Sec. 2.2.2. The indirect effect leads to additional DSBs through ionization of a water molecule leading to the production of a radical, which potentially diffuses trough the cell leading to additional DNA damage. The number of DSBs per path length s by process B is finally obtained by:

$$N_{\mathrm{DSB,B}}(E_{\mathrm{e}}, s) = \kappa \cdot N_{\mathrm{cluster}}(E_{\mathrm{e}}, s) = \kappa \cdot N_{\mathrm{I}}(E_{\mathrm{e}}, s) \cdot P_{\mathrm{cluster}}(E_{\mathrm{e}})\,. \tag{5.5}$$

The corresponding DSB yield per path length of the secondary electron $Y_{\mathrm{l,DSB,B}}$ can be written as:

$$Y_{\mathrm{l,DSB,B}}(E_{\mathrm{e}}) = \kappa \cdot \rho(E_{\mathrm{e}}) \cdot P_{\mathrm{cluster}}(E_{\mathrm{e}})\,. \tag{5.6}$$

Process A: This interaction process is relevant in the full electron energy range applicable in radiation biology. As depicted in the top panel of Fig. 5.1 a secondary electron is liberated by an incoming primary particle. The electron itself liberates further electrons on its path, which are called tertiary electrons in this work. Each further ionization initiated by a tertiary electron can potentially form a cluster with its original ionization point. With a certain probability both ionizations are positioned on opposite DNA strands within a maximum threshold distance in which case they are assumed to form a DSB. As tertiary electrons mostly have low kinetic energies [127], it is assumed that they induce all their DSBs through process B.

This assumption is valid as even high-energetic secondary electrons of 1 MeV liberate a spectrum of tertiary electrons with a mean energy of ≈60 eV, as visible in Fig. 3.10 D. Furthermore, electrons are most efficient in DSB induction at low kinetic energies. In order to calculate the total number of DSBs induced by a single tertiary electron until it stops, the DSB yield according to process B is integrated over the full electron track. Therefore, the DSB yield $\widetilde{Y}_{\mathrm{l,DSB,B}}(\tau')$ is written as a function of the electron track length τ', which itself is a function of the tertiary electron energy E_{tert} (see Fig. 3.10 C):

$$N_{\mathrm{DSB,tert}}(E_{\mathrm{tert}}) = \int_0^{\tau} \widetilde{Y}_{\mathrm{l,DSB,B}}(\tau')\, d\tau' \,. \tag{5.7}$$

with τ as the full track length of an electron at a specific kinetic energy. The function for $N_{\mathrm{DSB,tert}}$ can also be derived by an integration of the DSB yield as a function of electron energy instead of track length. Then, however, differentials need to be included in the calculation since a path element along the electron track is not always connected to the same energy loss at each position within the track.

As secondary electrons liberate a full spectrum of tertiary electrons with different kinetic energies, the average number of DSBs induced by a tertiary electron is calculated. There, the number of electrons induced by a single tertiary electron as a function of its energy is weighted by the corresponding tertiary electron energy spectrum. Thereby, the tertiary electron energy spectrum $S_{\mathrm{tert,e}}$ depend on the energy of the responsible secondary electron. Finally, the mean number of DSBs induced by a tertiary electron spectrum can be calculated as a function of the secondary electron energy E_{e} by:

$$\overline{N_{\mathrm{DSB,tert}}}(E_{\mathrm{e}}) = \frac{\int N_{\mathrm{DSB,tert}}(E_{\mathrm{tert}}) \cdot S_{\mathrm{tert,e}}(E_{\mathrm{e}}, E_{\mathrm{tert}}) dE_{\mathrm{tert}}}{\int S_{\mathrm{tert,e}}(E_{\mathrm{e}}, E_{\mathrm{tert}}) dE_{\mathrm{tert}}} \,. \tag{5.8}$$

The number of DSBs induced by process A is finally determined by multiplication of the number of ionizations (=tertiary electrons) per path length s of the secondary electron by the mean number of DSBs per liberated tertiary electron:

$$N_{\mathrm{DSB,A}}(E_{\mathrm{e}}, s) = \overline{N_{\mathrm{DSB,tert}}(E_{\mathrm{e}})} \cdot N_{\mathrm{I}}(E_{\mathrm{e}}, s) \,. \tag{5.9}$$

Correspondingly, the DSB yield per path length of the secondary electron is calculated as:

$$Y_{\mathrm{l,DSB,A}}(E_{\mathrm{e}}) = \overline{N_{\mathrm{DSB,tert}}(E_{\mathrm{e}})} \cdot \rho(E_{\mathrm{e}}) \,. \tag{5.10}$$

Note that an alternative approach for the description of process A is summarized in Sec. A.5 in the appendix.

Combination of process A and B: The total DSB yield obtained through the two biophysical processes described above is calculated as the sum of both single process yields:

$$Y_{\mathrm{l,DSB}}(E_{\mathrm{e}}) = Y_{\mathrm{l,DSB,A}}(E_{\mathrm{e}}) + Y_{\mathrm{l,DSB,B}}(E_{\mathrm{e}}) \,. \tag{5.11}$$

In the derivation above, the DSB yield is given per unit path length. It can also be expressed per local dose with the target density ρ and the nuclear volume V as:

$$Y_{\mathrm{d,DSB}}(E_\mathrm{e}) = \frac{Y_{\mathrm{l,DSB}}(E_\mathrm{e})}{LET(E_\mathrm{e})} \cdot \rho \cdot V \,. \tag{5.12}$$

This equation can be understood as follows: The fraction gives the number of DSBs per deposited energy. By multiplication with a specific mass ($m = \rho \cdot V$), the DSBs yield per dose is obtained with regard to this mass. For further calculations in this work, a nuclear volume of $V = 500$ µm^3 was used in order to be in line with the default parameters of the LEM together with the density of water $\rho = 1$ g/cm^3. The DSB yields per path length and per local dose are depicted in Fig. 5.2 as a function of (secondary) electron energy. The DSB yield per path length increases with electron energy up to a maximum, which can be found at ≈100 eV. The DSB yield per local dose reaches its maximum at even lower electron energies. At larger electron energies, the DSB yield per dose decreases again for both normalization approaches.

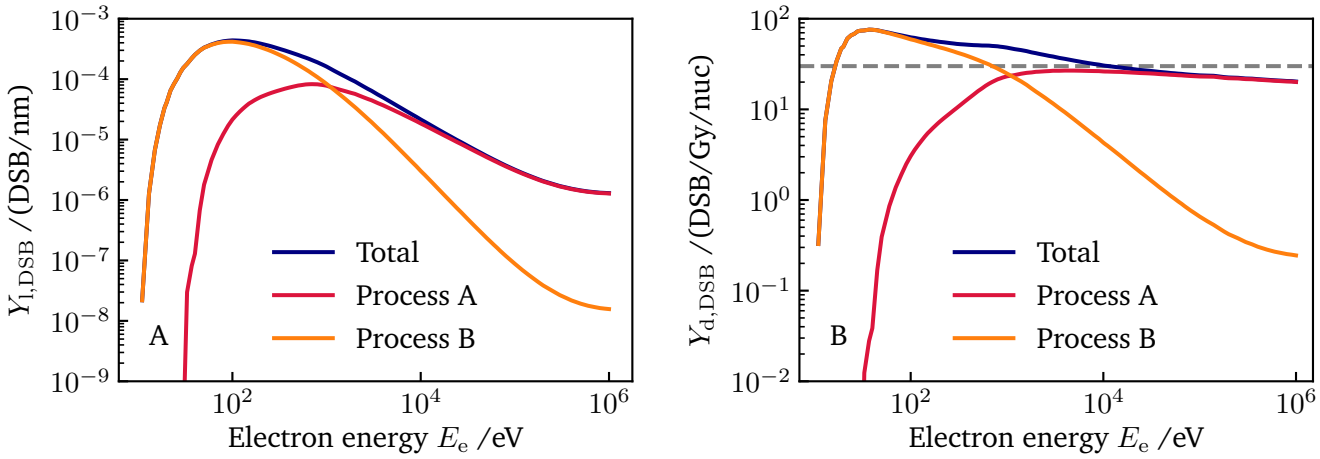

Fig. 5.2.: DSB yield per path length (A) and per local dose (B) by process A and B as a function of (secondary) electron energy. The parameters κ and t are chosen as 5.4·10^{-4} DSB/cluster and 4.2 nm, respectively. The blue curve is the sum of both DSB induction processes. The gray dashed line in B indicates a DSB yield of 30 DSB/Gy/nucleus, which is applied as a default value in the LEM.

The model described above contains two fit parameters κ and t. Their biophysical meanings and corresponding units are summarized in Tab. 5.1 and the determination of their values is described in Sec. 5.1.4.

Tab. 5.1.: Description of the free parameters used in the DSB induction model together with corresponding units.

Parameter	Description	Unit
κ	Number of DSBs per ionization cluster	DSB/cluster
t	Threshold distance between two (or more) ionizations to be able to form a DSB	nm

5.1.2. Local RBE of electrons for DSB induction

In the following, the local RBE of electrons is derived based on the DSB induction model described in the previous section. The RBE describes the ratio of doses of a reference radiation species and a test radiation, which lead to the same effect (see Eq. (2.16)). Typically the RBE is understood as a macroscopic quantity considering the average doses over the full biological sample. In this approach, however, a "local" RBE is derived, which describes the electrons' effectiveness in DSB induction locally. The spatial scales relevant here are chosen so small that the electrons' DSB yield and LET can be considered to be constant. The derivation of an equivalent "integral" RBE is described later in Sec. 5.1.3. The integral RBE corresponds to the RBE as it is typically measured in radiobiological experiments, considering the DSB induction along full electron tracks. An example of a local RBE is the η-factor applied in the LEM. It describes the enhanced occurrence of DSBs at large doses through the interaction of independent SSBs on the nanometer scale (="local"). The η-factor is described in Sec. 2.3.2 in detail. Whereas the η-factor takes into account additional DSBs through ionization clusters initialized by several independent electron tracks, the approach presented here includes additional DSBs within a single secondary electron track.

In the following, the derivation of the local RBE is given according to the classical RBE definition (d_{ref}/d) as a fraction of two doses together with a local definition of dose. The number of DSBs produced at a local dose d by an electron with DSB yield $Y_{\mathrm{d,DSB}}$ is given by a direct proportionality of the DSB number with dose:

$$N_{\mathrm{d,DSB}}(E_{\mathrm{e}}) = Y_{\mathrm{d,DSB}}(E_{\mathrm{e}}) \cdot d\,. \tag{5.13}$$

The local dose d is a quantity, which is also used in microdosimetry under the term "specific energy". The RBE is generally defined as the fraction of doses of two radiation species leading to the same effect. Here, the same number of induced DSBs is considered as the "same effect" ($N_{\mathrm{d,DSB,ref}} = N_{\mathrm{d,DSB}}(E_{\mathrm{e}})$). Thus, by solving Eq. (5.13) for the local dose d and inserting it into the classical definition of RBE, the RBE of a specific radiation species in relation to a reference radiation can be written as:

$$RBE_{\mathrm{DSB,local}}(E_{\mathrm{e}}) = \frac{d_{\mathrm{ref}}}{d} = \frac{N_{\mathrm{d,DSB,ref}}}{Y_{\mathrm{d,DSB,ref}}} \cdot \left(\frac{N_{\mathrm{d,DSB}}(E_{\mathrm{e}})}{Y_{\mathrm{d,DSB}}(E_{\mathrm{e}})}\right)^{-1} = \frac{Y_{\mathrm{d,DSB}}(E_{\mathrm{e}})}{Y_{\mathrm{d,DSB,ref}}}\,. \tag{5.14}$$

Inserting Eq. (5.12) into Eq. (5.14) for the DSB yields of the considered radiation species and a reference radiation species leads to the local RBE for DSB induction in its final form:

$$RBE_{\mathrm{DSB,local}}(E_{\mathrm{e}}) = \frac{Y_{\mathrm{l,DSB}}(E_{\mathrm{e}})}{LET(E_{\mathrm{e}})} \cdot \left(\frac{Y_{\mathrm{l,DSB,ref}}}{LET_{\mathrm{ref}}}\right)^{-1}\,. \tag{5.15}$$

In radiobiological experiments, the reference radiation is chosen by the experimenter. Typically high-energetic photons or X-rays are used as a reference in radiobiological experiments whereas monoenergetic electrons are often used in simulation studies. If monoenergetic electrons are chosen as a reference, the corresponding DSB yield $Y_{\mathrm{l,DSB,ref}}$ and LET LET_{ref} can be directly inserted into Eq. (5.15) to calculate the electron RBE. X-rays, however, induce a spectrum of secondary electrons. For such a mixture including various electron energies, the mean DSB yield per path length $\overline{Y_{\mathrm{l,DSB}}}_{\mathrm{ref}}$ and the mean LET $\overline{LET}_{\mathrm{ref}}$ need

to be calculated as spectral weights of the secondary electron spectrum at equilibrium S_{ref} of a reference radiation:

$$\overline{Y_{\mathrm{l,DSB}}}_{\mathrm{ref}} = \frac{\int S_{\mathrm{ref}}(E_{\mathrm{e}}) \cdot Y_{\mathrm{l,DSB}}(E_{\mathrm{e}})\, dE_{\mathrm{e}}}{\int S_{\mathrm{ref}}(E_{\mathrm{e}})\, dE_{\mathrm{e}}}\,, \tag{5.16}$$

$$\overline{LET}_{\mathrm{ref}} = \frac{\int S_{\mathrm{ref}}(E_{\mathrm{e}}) \cdot LET(E_{\mathrm{e}})\, dE_{\mathrm{e}}}{\int S_{\mathrm{ref}}(E_{\mathrm{e}})\, dE_{\mathrm{e}}}\,. \tag{5.17}$$

The two mean quantities can then be inserted into Eq. (5.15) to calculate the electron RBE if the reference radiation consists of a mixture of secondary electrons. The local RBE as a function of electron energy with monoenergetic 1 MeV electrons as well as with 250 kVp X-rays as reference radiation species is shown in Fig. 5.3. For X-rays the secondary electron spectrum as depicted in Fig. 2.2 B is used for the calculation. Similar to the DSB yield, the local RBE increases with increasing electron energy until it reaches a maximum at low kinetic energies of ≈80 eV. At higher electron energies the RBE drops again to smaller values. The choice of reference radiation influences the RBE curve as a linear scaling factor. Furthermore, it determines the electron energy at which the RBE reaches or crosses unity. The interpretation of the local RBE shall be clarified exemplary for a reference radiation of 1 MeV electrons: Figure 5.3 shows that electrons of ≈100 eV are nearly four times more effective in DSB induction than 1 MeV electrons. This means a four times larger DSB yield per deposited energy. The quantities refer to a "local" picture meaning that the corresponding energy depositions take place on a nanometer scale.

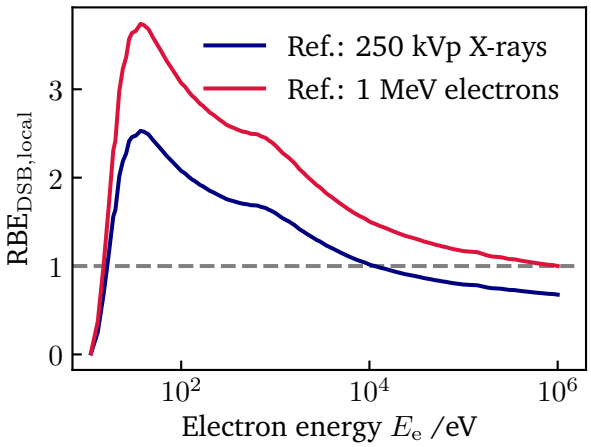

Fig. 5.3.: Local RBE as a function of electron energy with 1 MeV electrons and 250 kVp X-rays as a reference. For X-rays the corresponding secondary electron spectrum at equilibrium is considered. The minimum plotted electron energy corresponds to the ionization threshold of water, ≈12 eV.

Inserting the averaged quantities of Eq. (5.16) and (5.17) into Eq. (5.12) enables the calculation of the DSB yield per dose for a reference radiation consisting of a mixed electron radiation field. This is a quantity commonly determined in radiobiological measurements for DSB induction. For 250 kVp X-rays, typically a value of a few tens of DSBs/Gy/nucleus are reported. In the LEM, a DSB yield of 30 DSBs/Gy/nucleus is applied under the parameter named α_{DSB}.

5.1.3. Integral RBE of electrons for DSB induction

Complementing the derivation of the local RBE, in this section an equivalent expression is derived in an integral form. The derivation is performed analogous to the local RBE, replacing the local dose d by the integral dose D and the electron path length segment l by the total path length L. Thus, in the previous

chapter the indices l and d referred to local quantities and in this chapter the indices L and D indicate integral quantities. The term "integral" suggests that for the evaluation of an electron's effectiveness for DSB induction its full path is considered.

The total number of DSBs that a secondary electron induces on its full path including also electrons of further generations is determined by integrating the DSB yield per path length of both physical interaction processes over the full electron track τ'. Note that the DSB yield per path length is now given as a function of the track length τ', which is a function of the electron energy E_e:

$$N_{\mathrm{L,DSB}}(E_\mathrm{e}) = \int_0^{\tau} \widetilde{Y}_{\mathrm{l,DSB,B}}(\tau')d\tau' + \int_0^{\tau} \widetilde{Y}_{\mathrm{l,DSB,A}}(\tau')d\tau' = \int_0^{\tau} \widetilde{Y}_{\mathrm{l,DSB}}(\tau')d\tau' \,. \tag{5.18}$$

This relation was used earlier in a similar form for the description of the DSB induction process A (See Eq. (5.7) for comments on the integration method). The DSB yield as a function of electron path length $\widetilde{Y}_{\mathrm{l,DSB}}$ is depicted in Fig. 5.4 complementary to Fig. 5.2.

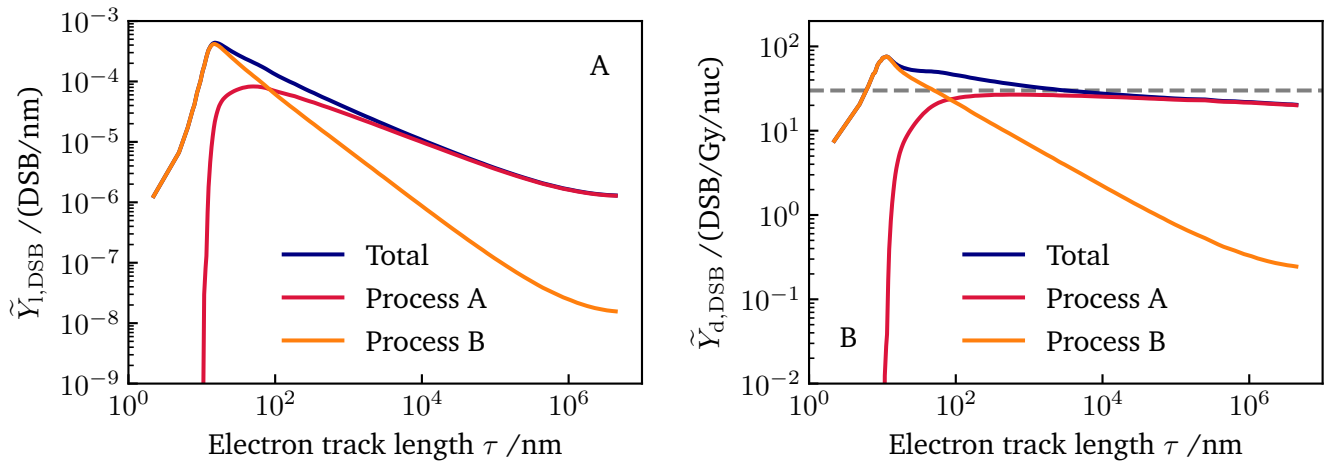

Fig. 5.4.: DSB yield per path length (A) and per local dose (B) by DSB induction process A and B as a function of electron track length. The plots are complementary to Fig. 5.2 in which the same quantities are shown as a function of the electron energy. The values of κ and t are chosen as in Fig. 5.2 and the gray dashed line in B indicates a DSB yield of 30 DSB/Gy/nucleus.

Along a full electron track, the electron does not only induce a total number of DSBs $N_{\mathrm{L,DSB}}$ but also loses all its kinetic energy E_e. Therefore, the DSB yield per integral dose D can be expressed as:

$$Y_{\mathrm{D,DSB}}(E_\mathrm{e}) = \frac{N_{\mathrm{L,DSB}}(E_\mathrm{e})}{E_\mathrm{e}} \cdot \rho \cdot V \,. \tag{5.19}$$

Note the comments for Eq. (5.12), which is the equivalent formulation in the corresponding "local" derivation of RBE. The equations (5.18) and (5.19) are plotted in Fig. 5.5 for both DNA induction processes A and B separately as well as for both processes combined. The number of DSBs induced by a full electron track increases with electron energy as higher energetic electrons possess larger electron track lengths. If the DSB yield is shown normalized to dose, the efficiency in DSB induction decreases again after it reaches a maximum at ≈100 eV.

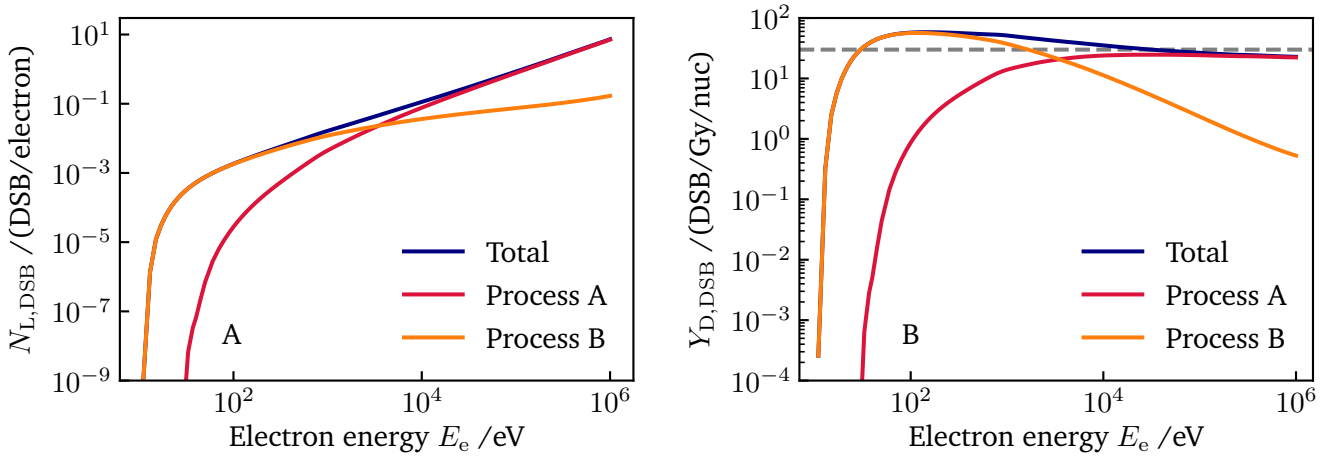

Fig. 5.5.: Number of electrons liberated per electron (A) and per Gy per cell nucleus (B). The values of κ and t are chosen as in Fig. 5.2 and the gray dashed line in B indicates a DSB yield of 30 DSB/Gy/nucleus.

Based on the quantities derived above, the integral RBE can also be calculated according to the classical definition of RBE (see Eq. (2.16)). In this integral approach the same effect is understood as the same number of induced DSBs in a macroscopic volume exposed to the dose D. The total number of DSBs induced by full electron tracks is calculated by multiplication of the DSB yield per dose $Y_{\mathrm{D,DSB}}$ with the macroscopic dose D:

$$N_{\mathrm{D,DSB}}(E_{\mathrm{e}}) = Y_{\mathrm{D,DSB}}(E_{\mathrm{e}}) \cdot D\,. \tag{5.20}$$

Solving Eq. (5.20) for the dose D and inserting it into the equation for the classical definition of RBE as a fraction of two doses leads to the integral RBE of electrons:

$$RBE_{\mathrm{DSB,integral}}(E_{\mathrm{e}}) = \frac{D_{\mathrm{ref}}}{D} = \frac{N_{\mathrm{D,DSB,ref}}}{Y_{\mathrm{D,DSB,ref}}} \cdot \left(\frac{N_{\mathrm{D,DSB}}(E_{\mathrm{e}})}{Y_{\mathrm{D,DSB}}(E_{\mathrm{e}})}\right)^{-1} = \frac{Y_{\mathrm{D,DSB}}(E_{\mathrm{e}})}{Y_{\mathrm{D,DSB,ref}}}\,. \tag{5.21}$$

By inserting the integral DSB yield $Y_{\mathrm{D,DSB}}$ from Eq. (5.19) for a specific radiation species and a reference radiation species into Eq. (5.21) the final form of the integral RBE is obtained:

$$RBE_{\mathrm{DSB,integral}}(E_{\mathrm{e}}) = \frac{N_{\mathrm{L,DSB}}(E_{\mathrm{e}})}{E_{\mathrm{e}}} \cdot \left(\frac{N_{\mathrm{L,DSB,ref}}}{E_{\mathrm{ref}}}\right)^{-1}\,. \tag{5.22}$$

with E_{ref} as the kinetic energy of the reference radiation. In accordance to the local RBE, a spectral weight of the DSB yield needs to be calculated if the reference radiation species consists of an electron energy mixture instead of monoenergetic electrons. Such a case is present for X-rays as a primary radiation species. Thus, the mean number of induced DSBs $\overline{N_{\mathrm{L,DSB_{ref}}}}$ and the mean electron energy $\overline{E_{\mathrm{e}}}_{\mathrm{ref}}$ are calculated as the spectral weight of the reference electron energy spectrum S_{ref}:

$$\overline{N_{\mathrm{L,DSB_{ref}}}} = \frac{\int S_{\mathrm{ref}}(E_{\mathrm{e}}) \cdot N_{\mathrm{L,DSB}}(E_{\mathrm{e}})\; dE_{\mathrm{e}}}{\int S_{\mathrm{ref}}(E_{\mathrm{e}})\; dE_{\mathrm{e}}}\,, \tag{5.23}$$

$$\overline{E_{\mathrm{e}}}_{\mathrm{ref}} = \frac{\int S_{\mathrm{ref}}(E_{\mathrm{e}}) \cdot E_{\mathrm{e}}\, dE_{\mathrm{e}}}{\int S_{\mathrm{ref}}(E_{\mathrm{e}})\, dE_{\mathrm{e}}}\,. \tag{5.24}$$

The dependence of the integral RBE on electron energy is presented in Fig. 5.6. As the RBE is a relative quantity, the enhanced effectiveness is plotted with 1 MeV electrons as well as with an initial secondary electron spectrum as induced by X-rays as a reference radiation species.

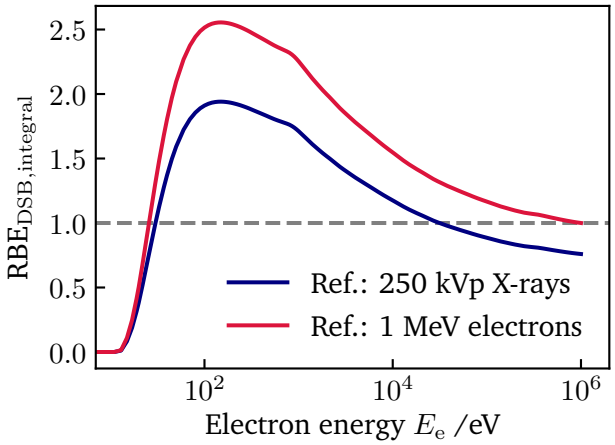

Fig. 5.6.: Integral RBE as a function of electron energy with 1 MeV electrons as a reference radiation as well as the initial secondary electron spectrum induced by X-rays. This figure is complementary to the local RBE plotted in Fig. 5.3.

In accordance to the derivation of the local quantities in the previous section, the DSB yield per integral dose can be calculated for a reference radiation consisting of a mixed secondary electron spectrum. Therefore, the averaged quantities of Eq. (5.23) and Eq. (5.24) are inserted into Eq. (5.19). If this quantity is evaluated for an initial secondary electron spectrum as induced by 250 kVp X-rays, it is also equal to the input parameter α_{DSB} in the LEM formalism, where it is assumed to be 30 DSB/Gy/nucleus. All parameters introduced in the previous sections are summarized in Tab. 5.2 together with a short description.

Finally, as a result of the analogous derivation, the local and integral RBE are connected through an integral relation with each other:

$$RBE_{\mathrm{DSB,integral}}(E_{\mathrm{e}}) = \frac{\int_0^{E_{\mathrm{e}}} RBE_{\mathrm{DSB,local}}(E'_{\mathrm{e}})\, dE'_{\mathrm{e}}}{E_{\mathrm{e}}}\,. \tag{5.25}$$

Here, both RBEs need to be defined towards the same reference radiation such as X-rays or 1 MeV electrons. Furthermore, for the local RBE the secondary electron spectrum at equilibrium is inserted into Eq. (5.16) and (5.17). For the integral definition of the RBE, the initial spectrum must be applied in Eq. (5.23) and (5.24). This relation can be verified by inserting the definitions of the local and integral RBE according to Eq. (5.15) and Eq. (5.22), respectively. By substitution of the energy differential by a track length differential, Eq. (5.25) can be verified.

5.1.4. Determination of free model parameters

The DSB induction model derived in Sec. 5.1.1 contains two free parameters: κ and t. The parameters' definitions and corresponding units are summarized in Tab. 5.1. Even though each parameter is connected to a clear biological/physical meaning their values are not directly measurable. Therefore, they are obtained by fitting the model according to three measurable properties:

Tab. 5.2.: Overview of the parameters introduced in the DSB induction model.

Variable	Description
E_e	(Secondary) electron energy
LET	Linear energy transfer
d	Local dose
D	Integral dose
$\overline{l}(E_\mathrm{e})$	Mean free path between ionizations for electrons
$\rho(E_\mathrm{e})$	Local ionization density for electrons
s	Electron path length
$N_\mathrm{I}(E_\mathrm{e}, s)$	Number of ionizations per path length s
κ	Number of DSBs per ionization cluster induced by a sec. electron
t	Maximum distance between two (or more) ionizations to be able to form a DSB
E_tert	Mean tertiary electron energy
$P_\mathrm{cluster}(E_\mathrm{e})$	Probability for ionization cluster within t along electron track
$N_\mathrm{cluster}(E_\mathrm{e}, s)$	Number of ionization clusters within track length s
$N_\mathrm{l,DSB,A}(E_\mathrm{e})$	Number of DSBs per path length s induced by process A
$Y_\mathrm{l,DSB,A}(E_\mathrm{e})$	DSB yield due to process A
$N_\mathrm{l,DSB,B}(E_\mathrm{e})$	Number of DSBs per path length s induced by process B
$Y_\mathrm{l,DSB,B}(E_\mathrm{e})$	DSB yield due to process B
$Y_\mathrm{l,DSB}(E_\mathrm{e})$	Total DSB yield per path length
$Y_\mathrm{d,DSB}(E_\mathrm{e})$	Total DSB yield per local dose
$N_\mathrm{d,DSB}(E_\mathrm{e})$	Number of DSBs induced by local dose d
$N_\mathrm{L,DSB}(E_\mathrm{e})$	Total number of DSBs induced along a full electron track
$Y_\mathrm{D,DSB}(E_\mathrm{e})$	DSB yield for a full electron track per integral dose
$Y_\mathrm{D,DSB,Dalton}(E_\mathrm{e})$	DSB yield for a full electron track per integral dose and DNA molecule mass
$N_\mathrm{D,DSB}(E_\mathrm{e})$	Number of DSBs induced by integral dose D
$N_\mathrm{DSB,tert}(E_\mathrm{tert})$	Number of DSBs induced by full tert. electron track
$RBE_\mathrm{DSB,integral}(E_\mathrm{e})$	Integral RBE of electrons for DSB induction
$RBE_\mathrm{DSB,local}(E_\mathrm{e})$	Local RBE of electrons for DSB induction
$S_\mathrm{ref}(E_\mathrm{e})$	Secondary electron spectrum of reference rad. species
$S_\mathrm{tert,e}(E_\mathrm{e}, E_\mathrm{tert})$	Tertiary electron energy spectrum
α_DSB	DSB yield per dose for X-rays (30 DSB/Gy/nuc.) as used in the LEM formalism

- **Integral number of DSBs induced per electron $\mathbf{N_{L,DSB}}$**: Eq. (5.18) is applied to fit experimental data on the number of DSBs induced by a single full electron track. This quantity is usually given in publications per Gy per Dalton and, therefore, correspondingly transformed in this step. As the fluctuation of values for the number of DSBs induced per electron are in a similar range if plotted logarithmically, the logarithm of the value was optimized in order to ensure a fair fit over the full electron energy range.

- **Integral RBE $\mathbf{RBE_{DSB,integral}}$**: The integral RBE for DSB induction is often determined in radiobiological experiments. Therefore, the free parameters κ and t are optimized such that Eq. (5.21) for the integral RBE best reproduces published measurement and simulation data. The collected dataset on the RBE for DSB induction includes data with several different reference radiation species. However, as monoenergetic electrons of high energy were used the most as a reference radiation in the determination of the RBE, 1 MeV electrons were chosen as a reference for fitting the DSB induction model. Note that the fit data consequently also includes RBE values with reference radiation species

other than 1 MeV electrons. Furthermore, if the RBE for DSB induction is published, typically also the DSB yield is given for the two radiation species. This data is used in the optimization process according to the first bullet point of this list. This potential double use of one dataset is discussed later in Sec. 5.2.3.

- **Average DSB yield per dose for X-rays $\overline{\mathbf{Y}_{\mathbf{D,DSB,ref}}}$**: X-rays are typically used as a reference radiation in practical radiobiological experiments and their corresponding DSB yield can be measured. In the LEM formalism a DSB yield of 30 DSB/Gy/nucleus is applied as default for this quantity. It can be calculated by Eq. (5.19) including the spectral averages of Eq. (5.23) and Eq. (5.24). In the optimization process, the free parameters are optimized such that the equation best fits a DSB yield of 30 DSB/Gy/nucleus for the initial secondary electron spectrum resulting from 250 kVp X-rays.

The mathematical optimization of the parameters κ and t was realized by simultaneously fitting the results of all three functions/quantities listed above to published data. The data used to fit the first two functions were collected from published experimental data and simulations that are described in detail in Sec. 3.5. In total, 76 experiments with measurement/simulation data on the number of DSBs induced per electron are included in the fit procedure. For 58 of these experiments additionally the integral RBE was measured or calculated. In order to ensure that all three fit objectives listed above are considered with a similar weight, the last one (concerning DSBs induced per Gy per nucleus for X-rays) was also included with a weight equal to 76 measurement points. According to the optimization procedure described above the values for the free parameters κ and t were obtained and their values are listed in Tab. 5.3.

Tab. 5.3.: Three sets of optimized values for the free parameters κ and t in the DSB induction model. (i. = ionization)

Set	**Description**	$\boldsymbol{\kappa}$ /(DSB/cluster)	$\boldsymbol{t}$ /nm	$\overline{\boldsymbol{Y}_{\mathbf{D,DSB,ref}}}$ /(DSB/Gy)
Default	Free fit	$5.384{\cdot}10^{-4}$	4.233 (=14.39 bp)	30.003
Set A	t fixed	$6.326{\cdot}10^{-4}$	2.94 (=10 bp)	30.003
Set B	t fixed	$4.473{\cdot}10^{-4}$	7.35 (=25 bp)	30.006

Next to the values obtained through a completely free fit, two more parameter sets are given. These were obtained by only optimizing κ while keeping t fix. Two values of t were considered (10 bp and 25 bp), as these are commonly used in the literature for a threshold distance of SSBs to interact and form a DSB. In the LEM IV, t is considered to be equal to 25 bp. With a conversion of 3.4 nm per bp [128, 121] this corresponds to 7.35 nm.

The schematic procedure of the optimization process is depicted in Fig. 5.7. The top row shows several physical properties of electrons used in the model. After optimization of the parameters κ and t by fitting to published data on the three radiobiological properties described in the list above, the final DSB yield per path length can be calculated. As a result, several local and integral quantities can be determined as e.g. the local and integral RBE.

The corresponding curves for the DSB yield per electron and for the integral RBE are shown for the default fit parameters together with published data in Fig. 5.8. The fitted model agrees well with experimental data over a large range of electron energies.

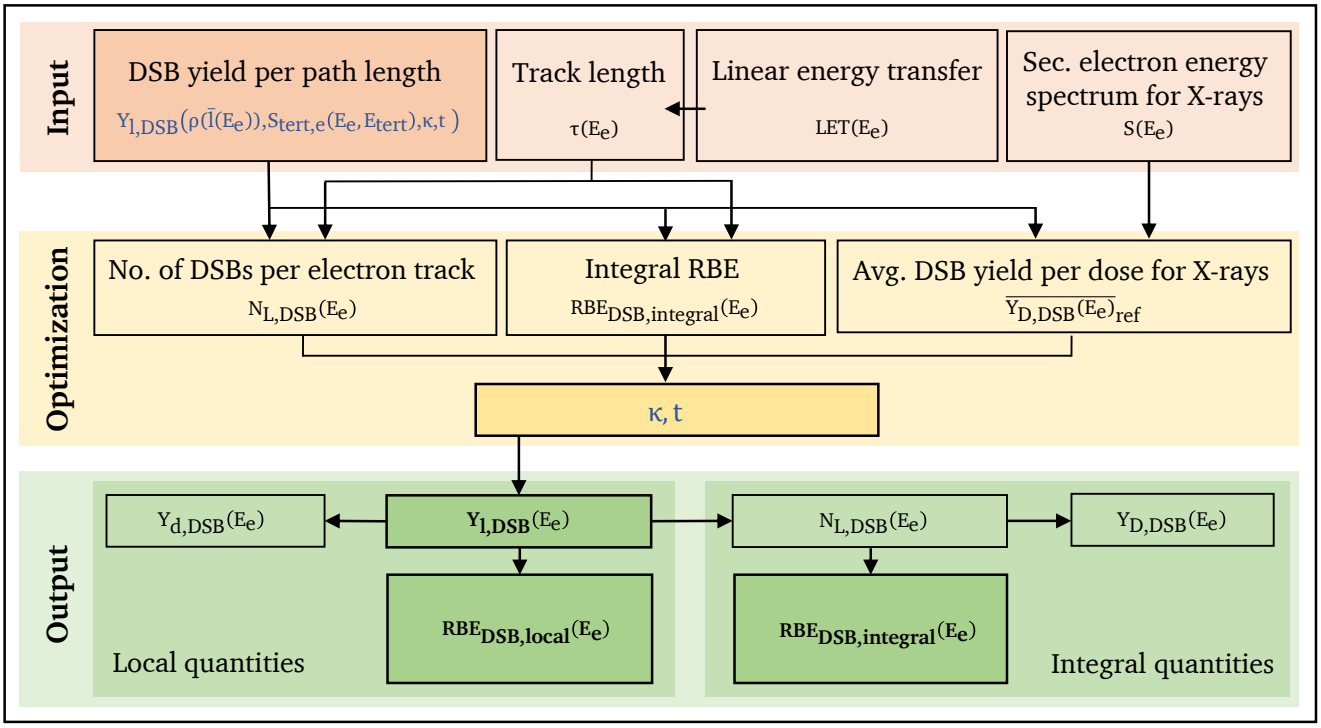

Fig. 5.7.: Schematic overview of parameter optimization of the DSB induction model.

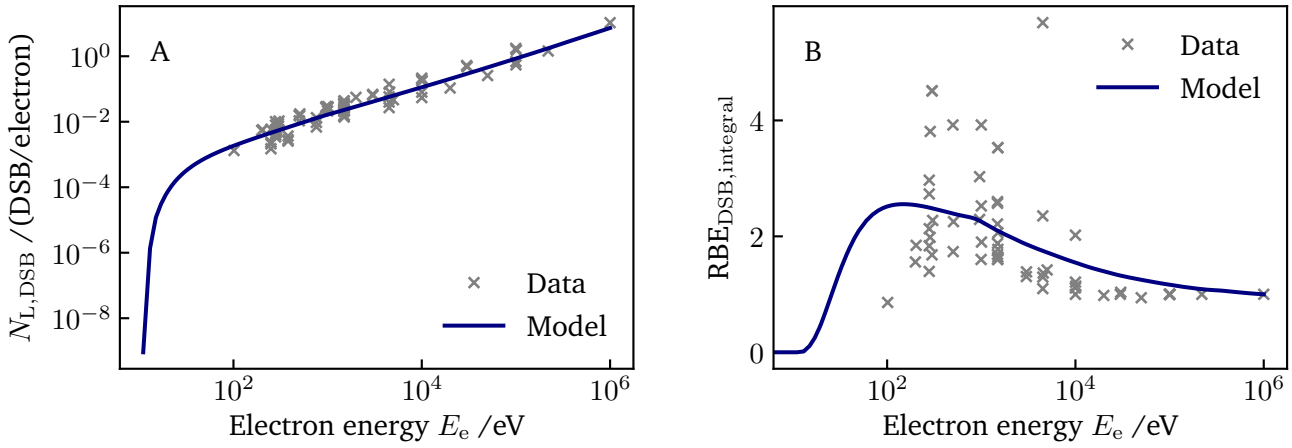

Fig. 5.8.: Number of DSBs created per secondary electron (A) and integral RBE for DSB induction (B). Next to measurement/simulation data, the curves obtained by the derived DSB model are plotted. The values of κ and t are equal to the default parameter set provided in Tab. 5.3.

As can be seen in Tab. 5.3 the values of all three parameter sets are close to each other. However, small changes in the corresponding local and integral RBEs are found as depicted in Fig. 5.9. A smaller value of t is connected to a larger value of κ and leads to a shift of the RBE maximum to slightly larger electron energies as well as to an increase of the maximum observed RBE value.

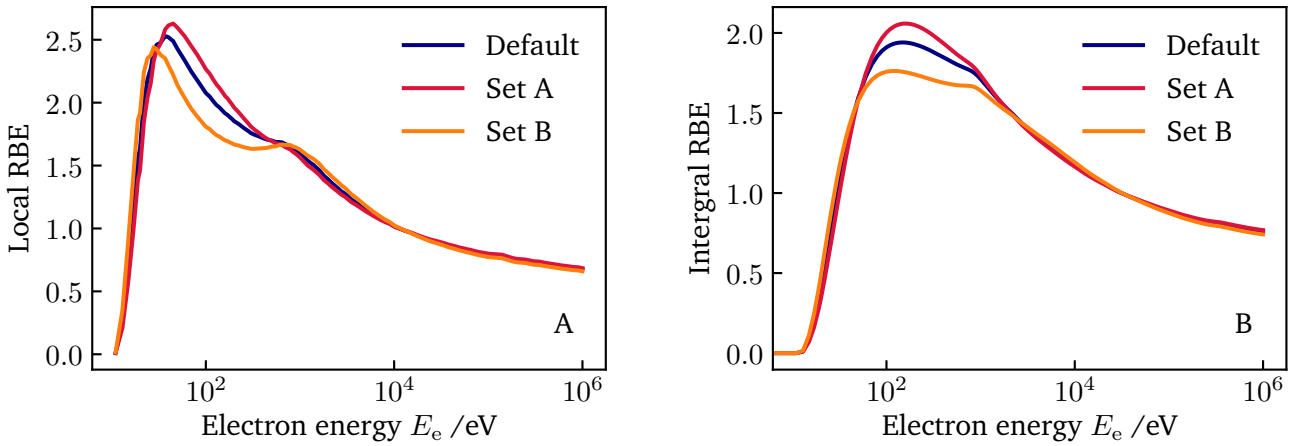

Fig. 5.9.: Comparison of local (A) and integral (B) RBE as a function of electron energy for three sets of free model parameters given in Tab. 5.3.

5.1.5. Evaluation of DSB induction for different radiation species

The largest fraction of biological damage is typically induced by secondary electrons liberated by the primary particle species. Thus, a secondary electron spectrum can be used as a first order measure of the biological effectiveness of any primary radiation species. To obtain such a measure in form of a mean RBE for DSB induction the electron energy spectrum S is first weighted with the electrons' LET as the local contribution of each electron to the absolute dose scales directly with its energy loss. Finally, the mean RBE θ_{local}, in the following also named DSB enhancement, of a secondary electron radiation field is calculated as a spectral weight of the local RBE:

$$\theta_{\mathrm{local}} = \frac{\int S(E_{\mathrm{e}}) \cdot LET(E_{\mathrm{e}}) \cdot RBE_{\mathrm{DSB,local}}(E_{\mathrm{e}})\, dE_e}{\int S(E_{\mathrm{e}}) \cdot LET(E_{\mathrm{e}})\, dE_{\mathrm{e}}}\,, \tag{5.26}$$

Secondary electron spectra change while the primary radiation species enters the target material until an equilibrium state is reached. The mean DSB enhancement θ_{local} can be calculated at each position within the build-up region by inserting the corresponding present secondary electron spectrum in Eq. (5.26). A schematic representation of the electron build-up effect is shown in Fig. 5.10. Here, the primary particle liberates a secondary electron spectrum consisting of three electrons of different energies at each artificial step in the medium (initial spectrum). In this simplified picture all electrons are assumed to be ejected in forward direction. The spatial extension of the electron build-up effect is determined by the range of secondary electrons, which carry a maximum kinetic energy and are ejected in the first step of the primary particle in the medium. After the completion of the build-up effect an equilibrium state is reached, which is constant from there on assuming that the energy of the primary particle is constant and the electron spectrum is the same at each step. The figure shows three areas, which represent different regions in which the mean DSB effectiveness is evaluated in the following part of this section. Area A marks the initial secondary electron spectrum in a local perspective and area B the same spectrum in an integral view. The letter C indicates a local perspective of the secondary electron spectrum in an equilibrium state.

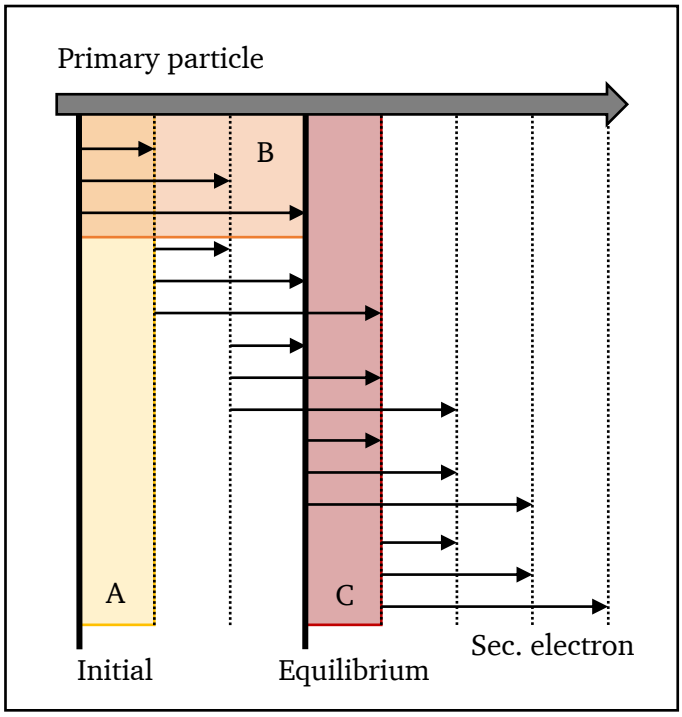

Fig. 5.10.: Schematic representation of the secondary electron build-up effect. The primary radiation liberates a spectrum of three electrons at each step through the medium. An equilibrium state is reached as soon as the highest-energetic electron stops, which was liberated in the initial step of the primary particle. A: Initial secondary electron spectrum in a local representation. B: Initial secondary electron spectrum in an integral representation. C: Electron spectrum at equilibrium state in a local representation.

In the previous section a formula for the $\mathrm{RBE}_{\mathrm{DSB}}$ of electrons was derived in a local and an integral perspective. The local perspective refers to small spatial scales at which the energy loss of the electrons can be neglected and the integral perspective includes full electron tracks. Fig. 5.10 shows that the local perspective of the spectrum at equilibrium leads to the same "total" electron spectrum as the integral perspective of the initial spectrum. This can be seen by comparing all arrow elements in the orange and red regions. Therefore, the corresponding mean DSB enhancement θ_{eq} for the secondary electron spectrum at equilibrium can be calculated in two ways:

$$\begin{aligned}\theta_{\mathrm{eq}} = \theta_{\mathrm{local,eq}} &= \frac{\int S_{\mathrm{eq}}(E_{\mathrm{e}}) \cdot LET(E_{\mathrm{e}}) \cdot RBE_{\mathrm{DSB,local}}(E_{\mathrm{e}})\, dE_e}{\int S_{\mathrm{eq}}(E_{\mathrm{e}}) \cdot LET(E_{\mathrm{e}})\, dE_{\mathrm{e}}} \\ &= \theta_{\mathrm{integral,init}} = \frac{\int S_{\mathrm{init}}(E_{\mathrm{e}}) \cdot E_{\mathrm{e}} \cdot RBE_{\mathrm{DSB,integral}}(E_{\mathrm{e}})\, dE_{\mathrm{e}}}{\int S_{\mathrm{init}}(E_{\mathrm{e}}) \cdot E_{\mathrm{e}}\, dE_{\mathrm{e}}}\,,\end{aligned} \tag{5.27}$$

with the the initial spectrum at the entry position of the projectile S_{init} and the spectrum in the equilibrium state S_{eq}. Note that the local and integral RBE are connected via Eq. (5.25) as introduced in the previous chapter.

In Fig. 5.11 A-C exemplary initial secondary electron spectra are depicted for several primary radiation species. For photons the electron spectra resemble a "box shape" with an additional peak at large energies for Co_{γ} radiation. In contrast to that, the spectra corresponding to ions as a primary radiation follow a E_{e}^{-2} behavior. Note that for ions, the spectra correspond to the ion track center ($r = 0$) whereas a radial differentiation is not applicable for photons due to their rather random energy deposition pattern. The term "Co_{γ}" refers to two photons of 1.173 and 1.332 MeV emitted during the decay of ^{60}Co to ^{60}Ni. As ^{60}Co decays via a β^--decay, additionally an electron is liberated. These electrons are, however, typically filtered out in radio-therapeutic applications. Note that these electrons, which are produced directly in the decay of ^{60}Co, are independent from the secondary electrons liberated by the photons created in the decay. Thus, Co_{γ} radiation is simulated as two photons of the above mentioned kinetic energies. The probability of their occurrence is assumed to be the same for both decay channels, which is an adequate approximation. Figure 5.11 D-F and G-I depict the integrands of the fractions needed for the calculations of the local (θ_{local}) and integral ($\theta_{\mathrm{intergal}}$) value of the DSB enhancement, respectively (see Eq. (5.27)). Here, the spectra S refer to the initial secondary electron spectra. The fractions of the integrals of the red and blue curves return the corresponding DSB enhancement factors of the considered primary radiation species.

Table 5.4 summarizes values of θ_{local} for several primary radiation species. The values are given for 250 kVp X-rays, Co_{γ} radiation and ions of different kinetic energies. The corresponding DSB enhancement values are calculated at two positions in the electron build-up region, for the initial spectrum at the entrance of the primary radiation in the target material and in an equilibrium state. The calculations are performed with secondary electron spectra obtained from Geant4(-DNA) simulations. Furthermore, if analytical models were available for the calculation of such spectra, the results were also determined based on the analytical models and are stated in parentheses.

For X-rays in the equilibrium state, the parameter $\theta_{\mathrm{local,eq}}$ equates to unity since the RBE is defined as the increased effectiveness in DSB induction compared to 250 kVp X-rays. Consequently, the calculation of $\theta_{\mathrm{local,eq}}$ for X-rays serves as an inherent model validation. In the case of Co_{γ} radiation, θ_{local} is smaller compared to X-rays, which is in agreement with experimental findings [129, 130]. This is due to the on average larger secondary electron energy for Co_{γ}. Higher energetic electrons induce more DSBs with regard to a full electron track. However, per dose unit low-energetic electrons are more effective in DSB induction. For all radiation species it is found that the mean DSB enhancement is smaller in the equilibrium state

Tab. 5.4.: Values for θ_{local} for several primary radiation species together with their energy and energy range of liberated secondary electrons. The values in brackets refer to calculations with analytically calculated energy spectra, whereas the initial values are calculated with spectra obtained by Geant4-DNA simulations. The first value in the bracket refers to a lower integration limit of 1 eV and the latter to a limit of 10 eV. This only impacts calculations for ions as in the analytical model the number of liberated electrons heads towards infinity for an electron energy $E_{\mathrm{e}} \to 0$ (see Sec. 3.3). Note that $\theta_{\mathrm{local,eq}} = \theta_{\mathrm{integral,init}}$.

Primary rad.	**Primary energy**	**Sec. energy E_{e}**	$\boldsymbol{\theta_{\mathrm{local,init}}}$	$\boldsymbol{\theta_{\mathrm{local,eq}}}$
250 kVp X-rays	$\lessapprox$250 keV	$\lessapprox$250 keV	1.31*	1.00*
Co_{γ}	1.173, 1.332 MeV	$\lessapprox$1.3 MeV	0.85* (0.84/0.84)	0.78* (0.78/0.78)
Ion ($r = 0$)	1 MeV/u	$\lessapprox$2.3 keV	2.10 (1.97/2.09)	1.49 (1.01/1.45)
Ion ($r = 0$)	10 MeV/u	$\lessapprox$23 keV	2.09 (1.97/2.09)	1.39 (1.01/1.39)
Ion ($r = 0$)	100 MeV/u	$\lessapprox$220 keV	2.08 (1.97/2.09)	1.28 (1.04/1.27)
Ion ($r = 0$)	100 MeV/u	$\lessapprox$220 keV	- (1.09/2.09)	- (0.98/1.13)

*For photons no Geant4-DNA models are available. Phys. interactions are simulated in a condensed history approach.

in comparison to the initial state of secondary electrons. This is due to the relationship between electron energy and range by $R \propto E_{\mathrm{e}}^{1.7}$. In the equilibrium the same energy spectrum is present as in the initial state *plus* higher energetic electrons, which were created upstream and still carry relatively large energies. Thus, an increased number of DSBs per dose unit is expected in the build-up region. However, the total number of DSBs in a small layer at the entrance of the target is not necessarily larger than in an analogous equilibrium situation as the dose is decreased in the electron build-up region. Different ions such as protons or carbon ions exhibit the same θ_{local} values if evaluated at the same kinetic energy in MeV/u, which is due to the nature of the shape of secondary electron spectra (find more details in Sec. 6.1.1). Furthermore, the general increase of biological effectiveness with LET is clearly reproduced for ions. The shown θ_{local} values describe the increased effectiveness for DSB induction by the increased probability of inducing ionization clusters for low-energetic electrons. Thereby, no interactions among different secondary electrons are considered. In certain scenarios, however, very high local doses can be reached in an irradiation (>100 Gy), where the interaction of separate electron tracks needs to be taken into account. This is the case for instance in the track core of high-LET ions. This effect is covered in the LEM by the η-factor as introduced in Sec. 2.3.2. Thus, to describe the total DSB enhancement in an ion track more precisely, both the θ- and η-factor need to be considered. However, the accuracy of the reflection of general RBE trends (such as the increase of RBE with decreasing ion energy) in the DSB enhancement values θ is remarkable considering the "simple" mechanistic approach behind the DSB induction model. The probability for DSB induction is calculated directly from the mean free path between two ionizations along an electron track, neglecting details such as the specific structural organization of DNA.

The above formalism enables the comparison of the DSB induction effectiveness for different secondary electron spectra associated with different primary radiation species. However, the total energy deposition of a primary radiation species is not necessarily the same as the total energy deposited by the secondary electrons. A large amount of energy of the primary radiation is transferred to electrons. But a certain amount of energy is also invested for excitations, scattering of the projectile or can be lost to overcome the binding energy of the liberated secondary electrons. Thus, if different primary radiation species should be compared concerning their effectiveness in DSB induction instead of only their secondary electron spectra, this effect needs to be taken into account. This point is further discussed in Sec. 5.2.6.

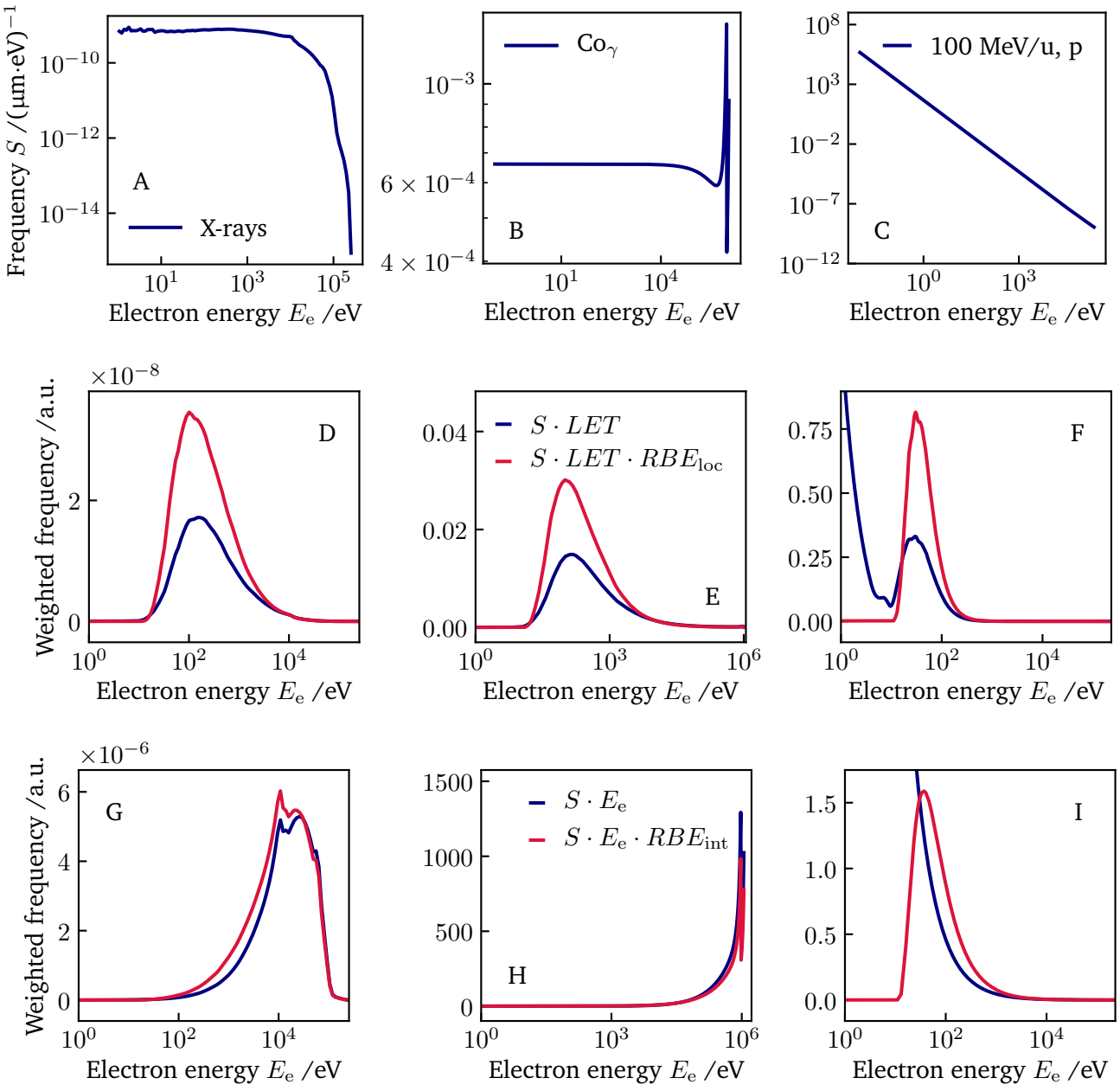

Fig. 5.11.: A-C: Initial secondary electron spectra for 250 kVp X-rays (A), Co$_\gamma$ radiation (B) and 100 MeV protons (C). For ions, the spectra correspond to the electron composition at the track center ($r = 0$). For X-rays the spectra are obtained from MC calculations and for Co$_\gamma$ and protons from analytical models. D-F and G-I: Integrands of Eq. (5.27) for the local and integral representation, respectively. The three panels in one column refer to the radiation species in the corresponding top panel.

5.2. Discussion

It is remarkable that the increased RBE of low-energetic electrons can be well reproduced considering the simple approach of discriminating between only two elementary processes leading to the formation of ionization clusters that may cause DSBs. In the following, several aspects of the derived model are discussed. First, the impact of the precision of radiation transport codes on the model are investigated, as MC codes were used to calculate physical properties applied in the model. These quantities are the mean free path between ionizations along an electron track, the electron LET and secondary electron spectra induced by primary electrons and X-rays. Next, the handling of very low electron energies are discussed, followed by an analysis of the measurement data used to fit the free parameters of the model. Finally, the model is compared to other RBE models available in the literature before the applicability of the model is discussed with regard to its assessment of the effectiveness of various photon radiation species. Finally, the impact of the fraction of the dose deposited by the primary radiation itself is analyzed.

5.2.1. Physical properties calculated by radiation transport codes

Measurement data of physical properties of low-energetic electrons are sparse and subject to large uncertainties [50]. Therefore, several physical properties, which are needed as an input for the derived DSB induction model, are calculated by the radiation transport code Geant4-DNA. In this section, the uncertainty of the applied cross sections is discussed with regard to the impact on the results of the DSB induction model.

One major physical property applied in the model is the mean free path of electrons between two ionizations. The corresponding simulations were performed with the default Geant4-DNA cross section data set "option 2" as described in Sec. 3.4. The low-energy radiation transport code Geant4-DNA provides three recommended sets of cross section data from which the user can choose. As for all three sets the compilation of cross section data and models varies, their application results in different values for the mean free path. The deviation between the models is in the range of a few percent as can be seen from Fig. 5.12 and the applied "option 2" leads to values that are positioned between the ones obtained with the two alternative options.

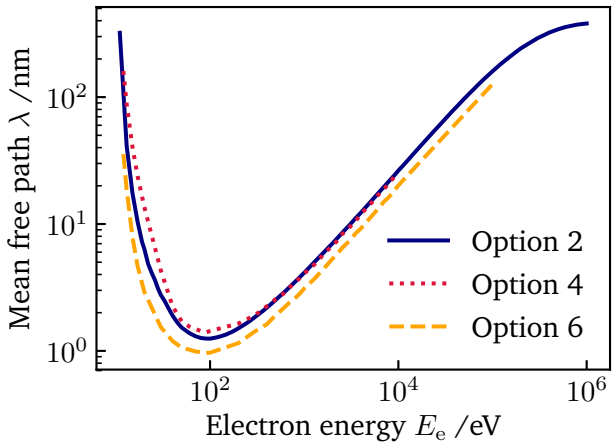

Fig. 5.12.: Electron mean free path between two ionizations as a function of electron energy calculated with three different sets of Geant4-DNA cross section data.

The variation among the three model options reflects the scarcity of mean free path measurements for low-energetic electrons. For instance international recommendations by e.g. ICRU reports are currently not available for values of the mean free path [47]. However, as the tendencies of all three options are similar and deviations relatively small, the impact of the option choice is expected to be of minor importance.

Next to the mean free path, the LET of electrons was derived from radiation transport calculations. The simulated values are depicted for all three sets of cross section options in Fig. 5.13. The maximum LET, which is found at ≈100 eV, varies about 25% between the options, whereas the values simulated with "option 2" are positioned between the other two options, which is in accordance with the findings of the mean free path. As official recommendations for stopping power values in the ICRU report 90 [101] are restricted to values ≥1 keV, a corresponding comparison of the precision of the radiation transport code concerning predictions of stopping power in the low-energy regime is not possible. The plotted LET values were used additionally for the calculation of the electrons' energy-dependent range. This was realized by inserting the simulated LET values into Eq. (2.7).

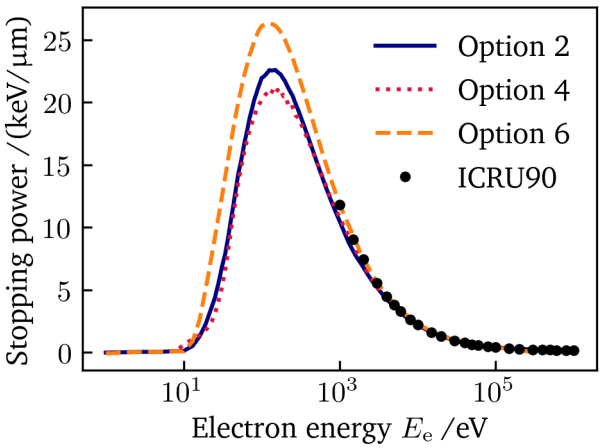

Fig. 5.13.: Electron stopping power as a function of electron energy simulated with three different sets of Geant4-DNA cross section data. Additionally, available stopping power data provided by the ICRU is displayed [101].

The variation between the cross section datasets reflects the uncertainty and general lack of measurement data for low-energetic electrons, especially in liquid water [50, 40, 131]. The determination of physical parameters and optimization of measurement techniques for low-energetic electrons is thus of great interest in radiobiology. Measurements of low-energetic electrons are challenging due to their short range as well as additional physical and chemical interaction mechanisms that are relevant at these energies [131, 132, 133].

For all MC simulations, water was used as a medium to simulate the biological cellular environment. This setting is eligible in a first approximation as eucaryotic cells are composed by 80% of water. However, simulation studies showed a dependence of the material on the obtained DSB yield [134, 135]. Therefore, for future simulations more advanced materials could be applied in the MC simulations that better reflect experimental scenarios. However, first, cross section data need to be well determined for such materials, which consist of more complex molecular structures compared to water.

To conclude, the choice of "option 2" interaction models for the applied Geant4-DNA simulations is justified. The values for the mean free path and the stopping power of electrons are positioned between the ones obtained with the alternative approaches. Considerable uncertainties occur mostly at very low secondary electron energies in the order of ≈10 eV. Hence this uncertainty will propagate into the considerable DSB amplification predicted in this thesis for such low energetic electrons.

5.2.2. Handling of electrons with energies below the ionization threshold

In the proposed model, DSBs are induced as a consequence of ionization clusters. Therefore, electrons below the ionization energy threshold of ≈12 eV are strictly-speaking assumed to have no biological effectiveness,

which is expressed by an RBE value of 0. As visible from RBE values in Fig. 5.3, electrons at the ionization threshold already show an RBE close to 0. Therefore, for later applications the electron RBE_{DSB} was extrapolated between the value found at the ionization threshold (≈12 eV) and the plot coordinates (0,0). By assigning an electron RBE >0 for electrons below the ionization threshold, findings by Sanche et al. are supposed to be reflected [136]. Sanche et al. reported the induction of DSBs by electrons below the ionization threshold due to electron resonances. Such resonances are responsible for the formation of transient anions, which may fragment by dissociation into a stable anion and a neutral radical or by decaying into dissociative electronically excited states [136]. The created fragments can further interact with the molecules present in the cell nucleus and lead to more complex chemical damage. Additionally, the formation of biological damage in form of DSBs can be enhanced by dissociation of a transient anion within the DNA molecule. The proposed interpolation effectively considers the existence of such processes.

5.2.3. Dataset for determination of free model fit parameters

The two free fit parameters κ and t are part of the formalism of the DSB induction model. Their values were obtained by fitting the model to measurement and simulation data available in the literature. The details of the optimization procedure are described in Sec. 5.1.4. One of the quantities used for the fitting process is the RBE of electrons for DSB induction for which there are 58 published values determined with several different reference radiation species. The developed model, however, is fixed to one specific reference radiation, which was set to 1 MeV electrons in the optimization process for the integral RBE. This choice is based on the fact, that high energetic electrons are the most prominent reference radiation species in the collected dataset. Note that, however, after the determination of κ and t the DSB induction model can also be applied for other reference radiation species. For instance to be compatible with the LEM formalism, a reference radiation of X-rays should be chosen.

The RBE is calculated as the fraction of the DSB yield of a certain radiation species and the DSB yield of a reference radiation species. In many radiobiological experiments, however, the DSB yield is determined only for one radiation species and no reference radiation. Consequently, no RBE can be calculated. Next to the RBE_{DSB}, data on the DSB yield for electrons were used in the optimization process of the free parameters of the DSB induction model. This means that for published datasets in which RBE values were provided, also the corresponding values for the DSB yield of electrons were used in the model fit. For experiments in which no RBE was given, only the DSB yield data is used. Therefore, for the 58 RBE datasets, the data are "used twice" in the optimization process but in a different form. This procedure is justified as the inclusion of both properties promises to lead to more precise values for k and t. On the one hand, more DSB yield data is available than data on the RBE. On the other hand, RBE data shows the advantage that systematic errors in measurements or simulations might be eliminated. For instance a systematic overestimation of the DSB yield would occur in the determination of the yield for the test radiation species as well as for the reference radiation species. Due to the above given definition of the RBE_{DSB} the influence of such systematic errors on the optimization of k and t could be reduced.

A large fraction of the reference data is obtained from simulation studies, which are based on certain physical assumptions and are thus also subject to systematic errors. Furthermore, in simulation studies, it is feasible to determine the RBE for many electron energies within one simulation setup whereas the corresponding measurement is connected to a large time effort. Therefore, in simulation studies DSB yield or RBE data is often provided for more energies than in experiments. This could lead to an unbalanced weighting of the independent data points in the optimization process as each data point was assigned the same weight. Additionally, for many data no error bars are published together with the measurement data, which disables a simple assignment of an error bar to each data point.

5.2.4. Comparison to other electron RBE models for DSB induction

The interaction mechanisms of low-energetic electrons are of great interest to the research community due to their increased biological effectiveness. Therefore, several measurement and simulation studies exist, determining the DSB yield of electrons. The existing model approaches are discussed in this section and compared to the approach followed in the present work.

Ultrasoft X-rays (0.5-1 keV) interact predominantly via photoionization with water, liberating secondary electrons with the same kinetic energy as the incident photons (minus the electron's binding energy). The Giant LOop Binary LEsion (GLOBLE) model enables a potential understanding of the origin of the increased effectiveness of ultrasoft X-rays. In accordance to the concept applied in the LEM, DSBs are either classified as isolated or clustered DSBs within DNA subunits (see Sec. 2.3.2). According to the GLOBLE approach the increased $\mathrm{RBE}_{\mathrm{DSB}}$ of ultrasoft X-rays could be explained by the increased DSB yield as a consequence of the high local ionization density [137, 38]. However, all DSBs are considered to lead to the same degree of damage except for the case of localized DSB clustering on the micrometer scale. This localized clustering of lesions as found for ions is one possible explanation of the increased effectiveness of ions in comparison to X-rays or photons. In accordance to the GLOBLE model, the DSB induction model developed in this work does not differentiate between the effectiveness of different DSB types. An alternative explanation for different radiation species is based on the "qualitative" differences of produced molecular lesions [138, 31]. Corresponding modeling approaches include the different types of DSBs on the nanometer scale by classifying DNA breaks according to their complexity. Nikjoo et al. proposed a detailed model with additional damage types called e.g. DSB+ or DSB++, pointing to additional SSBs in close proximity to the original DSB [30]. The classification of DNA damages proposed by Nikjoo is applied in the Monte Carlo damage simulation (MCDS) code [139] to calculate DSB yields for several different particles. Other models compute the induction of DNA damages using Monte Carlo track structure simulations in combination with geometrical models of the DNA and chromatin, such as the codes PARTRAC [124, 55], KURBUC [140], Geant4-DNA [125, 126, 141], a model by Nikjoo [134, 30, 142], DBREAK [143], MOCA8b [144] or PENELOPE [145, 146]. Other models apply a more simplistic approach, similar to the concept developed in this work, by investigating the occurrence of ionization clusters, which potentially lead to DNA damage [147, 148]. A further model approach developed by Bellamy et al. uses an empirical method to predict electron RBE [149]. It is based on the fractional deposition of absorbed dose by electrons of kinetic energies below a few keV. The model follows the empirical approach of Nikjoo and Goodhead who highlighted the relevance of electron track ends for the total radiation damage [150]. The predicted RBE values for DSB induction of electrons by the model of Bellamy et al. are in good agreement with the model results presented in this work.

Two other models are available in the literature for the prediction of the RBE with the endpoint of DSB induction for electrons, which follow a similar concept as the model presented in this work. In the following both approaches are compared in detail to the present model. The first model is a DSB model by Cucinotta et al. from 1999, which is based on the frequency of specific energy depositions in targets with the diameter of DNA [39, 121]. The second approach was published by Buch et al. in 2018 and considers the enhanced DSB yield due large local doses in an amorphous track structure model [38].

$\mathrm{RBE}_{\mathrm{DSB}}$ model by Cucinotta et al.: The RBE of electrons published by Cucinotta et al. [39] is based on data obtained in a simulation study of Goodhead and Nikjoo from 1989 [121]. The RBE is understood as the increased frequency of energy depositions above 120 eV in DNA by electron tracks with the reference of 100 keV electrons. In the publication by Cucinotta et al. the simulated RBE values for electrons are compared to measured values for the inactivation of V79 cells by X-rays. The model agrees well with the measurement

data. As it is based on the frequency of energy depositions, it is in the first place independent from the endpoint and is comparable to the model presented in this work. For both models the RBE is plotted over electron energy in Fig. 5.14. At smaller electron energies the model by Cucinotta et al. decreases faster towards a value of 0. However, at these energies the jagged shape of the model curve suggests that only few data points were simulated. At electron energies between 100 eV and 1 keV the model by Cucinotta et al. shows larger values compared to this work's model and at larger electron energies it declines slightly faster. As Cucinotta et al. applied 100 keV electrons as a reference radiation, his model crosses unity at 100 keV. As mentioned above, the model by Cucinotta et al. is based on simulation studies on the frequency of energy depositions of 120 eV within short segments of DNA. The MC simulations were performed in water with the radiation transport code MOCA8b of Paretzke from 1987 [151].

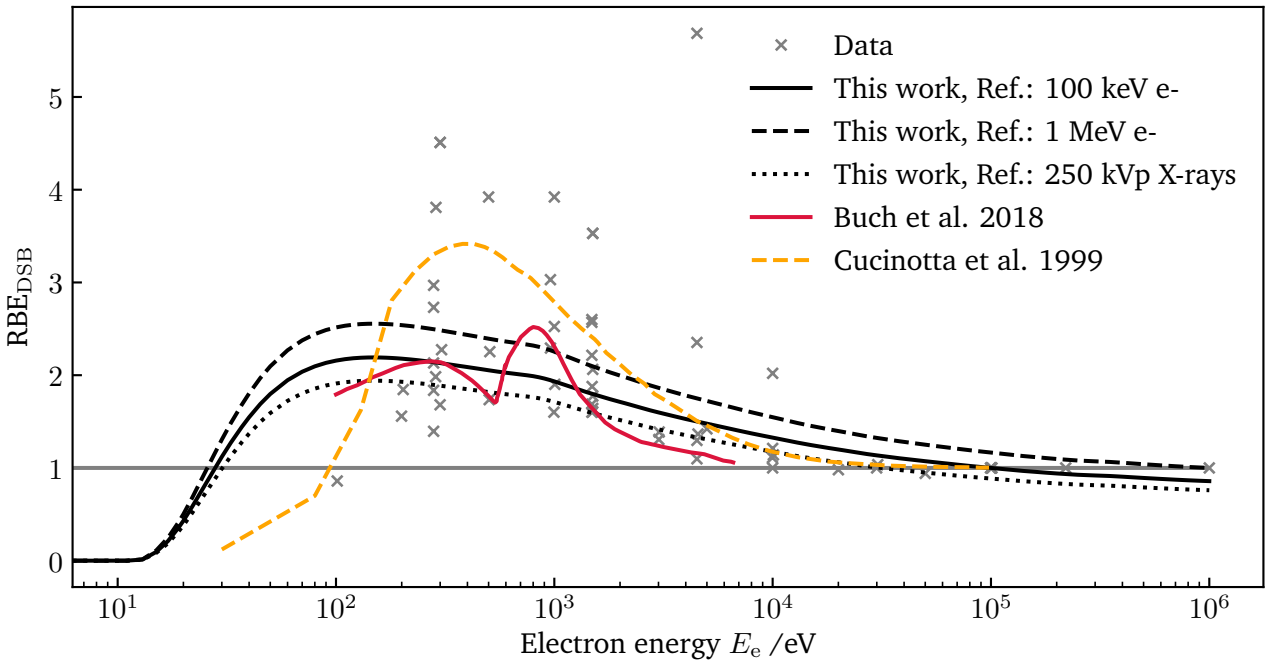

Fig. 5.14.: Integral RBE as a function of electron energy for the model developed in this work together with other published RBE models for DSB induction. Next to the model data, measurement and simulation data published in the literature is depicted (See Tab. A.5 for details on the collection of published data).

RBE$_{DSB}$ model by Buch et al.: Ultrasoft X-rays (0.5-1 keV) interact with the target material via the photoelectric effect liberating electrons with nearly the same kinetic energy as the incident photons. They exhibit larger RBE values compared to higher-energetic photons due to their rather localized dose distribution. The large local doses are a consequence of the ionization pattern of track ends of electrons, which occur within each electron track before the electron stops. Due to small mean free path values between ionizations at low electron energies, large local energy densities are obtained on the nanometer scale, leading to an enhanced probability of DSB induction. The model by Buch et al. [38] is a simulation study based on the amorphous track structure formed by secondary electrons liberated by ultrasoft X-rays. It makes use of the increased probability at large doses for SSBs to interact and lead to DSBs as described by the η-factor in the LEM concept (see 2.3.2 for details). The RBE$_{DSB}$ can thus be understood as the mean η-factor of the local dose profile induced by ultrasoft X-rays. The main difference between this work's model and the

model by Buch et al. is found in the origin for the increased DSB yield. The model developed in this work is independent of local dose distributions and predicts an increased DSB yield for low-energetic electrons due to the fact that at such energies the mean free path between two ionizations along an electron track is in the range of the diameter of DNA. In the model by Buch et al., however, the increased DSB yield for low-energetic electrons can be traced back to an inhomogeneous local dose distribution. Therefore, large local doses occur, leading to the interaction of SSBs with the result of an additional DSB. In the publication by Buch et al. RBE values between 100 eV and 5 keV are considered. The double-peak of the Buch model is due to the specific consideration of liberated Auger electrons. In the model developed in this work, the Auger effect is also indirectly included in the description of process A in the DSB induction model (See 5.1.1 for more details on physical processes A and B.). The number of DSBs induced by process A is calculated based on tertiary electron spectra, which were precalculated with Geant4-DNA simulations. The radiation transport code enables the activation of the Auger process leading to the characteristic peaks in electron energy spectra at ≈540 eV as visible in Fig. 3.11. Furthermore, the model by Buch et al. takes a yield of 30 DSBs/Gy/nucleus as a reference, which is assumed to be the case for 250 kVp X-rays. At larger electron energies, the model by Buch et al. predicts slightly smaller RBE values than the model proposed in this work. This can be traced back to the difference of the secondary electron spectra induced by ultrasoft X-rays in comparison to photons of larger energy.

In conclusion, the proposed RBE model as well as the approaches by Cucinotta et al. and Buch et al. all predict a similar function of the RBE of electrons in dependence on their kinetic energy. The models predict an increase of RBE at small electron energies leading to an RBE maximum at ≈100 eV−1 keV. At larger electron energies all models show a decrease of RBE, reaching a value of 1 at an electron energy that is determined by the choice of reference radiation. All three model predictions lie well within the range of available measurement data. In order to assess the precision of each model approach in more detail, additional measurement data is required. Thereby, measurements with low-energetic electrons are of special interest, however, the practical implementation of the corresponding measurement setup is complex [132, 133]. Additionally, in the last years much effort was put in a more precise prediction of the physical interactions of low-energetic electrons [47, 50, 51]. Therefore, it would be beneficial to re-simulate the RBE according to the concept of Cucinotta et al. or similar models with a state-of-the-art MC code.

5.2.5. DSB yield and RBE of different photon radiation qualities

The RBE of an ion is defined as the enhanced biological effectiveness in comparison to a reference radiation species. Even if the International Atomic Energy Agency (IAEA) recommend the use of ^{60}Co as a reference, in radiobiological experiments, a large range of photon sources is employed [152] . Each type of photon reference radiation induces a different secondary electron spectrum. Thus, a different effectiveness for DSB induction is expected for each type of photon radiation species. This behavior is reflected in the RBE values of the different radiation qualities as reported previously [129, 130, 153, 149, 154, 155]. This systematic could also be confirmed and explained by the DSB induction model presented in this work (see Sec. 5.1.5). Lower energetic photons liberate electrons with an on average lower kinetic energy. As low-energetic electrons (≈100 eV) are highly effective, lower-energetic photons show an increased mean $\mathrm{RBE}_{\mathrm{DSB}}$ in comparison to higher-energetic photons.

In radiobiological measurements mostly 250 kVp X-rays or γ-radiation originating from the decay of ^{60}Co are applied. The DSB induction model derived in this work predicts a decrease of the DSB yield for ^{60}Co radiation to ≈80% in comparison to the DSB yield of 250 kVp X-rays. This means that if the effectiveness of X-rays is evaluated with ^{60}Co radiation as a reference, an RBE value of ≈1.3 is obtained. This is slightly larger

or in the range of values reported in other simulation studies found in the literature [156, 157]. A similar simulation approach as the one derived in this work to estimate the $\mathrm{RBE}_{\mathrm{DSB}}$ for different photon radiation qualities was followed by Hsiao et al. [156]. They also assessed the mean effectiveness of a radiation species based on their secondary electron spectra. These energy spectra were calculated with the radiation transport code PENELOPE [146]. Furthermore, they used the Monte Carlo damage simulation (MCDS) code [139] to calculate DSB yields for electrons. The code is based on the simulation of different types of DNA lesions classified as initially introduced by Nikjoo [30]. They finally obtained the mean $\mathrm{RBE}_{\mathrm{DSB}}$ of different photon radiation species by a spectral weight (of the secondary electrons) of the DNA damage yields. Thus, Hsaio et al. applied a similar concept as Eq. (5.26). However, instead of inserting the RBE in the denominator of the fraction they directlyused DSB yields. Hsiao et al. found an $\mathrm{RBE}_{\mathrm{DSB}}$ of 1.1 for 220 kVp X-rays with Co_{γ} radiation as a reference, which is slightly smaller than the values reported in this work. A further modeling approach by Vassiliev et al. calculates the LQ parameters of different photon radiation qualities directly from the frequency averaged LET of the secondary electron spectra [157]. The obtained RBE values for 250 kVp X-rays are in the range of the values reported in this work. Next to the enhanced effectiveness for cell killing by low-energetic photon radiation, other radiobiological endpoints were investigated in previous studies. For instance an increased RBE was found for carcinogenesis in animals or neoplastic cell transformation or chromosome aberrations for mammography X-rays relative to ^{60}Co radiation [158, 159, 160, 161].

The International Commission on Radiological Protection (ICRP) has acknowledged that electrons and photons may have RBE values greater than unity. However, it still recommends a radiation weighting factor w_{R} of 1 [162]. This convention is due to several reasons. For instance the lack of precise information, simplicity and general practical considerations [163]. The precise assessment of the RBE for different photon radiation species is of special importance for risk assessment in which low-energetic X-rays are used in clinical applications as in routine mammography screenings. Such X-rays typically carry kinetic energies between 26 and 30 kVp and are thus more effective compared to high energy photons [164]. However, a large fraction of the epidemiological data used for corresponding risk assessment is based on measurements with high energetic photons [165]. Thus, the risk associated with mammography X-rays might be underestimated. The model proposed here was so far only applied to predict the effectiveness in DSB induction for two photon radiation species: 250 kVp X-rays and Co_{γ} radiation. However, the RBE can also be predicted for mammography X-rays according to the same concept. First estimations lead to RBE values between 1.5 and 2, which is in agreement with predictions by Vassiliev et al. or measurements by Depuydt et al. [164]. However, other measurement or simulation studies also determined smaller RBE values of $\approx$1.2 [166, 156]. The precise calculation and evaluation of the RBE for mammography X-rays with the model proposed in this work is still pending. The neglect of variable DSB yields of different photon radiation species is also critical if RBE values of different radiobiological experiments are compared. If different radiation qualities are used as a reference, different RBE values will be determined even if the effectiveness of the considered radiation species is the same. The large variety of applied photon reference radiation species becomes clear by investigating the spectrum of such species present in the PIDE database [28, 29]. In total, 18 different photon reference radiation species are among the listed experiments. First investigations indicate that the PIDE measurement data reflect the RBE dependencies on the choice of reference radiation species as described above.

5.2.6. Impact of energy fraction deposited by secondary electrons

In Sec. 5.1.5 the derived local and integral $\mathrm{RBE}_{\mathrm{DSB}}$ of electrons are applied to evaluate the effectiveness in DSB induction for different primary radiation species. The described formalism enables the comparison of the DSB induction effectiveness for different secondary electron spectra associated with different primary radiation species. Thus, θ describes the increased effectiveness of any secondary electron spectrum compared

to the secondary electron spectrum induced by a reference radiation. Thereby, the comparison refers to the same amount of total dose for both secondary electron mixtures. However, the total energy deposition of a primary radiation species is not necessarily the same as the total energy deposited by the liberated secondary electrons. A certain amount of energy is also invested for excitations, scattering of the projectile or can be lost to overcome the binding energy of the liberated secondary electrons. The fraction of energy loss of the primary particle transferred to electrons in form of their kinetic energy is calculated as

$$f_{\mathrm{e}} = \frac{E_{\mathrm{ioniz}} - E_{\mathrm{ioniz,bind}}}{E_{\mathrm{tot}}}\,, \tag{5.28}$$

with the ion's total energy loss E_{tot}, the ion's energy spent in ionization processes E_{ioniz} and the energy lost to overcome the electrons' binding energy $E_{\mathrm{ioniz,bind}}$. Correspondingly, the fraction of the ion's energy loss, which is not converted into kinetic energy of secondary electrons is determined as:

$$f_{\mathrm{rem}} = E_{\mathrm{tot}} - f_{\mathrm{e}}\,. \tag{5.29}$$

If different primary radiation species should be evaluated concerning their effectiveness in DSB induction instead if their secondary electron spectra, this effect must be taken into account. First simulation results are collected in Tab. 5.5. The table lists the amount and fraction of energy transferred to secondary electrons in ionization events as calculated by Geant4-DNA simulations for several primary radiation species relevant in radiobiology research. The values refer to energy depositions along a track of 1 µm, which enables a comparison to the LET for ions, which is typically given in units of keV/µm. The values for photon radiation (X-rays and Co_γ) have to be considered with caution as no "specialized" physics models exist for photons (as for ions or electrons) in the Geant4-DNA extension of the Geant4 toolkit. Therefore, photon interactions are simulated by a condensed history approach instead of a detailed simulation of the microscopic track structure (For details see Sec. 3.4).

Tab. 5.5.: Energy depositions by primary radiation along a track of 1 µm. E_{tot}: total energy deposited, E_{ioniz}: energy lost in ionization events, $E_{\mathrm{ioniz,bind}}$: energy lost to overcome binding energy, $E_{\mathrm{el}} = E_{\mathrm{ioniz}} - E_{\mathrm{ioniz,bind}}$: energy transferred to secondary electrons in form of their kinetic energy. The values in the parentheses refer to the percentage fraction of the corresponding deposited energy in comparison to the total energy deposited.

Primary radiation	$\boldsymbol{E_{\mathrm{tot}}}$ **/keV**	$\boldsymbol{E_{\mathrm{ioniz}}}$ **/keV**	$\boldsymbol{E_{\mathrm{ioniz,bind}}}$ **/keV**	$\boldsymbol{E_{\mathrm{el}}}$ **/keV**
250 kVp X-rays ($\lessapprox$250 keV)	$4.260{\cdot}10^{-3}$	$4.260{\cdot}10^{-3}$ (100%)	$0.025{\cdot}10^{-3}$ (0.59%)	$4.235{\cdot}10^{-3}$ (99.41%)
Co_γ (1.173, 1.332 MeV)	$3.947{\cdot}10^{-3}$	$3.947{\cdot}10^{-3}$ (100%)	$0.001{\cdot}10^{-3}$ (0.03%)	3.964 (100%)
Protons (1 MeV)	26.347	25.865 (98.17%)	5.812 (22.06%)	20.053 (76.11%)
Protons (5 MeV)	8.002	7.884 (98.53%)	1.562 (19.52%)	6.322 (79.01%)
Protons (10 MeV)	4.604	4.539 (98.56%)	0.873 (18.95%)	3.666 (79.63%)
Protons (50 MeV)	1.274	1.259 (98.80%)	0.226 (17.76%)	1.033 (81.08%)
Protons (100 MeV)	0.759	0.737 (97.05%)	0.171 (22.53%)	0.566 (74.57%)
Carbon ions (1 MeV/u)	632.486	632.460 (100%)	159.619 (25.24%)	472.841 (74.76%)

The study indicates that for photons a larger fraction of their energy is transferred to electrons in form of kinetic energy (≈99-100%) compared to ions (≈75-80%). A large fraction of secondary electrons liberated by ions are low-energetic. Thus, per electron a larger part of the ions' lost energy in an ionization event is "invested" to overcome the electrons' binding energy compared to photons. The findings reported in [37] are

in a similar range of 65-75% of the ions' energy loss being found experimentally in the secondary electron kinetic energy. A fraction of 15-25% of the total energy loss is reported to be spent to overcome the electron binding energy. The fraction of dose due to energy depositions of secondary electrons $f_{\mathrm{i,e}}$ is calculated as:

$$f_{\mathrm{i,e}} = \frac{D_{\mathrm{i,e}}}{D_{\mathrm{i,tot}}}\,, \tag{5.30}$$

with $D_{\mathrm{i,e}}$ as the dose due to energy depositions by the secondary electrons and $D_{\mathrm{i,tot}}$ as the total dose. The index refers to a specific radiation species i. If this effect is taken into account, the relative effectiveness of a primary radiation species with regard to the total dose deposition is calculated by:

$$\theta_{\mathrm{D}} = f_{\mathrm{i,e}} \cdot \theta_{\mathrm{i}}\,, \tag{5.31}$$

with θ_{i} as the relative DSB induction effectiveness of the secondary electrons, which contribute a fraction of $f_{\mathrm{i,e}}$ to the total dose. The above named formalism can be applied for the local as well as the integral DSB enhancement. As mentioned above, first investigations indicate that $f_{\mathrm{i,e}}$ is approximately 1 for photons and 0.8 for ions. Thus, as a result of the described dose scaling, the values for the mean DSB enhancements θ in Tab. 5.4 are reduced to ≈80% for ions, whereas they keep nearly unchanged for photons.

5.3. Conclusion

In the preceding chapter a DSB induction model was derived, which enables the assessment of the RBE of electrons concerning DSB induction in dependence on their kinetic energy. In the model the probability for DSB induction is calculated directly from the mean free path between two ionizations along an electron track in water. Only two possible mechanisms for the production of an ionization cluster are considered, which potentially lead to a DSB. This simple approach strongly contrasts with the large zoo of available DSB induction models, which explicitly simulate the shape of radiation track structures as well as the detailed structural organization of DNA on an atomic level for the prediction of DSB yields [124, 140, 125, 126, 141, 142, 143, 144, 145]. The derived model proved to be a powerful tool for the assessment of DSB yields of different primary radiation species. Therefore, the assumption is made that the majority of DSBs is induced by secondary electrons liberated by the primary radiation. Then the mean effectiveness of any primary radiation species can be estimated by weighting the RBE function for DSB induction of electrons with the secondary electron spectra. This is not only of special interest for different ion species but also for various photon radiation species. Whereas the International Commission on Radiological Protection (ICRP) still recommends a radiation weighting factor w_{R} of 1 [162] for photons and electrons due lack of precise information and simplicity [163] the presented model is a powerful tool for the assessment of the variable effectiveness for DSB induction for these radiation species. In the LEM I-IV the DSB yields are simply assumed to be the same for photons and ions. The new DSB induction model now enables a precise determination of the DSB yields based on the secondary electron spectra of any radiation species. The inclusion of the DSB induction model in the LEM formalism is described in the following chapter.

6. Implementation and validation of the Local Effect Model V

In the previous chapter, a DSB induction model was derived, which enables the determination of the RBE of electrons with the endpoint of DSB induction. The model proved to be a powerful tool for the assessment of the DSB yields of any radiation species based on their secondary electron spectra. In this chapter, its integration in the existing LEM formalism is described, which leads to more precise RBE predictions for ions.

In the LEM I-IV the simplified assumption is made that ions and photons induce the same number of DSBs per local dose unit. This procedure is valid in a first approximation. Furthermore, no complete and consistent description of the precise DSB yields of different radiation species was available at that time. The newly introduced DSB induction model fills this gap and enables the evaluation of the DSB yield based on the secondary electron spectra liberated by any primary radiation species. In the previous chapter the model was applied to calculate the DSB yields for different radiation species, which highlighted substantial differences between ions and photons. Thus, by inclusion of this effect in the LEM calculations, also an impact on RBE predictions of ions is expected. The model version including the new approach is called LEM V in the following.

6.1. Results

In this section, the results of the integration of the DSB induction model within the framework of the LEM are presented. After investigating the general impact of the new implementation on the RBE prediction, the new model version was tested by comparing its predictions to experimental data of the PIDE database. This systematic model validation of LEM V with the PIDE database follows the same approach as for the LEM IV presented in Chapter 4.

6.1.1. Application of the DSB induction model in the LEM framework

In the LEM IV, the radial DSB distribution within the ion track is determined in order to calculate the biological effect after irradiation. The number of DSBs induced is calculated based on the present local dose in small cylindrical shells around the ion track center. This step in the calculation process is the main part, which needs to be adjusted in the transition from LEM IV to LEM V. For the determination of the DSB distribution the probability for DSB induction is assumed to be proportional to the local dose that depends on the radial distance to the ion track center and is calculated according to the amorphous track structure model described in Sec. 2.1.4. Finally, the number of DSBs is calculated in the LEM IV by consideration of the DSB-enhancement $\eta(D)$ accounting for separate interacting electron tracks at high local doses as well as the knowledge that X-rays induce 30 DSB/Gy/nucleus. In this step, the assumption is made that X-rays induce the same number of DSBs per dose as ions. Differences in the DSB yields due to different secondary

electron spectra are neglected. In the LEM V, the direct dependence of DSB induction on secondary electron spectra was determined as introduced in the previous chapter. It was found that the secondary electron spectra for X-rays and ions differ, leading to different DSB yields per dose for both radiation species. With that knowledge, the number of DSBs distributed in radial cylindrical shells around the ion track can be determined more precisely and used in the new model version LEM V. As the secondary electron spectra for ions strongly depend on the radial distance to the ion track center, the DSB enhancement needs to be calculated as a function of the radial distance to the ion track center:

$$\theta_{\mathrm{local}}(r) = \frac{\int S_{\mathrm{rad}}(E_{\mathrm{e}}, r) \cdot LET(E_{\mathrm{e}}) \cdot RBE_{\mathrm{DSB,local}}(E_{\mathrm{e}})\, dE_e}{\int S_{\mathrm{rad}}(E_{\mathrm{e}}, r) \cdot LET(E_{\mathrm{e}})\, dE_{\mathrm{e}}}\,, \tag{6.1}$$

with S_{rad} as the secondary electron spectra in dependence on the radial distance to the ion track center r. Note that in the previous chapter the DSB enhancement for ions was exclusively calculated at $r = 0$. Conveniently, the electron energy spectra for several ions at the same kinetic energy in MeV/u have the same shape. They only differ in the absolute number of electrons liberated per path length of the ion as reflected in the LET. This is due to the fact that the specific acceleration energy of the ion defines its energy transfer to electrons, which determines the shape of the secondary electron spectra. Thus, two secondary electron spectra of two different ions A and B with the same kinetic energy per nucleon are connected via:

$$S_{\mathrm{rad,A}}(E_{\mathrm{e}}, r) \propto S_{\mathrm{rad,B}}(E_{\mathrm{e}}, r)\,, \tag{6.2}$$

Therefore, Eq. (6.1) is independent from the ion species and only depends on the ion's kinetic energy in MeV/u. For the calculation of θ_{local} the radial secondary electron spectra are calculated by the Kiefer-GSI model described in Sec. 3.3. The dependence of θ_{local} on r is depicted in Fig. 6.1 for several different ion energies. Generally, the DSB enhancement factor decreases with radial distance to the ion track center. However, at the edge of the ion track, the DSB yield increases again due to an enhanced fraction of low-energetic more effective electron energies in the secondary electron spectra.

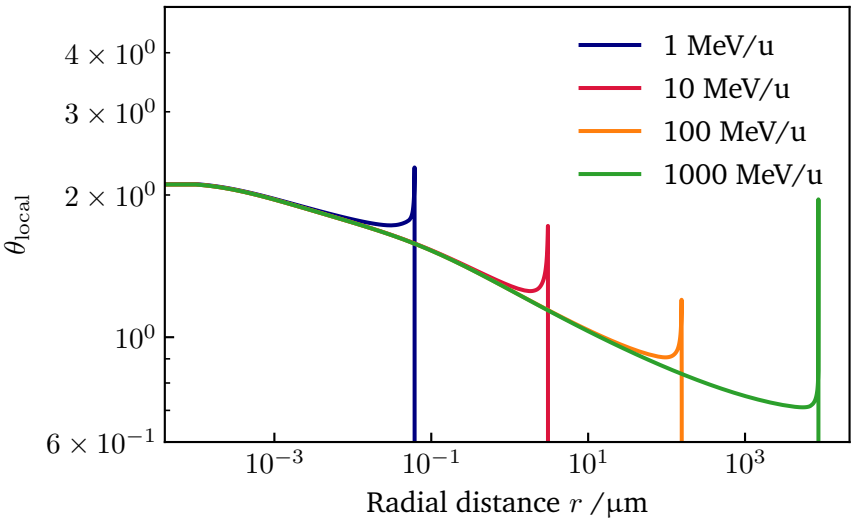

Fig. 6.1.: Radial DSB enhancement as a function of the radial distance to the ion track center at different ion energy levels. Note that the enhancement is independent of the ion species and only depends on ion energy. The underlying secondary electron spectra are calculated from the Kiefer-GSI model described in Sec. 3.3.

General implementation: The amorphous track structure model applied in the LEM depends on the LET of the ion. Thus, all equations following in this section also depend on the LET and hence on the kinetic

energy per nucleon of the ion. However, to keep the description of the formalism clear and simple, this dependency is not explicitly given in each equation.

In the LEM IV, the radial DSB distribution is calculated from the local dose d, the DSB enhancement factor η and the DSB yield of $\alpha_{\mathrm{DSB}} = 30$ DSB/Gy/nucleus, which is known from X-ray experiments:

$$K_{\mathrm{DSB}}(r) = d(r) \cdot \eta(d(r)) \cdot \alpha_{\mathrm{DSB}} \,. \tag{6.3}$$

The parameter $K_{\mathrm{DSB}}(r)$ can be understood as the total number of DSBs, which would be expected in a single cell nucleus if the whole nucleus was irradiated with the same local dose d as present at the radial distance r in the ion track. In Eq. (6.3) the the DSB enhancement η is included due additional DSBs due to large local doses in the ion track center. At this point, the DSB enhancement factor θ is added in the new LEM version. Therefore, both effects are combined to obtain the final DSB yield enhancement $\zeta(r)$ as shown in Eq. (6.4). This method ensures the independence of both effects as they both describe an enhancement of a DSB yield with regard to 30 DSB/Gy/nucleus as measured for X-rays:

$$\zeta(r) = 1 + [\eta(r) - 1] + [\theta_{\mathrm{local}}(r) - 1] \,. \tag{6.4}$$

The modified DSB density $\widetilde{K}_{DSB}(r)$ of the LEM V concept is finally obtained by Eq. (6.5):

$$\widetilde{K}_{\mathrm{DSB}}(r) = d(r) \cdot \zeta(r) \cdot \alpha_{\mathrm{DSB}} \,. \tag{6.5}$$

Compared to the formalism of LEM IV, the DSB enhancement factor $\eta(r)$ was replaced by the combined DSB enhancement factor $\zeta(r)$. The original dose profile, the modified profiles due to the two DSB enhancement components and the final dose profile are depicted in Fig. 6.2. The examples are given for ^{12}C ions for two energies. Note that η depends on the ion's LET in contrast to θ. In agreement with Fig. 6.1 the decreasing impact of θ_{local} with increasing radial distance is visible. Furthermore, the peaks of DSB enhancement as seen in 6.1 at large radii are not observed due to extremely small local doses at these radial distances to the ion track center.

After the calculation of the modified dose profile the number of DSBs is determined by MC methods in cylindrical shells around the ion track center. Afterwards, the calculation procedure of the LEM follows the same concept as for the LEM IV (see Sec. 2.3.2). Table 6.1 summarizes all parameters used in this section together with short descriptions.

Practical implementation in the LEM code: As a precise calculation of θ_{local} is time consuming, the values for θ_{local} were precalculated and stored in a look-up table. It contains pairs of radial distances to the ion track center and θ_{local} values for 63 ion energies between 0.01 and 8000 MeV/u. In the LEM calculation process an interpolation is performed between the ion energy as well as between the radii in order to find θ_{local} for the demanded ion energy and radius. As θ_{local} varies especially at very small and very large radii, the specific radii at which θ_{local} is given were chosen in an adaptive manner. This ensures a high resolution of the DSB enhancement values in critical areas. In total, for each ion energy, θ_{local} is provided at 100 radial distances. Notably all precalculated results of the DSB model introduced in the previous chapter are included in the θ_{local} values for these 63 ion energies and 100 radii.

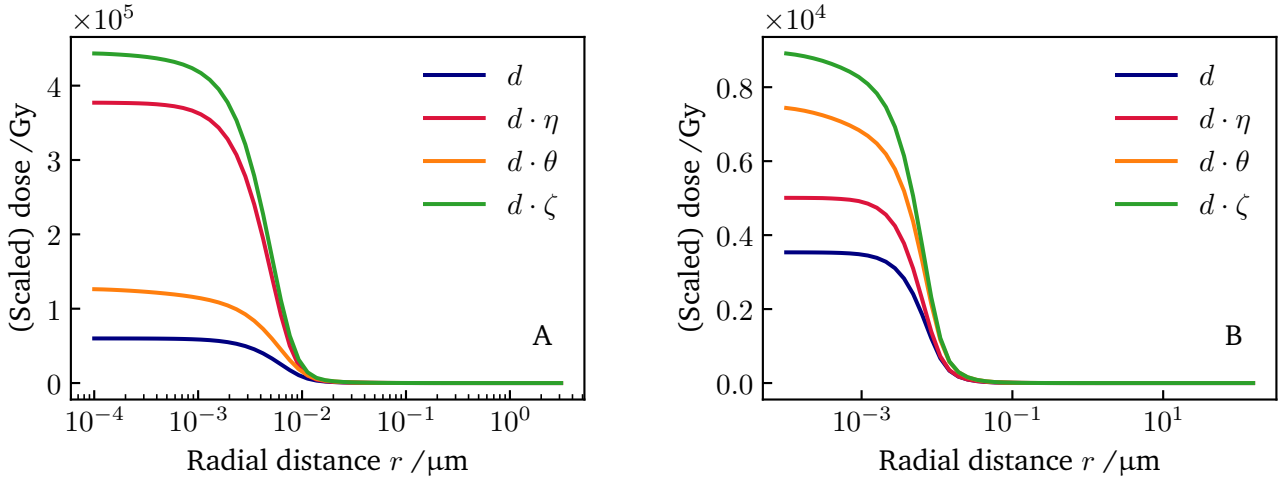

Fig. 6.2.: Modification of radial dose profile by DSB enhancement factors η and θ for carbon ions with kinetic energies of 10 MeV/u corresponding to 161 keV/µm (A) and 100 MeV/u corresponding to 26 keV/µm (B).

The inclusion of θ_{local} was implemented in the approximation method of the LEM. The corresponding implementation in the full simulation approach is still pending and beyond the scope of this work. Therefore, model adjustments were performed at three positions within the program:

- The formalism used to calculate the number of DSBs induced in the track structure inside the cell nucleus is adjusted. Therefore, the η-factor is replaced by the combined DSB enhancement ζ as shown in Eq. (6.5).

- If the radius of the ion track exceeds the radius of the cell nucleus, the contribution of the dose from outside the cell nucleus needs to be considered additionally. At these radial distances to the track center local doses are typically small such that η tends towards unity. The parameter θ_{local} is, however, independent of the local dose and is non-negligible at large track radii. Therefore, it is included by multiplication of the existing DSB probability with the mean DSB enhancement $\overline{\theta}_{\text{local}}$ outside the nuclear volume.

- For the determination of the LQ parameter of the ion curve β_{i}, the mean η-factor is included in the single particle approximation of LEM IV as described in Eq. (2.33). There, η is included as a mean ($\overline{\eta}$) over the whole ion track. In the new implementation, $\overline{\eta}$ is replaced by the combined mean DSB enhancement $\overline{\zeta}$. For the determination of the average DSB enhancement, the local dose as well as the area of the corresponding cylindrical ring around the ion track center are used as weights.

Compatibility of the new approach with LEM IV: In the LEM IV, the number of DSBs within the ion track is obtained directly from the local dose. Both, X-rays and ions, are assumed to induce the same number of DSBs per dose unit independent from the underlying secondary electron spectra. In the new approach, the probability for DSB induction is calculated according to the present secondary electron spectra. Therefore, the DSB enhancement is described as a relative increase/decrease of induced DSBs per dose compared to the DSBs produced by a secondary electron spectrum as present for X-rays (see Fig. 2.2). Compatibility of

Tab. 6.1.: Overview of the parameters used in the formalization of the LEM V together with their description.

Variable	Description
E_e	Secondary electron energy
LET	Linear energy transfer
r	Radial distance to ion track center
$RBE_\mathrm{DSB,local}$	RBE for DSB induction of electrons
α_DSB	DSB yield per Gy known from X-rays experiments (30 DSB/Gy/nucleus)
$d(r)$	Radial dose profile of ions based on amorphous track structure
$\eta(d)$	DSB yield enhancement due to conversion of SSBs to DSBs at large doses
$\theta_\mathrm{local}(r)$	DSB yield enhancement due to increased RBE of low-energetic electrons
$\zeta(r)$	Combined DSB yield enhancement of η and θ
$K_\mathrm{DSB}(r)$	Radial DSBs density as calculated in LEM IV
$\widetilde{K}_\mathrm{DSB}(r)$	Radial DSBs density as calculated in LEM V
$S_\mathrm{rad}(E_\mathrm{e}, r)$	Secondary electron energy spectrum

the new approach with LEM IV is thus given if the local DSB enhancement $\theta_\mathrm{local,X\text{-}rays}$ is equal to one if it is evaluated for a secondary electron spectrum initialized by X-rays in an equilibrium state $S_\mathrm{eq,X\text{-}rays}$:

$$\theta_\mathrm{local,X\text{-}rays} = \frac{\int S_\mathrm{eq,X\text{-}rays}(E_\mathrm{e}) \cdot LET(E_\mathrm{e}) \cdot RBE_\mathrm{DSB,local}(E_\mathrm{e})\, dE_\mathrm{e}}{\int S_\mathrm{eq,X\text{-}rays}(E_\mathrm{e}) \cdot LET(E_\mathrm{e})\, dE_\mathrm{e}}\,, \tag{6.6}$$

with the definition of the local RBE in Eq. (5.15) with X-rays as a reference radiation one obtains:

$$\theta_\mathrm{local,X\text{-}rays} = \frac{\int S_\mathrm{eq,X\text{-}rays}(E_\mathrm{e}) \cdot LET(E_\mathrm{e}) \cdot \frac{Y_\mathrm{l,DSB}(E_\mathrm{e})}{\overline{Y_\mathrm{l,DSB,X\text{-}rays}}} \cdot \frac{\overline{LET_\mathrm{X\text{-}rays}}}{LET(E_\mathrm{e})}\, dE_\mathrm{e}}{\int S_\mathrm{eq,X\text{-}rays}(E_\mathrm{e}) \cdot LET(E_\mathrm{e})\, dE_\mathrm{e}}\,. \tag{6.7}$$

Together with the definitions of the mean LET and the mean induced DSBs per path length in Eq. (5.16) and (5.17), respectively, one indeed finds:

$$\theta_\mathrm{local,X\text{-}rays} = \frac{\int LET(E_\mathrm{e}) \cdot S_\mathrm{eq,X\text{-}rays}(E_\mathrm{e})\, dE_\mathrm{e}}{\int Y_\mathrm{l,DSB,}(E_\mathrm{e}) \cdot S_\mathrm{eq,X\text{-}rays}(E_\mathrm{e})\, dE_\mathrm{e}} \cdot \frac{\int \left[LET(E_\mathrm{e}) \cdot S_\mathrm{eq,X\text{-}rays}(E_\mathrm{e}) \cdot \frac{Y_\mathrm{l,DSB,X\text{-}rays}}{LET(E_\mathrm{e})} \right] dE_\mathrm{e}}{\int S_\mathrm{eq,X\text{-}rays}(E_\mathrm{e}) \cdot LET(E_\mathrm{e})\, dE_\mathrm{e}} = 1\,. \tag{6.8}$$

As a result, the implementation of the newly introduced DSB enhancement factor θ in the existing LEM code has proven to be consistent with the formalism of LEM IV.

Determination of threshold dose D_t for LEM V: The threshold dose D_t describes the dose above which cell survival curves deviate from the typical LQ shape and re-transition to a purely linear shape. It is the only semi-empirical fit parameter of the LEM, which was adjusted accordingly for each new LEM version. Therefore, it is also newly optimized for the LEM version developed in this work. The parameter was optimized such that LEM predictions best fit RBE_α measurements with ^{12}C ions listed in the PIDE database. The RBE_α was chosen in order to be in line with the procedure followed for the determination of the D_t

formula for LEM IV. For the optimization of D_t the same mathematical structure as found for LEM IV was applied, which consists of an offset and a linear dependence on the $\alpha_\gamma/\beta_\gamma$ ratio of the photon survival curve:

$$D_t = x + y \cdot \frac{\alpha_\gamma}{\beta_\gamma} . \tag{6.9}$$

For the optimization of D_t, a χ^2-optimization is performed searching for the minimum of the function:

$$\Delta RBE = \sum_{i=1}^{n} \left(\frac{RBE_{\mathrm{PIDE,i}} - RBE_{\mathrm{Opt,i}}}{\Delta RBE_{\mathrm{PIDE,i}}} \right)^2 , \tag{6.10}$$

with $n = 244$ values for RBE_α measurements of the PIDE database. The parameter RBE_{PIDE} denotes the RBE value provided by the PIDE, $\Delta RBE_{\mathrm{PIDE}}$ the corresponding absolute error and RBE_{Opt} the RBE value predicted by the LEM, all for a specific combination of x and y. The values $x = 2.02 \pm 0.24$ Gy and $y = 0.91 \pm 0.02$ were found to lead to the best predictions for RBE_α. As D_t is a quantity connected to a relatively large uncertainty, for all following calculations x and y were rounded to $x = 2$ Gy and $y = 0.9$. Note that for the LEM IV, $x = 4$ Gy and $y = 1.1$ were found to lead to the best model predictions. After this calibration of D_t by coupling to the $\alpha_\gamma/\beta_\gamma$ ratio, D_t is no longer a "free" fit parameter.

Figure 6.3 shows the RBE_α predicted by the LEM V with the D_t formula of the previous LEM version and the new version of the D_t formula. Next to the predicted data, also measurement data from the PIDE database is depicted that was used to optimize the corresponding formula for the threshold dose D_t. The choice of D_t has no impact on very low LET values. At larger LETs the two options diverge whereas lower values of D_t, as optimized for LEM V, lead to a general decrease in predicted RBE values.

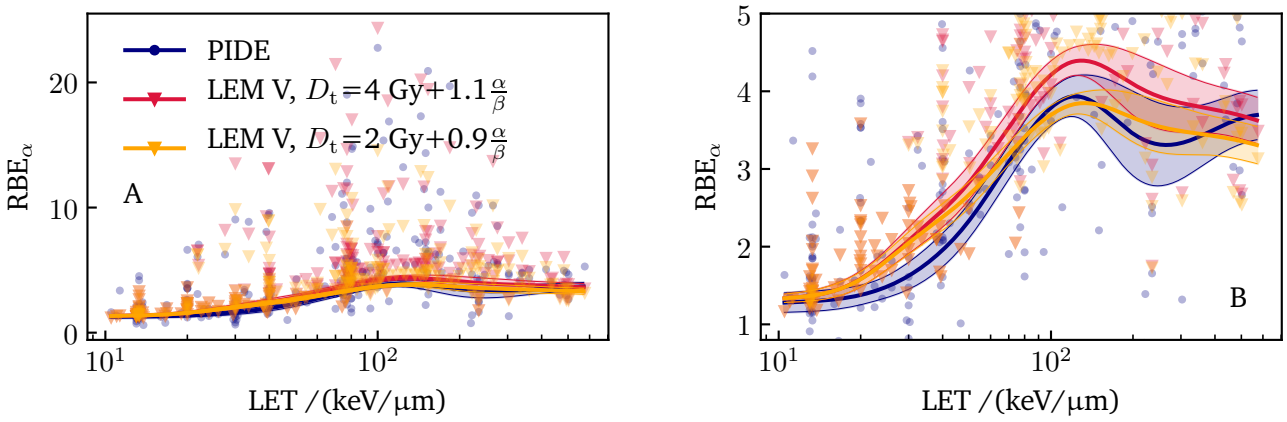

Fig. 6.3.: RBE_α as a function of LET for LEM V with the previous and newly optimized formula for D_t. Next to the two modeled curves, the measurement data of the PIDE database is shown that were used to find the optimal function of D_t. Panel B represents an enlargement of panel A to clarify the sensitivity of the model to the parameter choice. The solid lines represent running averages of the data points together with corresponding error bands indicating the standard error of the running averages.

Impact on mean DSB enhancement $\overline{\zeta}$: The dependence of the newly introduced DSB enhancement $\overline{\zeta}$ on the LET of an ion is shown in Fig. 6.4 for several ion species. Note that $\overline{\zeta}$ is calculated as a mean over

the full ion track and describes the combined DSB enhancement of the two enhancement factors $\overline{\eta}$ and $\overline{\theta}$ (see Eq. (6.4)). For LEM IV, no $\overline{\theta}$ exists and thus $\overline{\zeta} = \overline{\eta}$. For all ion species an increase of $\overline{\zeta}$ is seen with increasing LET. Comparing two LEM versions, the DSB enhancement is larger with the LEM V, which is the most pronounced at small LET values. Whereas the LEM IV tends towards unity at small LET values, LEM V predicts larger values for $\overline{\zeta}$, which better represents measurement data [167, 36]. A comparison of the DSB enhancement of LEM IV with predictions performed with the PARTRAC code can be found in [66].

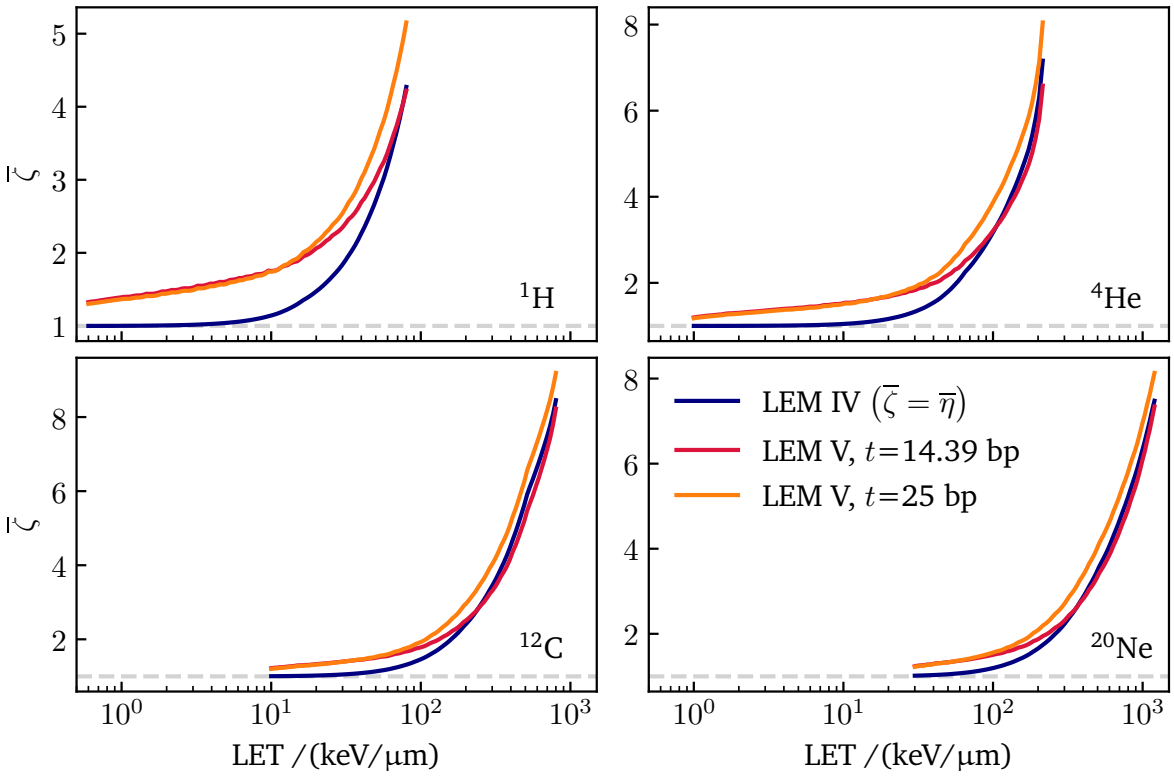

Fig. 6.4.: Mean DSB enhancement $\overline{\zeta}$ as a function of LET for several ion species. Note that for LEM IV $\overline{\zeta}$ is equal to $\overline{\eta}$. For model version V the results are shown with $t = 14.39$ bp and alternatively with $t = 25$ bp. The calculations are performed for ^{12}C ions and cells with the LQ parameters $\alpha_\gamma = 0.1\,\text{Gy}^{-1}$ and $\beta_\gamma = 0.3\,\text{Gy}^{-2}$.

Next to the LEM V calculation with a SSB threshold of 14.39 bp, a second approach for LEM V is shown. Here, the SSB threshold t is set to 25 bp, which corresponds to the parameter's default value within LEM IV. The parameter t plays a role for both DSB enhancement factors η and θ. While a larger value of t leads to a general increase of η, the change for θ depends on the radial distance to the ion track center. Larger values of t are connected to smaller values of κ and lead to a decrease of θ at small track distances and to an increase at larger distances. In total an increase of $\overline{\zeta}$ is observed for the larger SSB threshold of 25 bp. This reflects the fact that η is larger for larger values of t because of the increased probability for DSB production if a larger distance between SSBs is allowed as a maximum distance at which two SSBs can interact and form an additional DSB.

Impact on DSB distribution: The number of iDSBs, cDSBs and total DSBs are compared for LEM IV and V in Fig. 6.5 A-C exemplary for ^{12}C ions. For both model approaches the number of iDSBs increases with LET before it drops at large LET values. This drop is due to the gradual conversion of iDSBs to cDSBs

with increasing LET. Correspondingly, the number of cDSBs and total DSBs continually increases with LET. Fig. 6.5 D displays the dependence of the cluster index C (see Eq. (2.20)) on the LET for both model versions. At low to intermediate LET values C is slightly larger for LEM V in comparison to LEM IV. Figure 6.5 E and F clarify the relative change of the four aforementioned quantities. Most prominent is the increase of the total number of DSBs in low-intermediate LET ranges connected with an increase of the cluster index C.

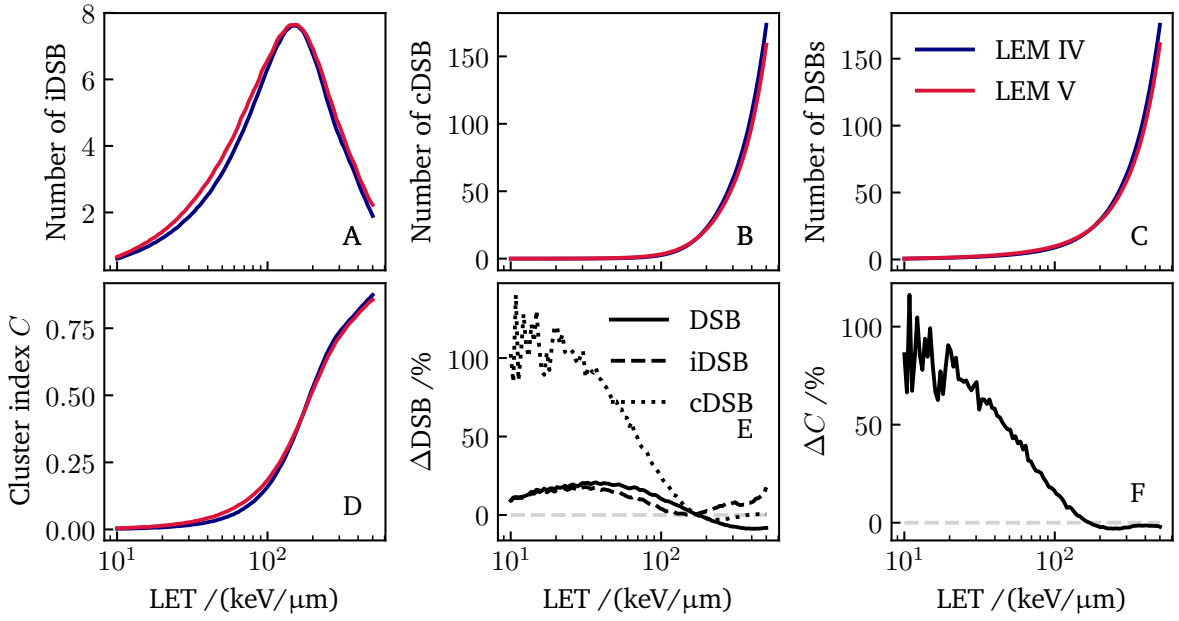

Fig. 6.5.: A-D: Amount of iDSBs, cDSBs, total number of DSBs and cluster index as a function of LET for model versions LEM IV (blue) and LEM V (red) for ^{12}C ions. E-F: Relative deviations of LEM V in comparison to LEM IV for quantities plotted in panel A-D. The calculations are performed for ^{12}C ions and cells with the LQ parameters $\alpha_\gamma = 0.1\,\mathrm{Gy}^{-1}$ and $\beta_\gamma = 0.3\,\mathrm{Gy}^{-2}$.

Impact on RBE prediction: The impact of the new model approach on RBE prediction is visualized in Fig. 6.6 for the RBE_α and the RBE at 10% cell survival level. For all displayed ion species (^{4}He, ^{12}C and ^{20}Ne) the general systematics are the same. At LET values smaller than ≈30-80 keV/µm the RBE is increased in the new model version in comparison to the previous one. This is due to the increased number of DSBs especially in form of cDSBs in that LET range. At larger LETs the RBE computed by the LEM V predicts smaller values compared to the previous model version. The RBE decreases slightly less pronounced for LEM V than for the LEM IV as visible for ^{12}C and ^{20}Ne ions in the overkill region. The relative changes in predicted values are more pronounced for the RBE_{10} than for the RBE_α for lower LET values and vice versa at larger LETs.

The stronger increase of RBE at low-LET values for LEM V is due to the influence of θ for the calculation of β_i in the approximation method of the LEM. Furthermore, a decrease of absolute values in the RBE maximum is observed while the corresponding LET values at which the maximum is found are similar for both model versions. Next to the LEM V calculation with a SSB threshold of 14.39 bp, again simulation results with an alternative values for the SSB threshold t of 25 bp is shown. In agreement of the parameter $\overline{\zeta}$ as a function of LET as depicted in Fig. 6.4 an increase of RBE is observed for the larger SSB threshold. This reflects the direct connection of the DSB enhancement $\overline{\zeta}$ on the predicted RBE value.

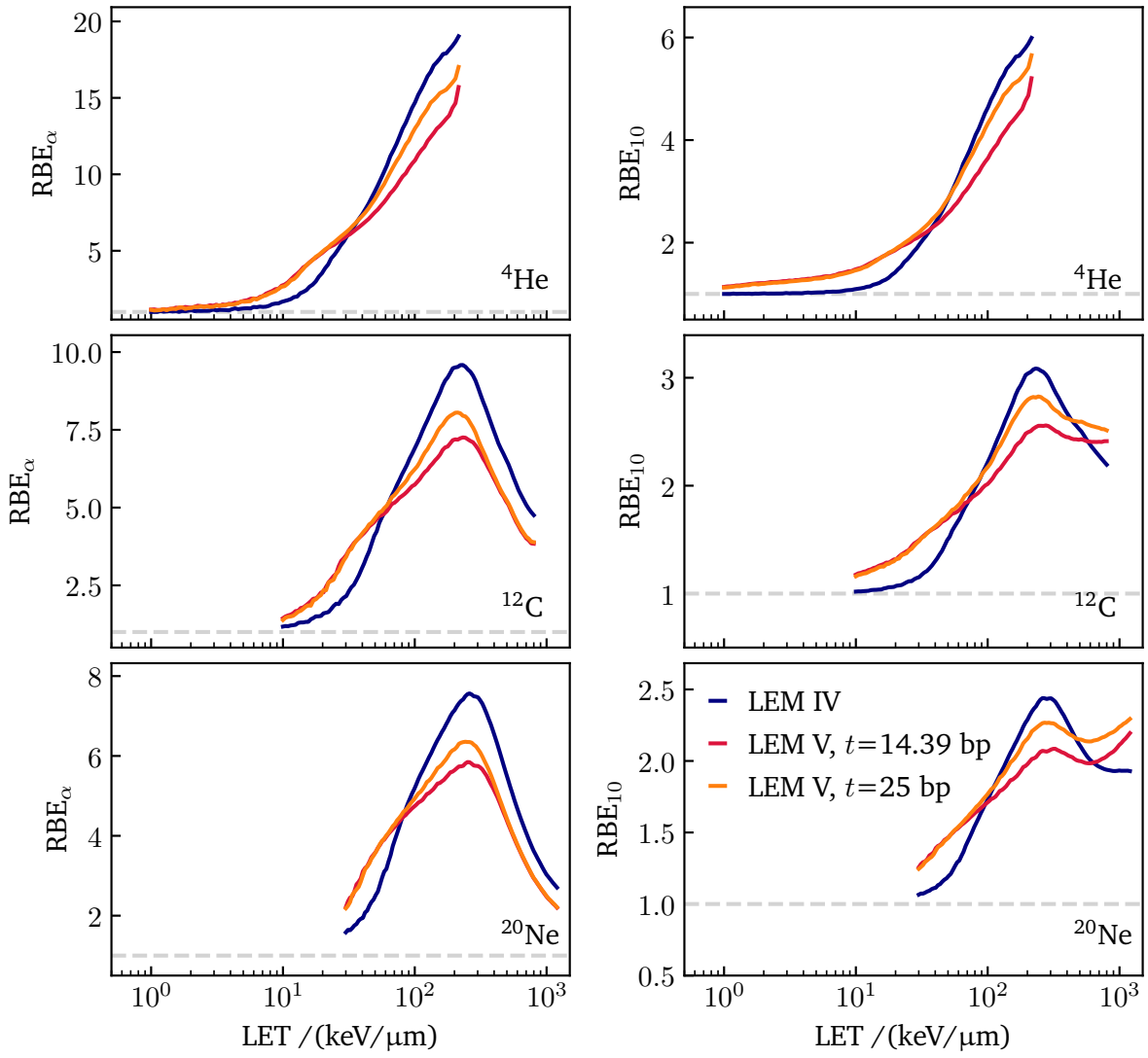

Fig. 6.6.: RBE as a function of LET for two cell survival levels and three different ion species calculated with the LEM IV and V. For model version V the results are shown with $t = 14.39$ bp and alternatively with $t = 25$ bp. The second value corresponds to the default of LEM IV. The calculations are performed for cells with the LQ parameters $\alpha_\gamma = 0.1\,\mathrm{Gy}^{-1}$ and $\beta_\gamma = 0.3\,\mathrm{Gy}^{-2}$.

6.1.2. LEM V validation with the PIDE database

In this section, the LEM V is validated by comparing model predictions to measurements provided by the PIDE database. The validation is performed complementary to the systematic analysis of LEM IV, which is presented in Chapter 4. The structure of the database and the validation procedure are introduced in Sec. 3.1. For the evaluation of the model accuracy the RBE is predicted for each cell survival experiment listed in the database. In Fig. 6.7, the predicted RBE is compared to the corresponding measured value for experimental data with ^{12}C ions.

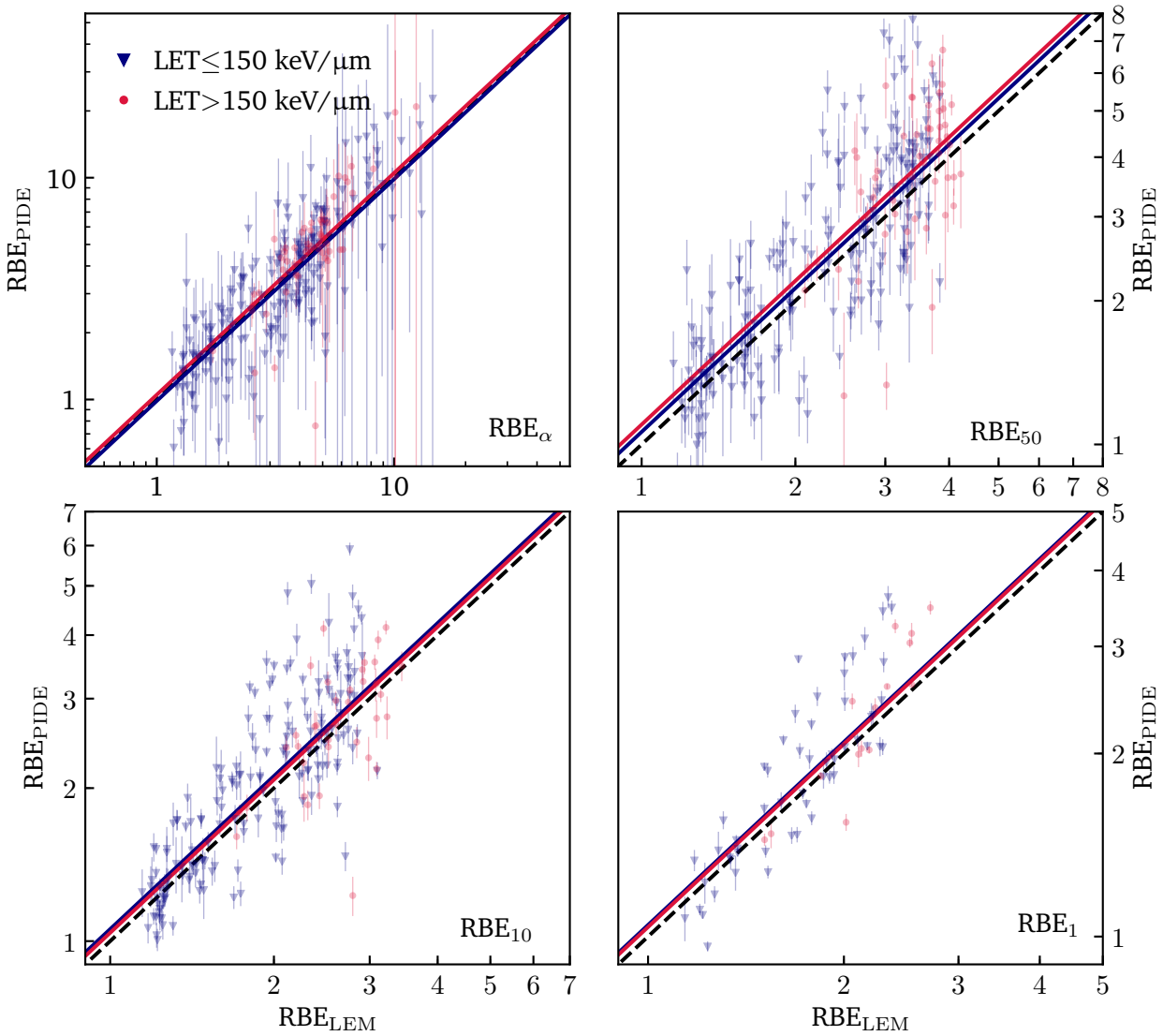

Fig. 6.7.: Scatter plot of RBE values measured (RBE$_{PIDE}$) and predicted (RBE$_{LEM}$) by the LEM V for ^{12}C ions at four different cell survival levels together with linear fits to the data. The error bars for the LEM V predictions are not displayed to keep the figure clear. For the calculations of the linear fits to the data the LEM errors are assumed to be in the same order as the PIDE errors and thus considered to be equal in a first approximation. The dashed line represents a 1:1 correspondence line, which facilitates the optical assessment of the model precision.

A direct comparison to Fig 4.1, which displays the analogous results for LEM IV, shows a clear improvement of the model accuracy with LEM V in comparison to LEM IV. The underestimation of RBE observed before for the subgroup of lower-LET experiments is reduced in the new model version. The slopes corresponding to the linear fit curves to the data in Fig. 6.7 are listed in Tab. 6.2 for the LEM IV and LEM V predictions. For LET values >150 keV/µm an overestimation of RBE was observed for LEM IV. In the newly implemented version of the model, this behavior transforms into a small underestimation of RBE. However, the absolute RBE deviations are smaller for LEM V with the only exception of RBE_{50}.

Tab. 6.2.: Slope with standard error for linear fits to data shown in the RBE-RBE scatter plot in Fig. 6.7. The values for LEM IV match the ones presented in Tab. 4.1.

		Fitted slope for			
LEM version	**LET range /(keV/µm)**	**RBE_{α}**	**RBE_{50}**	**RBE_{10}**	**RBE_{1}**
LEM IV	≤150	1.12 ± 0.03	1.16 ± 0.03	1.18 ± 0.02	1.19 ± 0.04
	>150	0.93 ± 0.04	0.96 ± 0.03	0.92 ± 0.03	0.94 ± 0.03
LEM V	≤150	0.99 ± 0.03	1.06 ± 0.03	1.06 ± 0.02	1.04 ± 0.03
	>150	1.05 ± 0.05	1.10 ± 0.04	1.04 ± 0.04	1.04 ± 0.03

In order to further investigate potential model deviations in dependence on the ion's LET, the RBE is plotted as a function of LET for several cell survival levels exemplary for ^{12}C ions in Fig. 6.8.

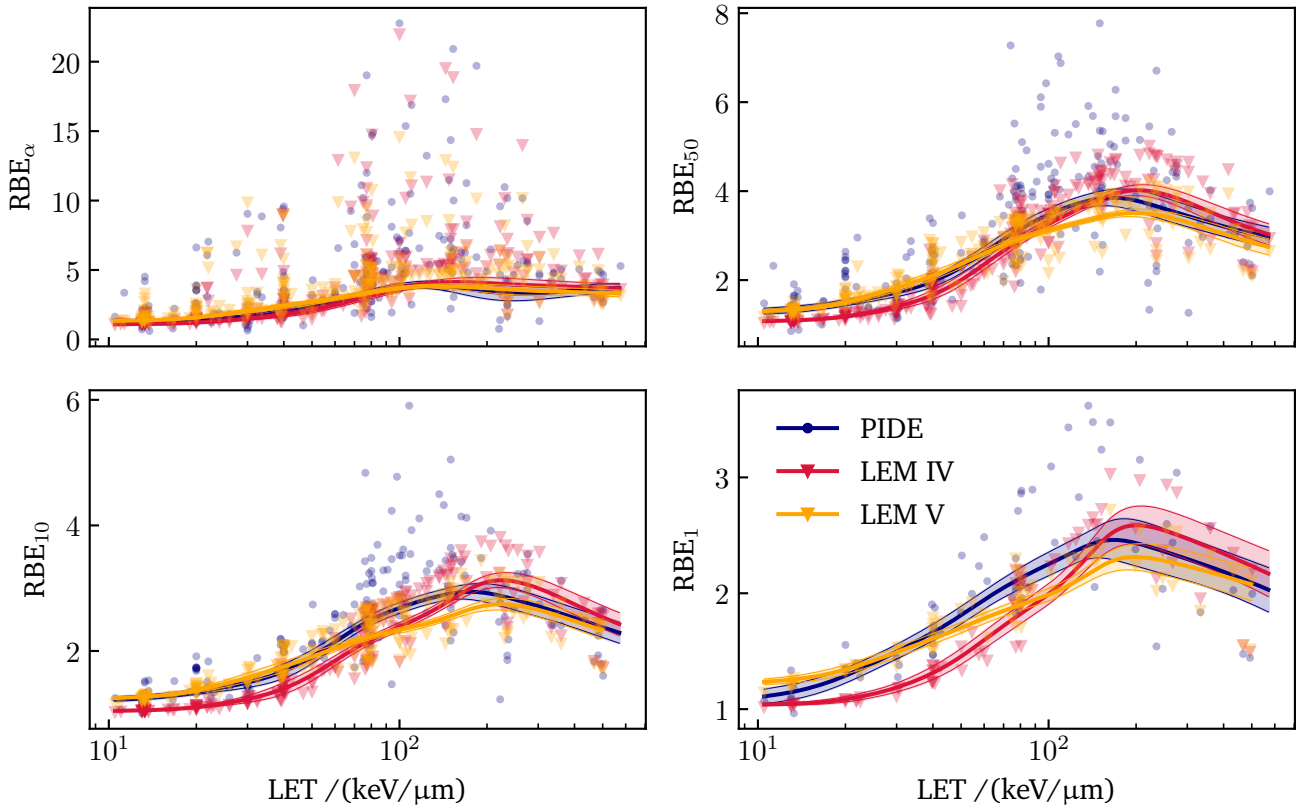

Fig. 6.8.: RBE as a function of LET for ^{12}C experiments listed in the PIDE as well as predicted by LEM IV and LEM V at four different effect levels. The solid lines represent running averages to the data points and the error bands indicate the corresponding standard errors.

The underestimation of RBE for low-LET values observed for LEM IV is decreased in LEM V, leading to a more precise prediction. At an LET value of ≈70 keV/µm the predictions of both model versions cross each other; Therefore, in an intermediate LET region between 70 keV/µm and 200 keV/µm still an underestimation of RBE is observed with the new model version. At larger LETs the model predictions of LEM V show a higher precision compared to predictions by LEM IV. The position of the RBE maximum is found at the same LET values for both model versions, however, absolute values of the RBE maximum are slightly smaller for LEM V. The dependencies shown in Fig. 6.8 are plotted for several different ion species at a cell survival level of 10% in Fig. 6.9.

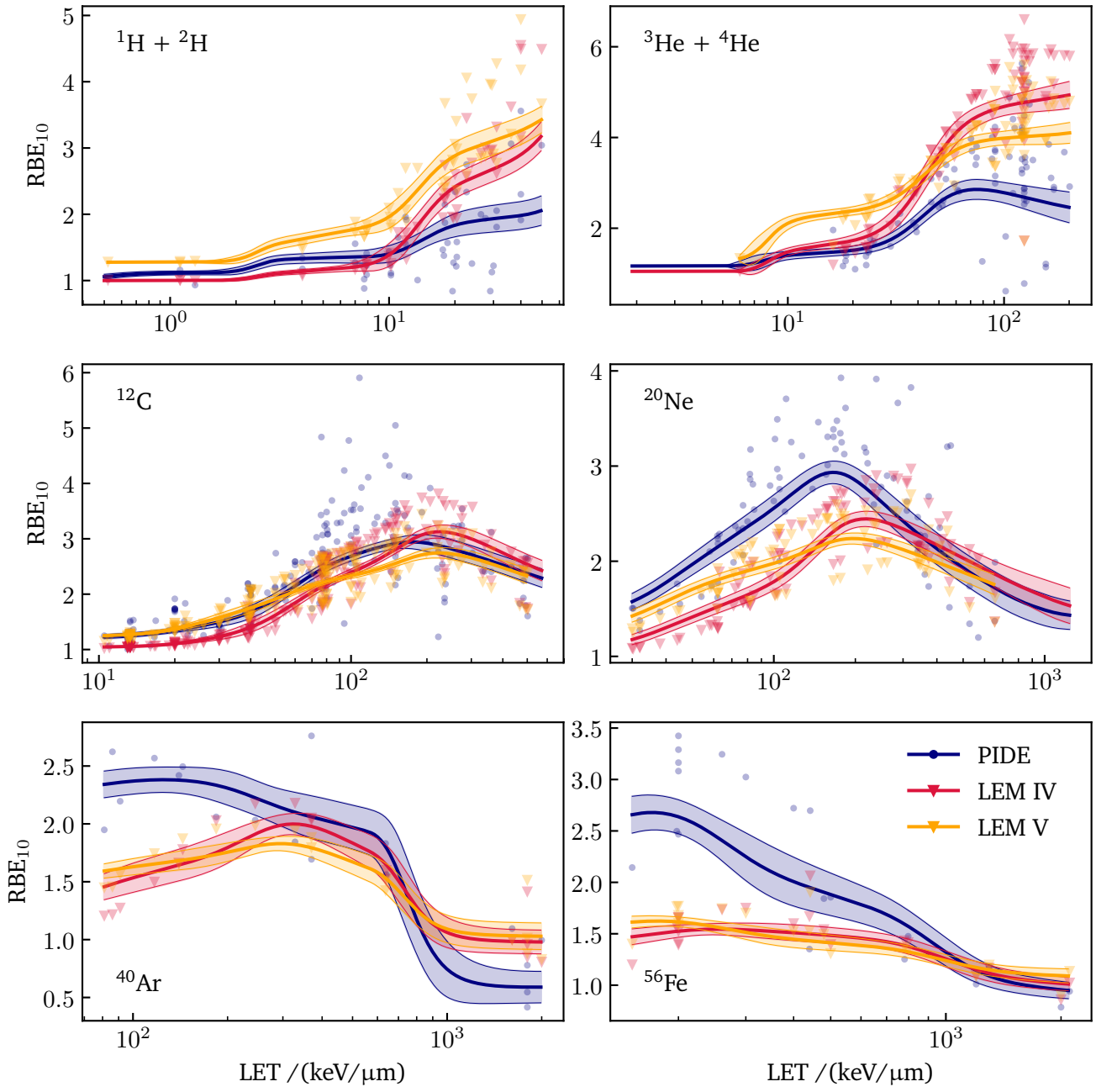

Fig. 6.9.: RBE as a function of LET for several ions listed in the PIDE as well as predicted by the LEM IV and LEM V at a cell survival level of 10%.

The general behavior observed for ^{12}C for the new model approach is also found for all other considered ion species. The predicted RBE values are increased in the low-LET range in comparison to LEM IV predictions. This leads to an overestimation of RBE for H and He ions in that LET area. However, it should be noted that for protons at an LET of ≈15 keV/µm corresponds to an energy of ≈2 MeV at which track segment conditions are not necessarily provided. However, they are assumed in the LEM, which might lead to remaining deviations in the RBE prediction. Additional uncertainties in the measurement data might be due to an enhanced usage of passive measurement techniques, which result in the presence of a fragment spectrum and therefore no "clean" experiment conditions. The strong initial rise observed in the running average for RBE predictions for helium for LET values between 5 and 20 keV/µm is most probably artificial and due to a lack of data in that LET region leading to large uncertainties in the running average. For heavier ions, the increased RBE values in the low-LET range lead to more precise predictions for LEM V in comparison to LEM IV. The crossing of the predicted RBE curves of LEM IV and LEM V is found at relative intermediate LET values, whose absolute values increase with increasing atomic number of the considered ion species. Directly beyond the RBE maximum, LEM V predicts decreased RBE values, which matches measurements for H, He, ^{12}C and ^{20}Ne. For heavier ions, however, this leads to a slightly enhanced underestimation in comparison to LEM IV. At even larger LET values as can be reached by heavier ions, the predicted RBE curves show a second intersection point after which LEM V predicts again slightly larger RBE values than LEM IV.

For each PIDE experiment the relative deviation of the predicted RBE in comparison to the measured value is calculated with the concept presented in Fig. 3.1 in the methods section. The relative model deviations were investigated in dependence on the LET and survival level exemplary for ^{12}C ions as shown in Fig. 6.10.

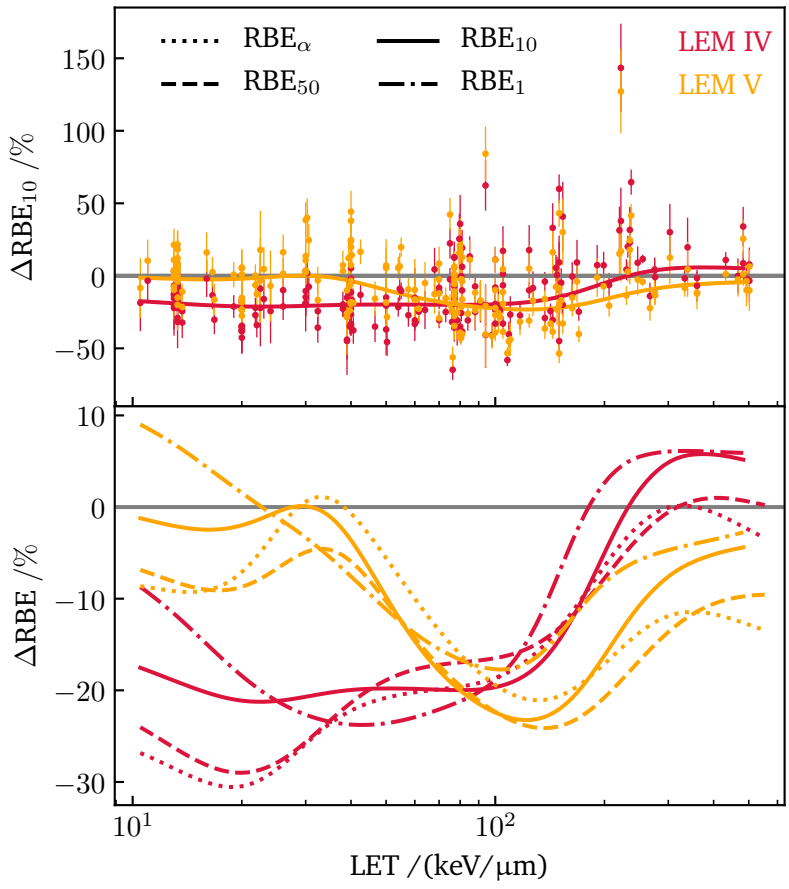

Fig. 6.10.: Relative deviations in RBE as a function of LET for ^{12}C as predicted by the LEM IV (red) and V (orange) compared to measurements listed in the PIDE database for several survival levels.

The top panel shows the relative model deviations for the RBE at 10% cell survival level. At LET values <70 kev/µm a clear improvement of the new model approach is visible due to a reduction of the model deviations. At intermediate LET values, the underestimation of the LEM remains at ≈-20% while at larger LETs the model accuracy increases again. However, for LET values >70 kev/µm a large scatter of measurement data is visible. In the bottom panel of Fig. 6.10 the running averages of the relative model deviations for PIDE experiments with ^{12}C ions are depicted for several cell survival levels. In general, it is found that for LET values <100 keV/µm model predictions are improved, whereas for higher LET values the model deviations are slightly larger for LEM V. Model deviations are smallest for an RBE at 1% cell survival.

The model deviations as presented in Fig. 6.10 for ^{12}C ions are displayed in Fig. 6.11 for several ion species exemplary for the RBE_{10}. For H and He ions an underestimation of RBE is observed for LEM IV, which switches to an overestimation for LEM V. At larger LET values as reached by He ions, the overestimation of RBE is reduced for LEM V in comparison to LEM IV predictions. However, it should be noted that in certain LET ranges fewer data points are available leading to a larger uncertainty of the running average (c.f. Fig. 6.9 for specific data points). For ions as ^{12}C and heavier an increased model accuracy is observed at small LET values for LEM V. In contrast to that, the RBE predictions are less affected by the model version at larger LETs.

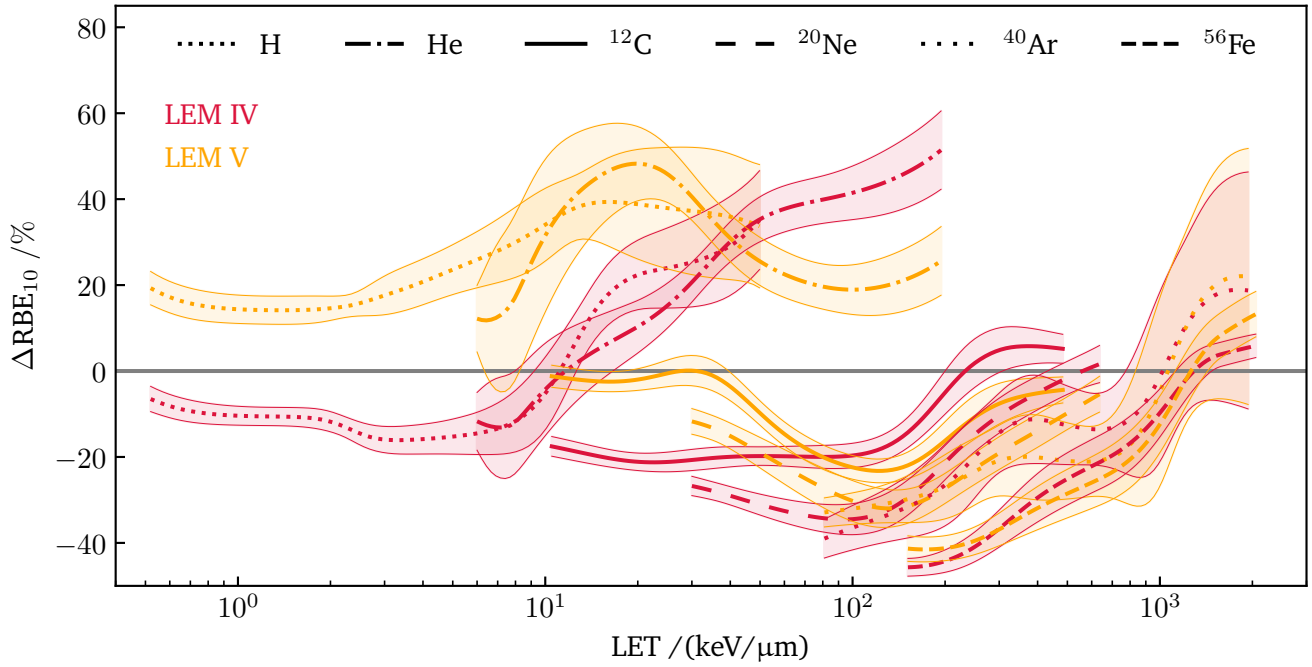

Fig. 6.11.: Relative deviations in model predictions for the RBE_{10} for several ions as a function of LET. The running averages for LEM IV and LEM V are shown in red and orange, respectively.

6.2. Discussion

In the previous section, the LEM implementation of the DSB induction model, which was derived in Chapter 5, is described. Afterwards the new model version LEM V was systematically validated and compared to LEM IV. In the following sections the corresponding results are discussed.

6.2.1. DSB enhancement in the LEM framework

The DSB amplification factor θ developed in this work is calculated by Eq. (6.1) as a mean RBE of an LET-weighted electron energy spectrum. In the following, several aspects concerning the determination of θ are discussed.

Secondary electron energy spectra: In this work, the radial secondary electron spectra applied for the determination of θ are calculated by the Kiefer-GSI model, which is described in Sec. 3.3 [56]. Even if the model includes several simplifications, such as the neglect of elastic scattering, its model predictions of radial electron energy spectra match well with corresponding spectra calculated with the MC radiation transport code Geant4-DNA. The direct comparison of both approaches is depicted in Fig. 3.13 in the methods section. Only at electron energies $<$100 eV a clear deviation between both methods is visible due to larger electron yields for the MC method for low-energetic electrons. However, electron interaction cross sections in this energy regime are sparse and subject to large uncertainties [50], which makes the assessment of the precision of both approaches difficult. Other methods exist for the description of radial electron spectra, as e.g. the model of Cucinotta et al. [123]. This approach is based on the description of the radial dose used in the Katz model as described in Sec. 2.3.1 and 2.1.4 [168]. It does not include the angular dependence on electron transmission, however, the general shape of the obtained radial electron energy spectra of Cucinotta et al. agrees well with the results of the Kiefer-GSI spectra used in this work [123, 39, 56].

Radial RBE model by Cucinotta et al.: The concept of amorphous track structure was successfully applied to describe dose depositions of secondary electrons in several biophysical models for predicting ion radiation effects beginning with the Katz model in 1967 [13, 14] or the LEM developed in the 1990s [122, 10]. However, several authors noted in [63, 123, 39] that the pure consideration of an amorphous track structure in radiobiological models could lead to the neglect of substantial physical effects. Thus, Cucinotta et al. propose the explicit inclusion of radial secondary electron spectra in the determination of physical or biological properties within the ion track. This approach even led to the first description of the mean electron RBE with radial distance to the ion track center in a similar manner as introduced in this work [39]. However, their approach differs in several points: First, Cucinotta et al. use a different description for the secondary electron spectra as described in the paragraph above. Second, they consider a different approach for the electron RBE through the frequency of energy depositions above 120 eV of full electron tracks leading to a dose of 1 Gy in a volume of a cell nucleus as discussed in Sec. 5.2.4 [121]. Thus, within the terminology of this thesis, the RBE of Cucinotta et al. is understood as an integral RBE, whereas in the present work, the local RBE is used for the determination of the mean RBE within an ion track. As the electron RBE over the track radius of an ion is rather a side product of Cucinotta's publication, their description of the function is kept short [39]. Therefore, it cannot clearly be assessed whether the electrons' LET is included in the calculation of the mean RBE (as done in this work) or not. The model by Cucinotta et al., however, shows the same characteristic features of the dependence of the mean electron RBE on the

radial distance to the ion track center. After an initial increase of RBE at small track radii, the RBE decreases again. At the edge of the ion track, both models predict a second increase of RBE due to the enhanced presence of highly-effective low-energetic electrons at these radial distances.

Fraction of dose delivered by secondary electrons: As discussed in Sec. 5.2.6 the fraction of total dose delivered by secondary electrons may differ considerably for different primary radiation species. For ions, this effect potentially plays a role in the core of the ion's track structure. Chatterjee included this effect in his amorphous track structure model by a dose "cap" in the track core, as described in Sec. 2.1.4 [58]. However, the applied equipartition model used to split the LET contributions equally in the core and penumbra region has proven to be insufficient and imaginative [37, 39]. In the LEM, a flat dose profile is assumed in a defined track core. As measurement data of dose profiles at such small radial distances are hardly feasible, the determination of the most precise modeling approach is difficult [57]. Thus, it is subject to further investigations to elaborate if the above described characteristics of energy transfer should be considered specifically in the LEM concept. This is of interest as ζ is defined as a DSB enhancement due to physical characteristics of secondary electrons. Thus, when the dose profile is weighted by ζ, strictly speaking, only the secondary electron dose should be included in the weighting process. As a result, the DSB enhancement ζ would need to be scaled down accordingly in the track core. Thus, an on average smaller DSB enhancement would be expected leading to a decreased RBE prediction. However, this could probably be partly compensated by larger values of the threshold dose D_{t}.

6.2.2. Impact of reference radiation species for RBE determination

The RBE of an ion is defined as the enhanced biological effectiveness in comparison to a reference radiation species. In radiobiological experiments several different photon sources are employed as a reference such as 250 kVp X-rays or γ-radiation originating from the decay of ^{60}Co. Their different effectiveness in DSB induction is shown in Sec. 5.1.5 and discussed in Sec. 5.2.5. In the LEM, the DSB yield enhancement factor ζ is defined as an enhancement with regard to the DSB yield for X-rays. This specific reference radiation species was chosen as it is predominantly used in radiobiological experiments and indirectly implemented in the LEM by setting the default parameters for the DSB and SSB yield accordingly. If a different radiation species than X-rays is requested, θ and η can be recalculated. As a result, the newly introduced modeling concept can be easily adjusted to alternative reference radiation species. Thus, RBE predictions for ions can be more individualized including the specific reference radiation chosen by the experimenter of a radiobiological measurement.

6.2.3. Comparison to previous LEM versions

After the successful termination of the carbon ion clinical trial at GSI, carbon ions were applied in several ion therapy centers e.g. in Heidelberg at HIT, in Marburg at MIT, in Pavia at CNAO or at the Shanghai Proton and Heavy Ion Center. Those cancer therapy centers use the initial implementation of the LEM (LEM I) for RBE determination during treatment planning. Over the years the LEM was constantly validated and revised leading to several model versions as summarized in Tab. 2.1. The latest version LEM IV was implemented into research-oriented treatment planning systems and other RBE modeling platforms [169, 170] but is not used in clinical practice. Comparisons of different model versions revealed that the LEM I predicts larger RBE values at lower LETs compared to LEM IV and vice-versa at larger LETs [60, 65, 12]. Thereby, LEM IV was found to better reproduce experimental data, especially in the critical high-LET region. The clinical

application of LEM I follows a more conservative approach as it leads to the delivery of an under-dosage in the entrance channel whereas LEM IV would potentially lead to an over-dosage. Furthermore, the application of LEM IV in treatment planning would lead to a decrease of the physical dose at the border of the target volume due to increased RBE values at the distal edge of the SOBP where high LET values are present [169]. In the center of the target volume the usage of LEM IV would lead to an increase of the physical dose. The application of LEM V seems to be promising in this regard as it shows an improved RBE predictions for low-LET ions as present in the entrance channel. However, the detailed characteristics of the new model in clinical applications need to be further investigated.

Model validation by comparison of predictions to in-vitro measurement data is a major step in the testing chain of an RBE model. However, in-vitro cell survival measurements differ from the radiation response of complex tissues or tumors. This is due to additional biological environment factors, which cannot be simply imitated in in-vitro experiments such as nutrition or oxygen supply [171]. Therefore, in order to reflect a more realistic tumor irradiation scenario, model comparisons to experimental in-vivo animal data are essential. First pre-clinical comparisons of the LEM predictions to in-vivo data were performed for the skin of minipigs irradiated with ^{12}C ions [172]. Later on, further model comparisons were performed investigating the normal tissue complication probability for the rat spinal chord [173, 22, 23, 24]. These systematic studies confirm the findings reported for the model comparison to in-vitro data. The LEM IV leads to an improved RBE prediction, especially in the crucial high-LET region in comparison to LEM I. However, in the low-LET region still a substantial underestimation of RBE was observed. First comparison of LEM V to the above mentioned in-vivo data revealed that the new model approach leads to a clearly improved model prediction of the LEM in the low-LET region.

Alternatively to the LEM, the MKM is used clinically, predominantly in Japanese cancer treatment facilities [15, 16, 17, 18]. Its simulation approach is described in Sec. 2.3.3. First comparisons of MKM with LEM I and LEM IV revealed that RBE predictions of MKM follow a similar shape as LEM IV [104, 174, 170]. In a published comparison for ^{12}C ions, the RBE predictions of the MKM match the presented experimental data slightly better. This is due to the tendency of LEM IV to underestimate the RBE of low-LET ions. As the LEM V solves this characteristic a comparison of the new model with the MKM is of great interest. However, model comparisons to single measurement sets potentially do not cover the whole characteristic of the measured property. The investigations in this work prove the large scatter of measurement data even for experiments performed under the same conditions as the same radiation quality, same cell line or even the same lab. Thus, a comparison of the LEM V and the MKM on the basis of a large experiment database as the PIDE is highly desirable in order to clearly determine strengths and weaknesses of each model. Note that both, the LEM and the MKM, use the photon LQ parameters as a model input. The MKM additionally requires the size of certain target domains, which can be understood as subunits of the cell nucleus.

6.2.4. Minimum RBE at large ion doses

Model approaches such as the theory of dual radiation action (TDRA) predict that high-LET radiation leads to an increase of the LQ parameter α in comparison to the corresponding parameter for photon radiation [63]. The LQ parameter β is, however, assumed to be independent of the radiation quality. This leads to the fact that the RBE is predicted to tend towards unity at large doses as the photon and ion survival curves run parallel to each other. The MKM, which is used in carbon ion therapy facilities in Japan, also makes the assumption that $\beta_{\mathrm{i}} = \beta_{\gamma}$ [16, 18, 170] and, thus, leads to the same RBE characteristics at large doses. Experimental data shows a contrasting behavior reporting RBE values, which clearly exceed unity in the discussed dose range. Therefore, other model approaches such as the concept of the $\mathrm{RBE}_{\mathrm{min}}$ were proposed [175]. The term $\mathrm{RBE}_{\mathrm{min}}$, represents the lower limit to which RBE tends at high doses per fraction

and is thus a saturation value. A method proposed by Carabe-Fernandez et al. enables the calculation of RBE values based on the assumption that both, α_{i} and β_{i} depend on LET. Two intrinsic parameters $\mathrm{RBE}_{\mathrm{min}}$ and $\mathrm{RBE}_{\mathrm{max}}$ are introduced for every cell line that refer to the minimum and maximum RBE that can possibly be obtained, respectively. They demonstrated that the inclusion of $\mathrm{RBE}_{\mathrm{min}}$ in their formulation for the calculation of RBE leads to an improved model accuracy [175]. However, it should be noted that the approach by Carabe-Fernandez et al. and other "linear" LET models can be understood as empirical parameterizations of the LQ model. This contrasts with the approaches of the LEM or the MKM, which perform real predictions of the effect after ion irradiation.

The inclusion of the DSB induction model within the LEM framework was implemented in the approximation method of the model. Thereby, the LQ parameter β_{i} of the ion survival curve is determined through a relation of the final slopes of the ion and photon cell survival curves as described in Sec. 2.3.2. For a single ion hit, the effect after ion radiation is always at least as large as the effect after the same dose delivered by photons as a consequence of the inhomogeneous dose distribution in ion tracks. The threshold dose D_{t} is assumed to be equal for both radiation species. As a result, both, the photon and ion cell survival curves run parallel at doses larger than D_{t} leading to the effect that the RBE tends towards unity at large doses as discussed in the paragraph above. Therefore, in the LEM IV, the η-factor is included in the formalism for ions as given in Eq. (2.33). Thus, the RBE asymptotically approaches $\overline{\eta}$ at large doses in that model version. However, in the low-LET region local doses are generally small leading to small mean DSB enhancements $\overline{\eta}$ in that LET range. Thus, also by inclusion of η in the calculation of the final slope of the ion cell survival curve, RBE values do not strongly exceed a value of 1 in the low-LET range for large doses. This behavior can be seen for small cell survival levels (=large doses) as present for the RBE_1 in Fig. 4.2 and Fig. 4.3 for the validation of LEM IV. In experiments, however, an RBE >1 is observed for ions with low LET values for several biological endpoints, in-vitro and in-vivo [22, 24].

In the new model version LEM V derived in this work not only the DSB enhancement η is considered for the determination of the LQ parameter β_{i}. Additionally, the DSB enhancement θ is taken into account, leading to the following relation of the final slopes s_{max} of the ion and photon cell survival curves:

$$\overline{\zeta} \cdot s_{\mathrm{max},\gamma} = s_{\mathrm{max,i}} \,, \tag{6.11}$$

whereas $\overline{\zeta}$ describes the mean combined DSB enhancement of η and θ as calculated by Eq. (6.4). As $\overline{\theta}$ clearly exceeds unity also for low-LET values, an RBE>1 is predicted with the new model approach in the corresponding LET and high dose regime as visible from the RBE_1 in Fig. 6.6, Fig. 6.8 and Fig. 6.9. The impact of the new model approach is further clarified in Fig. 6.12 where the RBE is plotted as a function of ion dose for both model versions. The calculations are performed for ^{12}C ions at an LET of 16 keV/µm for in-vitro as well as in-vivo experimental conditions as expressed by different photon LQ parameters. The figure clearly demonstrates the prediction of RBE values greater than unity even at large doses with the new model approach, which better reflects measurement data in comparison to predictions by LEM IV [22, 23, 24, 175]. Note that for the in-vivo calculation the value of the threshold dose was adjusted by $D_{\mathrm{t,in\text{-}vivo}} = 3.5 \cdot D_{\mathrm{t,in\text{-}vitro}}$. At ion doses exceeding D_{t} a slight increase of the RBE is visible for LEM V. This is probably due to the need of the inclusion of θ in manual RBE calculations and is subject to future research.

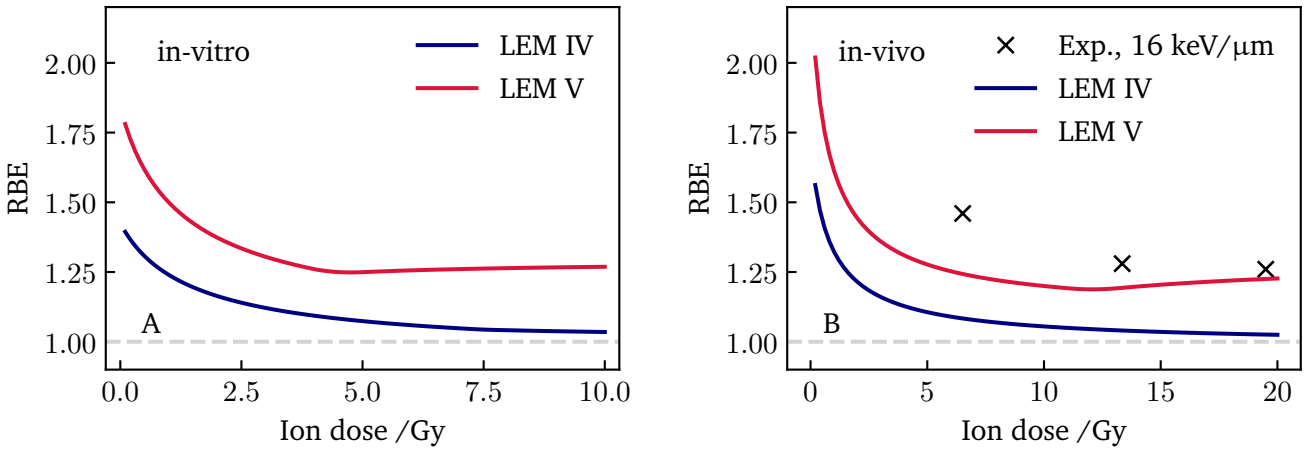

Fig. 6.12.: RBE as a function of dose calculated with the LEM IV and V. The RBE is evaluated for ^{12}C ions with an LET of 16 keV/µm in-vitro ($\alpha_\gamma = 0.1\,\mathrm{Gy}^{-1}$ and $\beta_\gamma = 0.03\,\mathrm{Gy}^{-2}$) and in-vivo ($\alpha_\gamma = 0.003\,\mathrm{Gy}^{-1}$ and $\beta_\gamma = 0.0015\,\mathrm{Gy}^{-2}$) in panel A and B, respectively. The experimental data shown in panel B is taken from [22, 23, 24].

6.3. Conclusion

In the preceding chapter the previously derived DSB induction model was applied to predict the effectiveness of ions based on their secondary electron spectra. As these vary considerably with the radial distance to the ion track center, the DSB enhancement θ was determined as a corresponding radius-dependent function. The DSB enhancement θ initially decreases with increasing radial distance and then increases again at large radii due to the enhanced occurrence of low-energetic highly-effective electrons at the edge of the ion track. The measurement of these peaks at large radial distances is, however, not feasible due to extremely small local doses, which lead to a small overall probability for DSB induction.

The application of the radial DSB enhancement in an ion track within the LEM framework led to more precise RBE predictions compared to previous model versions. This is especially pronounced in the critical low-LET region where the LEM IV predicts RBE values that tend towards unity. LEM V is able to reproduce the enhanced RBE above unity in the corresponding LET region and thus leads to a greater agreement with measurement data. These findings highlight that for an accurate RBE predictions not only effects need to be considered that occur at large local doses as described in the LEM with the η-factor since model version II. Additionally, for an accurate effect prediction the variable effectiveness of single secondary electrons need to be taken into account in dependence of their kinetic energy through the θ-factor. These two mechanistic concepts of lesion interaction on the nanometer scale occur alongside with the interaction of separate DSBs on the micrometer scale.

7. Final conclusions and outlook

The systematic model validation with the PIDE database enabled a quantification of the RBE underestimation of the LEM IV at high ion energies. This validation was the first of its kind, evaluating an RBE model with a comprehensive database including ion species ranging from protons to iron ions in a large energy range and for several cell types of different radiosensitivities. The model deviations could be traced back to a simplifying model assumption that photons and ions induce the same number of DSBs per local dose unit, which refers to local energy depositions in nanometer-sized volumes. Whereas the induction and interaction of lesions in the DNA on a micrometer scale is well characterized, its relevance on the nanometer scale is not completely understood, yet. Consequently, in this work, a mechanistic model was derived, which enables the assessment of the effectiveness of different radiation species on the nanometer scale. Thereby, the probability for DSB induction is solely determined from the probability of secondary electrons to induce localized ionization clusters. In contrast to most alternative biophysical models, this mechanistic concept does not rely on an explicit simulation of localized energy depositions in the radiation track or a detailed representation of the structural organization of DNA.

A major outcome of this work results from the universal applicability of the above mentioned electron DSB induction model as it can be applied to determine the effectiveness of any primary radiation species. This is possible since the majority of DSBs is induced not directly by the primary radiation species but rather by their secondary electrons. Even though the model was originally developed to predict DSB induction in ion tracks, it has proven to be also applicable to any other radiation species. For instance, the model was successfully applied to predict the increased effectiveness of X-rays in comparison to ^{60}Co radiation as observed in experiments. In future works, the DSB induction model could be further applied to assess the effectiveness of any other photon radiation species based on their secondary electron spectra. Thereby, mammography X-rays with kinetic energies of a few tens of keV are of special interest. In the epidemiological risk assessment of breast examinations their effectiveness is typically assumed to be equal to high-energetic photons. Due to lack of data, the ICRP officially recommends a radiation weighting factor for photons and electrons of unity [162]. This work demonstrates the clear dependence of the DSB induction effectiveness on the type and kinetic energy of the considered radiation species and enables a corresponding quantification.

The inclusion of the DSB induction model in the existing LEM framework led to a new model version LEM V, which shows an increased model accuracy in the critical low-LET (=high energy) regime. This is associated with the inclusion of an additional DSB enhancement effect that is quantified by the parameter θ in this work. It describes the mean effectiveness for DSB induction due to the enhanced effectiveness of low-energetic electrons and occurs independent but alongside of the η-factor. The η-factor accounts for the formation of additional DSBs as a result of the interaction of independent SSBs at large local doses. Thus, the inclusion of both mechanistic concepts of lesion interaction on the nanometer scale, which occur alongside the interactions of separate DSBs on the micrometer scale, proves to be essential for an accurate effect prediction.

In comparison to LEM I, LEM IV already led to a major improvement of the accuracy of RBE predictions in the low-energy range. However, it still shows an underestimation of RBE at high ion energies, predicting

RBE values of $\approx$1. The new model version LEM V led to more precise RBE predictions in this energy regime especially for carbon ions. Thus, the introduction of the θ-factor allows for a first mechanistic explanation for the enhanced RBE values observed in measurements with high-energetic ions, which clearly exceed unity. Accordingly, even high energetic ions liberate highly effective electrons, which lead to a DSB enhancement in the ion track core and thus to an enhanced effectiveness in comparison to photon radiation. This effect could not be explained consistently before. Next to this LET-dependent model improvement, an equivalent dose-dependent improvement is observed. If the RBE is investigated as a function of dose, the LEM IV tends towards unity at large doses and small LET values. The same behavior is found for other RBE models as the MKM, which is applied clinically in Japan. However, for instance in-vivo experiments on the dose tolerance of the rat spinal chord show RBE values clearly exceeding unity even at large ion doses, which could be first reproduced with the LEM V. This is due to the dose-independence of the DSB enhancement factor θ. Thus, the new LEM version solved several open issues of previous LEM versions and provides a mechanistic explanation of observed effects.

Finally, subsequent model tests are necessary to assess the model's suitability for clinical applications. A detailed comparison to in-vivo experimental data and the examination of the new concept in research-based treatment planning systems are foreseen. With the LEM, IV a potential over-dosage is expected in the healthy tissue in the entrance channel of the ion beam. In contrast to that, the LEM I overestimates the RBE in this energy regime leading to a potential under-dosage. Thus, the clinical application of the LEM I can be seen as a more conservative approach. As of now, the LEM V enables a precise RBE prediction for clinically applied carbon ions in the entrance channel in which higher energetic ions are predominantly present. Thus, its potential for clinical applications is promising. Next to an increased precision in radiotherapy treatment planning, the new model approach also enables an improved risk assessment for astronauts or cancer patients. The model improvements are, however, less pronounced for heavier ions as present in mixed space radiation fields. In order to enable a final assessment of the predictive power of the LEM V for such applications, a comprehensive comparison to other available RBE models needs to be performed.

Bibliography

[1] E. J. Hall and A. J. Giaccia. *Radiobiology for the Radiobiologist, Eighth edition*. Wolters Kluwer, 2019.

[2] M. Durante and F. A. Cucinotta. "Heavy ion carcinogenesis and human space exploration". In: *Nature Reviews Cancer* 8.6 (2008), pp. 465–472. DOI: 10.1038/nrc2391.

[3] M. Durante and F. A. Cucinotta. "Physical basis of radiation protection in space travel". In: *Reviews of Modern Physics* 83.4 (2011), pp. 1245–81. DOI: 10.1103/RevModPhys.83.1245.

[4] *World Health Organization.* URL: https://www.who.int/health-topics/cancer#tab=tab_1 (visited on 04/09/2021).

[5] *International agency for research on cancer*. URL: https://gco.iarc.fr/today/fact-sheets-cancers (visited on 04/09/2021).

[6] R. R. Wilson. "Radiological Use of Fast Protons". In: *Radiology* 47.5 (1946), pp. 487–491. DOI: 10.1148/47.5.487.

[7] M. Durante and H. Paganetti. "Nuclear physics in particle therapy: A review". In: *Reports on Progress in Physics* 79.9 (2016), pp. 1–59. DOI: 10.1088/0034-4885/79/9/096702.

[8] E. A. Blakely et al. "Heavy-ion radiobiology: cellular studies". In: *Advanced Radiation Biology* 11 (1984), pp. 295–389. DOI: 10.1016/B978-0-12-035411-5.50013-7.

[9] G. Kraft. "Tumore unter schwerem Beschuss. Krebstherapie mit Ionen in der klinischen Anwendung". In: *Physik in unserer Zeit* 40.4 (2009), pp. 196–202. DOI: 10.1002/piuz.200801204.

[10] M. Scholz et al. "Computation of cell survival in heavy ion beams for therapy". In: *Radiation and Environmental Biophysics* 36.1 (1997), pp. 59–66. DOI: 10.1007/s004110050055.

[11] T. Elsässer et al. "Quantification of the relative biological effectiveness for ion beam radiotherapy: Direct experimental comparison of proton and carbon ion beams and a novel approach for treatment planning". In: *International Journal of Radiation Oncology, Biology, Physics* 78.4 (2010), pp. 1177–1183. DOI: 10.1016/j.ijrobp.2010.05.014.

[12] T. Friedrich et al. "Calculation of the biological effects of ion beams based on the microscopic spatial damage distribution pattern". In: *International Journal of Radiation Biology* 88.1-2 (2012), pp. 103–107. DOI: 10.3109/09553002.2011.611213.

[13] J. J. Butts and R. Katz. "Theory of RBE for Heavy Ion Bombardment of Dry Enzymes and Viruses". In: *Radiation Research* 30.4 (1967), p. 855. DOI: 10.2307/3572151.

[14] R. Katz, S. C. Sharma, and M. Homayoonfar. "Detection of Energetic Heavy Ions". In: *Nuclear Instruments and Methods* 100 (1 1972), pp. 13–32. DOI: 10.1016/0029-554X(72)90264-9.

[15] R. B. Hawkins. "A microdosimetric-kinetic model of cell death from exposure to ionizing radiation of any LET, with experimental and clinical applications". In: *International Journal of Radiation Biology* 69.6 (1996), pp. 739–755. DOI: 10.1080/095530096145481.

[16] R. B. Hawkins. “A microdosimetric-kinetic model for the effect of non-poisson distribution of lethal lesions on the variation of RBE with LET”. In: *Radiation Research* 160.1 (2003), pp. 61–69. DOI: 10.1667/RR3010.

[17] Y. Kase et al. “Microdosimetric measurements and estimation of human cell survival for heavy-ion beams”. In: *Radiation Research* 166.4 (2006), pp. 629–638. DOI: 10.1667/RR0536.1.

[18] T. Inaniwa et al. “Treatment planning for a scanned carbon beam with a modified microdosimetric kinetic model”. In: *Physics in Medicine and Biology* 55.22 (2010), pp. 6721–6737. DOI: 10.1088/0031-9155/55/22/008.

[19] R. Grün et al. “Systematics of relative biological effectiveness measurements for proton radiation along the spread out Bragg peak : experimental validation of the local effect model”. In: *Physics in Medicine and Biology* 62 (2017), pp. 890–908. DOI: 10.1088/1361-6560/62/3/890.

[20] M. Krämer et al. “Helium ions for radiotherapy? Physical and biological verifications of a novel treatment modality”. In: *Medical Physics* 43.4 (2016), pp. 1995–2004. DOI: 10.1118/1.4944593.

[21] O. Sokol et al. “Oxygen beams for therapy: Advanced biological treatment planning and experimental verification”. In: *Physics in Medicine and Biology* 62.19 (2017), pp. 7798–7813. DOI: 10.1088/1361-6560/aa88a0.

[22] M. Saager et al. “Split dose carbon ion irradiation of the rat spinal cord : Dependence of the relative biological effectiveness on dose and linear energy transfer”. In: *Radiotherapy and oncology* 117.2 (2015), pp. 358–363. DOI: 10.1016/j.radonc.2015.07.006.

[23] M. Saager et al. “Late normal tissue response in the rat spinal cord after carbon ion irradiation”. In: *Radiation Oncology* 13.1 (2018), pp. 1–9. DOI: 10.1186/s13014-017-0950-5.

[24] M. Saager et al. “Fractionated carbon ion irradiations of the rat spinal cord: Comparison of the relative biological effectiveness with predictions of the local effect model”. In: *Radiation Oncology* 15.1 (2020), pp. 1–10. DOI: 10.1186/s13014-019-1439-1.

[25] F. Tommasino et al. “A DNA Double-Strand Break Kinetic Rejoining Model Based on the Local Effect Model”. In: *Radiation Research* 180.5 (), pp. 524–538. DOI: 10.1667/RR13389.1.

[26] L. Herr et al. “A model of photon cell killing based on the spatio-temporal clustering of DNA damage in higher order chromatin structures”. In: *PLoS ONE* 9.1 (2014). DOI: 10.1371/journal.pone.0083923.

[27] A. I. Hufnagl, M. Scholz, and T. Friedrich. “Modelling radiation induced neoplastic cell transformation in vitro and tumor induction in vivo with the local effect model (LEM)”. In: *Radiation Research* 195.5 (2021), pp. 427 –440. DOI: 10.1667/RADE-20-00160.1.

[28] T. Friedrich et al. “Systematic analysis of RBE and related quantities using a database of cell survival experiments with ion beam irradiation”. In: *Journal of Radiation Research* 54.3 (2013), pp. 494–514. DOI: 10.1093/jrr/rrs114.

[29] T. Friedrich, T. Pfuhl, and M. Scholz. “Update of the particle irradiation data ensemble (PIDE) for cell survival”. In: *Journal of Radiation Research* (2021). published online. DOI: 10.1093/jrr/rrab034.

[30] H. Nikjoo et al. “Computational modelling of low-energy electron-induced DNA damage by early physical and chemical events”. In: *International Journal of Radiation Biology* 71.5 (1997), pp. 467–483. DOI: 10.1080/095530097143798.

[31] A. Schipler and G. Iliakis. “DNA double-strand-break complexity levels and their possible contributions to the probability for error-prone processing and repair pathway choice”. In: *Nucleic Acids Research* 41.16 (2013), pp. 7589–7605. DOI: 10.1093/nar/gkt556.

[32] B. Jakob et al. “Differential Repair Protein Recruitment at Sites of Clustered and Isolated DNA Double-Strand Breaks Produced by High-Energy Heavy Ions”. In: *Scientific reports* 10.1 (2020), p. 1443. DOI: 10.1038/s41598-020-58084-6.

[33] T. Friedrich et al. “DNA damage interactions on both nanometer and micrometer scale determine overall cellular damage”. In: *Scientific Reports* 8.1 (2018), pp. 1–10. DOI: 10.1038/s41598-018-34323-9.

[34] T. Pfuhl, T. Friedrich, and M. Scholz. “Prediction of Cell Survival after Exposure to Mixed Radiation Fields with the Local Effect Model”. In: *Radiation Research* 193.2 (2020), pp. 130–142. DOI: 10.1667/RR15456.1.

[35] K. M. Prise et al. “A review of DSB induction data for varying quality radiations”. In: *International Journal of Radiation Biology* 74.2 (1998), pp. 173–184. DOI: 10.1080/095530098141564.

[36] K. M. Prise et al. “A review of studies of ionizing radiation-induced double-strand break clustering”. In: *Radiation Research* 156.5 II (2001), pp. 572–576. DOI: 10.1667/0033-7587(2001)156[0572:arosoi]2.0.co;2.

[37] G. Kraft and M. Krämer. *Linear Energy Transfer and Track Structure*. Vol. 17. Academic Press, San Diego, 1993, pp. 1–52. DOI: 10.1016/B978-0-12-035417-7.50004-0.

[38] T. Buch et al. “Modeling Radiation Effects of Ultrasoft X Rays on the Basis of Amorphous Track Structure”. In: *Radiation Research* 189.1 (2018), pp. 32–43. DOI: 10.1667/rr14653.1.

[39] F. A. Cucinotta, H. Nikjoo, and D. T. Goodhead. “Applications of amorphous track models in radiation biology”. In: *Radiation and Environmental Biophysics* 38.2 (1999), pp. 81–92. DOI: 10.1007/s004110050142.

[40] H. Nikjoo and L. Lindborg. “RBE of low energy electrons and photons”. In: *Physics in Medicine and Biology* 55.10 (2010), R65–R109. DOI: 10.1088/0031-9155/55/10/R01.

[41] D. Schardt, T. Elsässer, and D. Schulz-Ertner. “Heavy-ion tumor therapy: Physical and radiobiological benefits”. In: *Reviews of Modern Physics* 82.1 (2010), pp. 383–425. DOI: 10.1103/RevModPhys.82.383.

[42] H. Krieger. *Grundlagen der Strahlungsphysik und des Strahlenschutzes*. Vol. 44. 8. 2012, p. 085201. ISBN: 978-3-8348-1815-7. DOI: 10.1007/978-3-8348-2238-3. arXiv: arXiv:1011.1669v3.

[43] E. B. Podgorsak. *Radiation Physics for Medical Physicists (Biological and Medical Physics, Biomedical Engineering)*. 2010, p. 700. ISBN: 3642008747.

[44] W. D. Newhauser and R. Zhang. “The physics of proton therapy”. In: *Physics in Medicine and Biology* 60.8 (2015), R155–R209. DOI: 10.1088/0031-9155/60/8/R155.

[45] G. Kraft, M. Scholz, and U. Bechthold. “Tumor therapy and track structure”. In: *Radiation and Environmental Biophysics* 38 (1999), pp. 229–237. DOI: 10.1007/s004110050163.

[46] A. Alexandrov et al. *FOOT Conceptual Design Report*. Tech. rep. Aug. 2017. DOI: 10.13140/RG.2.2.28904.78080.

[47] S. Incerti et al. “Geant4-DNA example applications for track structure simulations in liquid water: A report from the Geant4-DNA Project”. In: *Medical Physics* 45.8 (2018), e722–e739. DOI: 10.1002/mp.13048.

[48] U. Weber and G. Kraft. “Comparison of Carbon Ions Versus Protons”. In: *The Cancer Journal* 15 (4 2009), pp. 325–332. DOI: 10.1097/PPO.0b013e3181b01935.

[49] M. A. Bernal et al. “Track structure modeling in liquid water: A review of the Geant4-DNA very low energy extension of the Geant4 Monte Carlo simulation toolkit”. In: *Physica Medica* 31.8 (2015), pp. 861–874. DOI: 10.1016/j.ejmp.2015.10.087.

[50] S. Incerti et al. “Comparison of GEANT4 very low energy cross section models with experimental data in water”. In: *Medical Physics* 37.9 (2010), pp. 4692–4708. DOI: 10.1118/1.3476457.

[51] S. Incerti et al. “The Geant4-DNA project: The Geant4-DNA collaboration”. In: *International Journal of Modeling, Simulation, and Scientific Computing* 1.2 (2010), p. 157. arXiv: 0910.5684.

[52] M. Krämer and G. Kraft. “Calculations of heavy-ion track structure”. In: *Radiation and Environmental Biophysics* 33.2 (1994), pp. 91–109. DOI: 10.1007/BF01219334.

[53] M. Krämer. “Calculation of heavy-ion track structure”. In: *Nuclear Inst. and Methods in Physics Research, B* 105.1-4 (1995), pp. 14–20. DOI: 10.1016/0168-583X(95)00538-2.

[54] M. Krämer and M. Durante. “Ion beam transport calculations and treatment plans in particle therapy”. In: *European Physical Journal D* 60.1 (2010), pp. 195–202. DOI: 10.1140/epjd/e2010-00077-8.

[55] W. Friedland et al. “Track structures, DNA targets and radiation effects in the biophysical Monte Carlo simulation code PARTRAC”. In: *Mutation Research - Fundamental and Molecular Mechanisms of Mutagenesis* 711.1-2 (2011), pp. 28–40. DOI: 10.1016/j.mrfmmm.2011.01.003.

[56] J. Kiefer and H. Straaten. “A model of ion track structure based on classical collision dynamics.” In: *Physics in medicine and biology* 31.11 (1986), pp. 1201–1209. DOI: 10.1088/0031-9155/31/11/002.

[57] T. Elsässer et al. “Impact of Track Structure Calculations On Biological Treatment Planning in Carbon Ion Radiotherapy”. In: *New Journal of Physics* 10.7 (2008), p. 075005. DOI: 10.1118/1.2962612.

[58] A. Chatterjee and H. J. Schaefer. “Microdosimetric structure of heavy ion tracks in tissue”. In: *Radiation and Environmental Biophysics* 13.3 (1976), pp. 215–227. DOI: 10.1007/BF01330766.

[59] Y. Kase. “Biophysical calculation of cell survival probabilities using amorphous track structure models for heavy- ion irradiation”. In: *Physics in Medicine and Biology* 1 (53 2008), pp. 37–59. DOI: 10.1088/0031-9155/53/1/003.

[60] T. Elsässer and M. Scholz. “Cluster Effects within the Local Effect Model”. In: *Radiation Research* 167.3 (2007), pp. 319–329. DOI: 10.1667/RR0467.1.

[61] E. A. Blakely et al. “Inactivation of human kidney cells by high-energy monoenergetic heavy-ion beams”. In: *Radiation Research* 80.1 (1979), pp. 122–160. DOI: 10.2307/3575121.

[62] S. J. McMahon. “The linear quadratic model: Usage, interpretation and challenges”. In: *Physics in Medicine and Biology* 64.1 (2019), 01TR01. DOI: 10.1088/1361-6560/aaf26a.

[63] A. M. Kellerer and H. H. Rossi. “The theory of dual radiation action”. In: *Current Topics in Radiation Research Quarterly* 8 (1974), pp. 85–158. DOI: 10.1080/09553007514550401.

[64] Y. Furusawa et al. “Inactivation of aerobic and hypoxic cells from three different cell lines by accelerated He-3-,C-12- and Ne-20-ion beams”. In: *Radiation Research* 154.5 (2000), pp. 485–496. DOI: 10.1667/0033-7587(2000)154{[}0485:IOAAHC]2.0.CO;2.

[65] T. Elsässer, M. Krämer, and M. Scholz. “Accuracy of the local effect model for the prediction of biologic effects of carbon ion beams in vitro and in vivo”. In: *International Journal of Radiation Oncology, Biology, Physics* 71.3 (2008), pp. 866–872. DOI: https://doi.org/10.1016/j.ijrobp.2008.02.037.

[66] T. Friedrich, M. Durante, and M. Scholz. “Simulation of DSB yield for high LET radiation”. In: *Radiation Protection Dosimetry* 166.1-4 (2015), pp. 61–65. DOI: 10.1093/rpd/ncv147.

[67] P. J. Johnston, P. L. Olive, and P. E. Bryant. “Higher-Order Chromatin Structure-Dependent Repair of DNA Double-Strand Breaks: Modeling the Elution of DNA from Nucleoids”. In: *Radiation Research* 148 (1997), pp. 561–567. DOI: 10.2307/3579731.

[68] P. J. Johnston et al. “Higher-Order Chromatin Structure-Dependent Repair of DNA Double-Strand Breaks: Factors Affecting Elution of DNA from Nucleoids”. In: *Radiation Research* 149 (1998), pp. 533–542. DOI: 10.2307/3578376.

[69] J. Ostashevsky. “A Polymer Model for the Structural Organization of Chromatin Loops and Minibands in Interphase Chromosomes”. In: *Molecular Biology of the Cell* 9 (1998), pp. 3031–3040. DOI: 10.1091/mbc.9.11.3031.

[70] H. Yokota et al. “Evidence for the organization of chromatin in megabase pair - arranged along a random walk path in the human G0/G1”. In: *Journal of Cell Biology* 130.6 (1995), pp. 1239–1249. DOI: 10.1083/jcb.130.6.1239.

[71] M. Astrahan. “Some implications of linear-quadratic-linear radiation dose-response with regard to hypofractionation”. In: *Medical Physics* 35.9 (2008), pp. 4161–4172. DOI: 10.1118/1.2969065.

[72] M. Guerrero and X. Allen Li. “Extending the linear-quadratic model for large fraction doses pertinent to stereotactic radiotherapy”. In: *Physics in Medicine and Biology* 49.20 (2004), pp. 4825–4835. DOI: 10.1088/0031-9155/49/20/012.

[73] C. Park et al. “Universal Survival Curve and Single Fraction Equivalent Dose: Useful Tools in Understanding Potency of Ablative Radiotherapy”. In: *International Journal of Radiation Oncology Biology Physics* 70.3 (2008), pp. 847–852. DOI: 10.1016/j.ijrobp.2007.10.059.

[74] M. Krämer and M. Scholz. “Rapid calculation of biological effects in ion radiotherapy”. In: *Physics in Medicine and Biology* 51.8 (2006), pp. 1959–1970. DOI: 10.1088/0031-9155/51/8/001.

[75] M. Zaider and H. H. Rossi. “The Synergistic Effects of Different Radiations”. In: *Radiation Research* 83 (1980), pp. 732–739. DOI: 10.2307/3575352.

[76] G. K. Y. Lam. “The Survival Response of a Biological System to Mixed Radiations”. In: *Radiation Research* 110.2 (May 1987), pp. 232–243. DOI: 10.2307/3576901.

[77] R. J. Tallarida. “Quantitative Methods for Assessing Drug Synergism”. In: *Genes and Cancer* 2.11 (2012), pp. 1003–1008. DOI: 10.1177/1947601912440575.

[78] C. Fournier et al. “The fate of a normal human cell traversed by a single charged particle”. In: *Scientific Reports* 2 (643 2012). DOI: 10.1038/srep00643.

[79] A. Bothe. *Investigation of statistical properties of cell survival curves and the relative biological effectiveness of ion radiation (Master thesis, TU Darmstadt)*. 2016.

[80] B. Phoenix et al. “Do the various radiations present in BNCT act synergistically? Cell survival experiments in mixed alpha-particle and gamma-ray fields”. In: *Applied Radiation and Isotopes* 67 (2009), pp. 318–320. DOI: 10.1016/j.apradiso.2009.03.097.

[81] Y. Demizu et al. “Cell biological basis for combination radiotherapy using heavy-ion beams and high-energy X-rays”. In: *Radiotherapy and Oncology* 71 (2004), pp. 207–211. DOI: 10.1016/j.radonc.2004.03.008.

[82] B. K. Lind et al. “Repairable-Conditionally Repairable Damage Model Based on Dual Poisson Processes”. In: *Radiation Research* 160.3 (2003), pp. 366–375. DOI: 10.1667/0033-7587(2003)160.

[83] N. Geary. “Understanding synergy”. In: *American Journal of Physiology-Endocrinology and Metabolism* 304.3 (2012), E237–E253. DOI: 10.1152/ajpendo.00308.2012.

[84] G. G. Steel and M. J. Peckham. “Exploitable mechanisms in combined radiotherapy-chemotherapy: The concept of additivity”. In: *International Journal of Radiation Oncology, Biology, Physics* 5.1 (1979), pp. 85–91. DOI: 10.1016/0360-3016(79)90044-0.

[85] C. I. Bliss. “The toxicity of poisons applied jointly”. In: *Annals of Applied Biology* 26.3 (1939), pp. 585–615. DOI: 10.1111/j.1744-7348.1939.tb06990.x.

[86] G. W. Barendsen et al. “Effects of Different Ionizing Radiations on Human Cells in Tissue Culture: II. Biological Experiments”. In: *Radiation Research* 13.6 (1960), pp. 841–849. DOI: 10.2307/3570859.

[87] R. P. Bird et al. “The Sequential Irradiation of Mammalian Cells with X Rays and Charged Particles of High LET”. In: *Radiation Research* 93.3 (1983), pp. 444–452. DOI: 10.2307/3576024.

[88] N. J. Mcnally et al. “Interaction between X-ray and α -particle Damage in V79 Cells”. In: *International Journal of Radiation Biology* 53.6 (1988), pp. 917–920. DOI: 10.1080/09553008814551281.

[89] M. R. Raju and J. H. Jett. “RBE and OER Variations of Mixtures of Plutonium Alpha Particles and X-Rays for Damage to Human Kidney Cells (T-1)”. In: *Radiation Research* 60.3 (1974), pp. 473–481. DOI: 10.2307/3574026.

[90] A. L. Brooks et al. “The Combined Effects of α-particles and X-rays on Cell Killing and Micronuclei Induction in Lung Epithelial Cells”. In: *International Journal of Radiation Biology* 58.5 (1990), pp. 799–811. DOI: 10.1080/09553009014552181.

[91] Y. Furusawa, M. Aoki, and M. Durante. “Simultaneous Exposure of Mammalian Cells to Heavy Ions and X-Rays”. In: *Advanced Space Research* 30.4 (2002), pp. 877–884. DOI: 10.1016/S0273-1177(02)00409-X.

[92] N. Tilly et al. “Comparison of cell survival models for mixed LET radiation”. In: *International Journal of Radiation Biology* 75.2 (1999), pp. 233–243. DOI: 10.1080/095530099140690.

[93] F. Q. H. Ngo, E. A. Blakely, and C. A. Tobias. “Sequential Exposures of Mammalian Cells to Low- and High-LET Radiations”. In: *Radiation Research* 78 (1981), pp. 59–78. DOI: 10.2307/3577055.

[94] T. Friedrich. *A detailed track structure model, private communication*. 2017.

[95] A. Ferrari et al. “FLUKA: a multi-particle transport code”. In: *Technical Report CERN* 10, INFN/T.October 2005 (2005), pp. 1–402. DOI: 10.5170/CERN-2005-010.

[96] T. T. Böhlen et al. “The FLUKA Code: Developments and challenges for high energy and medical applications”. In: *Nuclear Data Sheets* 120 (2014), pp. 211–214. DOI: 10.1016/j.nds.2014.07.049.

[97] S. Agostinelli et al. “Geant 4 — a simulation toolkit”. In: *Nuclear Instruments and Methods in Physics Research A* 506 (2003), pp. 250–303. DOI: 10.1016/S0168-9002(03)01368-8.

[98] J. Allison et al. “Geant4 developments and applications”. In: *IEEE Transactions on Nuclear Science* 53.1 (2006), pp. 270–278. DOI: 10.1109/TNS.2006.869826.

[99] J. Allison et al. “Recent developments in GEANT 4”. In: *Nuclear Instruments and Methods in Physics Research A* 835 (2016), pp. 186–225. DOI: 10.1016/j.nima.2016.06.125.

[100] Y.-K. Kim et al. *Electron-Impact Cross Sections for Ionization and Excitation Database - NIST Standard Reference Database 107*. Tech. rep. 2004. DOI: https://dx.doi.org/10.18434/T4KK5C.

[101] H. G. Menzel. “Key Data for Ionizing-Radiation Dosimetry: Measurement Standards and Applications”. In: *Journal of the ICRU* 14.1 (2014), pp. 1–118. DOI: 10.1093/jicru/ndw029.

[102] T. Pfuhl, T. Friedrich, and M. Scholz. “Comprehensive validation of the Local Effect Model IV - in preparation”. In: *Medical Physics* (2021).

[103] T. Friedrich, M. Durante, and M. Scholz. “Modeling Cell Survival after Photon Irradiation Based on Double-Strand Break Clustering in Megabase Pair Chromatin Loops”. In: *Radiation Research* 178.5 (2012), pp. 385–394. DOI: 10.1667/RR2964.1.

[104] S. Mein et al. “Assessment of RBE-Weighted Dose Models for Carbon Ion Therapy Toward Modernization of Clinical Practice at HIT: In Vitro, in Vivo, and in Patients”. In: *International Journal of Radiation Oncology Biology Physics* 108.3 (2020), pp. 779–791. DOI: 10.1016/j.ijrobp.2020.05.041.

[105] S. Mein et al. “Biophysical modeling and experimental validation of relative biological effectiveness (RBE) for 4He ion beam therapy”. In: *Radiation Oncology* 14.1 (2019), pp. 1–16. DOI: 10.1186/s13014-019-1295-z.

[106] Y. Lin et al. “Biological modeling of gold nanoparticle enhanced radiotherapy for proton therapy”. In: *Physics in Medicine and Biology* 60.10 (2015), pp. 4149–4168. DOI: 10.1088/0031-9155/60/10/4149. URL: http://dx.doi.org/10.1088/0031-9155/60/10/4149.

[107] H. Paganetti et al. “Relative biological effectiveness (RBE) values for proton beam therapy”. In: *International Journal of Radiation Oncology Biology Physics* 53.2 (2002), pp. 407–421. DOI: 10.1016/S0360-3016(02)02754-2.

[108] T. Friedrich et al. “Sensitivity analysis of the relative biological effectiveness predicted by the local effect model”. In: *Physics in Medicine and Biology* 58.19 (2013), pp. 6827–6849. DOI: 10.1088/0031-9155/58/19/6827.

[109] E. G. Huang et al. “Simulating galactic cosmic ray effects: Synergy modeling of murine tumor prevalence after exposure to two one-ion beams in rapid sequence”. In: *Life Sciences in Space Research* 25.October 2019 (2020), pp. 107–118. DOI: 10.1016/j.lssr.2020.01.001.

[110] A. Bertolet and A. Carabe. “Modelling dose effects from space irradiations: Combination of high-let and low-let radiations with a modified microdosimetric kinetic model”. In: *Life* 10.9 (2020), pp. 1–14. DOI: 10.3390/life10090161.

[111] W. D. Ham et al. “Synergy Theory in Radiobiology”. In: *Radiation Research* 189.3 (2018), pp. 225–237. DOI: 10.1667/RR14948.1.

[112] E. G. Huang et al. “Synergy theory for murine Harderian gland tumours after irradiation by mixtures of high-energy ionized atomic nuclei”. In: *Radiation and Environmental Biophysics* 58.2 (2019), pp. 151–166. DOI: 10.1007/s00411-018-00774-x.

[113] T. C. Slaba et al. “Determination of Chromosome Aberrations in Human Fibroblasts Irradiated by Mixed Fields Generated with Shielding”. In: *Radiation Research* 194.3 (2020), pp. 246–258. DOI: 10.1667/RR15366.1.

[114] M. Krämer and M. Scholz. “Treatment planning for heavy-ion radiotherapy: Calculation and optimization of biologically effective dose”. In: *Physics in Medicine & Biology* 45 (2000), pp. 3319–3330. DOI: 10.1088/0031-9155/45/11/314.

[115] N. J. McNally, J. de Ronde, and M. Hinchliffe. “Survival of V79 Cells Following Simultaneous Irradiation with X-rays and Neutrons in Air or Hypoxia”. In: *International Journal of Radiation Biology and Related Studies in Physics, Chemistry and Medicine* 48.5 (1985), pp. 847–855. DOI: 10.1080/09553008514551941.

[116] I. Chiolo et al. “Double-strand breaks in heterochromatin move outside of a dynamic HP1a domain to complete recombinational repair”. In: *Cell* 144.5 (2011), pp. 732–744. DOI: 10.1016/j.cell.2011.02.012.

[117] S. V. Costes et al. “Spatiotemporal characterization of ionizing radiation induced DNA damage foci and their relation to chromatin organization”. In: *Mutation Research - Reviews in Mutation Research* 704.1-3 (2010), pp. 78–87. DOI: 10.1016/j.mrrev.2009.12.006.

[118] J. Mirsch et al. “Direct measurement of the 3-dimensional DNA lesion distribution induced by energetic charged particles in a mouse model tissue”. In: *Proceedings of the National Academy of Sciences of the United States of America* 112.40 (2015), pp. 12396–12401. DOI: 10.1073/pnas.1508702112.

[119] V. Mladenova, E. Mladenov, and G. Iliakis. “Novel biological approaches for testing the contributions of single DSBs and DSB clusters to the biological effects of high LET radiation”. In: *Frontiers in Oncology* 6.JUN (2016), p. 163. DOI: 10.3389/fonc.2016.00163.

[120] S. V. Costes et al. “Image-based modeling reveals dynamic redistribution of DNA damage into nuclear sub-domains”. In: *PLoS Computational Biology* 3.8 (2007), pp. 1477–1488. DOI: 10.1371/journal.pcbi.0030155.

[121] D. T. Goodhead and H. Nikjoo. “Track structure analysis of ultrasoft x-rays compared to high- and low-LET radiations”. In: *International Journal of Radiation Biology* 55.4 (1989), pp. 513–529. DOI: 10.1080/09553008914550571.

[122] M. Scholz and G. Kraft. “Track structure and the calculation of biological effects of heavy charged particles”. In: *Advances in Space Research* 18.1-2 (1996), pp. 5–14. DOI: 10.1016/0273-1177(95)00784-C.

[123] F. A. Cucinotta, R. Katz, and J. W. Wilson. “Radial distribution of electron spectra from high-energy ions”. In: *Radiation and Environmental Biophysics* 37.4 (1998), pp. 259–265. DOI: 10.1007/s004110050127.

[124] W. Friedland et al. “Comprehensive track-structure based evaluation of DNA damage by light ions from radiotherapy-relevant energies down to stopping”. In: *Scientific Reports* 7.March (2017), pp. 1–15. DOI: 10.1038/srep45161.

[125] K. P. Chatzipapas et al. “Quantification of DNA double-strand breaks using Geant4-DNA”. In: *Medical Physics* 46.1 (2019), pp. 405–413. DOI: 10.1002/mp.13290.

[126] L. Petrolli et al. “Can We Assess Early DNA Damage at the Molecular Scale by Radiation Track Structure Simulations? A Tetranucleosome Scenario in Geant4-DNA”. In: *Frontiers in Physics* 8.October (2020), pp. 1–7. DOI: 10.3389/fphy.2020.576284.

[127] J. B. Renner. *Untersuchung von Ionisationsmustern im Kontext amorpher Bahnstruktur (Master thesis, TU Darmstadt)*. 2017.

[128] Y. Matsuya et al. “A simplified cluster analysis of electron track structure for estimating complex dna damage yields”. In: *International Journal of Molecular Sciences* 21.5 (2020). DOI: 10.3390/ijms21051701.

[129] M. A. Hill. “The variation in biological effectiveness of X-rays and gamma rays with energy”. In: *Radiation Protection Dosimetry* 112.4 (2004), pp. 471–481. DOI: 10.1093/rpd/nch091.

[130] N. Hunter and C. R. Muirhead. “Review of relative biological effectiveness dependence on linear energy transfer for low-LET radiations”. In: *Journal of Radiological Protection* 29.1 (2009), pp. 5–21. DOI: 10.1088/0952-4746/29/1/R01.

[131] Y. Zheng and L. Sanche. “Effective and absolute cross sections for low-energy (1-30 eV) electron interactions with condensed biomolecules”. In: *Applied Physics Reviews* 5.2 (2018). DOI: 10.1063/1.5010916.

[132] H. K. Kim et al. “Enhanced production of low energy electrons by alpha particle impact”. In: *Proceedings of the National Academy of Sciences of the United States of America* 108.29 (2011), pp. 11821–11824. DOI: 10.1073/pnas.1104382108.

[133] F. King et al. “Status of the Frankfurt low energy electrostatic storage ring (FLSR)”. In: *Physica Scripta* T166.T166 (2015), p. 014064. DOI: 10.1088/0031-8949/2015/T166/014064.

[134] H. Nikjoo et al. “Quantitative modelling of DNA damage using Monte Carlo track structure method”. In: *Radiation and Environmental Biophysics* 38.1 (1999), pp. 31–38. DOI: 10.1007/s004110050135.

[135] L. Zhang and Z. Tan. “A new calculation on spectrum of direct DNA damage induced by low-energy electrons”. In: *Radiation and Environmental Biophysics* 49.1 (2010), pp. 15–26. DOI: 10.1007/s00411-009-0262-8.

[136] L. Sanche. “Low energy electron-driven damage in biomolecules”. In: *European Physical Journal D* 35.2 (2005), pp. 367–390. DOI: 10.1140/epjd/e2005-00206-6.

[137] T. Friedrich, M. Durante, and M. Scholz. “Modeling cell survival after irradiation with ultrasoft X rays using the giant loop binary lesion model”. In: *Radiation Research* 181.5 (2014), pp. 485–494. DOI: 10.1667/RR13518.1.

[138] M. N. Cornforth. “Occam’s broom and the dirty DSB: cytogenetic perspectives on cellular response to changes in track structure and ionization density”. In: *International Journal of Radiation Biology* (2020). published online. DOI: 10.1080/09553002.2019.1704302.

[139] V. A. Semenenko and R. D. Stewart. “A fast Monte Carlo algorithm to simulate the spectrum of DNA damages formed by ionizing radiation”. In: *Radiation Research* 161.4 (2004), pp. 451–457. DOI: 10.1667/RR3140.

[140] H. Nikjoo et al. “Track-structure codes in radiation research”. In: *Radiation Measurements* 41.9-10 (2006), pp. 1052–1074. DOI: 10.1016/j.radmeas.2006.02.001.

[141] P. Pater et al. “On the consistency of Monte Carlo track structure DNA damage simulations”. In: *Medical Physics* 41.12 (2014). DOI: 10.1118/1.4901555.

[142] H. Nikjoo et al. “Modelling of DNA damage induced by energetic electrons (100 eV to 100 keV)”. In: *Radiation Protection Dosimetry* 99.1-4 (2002), pp. 77–80. DOI: 10.1093/oxfordjournals.rpd.a006843.

[143] R. Watanabe and K. Saito. “Monte Carlo simulation of strand-break induction on plasmid DNA in aqueous solution by monoenergetic electrons”. In: *Radiation and Environmental Biophysics* 41.3 (2002), pp. 207–215. DOI: 10.1007/s00411-002-0161-8.

[144] D. E. Charlton, H. Nikjoo, and J. L. Humm. “Calculation of initial yields of single- and double-Strand breaks in cell nuclei from electrons, protons and alpha particles”. In: *International Journal of Radiation Biology* 56.1 (1989), pp. 1–19. DOI: 10.1080/09553008914551141.

[145] M. A. Bernal and J. A. Liendo. “An investigation on the capabilities of the PENELOPE MC code in nanodosimetry”. In: *Medical Physics* 36.2 (2009), pp. 620–625. DOI: 10.1118/1.3056457.

[146] F. Salvat, J. M. Fernandez-Varea, and J. Sempau. *PENELOPE-2006 : A Code System for Monte Carlo Simulation of Electron and Photon Transport*. Tech. rep. 2006.

[147] V. Michalik. “Particle track structure and its correlation with radiobiological endpoint”. In: *Physics in Medicine and Biology* 36.7 (1991), pp. 1001–1012. DOI: 10.1088/0031-9155/36/7/008.

[148] F. Van Den Heuvel. “A closed parameterization of DNA-damage by charged particles, as a function of energy - A geometrical approach”. In: *PLoS ONE* 9.10 (2014). DOI: 10.1371/journal.pone.0110333. arXiv: 1309.7563.

[149] M. Bellamy et al. “An empirical method for deriving rbe values associated with electrons, photons and radionuclides”. In: *Radiation Protection Dosimetry* 167.4 (2015), pp. 664–670. DOI: 10.1093/rpd/ncu358.

[150] H. Nikjoo and D. T. Goodhead. “Track structure analysis illustrating the prominent role of low-energy electrons in radiobiological effects of low-LET radiations”. In: *Physics in Medicine and Biology* 36.2 (1991), pp. 229–238. DOI: 10.1088/0031-9155/36/2/007.

[151] H. G. Paretzke. *Kinetics of Nonhomogeneous Processes*. Ed. by G. R. Freeman. Wiley, New York, 1987. Chap. Radiation, pp. 89–170.

[152] *Absorbed Dose Determination in External Beam Radiotherapy*. Technical Reports Series 398. Vienna: International atomic energy agency, 2001. URL: https://www.iaea.org/publications/5954/absorbed-dose-determination-in-external-beam-radiotherapy.

[153] A. Panteleeva et al. “Clonogenic survival of human keratinocytes and rodent fibroblasts after irradiation with 25 kV x-rays”. In: *Radiation and Environmental Biophysics* 42.2 (2003), pp. 95–100. DOI: 10.1007/s00411-003-0199-2.

[154] V. Paget et al. “Multiparametric radiobiological assays show that variation of X-ray energy strongly impacts relative biological effectiveness: comparison between 220 kV and 4 MV”. In: *Scientific Reports* 9.1 (2019), pp. 1–10. DOI: 10.1038/s41598-019-50908-4.

[155] G. T. Selvan, K. Kanagaraj, and P. Venkatachalam. “The relative biological effectiveness of high-energy clinical 3 and 6 MV X-rays for micronucleus induction in human lymphocytes”. In: *International Journal of Radiation Biology* 97.5 (2021), pp. 687–694. DOI: 10.1080/09553002.2021.1906972.

[156] Y. Hsiao and R. D. Stewart. “Monte Carlo simulation of DNA damage induction by x-rays and selected radioisotopes”. In: *Physics in Medicine and Biology* 53.1 (2008), pp. 233–244. DOI: 10.1088/0031-9155/53/1/016.

[157] O. N. Vassiliev et al. “A simple model for calculating relative biological effectiveness of X-rays and gamma radiation in cell survival”. In: *The British journal of radiology* 93.1112 (2020), p. 20190949. DOI: 10.1259/bjr.20190949.

[158] D. Frankenberg et al. “Erratum: Enhanced neoplastic transformation by mammography X rays relative to 200 kVp X rays: Indication for a strong dependence on photon energy of the RBEM for various end points”. In: *Radiation Research* 158.1 (2002), p. 126. DOI: 10.1667/0033-7587(2002)158[0126:E]2.0.CO;2.

[159] M. Frankenberg-Schwager et al. “Neoplastic transformation of a human hybrid cell line by alpha particles in relation to mammography X rays”. In: *Radiation Protection Dosimetry* 122.1-4 (2006), pp. 180–184. DOI: 10.1093/rpd/ncl457.

[160] W. Göggelmann et al. “Re-evaluation of the RBE of 29 kV x-rays (mammography x-rays) relative to 220 kV x-rays using neoplastic transformation of human CGL1-hybrid cells”. In: *Radiation and Environmental Biophysics* 42.3 (2003), pp. 175–182. DOI: 10.1007/s00411-003-0210-y.

[161] M. Mestres et al. “RBE of X rays of different energies: A cytogenetic evaluation by FISH”. In: *Radiation Research* 170.1 (2008), pp. 93–100. DOI: 10.1667/RR1280.1.

[162] ICRP. *The 2007 Recommendations of the International Commission on Radiological Protection*. Tech. rep. 37. 2007, pp. 2–4. DOI: 10.3109/00016925409177277.

[163] G. Dietze and W. G. Alberts. “Why it is advisable to keep wR=1 and Q=1 for photons and electrons”. In: *Radiation Protection Dosimetry* 109.4 (2004), pp. 297–302. DOI: 10.1093/rpd/nch305.

[164] J. Depuydt et al. “DNA double strand breaks induced by low dose mammography X-rays in breast tissue: A pilot study”. In: *Oncology Letters* 16.3 (2018), pp. 3394–3400. DOI: 10.3892/ol.2018.9024.

[165] U.S. Environmental Protection Agency. “EPA Radiogenic Cancer Risk Models and Projections for the U.S. Population”. In: *EPA Publication 402-R-11-001* April (2011).

[166] M. Kühne et al. “DNA double-strand break misrejoining after exposure of primary human fibroblasts to CK characteristic X rays, 29 kVp X Rays and 60Co γ rays”. In: *Radiation Research* 164.5 (2005), pp. 669–676. DOI: 10.1667/RR3461.1.

[167] G. Taucher-Scholz, J. Heilmann, and G. Kraft. “Induction and rejoining of DNA double-strand breaks in cho cells after heavy ion irradiation”. In: *Advances in Space Research* 18.1-2 (1996), pp. 83–92. DOI: 10.1016/0273-1177(95)00794-F.

[168] E. J. Kobetich and R. Katz. “Energy deposition by electron beams and δ rays”. In: *Physical Review* 170.2 (1968), pp. 391–396. DOI: 10.1103/PhysRev.170.391.

[169] R. Grün et al. “Impact of enhancements in the local effect model (LEM) on the predicted RBE-weighted target dose distribution in carbon ion therapy”. In: *Physics in Medicine and Biology* 57.22 (2012), pp. 7261–7274. DOI: 10.1088/0031-9155/57/22/7261.

[170] R. D. Stewart et al. “A comparison of mechanism-inspired models for particle relative biological effectiveness (RBE)”. In: *Medical Physics* 45.11 (2018), e925–e952. DOI: 10.1002/mp.13207.

[171] C. P. Karger and P. Peschke. “RBE and related modeling in carbon-ion therapy”. In: *Physics in Medicine and Biology* 63.1 (2018). DOI: 10.1088/1361-6560/aa9102.

[172] T. Zacharias et al. “Acute response of pig skin to irradiation with 12C-ions or 200 kV x- rays”. In: *Acta Oncologica* 36.6 (1997), pp. 637–642. DOI: 10.3109/02841869709001328.

[173] C. P. Karger et al. “Radiation tolerance of the rat spinal cord after 6 and 18 fractions of photons and carbon ions: Experimental results and clinical implications”. In: *International Journal of Radiation Oncology Biology Physics* 66.5 (2006), pp. 1488–1497. DOI: 10.1016/j.ijrobp.2006.08.045.

[174] T. J. Dahle et al. “Sensitivity study of the microdosimetric kinetic model parameters for carbon ion radiotherapy”. In: *Physics in Medicine and Biology* 63.22 (2018). DOI: 10.1088/1361-6560/aae8b4.

[175] A. Carabe-Fernandez, R. G. Dale, and B. Jones. “The incorporation of the concept of minimum RBE (RBEmin) into the linear-quadratic model and the potential for improved radiobiological analysis of high-LET treatments”. In: *International Journal of Radiation Biology* 83.1 (2007), pp. 27–39. DOI: 10.1080/09553000601087176.

[176] D. Frankenberg et al. “Effectiveness of 1.5 kev aluminium k and 0.3 kev carbon k characteristic x-rays at inducing DNA double-Strand breaks in yeast cells”. In: *International Journal of Radiation Biology* 50.4 (1986), pp. 727–741. DOI: 10.1080/09553008614551121.

[177] J. Fulford et al. “Yields of SSB and DSB induced in DNA by AlK ultrasoft X-rays and α-particles: Comparison of experimental and simulated yields”. In: *International Journal of Radiation Biology* 77.10 (2001), pp. 1053–1066. DOI: 10.1080/09553000110069308.

[178] M. Folkard et al. “Measurement of DNA damage by electrons with energies between 25 and 4000 EV”. In: *International Journal of Radiation Biology* 64.6 (1993), pp. 651–658. DOI: 10.1080/09553009314551891.

[179] B. Fayard et al. “Cell inactivation and double-strand breaks: The role of core ionizations, as probed by ultrasoft X rays”. In: *Radiation Research* 157.2 (2002), pp. 128–140. DOI: 10.1667/0033-7587(2002)157[0128:CIADSB]2.0.CO;2.

[180] A. Eschenbrenner et al. “Strand breaks induced in plasmid DNA by ultrasoft X-rays: Influence of hydration and packing”. In: *International Journal of Radiation Biology* 83.10 (2007), pp. 687–697. DOI: 10.1080/09553000701584106.

[181] S. W. Botchway et al. “Induction and rejoining of DNA double-strand breaks in Chinese hamster V79-4 cells irradiated with characteristic aluminum K and copper L ultrasoft X rays”. In: *Radiation Research* 148.4 (1997), pp. 317–324. DOI: 10.2307/3579516.

[182] C. M. De Lara et al. “Dependence of the yield of DNA double-strand breaks in Chinese hamster V79-4 cells on the photon energy of ultrasoft X rays”. In: *Radiation Research* 155.3 (2001), pp. 440–448. DOI: 10.1667/0033-7587(2001)155[0440:DOTYOD]2.0.CO;2.

[183] W. Friedland et al. “Simulation of DNA fragment distributions after irradiation with photons”. In: *Radiation and Environmental Biophysics* 38.1 (1999), pp. 39–47. DOI: 10.1007/s004110050136.

[184] W. Friedland et al. “Monte carlo simulation of the production of short DNA fragments by low- linear energy transfer radiation using higher-order DNA models”. In: *Radiation Research* 150.2 (1998), pp. 170–182. DOI: 10.2307/3579852.

[185] Y. Matsuya et al. “Modeling of yield estimation for DNA strand breaks based on Monte Carlo simulations of electron track structure in liquid water”. In: *Journal of Applied Physics* 126.12 (2019). DOI: 10.1063/1.5115519.

List of Figures

List of Tables

List of Abbreviations

BEB binary encounter bethe

cDSB complex double-strand-break

CT computer tomography

DNA deoxyribonucleic acid

DSB double-strand-break

GLOBLE Giant LOop Binary LEsion

GSI GSI Helmholtzzentrum für Schwerionenforschung GmbH

HSG human salivary gland

HZE high energy and charge

IAEA International Atomic Energy Agency

ICRP International Commission on Radiological Protection

ICRU International Commission on Radiation Units and Measurements

iDSB isolated double-strand-break

LAM lesion additivity model

LBL Lawrence Berkeley Laboratory

LEM local effect model

LET linear energy transfer

LQ linear-quadratic

LQL linear-quadratic-linear

mbp mega base pair

MC Monte Carlo

MCDS Monte Carlo damage simulation

MKM microdosimetric-kinetic model

NIRS National Institute of Radiological Sciences

PIDE Particle Irradiation Data Ensemble

RBE relative biological effectiveness

SSB single-strand-break

SOBP spread-out Bragg peak

TDRA theory of dual radiation action

WHO World Health Organization

ZRM Zaider-Rossi model

Curriculum vitae

Personal data	
Last name:	Pfuhl
First name:	Tabea
Nationality:	German

University studies	
04/2018 - 07/2021	PhD student at GSI Helmholtzzentrum for heavy ion research and Technical University Darmstadt; Member of the HGS-HIRe graduate school
10/2015 - 02/2018	M.Sc. Biophysics (Goethe University Frankfurt)
10/2012 - 09/2015	B.Sc. Biophysics (Goethe University Frankfurt)

School education	
06/2012	General higher education entrance qualification (Abitur), Edith-Stein-Schule Darmstadt

Awards, stipends and patents	
10/2019	Giersch Excellence Award – in recognition of outstanding achievements in the doctoral thesis project
11/2018	Christoph-Schmelzer Prize – for an outstanding master's thesis in the field of tumor therapy with heavy ions
09/2018	Poster award of the German Association of Medical Physics – for an outstanding poster in the field of dosimetry in medicine and radiation physics
06/2018	Award of the Walter-Greiner Gesellschaft zur physikalischen Grundlagenforschung e.V. – Best final grade of the physics department in the year 2018
2014 - 2017	Deutschlandstipendiatin – Scholarship sponsored by the German federal government and by Merck KGaA (received twice)
06/2015	Patent – Co-inventor of the "non-invasive substance analysis"

Publications	
05/2021	T. Pfuhl, T. Friedrich, M. Scholz. "Comprehensive validation of the Local Effect Model with the PIDE database". Med. Phys. (2021), in preparation
04/2021	L. Derksen, T. Pfuhl, R. Engenhart-Cabillic, K. Zink, K. Baumann. "Investigating the feasibility of TOPAS-nBio for Monte Carlo track structure simulations by adapting GEANT4-DNA examples application". Phys. Med. Biol. (2021), under revision
04/2021	T. Friedrich, T. Pfuhl, M. Scholz. "Update of the particle irradiation data ensemble (PIDE) for cell survival". JRR. (2021), published online
02/2020	T. Pfuhl, T. Friedrich, M. Scholz. "Prediction of cell survival after exposure to mixed radiation fields with the Local Effect Model". Radiat. Res. (2020), 193, 130–142.
12/2019	T. Pfuhl, F. Horst, C. Schuy, U. Weber. "Comment on: “Technical note: Simulation of dose buildup in proton pencil beams” [Med Phys. 46(8): 3734–3738 (2019)]". Med. Phys. (2019), 46: 5876-5877
08/2018	T. Pfuhl, F. Horst, C. Schuy, U. Weber. "Dose build-up effects induced by delta electrons and target fragments in proton Bragg curves – measurements and simulations". Phys. Med. Biol. (2018), 63 175002
01/2018	T. Pfuhl, F. Horst, C. Schuy, J. Stroth, U. Weber. "Dose build-up effects in clinical proton Bragg curves". GSI-FAIR Sci. Rep. 2017. (2018) GSI Report 2018-1, 298

Conference contributions	
10/2020	Radiation Research Society Annual Meeting 2020 (Poster) – Prediction of cell survival after exposure to mixed radiation fields with the Local Effect Model
09/2020	Particle Therapy Co-operative Group 2020 online meeting (Oral poster) – Comprehensive validation of the Local Effect Model with the PIDE database
08/2019	16th International Congress for Radiation Research (Poster) – Prediction of cell survival after exposure to mixed radiation fields with the Local Effect Model
09/2018	49th Annual Conference of the German Association of Medical Physics (Poster) – Dose build-up effects in proton Bragg curves
05/2018	57th Annual Conference of the Particle Therapy Co-operative Group (PTCOG57, Poster) – Dose build-up effects in proton Bragg curves
10/2017	GIERSCH International Symposium: Current status and future perspectives in particle therapy (Poster) – Dose build-up effects in clinical proton Bragg curves

Acknowledgments

First of all, I would like to thank Michael Scholz for the close supervision over the last years. Thank you for making sure that I kept on track with my topic and for your attention to detail. I benefited greatly during my PhD from your expertise in radiobiological modeling and large experience in clinical applications. Thank you also to Thomas Friedrich for your great support especially concerning mathematical formulations of many physical and methodological challenges I encountered within my work. You revealed to me a completely new view on how to approach and solve several biophysical problems. I would also like to thank the whole group "radiobiological modeling" not only for fruitful discussions in our weekly meetings but also for several fun events outside GSI.
Furthermore, I would like to thank Prof. Barbara Drossel, Prof. Alexander Löwer and Prof. Thorsten Kröll for agreeing to be part of my PhD examination committee.
Next, I would like to thank Uli Weber, who was a member of my PhD committee. I really appreciate your unbiased view on the results of my work in our biannual meetings. Thank you for asking the right critical questing, which helped me to keep an eye on the big picture of the whole project. Thank you Kilian Baumann and Larissa Derksen from THM in Gießen for our little collaboration concerning Geant4-DNA topics. I really enjoyed our discussions concerning challenges of simulations of track structures and low-energetic electrons. I appreciated the comfortable environment in our meetings. I would like to thank Nick Henthorn, who spent a part of his postdoc in our group. Thank you for supporting me with my first Geant4-DNA Monte Carlo simulations and also for fun times at the Christmas market.
A great thanks also goes out to my friends from GSI. First of all, to my former colleague Antonia. Thank you for many great discussions at GSI, a lot of fun in our free time and for becoming such a good friend. Furthermore, I would like to thank Celine and Kim for lots of little talks in the office and fun events outside work. I especially miss our lively lunch times in the canteen before the corona restrictions. Besides, I would like to say "Thank you" to Claire from the space radiation physics group not only for proofreading my thesis, but also for helping me to take my mind off work by joining me for nice walks on the weekends. Thank you, Felix, for proofreading my work and also for several inspiring discussions about RBE related topics.
I felt very welcomed in the whole GSI Biophysics department since the start of my masters thesis in 2017. I had an absolutely amazing time thanks to the motivated, highly interdisciplinary and international group. For most of my questions I found experts in our department, who could help me to answer them. Next, I would like to thank the graduate school HGS-HIRe for the support during my PhD. I really appreciated the opportunity to attend the highly-qualified softskill courses and summer schools as well as the financial support for trips to scientific conferences.
Finally, a great "Thank you" goes out to my family. Thank you for always believing in me and for supporting me in my decisions. Thank you for many nice weekend events, especially in the last months of my thesis, when I could hardly take my mind of the last issues to solve. Thank you especially to my boyfriend Matthias for always listening to my ideas and thoughts about the thesis and for being a great home office colleague for the full last year. Thank you for being such a kind partner at all times. I really appreciate your bright mind, which is unique on this planet.

A. Appendix

LQ parameters for cell survival after mixed fields irradiation

Tab. A.1.: Fit parameters for experimental data obtained according to the LQ model for pure photon and ion irradiations. If the LQ fit resulted in a negative value for β, a purely exponential fit is applied, which is stated by "0" in the column for the β parameter.

ID	α_γ /Gy^{-1}	β_γ /Gy^{-2}	D_t /Gy	α_i /Gy^{-1}	β_i /Gy^{-2}
1	0.186±0.014	0.027±0.002	11.6 ±0.8	0.944±0.063	0.014±0.016
2	0.186±0.014	0.027±0.002	11.6 ±0.8	0.944±0.063	0.014±0.016
3	0.182±0.033	0.016±0.004	16.5 ±3.9	0.833±0.014	0
4	0.182±0.033	0.016±0.004	16.5±3.9	0.833±0.014	0
5	0.113±0.024	0.029±0.003	8.3±1.1	0.360±0.266	0.164±0.073
6	0.113±0.024	0.029±0.003	8.3±1.1	0.797±0.057	0.106±0.018
7	0.195±0.009	0.028±0.001	11.7±0.5	0.592±0.008	0.047±0.002
8	0.189±0.023	0.013±0.002	20.0±3.2	0.838±0.008	0
9	0.189±0.023	0.013±0.002	20.0±3.2	0.838±0.008	0
10	0.189±0.023	0.013±0.002	20.0±3.2	0.838±0.008	0
11	0.189±0.023	0.013±0.002	20.0±3.2	0.838±0.008	0
12	0.189±0.023	0.013±0.002	20.0±3.2	0.838±0.008	0
13	0.189±0.023	0.013±0.002	20.0±3.2	0.795±0.023	0
14	0.189±0.023	0.013±0.002	20.0±3.2	0.795±0.023	0

Tab. A.2.: Fit parameters for experimental data obtained according to the LQ model for mixed irradiations. If the LQ fit resulted in a negative value for β, a purely exponential fit is applied, which is stated by "0" in the column for the β parameter.

ID	α_{mix} /Gy^{-1}	β_{mix} /Gy^{-2}	c
1	0.461±0.026	0.037±0.004	
2	0.318±0.015	0.018±0.002	
3	0.547±0.047	0.013±0.008	
4	0.428±0.044	0.015±0.005	
5	0.411±0.099	0.025±0.019	
6	0.43±0.010	0.059±0.023	
7	0.280±0.013	0.047±0.002	
8	0.486±0.009	0.016±0.001	
9	0.244±0.030	0.007±0.002	0.794±0.840
10	0.229±0.037	0.013±0.004	2.089±0.088
11	0.219±0.045	0.016±0.006	3.010±0.072
12	0.381±0.004	0	3.569±0.021
13	1.049±0.018	0	1.222±0.053
14	1.347±0.057	0	2.291±0.165

Tab. A.3.: LEM simulation data: Fit parameters according to the LQ model for the data points obtained with the LEM. Both, the results for the pure simulated ion curves and also for the mixed survival curves, are given. If the LEM predictions resulted in $\beta < 10^{-3}$, the value for the corresponding LQ parameter is given as "0".

	LEM - Ion		**LEM - Mix**		
ID	α_{i} /Gy^{-1}	β_{i} /Gy^{-2}	α_{mix} /Gy^{-1}	β_{mix} /Gy^{-2}	c_{mix}
1	0.378±0.010	0.019±0.001	0.267±0.008	0.025±0.001	
2	0.378±0.010	0.019±0.001	0.225±0.004	0.025±0.000	
3	0.668±0.003	0.002±0.000	0.473±0.005	0.008±0.001	
4	0.668±0.003	0.002±0.000	0.309±0.009	0.013±0.001	
5	0.595±0.003	0.003±0.000	0.453±0.005	0.008±0.000	
6	0.852±0.001	0	0.647±0.005	0.003±0.000	
7	0.501±0.010	0.021±0.001	0.274±0.010	0.031±0.002	
8	0.822±0.003	0.001±0.000	0.573±0.004	0.007±0.000	
9	0.822±0.003	0.001±0.000	0.271±0.011	0.008±0.001	0.793±0.023
10	0.822±0.003	0.001±0.000	0.323±0.021	0.007±0.002	2.021±0.045
11	0.822±0.003	0.001±0.000	0.394±0.017	0.002±0.002	2.766±0.036
12	0.822±0.003	0.001±0.000	0.440±0.013	0.000±0.001	3.414±0.029
13	0.822±0.003	0.001±0.000	0.991±0.010	0	1.378±0.036
14	0.822±0.003	0.001±0.000	1.058±0.012	0	2.442±0.043

Tab. A.4.: ZRM and LAM simulation data: Fit parameters according to the LQ model for the simulated mixed survival curves. If the model predictions resulted in $\beta < 10^{-3}$, the value for the corresponding LQ parameter is given as "0".

	ZRM			LAM		
ID	α_{mix} /Gy^{-1}	β_{mix} /Gy^{-2}	c_{mix}	α_{mix} /Gy^{-1}	β_{mix} /Gy^{-2}	c_{mix}
1	0.565±0.000	0.020±0.000		0.598±0.002	0.021±0.000	
2	0.338±0.000	0.024±0.000		0.364±0.002	0.025±0.000	
3	0.508±0.000	0.004±0.000		0.532±0.002	0.009±0.000	
4	0.312±0.000	0.010±0.000		0.330±0.002	0.014±0.000	
5	0.237±0.000	0.083±0.000		0.237±0.000	0.083±0.000	
6	0.455±0.000	0.061±0.000		0.470±0.000	0.061±0.000	
7	0.308±0.007	0.039±0.001		0.313±0.008	0.039±0.001	
8	0.514±0.000	0.003±0.000		0.533±0.002	0.008±0.000	
9	0.189±0.000	0.013±0.000	0.788±0.000	0.230±0.000	0.012±0.000	0.789±0.001
10	0.189±0.000	0.013±0.000	1.978±0.000	0.277±0.001	0.011±0.000	1.980±0.001
11	0.189±0.000	0.013±0.000	2.765±0.000	0.303±0.001	0.010±0.000	2.768±0.001
12	0.189±0.000	0.013±0.000	3.461±0.000	0.323±0.001	0.010±0.000	3.463±0.001
13	0.795±0.000	0	1.270±0.000	0.913±0.004	0	1.319±0.013
14	0.795±0.000	0	2.344±0.000	0.973±0.005	0	2.407±0.017

Measurement and simulation data used for DSB induction model optimization

Tab. A.5.: Data used to optimize the free parameters κ and t in the DSB induction model.

Publication	**Radiat.**	E_{e} **/eV**	**Unit**	**#DSB**	**Method**	**Ref.**	**RBE**
Kuhne et al. 2005 [166]	CK	286	$(\mathrm{Gy{\cdot}Gbp})^{-1}$	12.1	Exp	Co_γ	2.0
Frankenberg et al. 1986 [176]	CK	287	$(\mathrm{Gy{\cdot}Da{\cdot}10^{11}})^{-1}$	1.6	Exp	Co_γ	3.8
	AlK	1486	$(\mathrm{Gy{\cdot}Da{\cdot}10^{11}})^{-1}$	0.93	Exp	Co_γ	2.2
O'Neill et al 1997 [40]	AlK	1486	$(\mathrm{Gy{\cdot}Da{\cdot}10^{11}})^{-1}$	1.3	Exp	Co_γ	2.6
	AlK	1486	$(\mathrm{Gy{\cdot}Da{\cdot}10^{11}})^{-1}$	1.6	Exp	Co_γ	1.6
Fulford et al. 2001 [177]	AlK	1486	$(\mathrm{Gy{\cdot}Da{\cdot}10^{11}})^{-1}$	2.7	Exp	Co_γ	1.7
Folkard et al 1993 [178]	e	50	$(\mathrm{Gy{\cdot}Da{\cdot}10^{11}})^{-1}$	3.19	Exp	-	-
	e	100	$(\mathrm{Gy{\cdot}Da{\cdot}10^{11}})^{-1}$	1.93	Exp	-	-
	e	250	$(\mathrm{Gy{\cdot}Da{\cdot}10^{11}})^{-1}$	2.2	Exp	-	-
	e	500	$(\mathrm{Gy{\cdot}Da{\cdot}10^{11}})^{-1}$	2.95	Exp	-	-
	e	2000	$(\mathrm{Gy{\cdot}Da{\cdot}10^{11}})^{-1}$	2.6	Exp	-	-
	e	1000	$(\mathrm{Gy{\cdot}Da{\cdot}10^{11}})^{-1}$	2.6	Exp	-	-
	e	1500	$(\mathrm{Gy{\cdot}Da{\cdot}10^{11}})^{-1}$	2.7	Exp	-	-
Fayard et al 2002 [179]	USXR	250	$(\mathrm{Gy{\cdot}Da{\cdot}10^{11}})^{-1}$	0.89	Exp	-	-
	USXR	380	$(\mathrm{Gy{\cdot}Da{\cdot}10^{11}})^{-1}$	0.9	Exp	-	-
	USXR	760	$(\mathrm{Gy{\cdot}Da{\cdot}10^{11}})^{-1}$	1.17	Exp	-	-
Eschenbr. et al 2007 [180]	USXR	250	$(\mathrm{Gy{\cdot}Da{\cdot}10^{11}})^{-1}$	0.56	Exp	-	-
	USXR	380	$(\mathrm{Gy{\cdot}Da{\cdot}10^{11}})^{-1}$	0.63	Exp	-	-
	USXR	760	$(\mathrm{Gy{\cdot}Da{\cdot}10^{11}})^{-1}$	0.85	Exp	-	-

Publication	Radiat.	E_e /eV	Unit	#DSB	Method	Ref.	RBE
	USXR	250	$(Gy{\cdot}Da{\cdot}10^{11})^{-1}$	0.79	Exp	-	-
	USXR	380	$(Gy{\cdot}Da{\cdot}10^{11})^{-1}$	0.7	Exp	-	-
	USXR	760	$(Gy{\cdot}Da{\cdot}10^{11})^{-1}$	1.64	Exp	-	-
Botchway et al 1997 [181]	AlK	1486	$(Gy{\cdot}Da{\cdot}10^{11})^{-1}$	2.2	Exp	Co_γ	2.6
	CuL	960	$(Gy{\cdot}Da{\cdot}10^{11})^{-1}$	2.6	Exp	Co_γ	3.0
De Lara 2001 [182]	CK	280	$(Gy{\cdot}cell)^{-1}$	112	Exp	Co_γ	2.7
	AlK	1490	$(Gy{\cdot}cell)^{-1}$	77	Exp	Co_γ	1.9
	TiK	4550	$(Gy{\cdot}cell)^{-1}$	56	Exp	Co_γ	1.4
	CuL	960	$(Gy{\cdot}cell)^{-1}$	94	Exp	Co_γ	2.3
Friedland et al. 1999 [183]	AlK	1500	$(Gy{\cdot}Gbp)^{-1}$	13.3	Sim	Co_γ	1.6
	CK	280	$(Gy{\cdot}Gbp)^{-1}$	11.3	Sim	Co_γ	1.4
Nikjoo et al. 1997 [30]	e	100	$(Gy{\cdot}Da{\cdot}10^{11})^{-1}$	1.5	Sim	e	2.9
	e	300	$(Gy{\cdot}Da{\cdot}10^{11})^{-1}$	2.3	Sim	e	4.5
Nikjoo et al. 1999 [134]	e	300	$(Gy{\cdot}Da{\cdot}10^{11})^{-1}$	2.3	Sim	e	4.5
Nikjoo et al. 1997 [30]	e	500	$(Gy{\cdot}Da{\cdot}10^{11})^{-1}$	2	Sim	e	3.9
	e	1000	$(Gy{\cdot}Da{\cdot}10^{11})^{-1}$	2	Sim	e	3.9
	e	1500	$(Gy{\cdot}Da{\cdot}10^{11})^{-1}$	1.8	Sim	e	3.5
Nikjoo et al. 1999 [134]	e	1500	$(Gy{\cdot}Da{\cdot}10^{11})^{-1}$	1.8	Sim	e	3.5
Nikjoo et al. 1997 [30]	e	4500	$(Gy{\cdot}Da{\cdot}10^{11})^{-1}$	2.9	Sim	e	5.7
Nikjoo et al. 1999 [134]	e	4500	$(Gy{\cdot}Da{\cdot}10^{11})^{-1}$	1.2	Sim	e	2.4
Nikjoo et al. 2002 [142]	e	4500	$(Gy{\cdot}Da{\cdot}10^{11})^{-1}$	0.56	Sim	e	1.1
	e	10000	$(Gy{\cdot}Da{\cdot}10^{11})^{-1}$	0.51	Sim	e	1
	e	20000	$(Gy{\cdot}Da{\cdot}10^{11})^{-1}$	0.5	Sim	e	1.0
	e	50000	$(Gy{\cdot}Da{\cdot}10^{11})^{-1}$	0.48	Sim	e	0.9
	e	100000	$(Gy{\cdot}Da{\cdot}10^{11})^{-1}$	0.51	Sim	e	1.0
Watanabe et al. 2002 [143]	e	100	$(Gy{\cdot}Da{\cdot}10^{11})^{-1}$	1.7	Sim	e	1.7
	e	1000	$(Gy{\cdot}Da{\cdot}10^{11})^{-1}$	2.5	Sim	e	2.5
	e	10000	$(Gy{\cdot}Da{\cdot}10^{11})^{-1}$	2	Sim	e	2.0
	e	1000000	$(Gy{\cdot}Da{\cdot}10^{11})^{-1}$	0.99	Sim	e	1.0
Goodhead 1989 [121]	Ck	280	$(Gy{\cdot}Da{\cdot}10^{11})^{-1}$	1.9	Sim	e	3.0
	AlK	1500	$(Gy{\cdot}Da{\cdot}10^{11})^{-1}$	1.32	Sim	e	2.1
	TiK	4500	$(Gy{\cdot}Da{\cdot}10^{11})^{-1}$	0.83	Sim	e	1.3
	e	100000	$(Gy{\cdot}Da{\cdot}10^{11})^{-1}$	0.64	Sim	e	1.0
Friedland et al. 1998 [184]	e	14.98	$(Gy{\cdot}Da{\cdot}10^{11})^{-1}$	0	Sim	e	0
	e	20.07	$(Gy{\cdot}Da{\cdot}10^{11})^{-1}$	0	Sim	e	0
	e	25.13	$(Gy{\cdot}Da{\cdot}10^{11})^{-1}$	0	Sim	e	0.0
	e	32.27	$(Gy{\cdot}Da{\cdot}10^{11})^{-1}$	0.31	Sim	e	0.2
	e	40.03	$(Gy{\cdot}Da{\cdot}10^{11})^{-1}$	0.49	Sim	e	0.3
	e	49.69	$(Gy{\cdot}Da{\cdot}10^{11})^{-1}$	0.73	Sim	e	0.4
	e	64.49	$(Gy{\cdot}Da{\cdot}10^{11})^{-1}$	0.94	Sim	e	0.6
	e	80.12	$(Gy{\cdot}Da{\cdot}10^{11})^{-1}$	1.27	Sim	e	0.8
	e	99.59	$(Gy{\cdot}Da{\cdot}10^{11})^{-1}$	1.64	Sim	e	1.0
	e	199.61	$(Gy{\cdot}Da{\cdot}10^{11})^{-1}$	2.54	Sim	e	1.6
	e	299.76	$(Gy{\cdot}Da{\cdot}10^{11})^{-1}$	2.74	Sim	e	1.7
	e	503.04	$(Gy{\cdot}Da{\cdot}10^{11})^{-1}$	2.83	Sim	e	1.7
	e	995.62	$(Gy{\cdot}Da{\cdot}10^{11})^{-1}$	2.61	Sim	e	1.6

Publication	Radiat.	E_e /eV	Unit	#DSB	Method	Ref.	RBE
	e	3010.8	$(Gy{\cdot}Da{\cdot}10^{11})^{-1}$	2.13	Sim	e	1.3
	e	9978.58	$(Gy{\cdot}Da{\cdot}10^{11})^{-1}$	1.81	Sim	e	1.1
	e	29939.54	$(Gy{\cdot}Da{\cdot}10^{11})^{-1}$	1.63	Sim	e	1.0
	e	99584.97	$(Gy{\cdot}Da{\cdot}10^{11})^{-1}$	1.63	Sim	e	1.0
Zhang et al. 2010 [135]	e	280	$(Gy{\cdot}Da{\cdot}10^{11})^{-1}$	1.15	Sim	-	-
	e	1500	$(Gy{\cdot}Da{\cdot}10^{11})^{-1}$	0.87	Sim	-	-
Charlton et al. 1989 [144]	e	280	$(Gy{\cdot}Da{\cdot}10^{11})^{-1}$	2.64	Sim	-	-
	e	1500	$(Gy{\cdot}Da{\cdot}10^{11})^{-1}$	2.06	Sim	-	-
Matsuya 2019 [185]	e	10	$(Gy{\cdot}Da{\cdot}10^{11})^{-1}$	0	Sim	e	0
	e	14.99	$(Gy{\cdot}Da{\cdot}10^{11})^{-1}$	0	Sim	e	0
	e	20.05	$(Gy{\cdot}Da{\cdot}10^{11})^{-1}$	0.01	Sim	e	0.0
	e	24.94	$(Gy{\cdot}Da{\cdot}10^{11})^{-1}$	0.02	Sim	e	0.0
	e	30.06	$(Gy{\cdot}Da{\cdot}10^{11})^{-1}$	0.12	Sim	e	0.1
	e	39.79	$(Gy{\cdot}Da{\cdot}10^{11})^{-1}$	0.27	Sim	e	0.2
	e	50	$(Gy{\cdot}Da{\cdot}10^{11})^{-1}$	0.43	Sim	e	0.3
	e	65.5	$(Gy{\cdot}Da{\cdot}10^{11})^{-1}$	0.7	Sim	e	0.5
	e	81.46	$(Gy{\cdot}Da{\cdot}10^{11})^{-1}$	0.92	Sim	e	0.6
	e	101.31	$(Gy{\cdot}Da{\cdot}10^{11})^{-1}$	1.22	Sim	e	0.9
	e	203.13	$(Gy{\cdot}Da{\cdot}10^{11})^{-1}$	2.62	Sim	e	1.8
	e	304.55	$(Gy{\cdot}Da{\cdot}10^{11})^{-1}$	3.23	Sim	e	2.3
	e	506.55	$(Gy{\cdot}Da{\cdot}10^{11})^{-1}$	3.2	Sim	e	2.3
	e	1005.21	$(Gy{\cdot}Da{\cdot}10^{11})^{-1}$	2.7	Sim	e	1.9
	e	3021.83	$(Gy{\cdot}Da{\cdot}10^{11})^{-1}$	1.97	Sim	e	1.4
	e	10078.18	$(Gy{\cdot}Da{\cdot}10^{11})^{-1}$	1.62	Sim	e	1.1
	e	30296.88	$(Gy{\cdot}Da{\cdot}10^{11})^{-1}$	1.47	Sim	e	1.0
	e	101043.78	$(Gy{\cdot}Da{\cdot}10^{11})^{-1}$	1.42	Sim	e	1.0
Pater et al. 2014 [141]	e	280	$(Gy{\cdot}Gbp)^{-1}$	8.1	Sim	e	2.1
	e	1500	$(Gy{\cdot}Gbp)^{-1}$	6.1	Sim	e	1.6
	e	5000	$(Gy{\cdot}Gbp)^{-1}$	5.4	Sim	e	1.4
	e	10000	$(Gy{\cdot}Gbp)^{-1}$	4.6	Sim	e	1.2
	e	220000	$(Gy{\cdot}Gbp)^{-1}$	3.8	Sim	e	1.0
Bernal et al. 2009 [145]	CK	280	$(Gy{\cdot}Gbp)^{-1}$	9	Sim	Co_γ	1.8
	AlK	1500	$(Gy{\cdot}Gbp)^{-1}$	8.7	Sim	Co_γ	1.8

Simplified approach to describe DSB induction process A

In the derived model two physical processes are considered to describe the induction of DSBs by secondary electrons (See Sec. 5.1.1). Process A includes the production of DSBs by ionizations of tertiary electrons and by electrons of later generations. In comparison to that, process B describes the origin of DSBs, which are a consequence of two ionizations in close vicinity directly induced by a secondary electron along its path. The DSB induction by process A is determined by consideration of the specific tertiary electron spectrum induced by secondary electrons of a fixed kinetic energy. The amount of DSBs is finally obtained by weighting the tertiary electron spectrum by the expected amount of DSBs per tertiary electron in dependence on their energy. Next to this approach a second approach was followed and tested in which the mean tertiary electron

energy was determined directly from the mean energy calculated from the tertiary electron energy spectra. The amount of DSBs was assumed to follow a linear relation with the mean tertiary electrons' kinetic energy. Thus, the DSB yield per path length traveled by the secondary electron through process A can be calculated by:

$$Y_{\mathrm{l,DSB,A}}(E_{\mathrm{e}}) = \kappa_1 \cdot \overline{E}_{\mathrm{t}}(E_{\mathrm{e}}) \cdot \rho(E_{\mathrm{e}})\,, \tag{A.1}$$

with the ionization density ρ and the mean energy of tertiary electrons $\overline{E}_{\mathrm{t}}$ liberated by a secondary electron of kinetic energy E_{e}. The alternative description of process A exhibits the advantage that the formalism is slightly simpler as only the mean energy of the tertiary electrons is considered for the determination of the number of induced DSBs. In contrast to that, in the original approach the full tertiary electron spectra are included in the analysis. On the other hand, the alternative approach requires an additional fit parameter κ_1 that describes the amount of DSBs induced per tertiary electron in dependence on the mean tertiary electron energy. As a result, for the optimization of the free model fit parameters a third parameter needs to be determined, which increases the computation time of the optimization algorithm. The values for the obtained fit parameters are listed in Tab. A.6 for a completely free fit and for two options of a fixed value of the threshold distance t. The values are in the same range as for the original model, which confirms the applicability of both approaches. However, the original approach was applied within this work as it describes the underlying physics more precisely due to the explicit consideration of the tertiary electron spectra.

Tab. A.6.: Three sets of optimized values for the free parameters κ_1, κ and t in the DSB induction model with the alternative description of process A. (i. = ionization)

Set	**Description**	$\boldsymbol{\kappa_1}$ /(DSB/eV^{-1}/i.)	$\boldsymbol{\kappa}$ /(DSB/cluster)	$\boldsymbol{t}$ /nm	$\overline{\boldsymbol{Y}_{\mathbf{D,DSB,ref}}}$ /(DSB/Gy)
Default	Free fit	$9.167{\cdot}10^{-6}$	$5.054{\cdot}10^{-4}$	10.866 (=36.94 bp)	30.001
Set A	t fixed	$1.087{\cdot}10^{-5}$	$7.306{\cdot}10^{-4}$	2.94 (=10 bp)	29.999
Set B	t fixed	$9.792{\cdot}10^{-6}$	$5.479{\cdot}10^{-4}$	7.35 (=25 bp)	30.033

The DSB yield per path length and the local RBE according to the three fit parameter sets are depicted in Fig. A.1. By comparing the depicted DSB yield per path length to the same quantity in the original approach as depicted in Fig. 5.2, it is visible that both approaches show total DSB yields of the same shape and magnitude. Process A, however, which is less pronounced at small electron energies, shows a steeper decrease towards small electron energies in the original approach. This is due to the fact, that tertiary electron spectra are considered specifically. These spectra are calculated by MC simulations, which exhibit an ionization threshold of ≈12 eV. Below that, no tertiary electrons are liberated and thus, also no DSBs can be induced. In the alternative approach presented here, the mean tertiary electrons' energy is determined before the corresponding quantity is linearly interpolated between 12 and 0 eV. The local RBE follows a similar shape for both approaches and only diverges in the absolute values of the maximum RBE at ≈80 eV. Whereas the maximum local RBE values for the original approach are in the order of ≈2.5 the alternative approach leads to maximum values of ≈3.0 (See Fig. 5.9 for original approach).

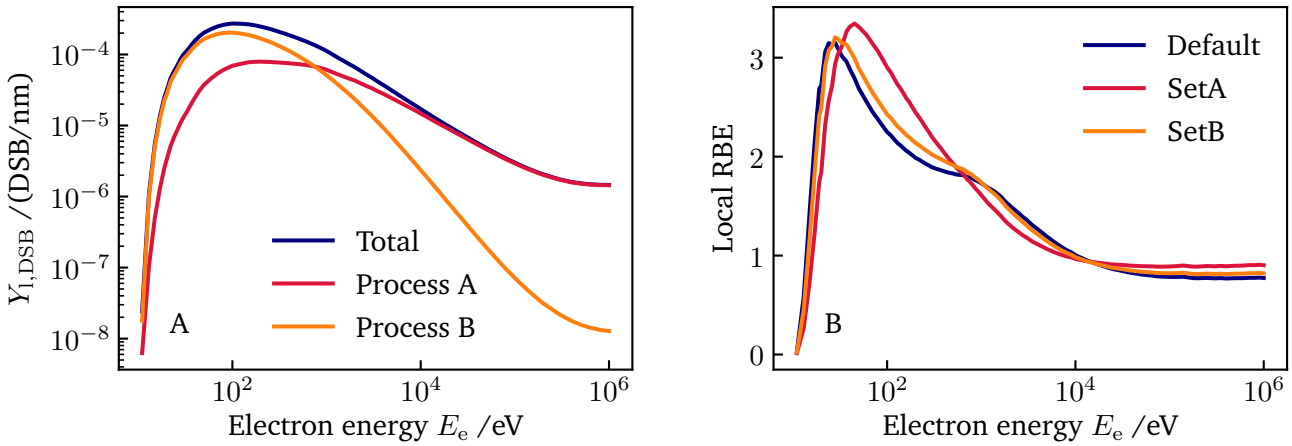

Fig. A.1.: DSB yield per path length and local RBE of electrons as a function of electron energy for the three sets of parameters for κ_1, κ and t as listed in Tab. A.6.